

Polytechnic Institute of New York

DOE/ET/11056-T3
Aerodynamics Laboratories

& **MASTER**

Electrical Engineering
Department

RECEIVED BY TIC APR 9 1981

Research and Development Studies for
MHD/Coal Power Flow Train Components

DOE Contract No. AC01-78ET11056
(Formerly ET-78-C-01-3084)

Technical Progress Report
for the Period 1 Sept. 79 - 31 Aug. 80

Prepared for
U.S. Dept. of Energy
MHD Div. of Fossil Energy
Washington, D.C. 20545

Principal Investigator: Martin H. Bloom

Participating Senior Staff:

M.H. Bloom
B. Cheo
S. Kuo
S. Lederman
E. Levi
M. Matalon
P. Sforza
Z. Zabar

Polytechnic Institute of New York
Aerodynamics Laboratories and Electrical Engineering Dept.
Long Island Center, Rt. 110, Farmingdale, N.Y. 11735

POLY M/AE Report No. 80-33

DISCLAIMER

This report was prepared as an account of work sponsored by an agency of the United States Government. Neither the United States Government nor any agency Thereof, nor any of their employees, makes any warranty, express or implied, or assumes any legal liability or responsibility for the accuracy, completeness, or usefulness of any information, apparatus, product, or process disclosed, or represents that its use would not infringe privately owned rights. Reference herein to any specific commercial product, process, or service by trade name, trademark, manufacturer, or otherwise does not necessarily constitute or imply its endorsement, recommendation, or favoring by the United States Government or any agency thereof. The views and opinions of authors expressed herein do not necessarily state or reflect those of the United States Government or any agency thereof.

DISCLAIMER

Portions of this document may be illegible in electronic image products. Images are produced from the best available original document.

The following pages are an exact representation of what is in the original document folder.

Research and Development Studies for
MHD/Coal Power Flow Train Components

DOE Contract No. AC01-78ET11056
(Formerly ET-78-C-01-3084)

Technical Progress Report
for the Period 1 Sept. 79 - 31 Aug. 80

CONTENTS

	Page
Introduction	1
Work Plan	1
Technical Progress	3
a. Power Take-off and MHD Channel	3
b. Flow Modeling	13
c. Diagnostic System	14
Appendices List	16
Appendices	

DISCLAIMER

This book was prepared as an account of work sponsored by an agency of the United States Government. Neither the United States Government nor any agency thereof, nor any of their employees, makes any warranty, express or implied, or assumes any legal liability or responsibility for the accuracy, completeness, or usefulness of any information, apparatus, product, or process disclosed, or represents that its use would not infringe privately owned rights. Reference herein to any specific commercial product, process, or service by trade name, trademark, manufacturer, or otherwise, does not necessarily constitute or imply its endorsement, recommendation, or favoring by the United States Government or any agency thereof. The views and opinions of authors expressed herein do not necessarily state or reflect those of the United States Government or any agency thereof.

INTRODUCTION

The aim of this program is to contribute to certain facets of the development of the MHD/coal power system, and particularly the CDIF of DOE with regard to its flow train. Consideration is given specifically to the electrical power take-off, the diagnostic and instrumentation systems, the combustor and MHD channel technology, and electrode alternatives. Within the constraints of the program, high priorities were assigned to the problems of power take-off and the related characteristics of the MHD channel, and to the establishment of a non-intrusive, laser-based diagnostic system. The next priority was given to the combustor modeling and to a significantly improved analysis of particle combustion. Electrode studies were held in abeyance, being assigned a low priority here by necessity.

A revised work plan consistent with the planned effort level was provided for the period prior to 31 Aug. 79 in Polytechnic's communication to DOE/MHD. This revised work plan enumerated the following tasks:

WORK PLAN

- I. Power take-off
 - A. Evaluate current and voltage consolidation schemes.
 - B. Design prototype consolidation schemes.
- II. Combustor
 - a. Undertake orientation studies
 - b. Check simple design codes in current use
 - c. Initiate effort to place in operation an equilibrium chemistry combustion code for hydrocarbons.

III. MHD Channel

- a. Evaluate current-distribution effects in a one-dimensional analysis.
- b. Evaluate boundary layer effects in a two-dimensional model.

IV. Diagnostics and Instrumentation

- a. Purchase laser, data acquisition and data analysis equipment for a laboratory set-up leading to a prototype design of a non-intrusive diagnostic system.
- b. Check out equipment delivered, and evaluate its performance relative to vendor's claims.
- c. Design system for measuring compositions, temperatures and velocities relevant to electrical conductivity in the MHD channel and relevant to combustion-effectiveness and environmental effects in an MHD/coal system type of environment. Consider both spontaneous Raman and "CARS" systems.
- d. Provide documentation leading to the setting up of a field-operational system.
- e. Obtain preliminary data in laboratory flows.

V. Gaseous electrodes (Hold in abeyance).

It should be noted that the MHD boundary layer task (III b.) was only carried to the set-up stage. Work on solving the governing equations numerically was held in abeyance. One reason for this was that a "target of opportunity" was perceived with respect to an analysis of particle combustion of carbon, which could be

improved substantially by the use of newly-developed asymptotic methods. It was considered important to achieve this gain in a timely manner. Therefore the MHD boundary layer task was postponed, and the particle combustion analysis was pursued. The results were very successful, and will be depicted in the body of this report. The combustion analysis is relevant to the Combustor task (II).

The other tasks enumerated were carried forth reasonably within the plan for the period up to 31 Aug. 78, as set forth in the Technical Progress Report for that period. However, the work of that period pointed to the need for continued efforts, essentially along the same topical lines as those enumerated above. This then formed the basis for the work plan for the period from 1 Sept. 79 - 31 Aug. 80. It is expected that the original work plan envisaged on this program, which was planned for a more extensive effort, will be revised for consistency with the work plan now being implemented.

Using the prior Technical Progress Report on this contract as a reference, we shall now describe the work in the enumerated areas during the period prior to 31 Aug. 80.

TECHNICAL PROGRESS

a. Power Take-Off (Work Plan item I) and MHD Channel (Work Plan Item III)

In this area, the prior technical report devoted Part I, Section 2 to a "Study of Voltage Consolidation Schemes". This section included a circuit invented by L. Birenbaum, and a combined inversion and consolidation circuit by Z. Zabar. Further Part I, Section 3 set forth a "Preliminary Design for the Power Take-Off

of Singly-Loaded Magnetohydrodynamic Channels" by E. Levi. This was subsequently published in the Journal of Energy Conversion and Management (Vol. 20, pp. 33-39, 1979). Pergamon Press. A copy is attached as Appendix A. Finally Part I, Section 3 dealt with "Electrical Non-Uniformities in Diagonally Connected Generators", by S. Kuo, B. Cheo, and E. Levi. This has been published in the Journal of Energy (AIAA Vol. 4, No. 2, p. 88, Mar-Apr. 1980). A copy is attached as Appendix B. The further work in this connection has resulted in two additional papers, one dealing with true two-dimensional effects in the MHD channel, and the other with effects of wall leakage on non-uniformities in diagonally connected MHD generators.

The first new paper is entitled "Two-Dimensional Power Take-Off Analysis in Diagonal Conducting Wall Channels" by S. Kuo and E. Levi. This has been submitted for publication.

It shows that a true two-dimensional analysis of diagonal-conducting-wall MHD channels leads to design principals for the power take-off and good quantitative agreement with the experimental data. Also it investigates analytically the effect of power take-off schemes on the output power level, and finds that it is possible to design the electrical circuit of the channel with passive elements in the take-off region, and thus to achieve a fairly even load current distribution under changing load conditions. This analysis explains quirks in the current distributions which were observed in the seventh test of the U-25B facility of the USSR. The complete paper is included here as Appendix C.

The second paper is entitled: "The Effect of Wall Leakage on

Non-Uniformities in Diagonally Connected MHD Generators" by S. Kuo, E. Levi and B. Cheo. This paper has been accepted for publication by the Journal of Energy of AIAA. The entire paper is included here as Appendix D.

In this paper the effect of wall leakage, symmetric as well as asymmetric is examined in the linear and non-linear regimes.

It is found that

1. The range of wavelength in the nonuniformities is reduced, and in the asymmetric anode and cathode case splits into 2 separate pass-bands. The mechanism responsible for quenching the short wave-length non-uniformities is non-linear mode-mode coupling in the case of wall leakage, and the wall leakage itself when it is strong.
2. Depending upon wavelength, forward waves can propagate both upstream and downstream, backward waves only upstream. In the case of asymmetric characteristics, the spacial non-uniformities are accompanied by temporal oscillations.
3. The growth rate of instabilities is minimal when the leakage at the cathode wall is four times that of the anode wall. This can occur naturally due to preferential deposition of seed at the cathodes, or by adding a voltage divider externally, as has been the USSR practice in the U-25 facility.
4. In all cases, a resistance introduced in the diagonal bars reduces the growth rate by a constant. The frequency of the temporal oscillations is inversely proportional to the inductance of the frame circuit.

In connection with power consolidation of the MHD generator, studies were undertaken of the dynamic behavior of the channel and in particular of the arcs, because the previously-derived equivalent circuit did not describe adequately the channel interface under transient conditions.

Z. Zabar, in collaboration with H. M. Abramowitz (a doctoral student, also associated with the Bell Laboratories) are taking the following approaches to analyze power take-off schemes:

In order to limit the available techniques, it was decided to limit the analysis to a Faraday connection scheme for power take-off. The major emphasis is to examine the channel and the consolidation circuitry under discontinuous current from each electrode pair and compare the results to a channel utilizing continuous current takeoff schemes. The expectation is to chop the current between different electrode pairs and reduce the size and cost of the consolidation circuitry.

Of major importance to the analysis is the channel model utilized. A number of models have been used and this area is constantly undergoing change as the computer simulation results are examined. Some models are only relevant to a continuous current consolidation scheme containing resistive type elements to simulate the plasma impedance and voltage drop. The final model must contain a good model for the transient conditions in the boundary layer (Fig. 1) and must contain parasitic inductance and capacitance of the plasma.

The thrust of the study is in the power consolidation scheme of the MHD channel. The study can be subdivided into two categories 1) that of continuous current loads and 2) switched loads

attached to each electrode pair. Figure 2 depicts the continuous current takeoff scheme having each electrode pair attached to a constant load. Figure 3 depicts the same channel with a single load and current loading equivalent to Figure 2.

Channels containing 3, 5, and 10 electrode pairs have been analyzed. This analysis resulted in the following:

1. Channel edge - The end electrode pairs of the simulated channel must be graded to an increasing impedance to reduce the effect of the abrupt discontinuity.
2. Current loading - The grading effect was also necessary to limit the number of electrode pairs contributing to the output current (Fig. 3). The internal impedance of the plasma model was insufficient to limit the current contribution of the exterior electrode pairs.
3. Channel Consolidation limit - Resulting from the current flow in opposite direction in the anode and cathode areas of a single load condition (Fig. 3). Along one path the resistive voltage drop adds to the Hall voltage produced and causes breakdown conditions (Fig. 4). This puts a practical limit on the amount of current available to a single electrode pair and sets an upper boundary on the number of electrode pairs that can be consolidated in this fashion.

The final phase is to add switching elements to each electrode pair and switch a single load between these electrode pairs. Figure 5 depicts a simplified scheme using this approach.

Studies are presently under way analyzing the effects of the switching process on adjacent electrode pairs and the transients

that concern practical application as the parasitic inductance of the load and plasma parasitics are included. Presently a scheme utilizing 3 electrode pair sets are under investigation to provide information necessary to the potential feasibility of this approach. Switching times, frequency, and waveforms will be examined to provide several output waveforms and provide the analysis necessary to optimize the power consolidation in terms of size and cost.

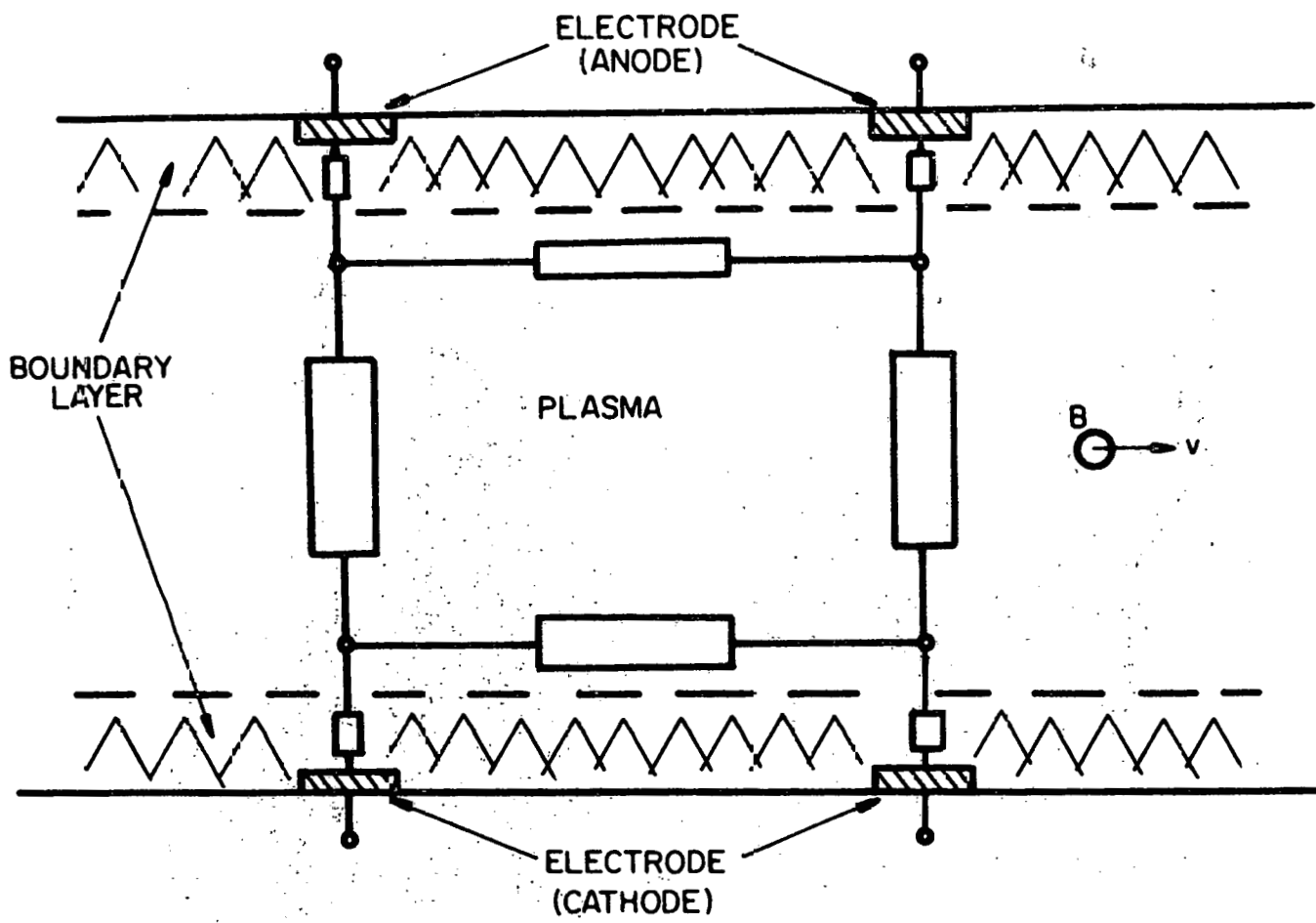


FIG. I GENERALIZED MODEL OF MHD CHANNEL

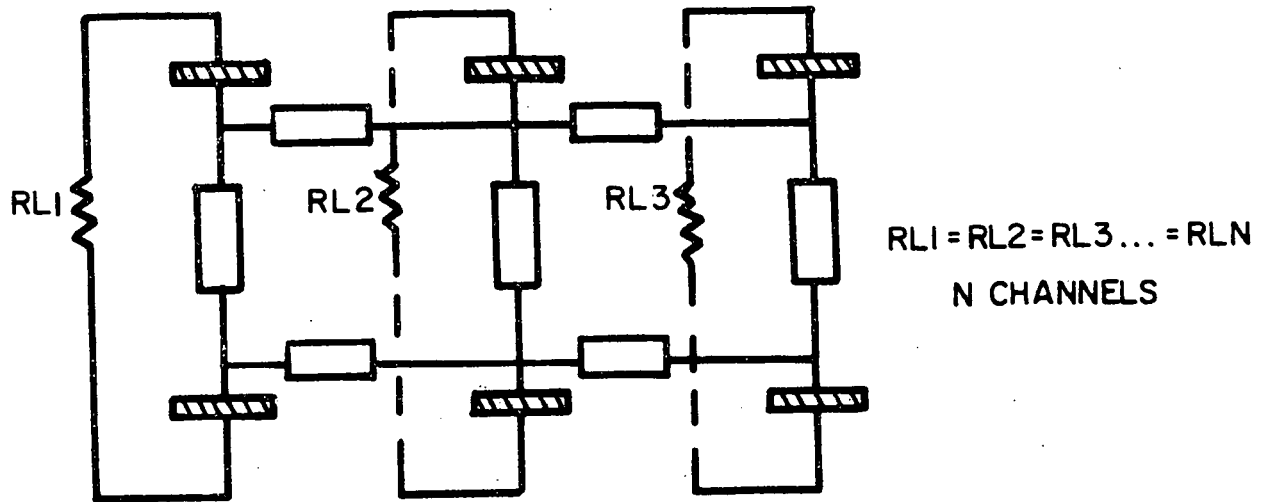


FIG. 2 FARADAY CHANNEL CONTINUOUS CURRENT FROM EACH ELECTRODE PAIR

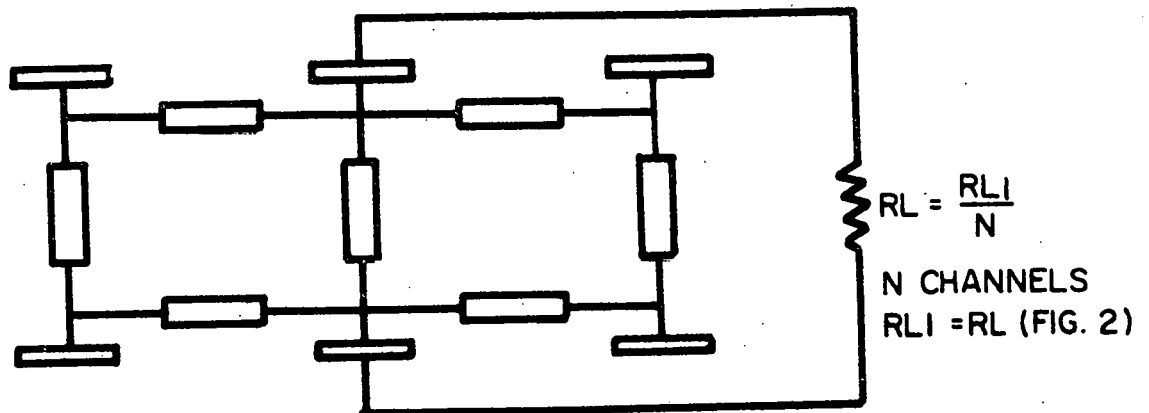


FIG. 3 FARADAY CHANNEL SINGLE-CONTINUOUS CURRENT

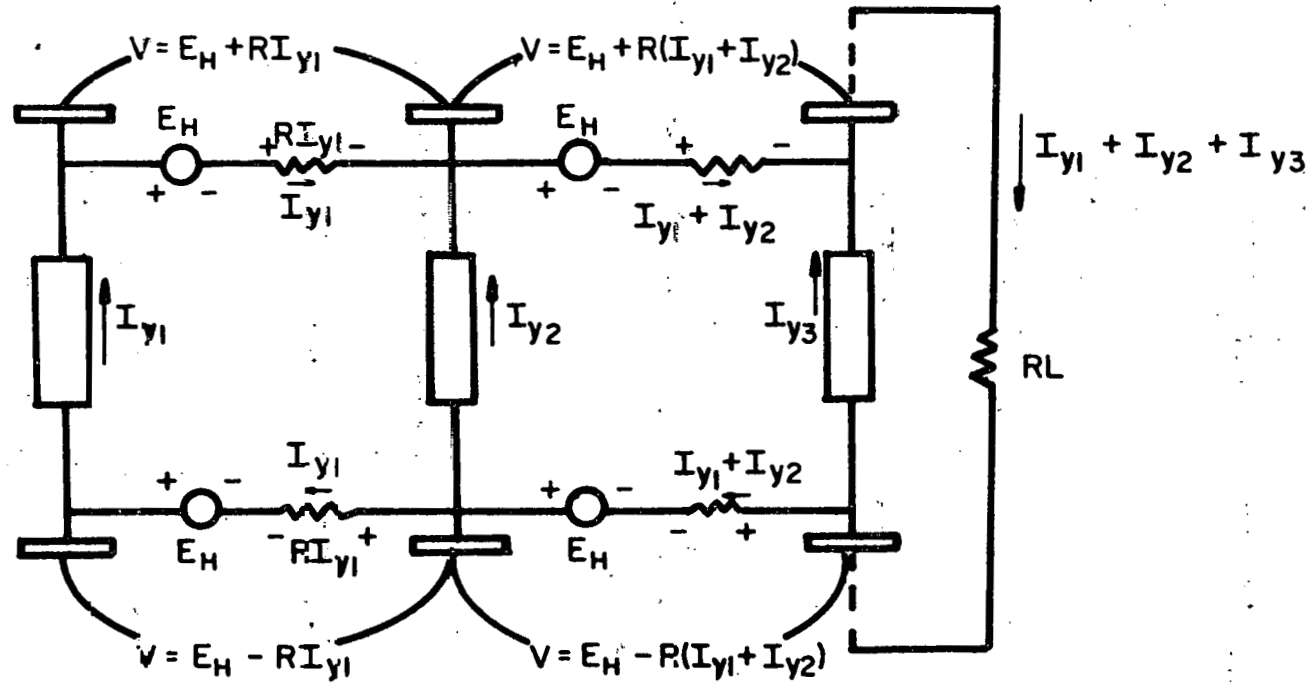
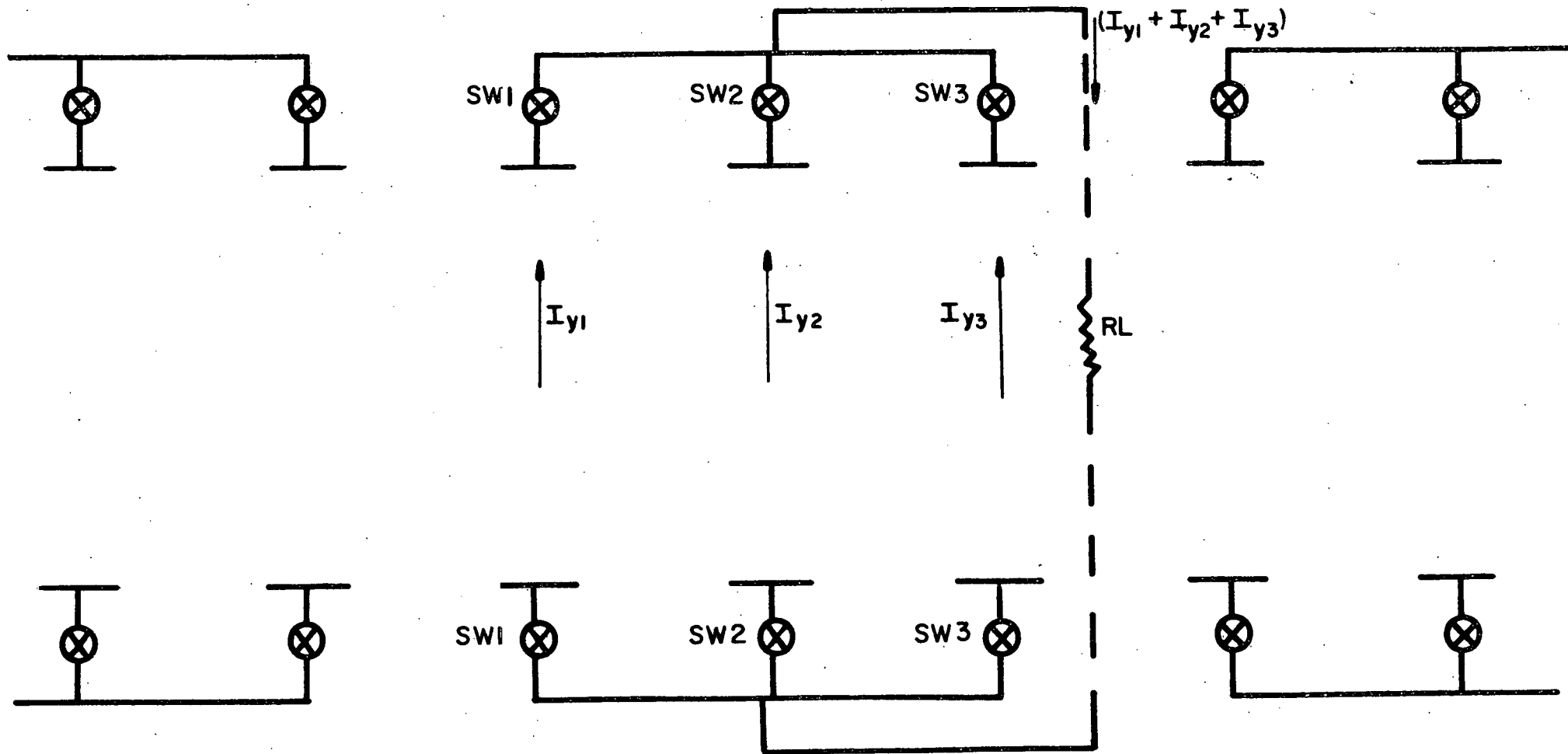


FIG. 4 HALL VOLTAGE DIFFERENTIAL - SINGLE LOAD OUTPUT



**FIG. 5 FARADAY CHANNEL - SWITCHED OUTPUT,
3 ELECTRODE PAIRS PER LOAD**

b. Flow Modeling (Work Plan Item II)

The effort in this area has resulted in a report entitled a "One-Dimensional Flow Model for Coal Combustors" by W. O. Peter and P. M. Sforza. This includes a code to deal with chemical equilibrium. Radiative heat losses can also be accounted for. The results obtained thus far are consistent with those available in the current literature. A preliminary version of this report is included here as Appendix G.

The combustion of a solid particle, in this case carbon, has been the subject of an innovative analysis by M. Matalon. In this work quasi-steady burning of a particle which undergoes gasification at its surface is dealt with by the use of asymptotic methods (for large values of the activation energy). The model considers a homogeneous reaction in the gas phase. The burning rate M is found as a function of the gas phase Damköhler number D_g for the whole range $0 < D_g < \infty$. The monotonic $M(D_g)$ curve, obtained for relatively very hot or very cold particles, describes the gradual transition from frozen flow to equilibrium. For moderate particle temperatures the transition is abrupt and the $M(D_g)$ curve is either S-shaped or Z-shaped. In the former the burning is enhanced at ignition while in the latter it is slowed down; this depends on the relative importance of the two competitive surface reactions. At extinction, the reverse is true: burning is slowed down in the case of an S curve and is enhanced in the case of a Z curve.

c. Diagnostic System (Work Plan Item IV)

The features of the program to develop a laser-based non-intrusive system for the diagnostics of the hostile flow environment of the MHD/Coal power system was described in the prior Technical Progress Report. The fundamental principles and five alternative arrangements were depicted therein. The general aim is to provide spatially-resolved, and to a certain extent time-resolved measurements of flow concentrations and temperatures, with a view toward identifying flow non-uniformities and turbulent characteristics, as well as more gross behavior. Clearly the complex nature of the high-temperature, three-dimensional, particle and slag-laden flow within the confined flow passage present problems of great difficulty in this regard. However, it is believed that the worthwhile goal here can be achieved. Appendix E. by S. Lederman presents a general view of this work in addition to the prior Progress Report.

In the present period, an effort has been focussed on using a single high-power pulsed laser source to drive simultaneously a CARS system and a spontaneous Raman scattering system. This simultaneous feature provides a great amount of information at a particular point and time. The system has worked successfully with a Ruby laser and a stimulated Raman cell to generate the Stokes line of the specie of interest for the CARS measurement. With this Stokes line as one of the laser lines of the CARS system, the Ruby laser line is employed as the driving line for CARS. A note describing this system has been submitted by S. Lederman and C. Posillico for publication. It is entitled "A Unified Spontaneous Raman and CARS System" and is included here as Appendix F.

Another version of this system is also nearing completion. It involves doubling the Ruby laser line, pumping a tunable dye laser to generate the Stokes line of the specie of interest and to be subjected to CARS, and utilizing the remainder to generate the spontaneous Raman spectrum of the flow field.

A replacement for the previously-tried multichannel spectrum analyzer which was not satisfactory for our purpose, has now been incorporated into the system. The new analyzer is an OMAII, and appears to be working properly.

A laboratory set-up for generating coal flames is being constructed, so that the diagnostic system can be applied to them.

A method has been devised for reducing substantially the size of the laser system which would eventually be applied to a flow system in the field. Likewise a method for maintaining clear viewing windows in a practical environment has been proposed and will be developed further.

This work has resulted in a series of 3 papers being published in the journal "Combustion and Flame". These papers, listed below, are included here as Apendices H, I and J.

- H. Matalon, Moshe: "Complete Burning and Extinction of a Carbon Particle in an Oxidizing Atmosphere". POLY M/AE Report 80-16.
- I. Matalon, Moshe: "Weak Burning and Gas-Phase Ignition About a Carbon Particle in an Oxidizing Atmosphere". POLY M/AE Report 80-21.
- J. Matalon, Moshe: "Combustion of a Solid Particle". POLY M/AE Report 80-30.

LIST OF APPENDICES

- Appendix A: "Preliminary Design for the Power Take-off of Singly-Loaded Magnetohydrodynamic Channels" by Enrio Levi.
- Appendix B: "Electrical Nonuniformities in Diagonally Connected Generators" by S. Kuo, B. Cheo, and E. Levi.
- Appendix C: "Two-dimensional Power Take-off Analysis in Diagonal Conducting Wall Channels" by S. Kuo and E. Levi.
- Appendix D: "Wall Leakage Effect on Non-uniformities in Diagonal MHD-Channels" by S. Kuo, E. Levi, and B. Cheo.
- Appendix E: "Developments in Laser-Based Diagnostics" by S. Lederman.
- Appendix F: "A Unified Spontaneous Raman and Cars System" by S. Lederman and C. Posillico.
- Appendix G: "One-Dimensional Flow Model for Coal Combustors" by Walter Peter and Dr. Pasquale M. Sforza.
- Appendix H: "Complete Burning and Extinction of a Carbon Particle in an Oxidizing Atmosphere" by Moshe Matalon.
- Appendix I: "Weak Burning and Gas-Phase Ignition About a Carbon Particle in an Oxidizing Atmosphere" by Moshe Matalon.
- Appendix J: "Combustion of a Solid Particle" by Moshe Matalon.

PRELIMINARY DESIGN FOR THE POWER TAKE-OFF OF SINGLY-LOADED MAGNETOHYDRODYNAMIC CHANNELS

ENRICO LEVI

Polytechnic Institute of New York, 333 Jay Street, Brooklyn, NY 11201, U.S.A.

(Received 17 July 1979)

Abstract—A one-dimensional analysis of diagonal-conducting-wall MHD channels leads to design principles for the power take-off and good qualitative agreement with experimental data. Analytical refinements which account for two- and three-dimensional effects enhance the accuracy of performance predictions.

MHD Power take-off Diagonal conducting wall channels Diode scheme

NOMENCLATURE

- a = proportionality coefficient (equation 1)
 A = cross-sectional area, anode
 A_k = collecting area of the cathode
 b = scaling parameter (equation 9)
 B = applied magnetic field induction
 E = electric field intensity
 E_d = equivalent electric field associated with effective voltage drop
 I = current in the channel
 I_l = load current
 $I_{l,n}$ = nominal load current
 J = current density
 K = current entering the channel, cathode
 M = number of overlapping electrodes
 N = number of conducting diodes
 r = ballast resistance per unit length
 R = ballast resistance in each branch
 u = flow velocity
 x, y, z = coordinates
 Δ = increment
 $\beta = -\arctan(E_y/E_x)$
 σ = conductivity
 $\varphi = \tan \beta$
 Ω = Hall parameter
Subscripts
 f = forward
 l = load
 l,n = nominal load
 m = summation index
 n = branch number
 s = short-circuit
 x, y = x, y directions

I. INTRODUCTION

One of the major problems standing in the way of economic and reliable generation of electric power by magnetohydrodynamic (MHD) means stems from the need to segment the anodes and the cathodes of the channel. Continuous electrodes would short-circuit the Hall potential which results from the anisotropy of the plasma. A very large number of electrically insulated loads is required, when each pair of opposite electrode segments is separately loaded (Faraday

connection). The Hall component of field, however, being in the direction of flow, skews the equipotential surfaces. It becomes then possible to connect the anode and cathode segments in series by means of diagonal links. This connection scheme was first proposed by de Montardy [1] and realized by Dicks [2] in his diagonal conducting wall (DCW) channel, which consists of a stack of metallic electrode modules, similar to window frames, insulated from one another. The diagonal connection permits the use of a single load, as shown in Fig. 1. Hence, power take-off in a DCW channel should, in principle, be a simple process. However, two important problems still remain to be solved. The first is the optimization of the positions of the inlet and outlet connections with changing load. The second is the distribution of load current over a number of electrodes.

A scheme for the power take-off in DCW channels has been proposed by Brogan [3] for the U.S. channel to be tested in the Soviet U-25 facility. The same scheme is currently being used in the U-25 B channels [4].

The scheme, which is sketched in Fig. 1, takes advantage of the low Hall field prevailing in the fringing field of the magnet, where the inlet and outlet regions of the channel are located. In these regions the resistive voltage drop caused by the flow of the load current within the channel may exceed the motion-induced voltage [5]. As a result, in each of these regions there exists a frame at which the Hall field vanishes; in the outer sections of the channel lying beyond these frames, the Hall field changes sign and is in the same direction as the load current. It follows that, there, part of the output power of the generator is reabsorbed.

In order to avoid this loss of output, the outer sections should be rendered ineffective; in the Brogan scheme for connection to the load, the outer frames are short-circuited. In so doing, the additional objective of distributing the load current among a number of leads and frames is achieved.

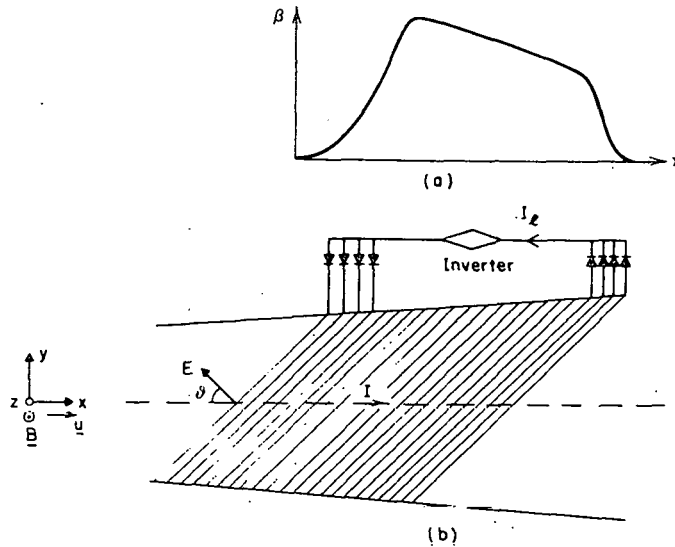


Fig. 1. DCW channel configuration; (a) Magnetic field profile; (b) Power take-off and coordinate system.

The location of the point of field reversal and, hence, the number of leads to be short-circuited varies with changing operating conditions. To allow for these variations a diode is inserted in each lead. All diodes located between the inlet and outlet points of field reversal are expected to block the passage of current [3].

The main advantage of this scheme is its simplicity and, therefore, its low cost and reliability.

One disadvantage of the short-circuit scheme is the strong tendency toward nonuniformity of current distribution among the leads. This is undesirable, because it may lead to overload and damage in some of the power take-off electrodes and frames [6].

Furthermore, such a nonuniformity is propagated with the active region of the channel by the diagonal connections. The problem is compounded by the natural trend of diagonal channels to distribute the current unevenly among adjacent frames, as a result of the arc-mode transfer of current to the electrodes [7]. Dangerous current concentrations may result when the wavelength of the nonuniformity, impressed on the take-off leads, corresponds to the wavelength of one of the natural non-uniformity modes of the channel.

For this reason, it has been Soviet practice to insert ballast, or equalizing resistors in series with diodes. The presence of these resistors, however, changes the fundamental mode of operation of the power take-off and complicates the task of the designer. The Hall voltage profile becomes a function of the resistor values and the designer is faced with the task of determining the size of the resistors, in addition to determining the location and number of leads.

The following sections present an analysis of the diode scheme for power take-off, that is based on the one-dimensional theory of diagonal channel perform-

ance [8]. The range of validity of this analysis is checked against data obtained in tests with the #1 channel of the U-25 B facility. Also included are guiding principles for the design of such a power take-off.

II. BASIC RELATIONS

Consider the configuration and vector orientation of Fig. 1. The Hall field E_x can be expressed as a function of the current I flowing in the channel [8], and cast in the form

$$E_x = a(I - I_s) \quad (1)$$

where

$$a = \frac{1 + \Omega^2}{(1 + \phi^2)A\sigma}$$

$$I_s = \frac{A\sigma}{1 + \Omega^2} (\Omega + \phi)(uB - E_d)$$

Ω = Hall parameter

σ = conductivity

E_d = equivalent electric field associated with effective electrode voltage drop

A = channel cross section

$\phi = -E_y/E_x = \tan \theta$

The current I_s corresponds to short-circuit conditions ($E_x = 0$); it is a function of the axial coordinate x and is indicative of the profiles of velocity, plasma conductivity, and magnetic field.

To establish the constraints imposed by the connections external to the channels, we examine Fig. 2 which represents the inlet section; similar relations

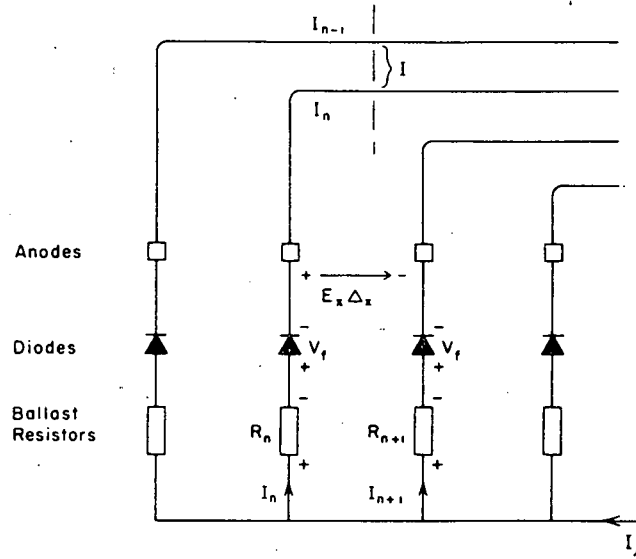


Fig. 2. Inlet connection.

hold for the outlet. Applying Kirchhoff's law to the n th and $(n + 1)$ th branches, we obtain:

$$E_x \Delta x = R_{n+1} I_{n+1} + V_f - R_n I_n - V_f$$

or

$$E_x = \frac{R_{n+1} I_{n+1} - R_n I_n}{\Delta x} \quad (2)$$

where

R = resistance

V_f = forward voltage drop of diode

Δx = segmentation pitch

Moreover, we observe that

$$I_n > 0 \quad (3)$$

$$I = \sum_1^n I_m \quad (4)$$

$$I_t = \sum_1^N I_m \quad (5)$$

where N is the number of conducting diodes. This set of equations completely determines the system.

III. DESIGN CONSIDERATIONS

The nominal load current $I_{t,n}$ should be evenly spread among a number of leads, approximately equal to the number of parallel branches in the channel; i.e. the number of overlapping electrodes. If we let this number be M then the current in each is specified as

$$I_m = \frac{I_{t,n}}{M} \quad (6)$$

In order to determine the value of the resistances and the location of the power take-off connection, we observe that, in order to minimize the external ohmic losses, E_x should be minimized, and, in order to avoid absorption of power in the channels, E_x should be negative.

Since, according to equation (1), E_x is proportional to the difference between I and I_s , it is expedient to plot these currents.

For example, the situation prevailing at the inlet section of the channel (Fig. 2) is depicted in Fig. 3 for various locations of power take-offs, having uniform current distributions among the leads. It is seen that location 1 is undesirable, since there exists a large region where E_x is positive and hence the channel absorbs power. Location 3 is also undesirable, since the channel is not fully utilized, while position 2

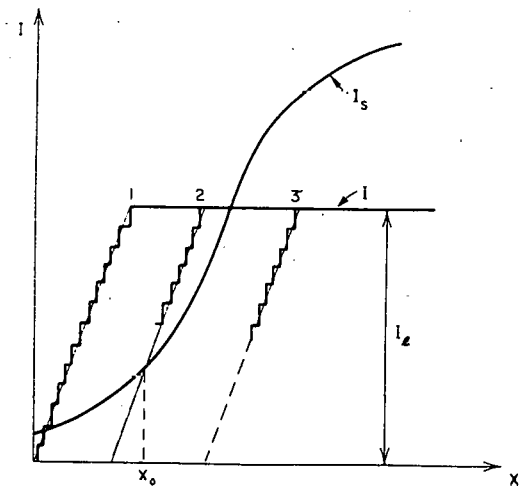


Fig. 3. Current in the channel and short-circuit current.

seems to be a reasonable compromise. The branch corresponding to position x_0 will require no resistance while the branch corresponding to an arbitrary point x will require a resistance:

$$R = \left| \frac{1}{I_m} \int_x^{x_0} E_x dx \right| \quad (7)$$

The resistance is thus proportional to the area contained between the curves I and I_s .

It follows that I_s and, hence, the field of the magnet should be designed, so as to decay over a region corresponding to the extent of the overlapping electrodes.

The resistances given by equation (7) are the minimum resistances required to give the desired current distribution. The same uniform distribution could be obtained by adding equal resistances in all branches. This may be required in order to avoid dangerous current concentrations under off-design and fault conditions.

IV. CURRENT DISTRIBUTION IN THE ABSENCE OF RESISTORS

In order to get a feeling of the current distribution for a given set of resistances we note that the pitch Δx is usually small as compared with the extent of overlapping electrodes. In the limit of $\Delta x \rightarrow 0$, the set formed by equation (1) through (7) becomes:

$$K_y \frac{dr}{dx} + r \frac{dK_y}{dx} = \frac{1 + \Omega^2}{(1 + \phi^2)A\sigma} \left[\int_0^x K_y dx - I_s \right] \quad (8)$$

where K_y is the current entering the channel per meter length in the y direction and $r(x) = R\Delta x$ is the external ballast resistance of a unit length. In general, this is a second order linear differential equation with variable parameters.

It is instructive to consider first the conditions contemplated for the U.S. U-25 channel when r and therefore E_x vanish identically. Equating the left hand side of equation (8) to zero, we find that K_y is given by the slope of I_s and, hence, a reasonably uniform current distribution obtains when the connection is located in a region in which I_s varies linearly. This conclusion is independent of the value of load current.

We also observe that the condition $E_x = 0$ forces the current I in the channel to assume the value I_s everywhere. It follows that the first diode to block is the one for which I_s is greater than the load I_l . More diodes start conducting as I_l increases. Therefore, enough diodes must be installed to carry the maximum load current I_l ; otherwise, the last conducting diode will carry the difference between I_l and I_s .

V. CURRENT DISTRIBUTION WITH EQUAL RESISTORS

Equation (8) can be solved in closed form when Ω is small and the branch resistors are equal [$r = f(x)$].

This is the case in the power take-off for the U-25 B channel.

Denoting the Fourier transform with a bar on top we have:

$$\bar{K}_y = \frac{p[-b^2 \bar{I}_s + K_y(0)]}{(p+b)(p-b)} \quad (9)$$

where

$$b^2 = \frac{1 + \Omega^2}{(1 + \phi^2)A\sigma r} = \frac{a}{r}$$

Assuming a linear rise in I_s or

$$I_s = \frac{K_s}{p^2} \quad (10)$$

we get

$$K_y = K_s + (K_y(0) - K_s) \cosh bx \quad (11)$$

and

$$I = \int_0^x K_y dx = K_s x + \frac{K_y(0) - K_s}{b} \sinh bx \quad (12)$$

Here, the second term to the right denotes the deviation from the case of ballast resistors and b , which is a measure of the ratio of internal to external resistance, becomes a scaling parameter.

We observe that the current density K_y is larger or smaller than the one corresponding to short circuit, depending on the initial value $K_y(0)$. Assuming that the conducting diodes range from $x = 0$ to $x = x_1$ and making $I = I_l$ in equation (12), we obtain:

$$K_y(0) = K_s + \frac{b(I_l - K_s x_1)}{\sinh bx_1} \quad (13)$$

We note that, for the design conditions $I_l = I_{l,n}$ it is possible to choose the number of diodes and hence x_1 , so that the current distribution is uniform. This conforms with the prediction of Section III, that a uniform distribution is not changed by the addition of arbitrary, but equal branch resistances. Any current overload will cause the distribution to increase rapidly with increasing x . If the number of diodes is adequate, then some will block. x_1 is then the unknown location of the last conducting diode, and is obtained by first making K_y equal to zero in equation (11). Then introducing the corresponding relation

$$\cosh bx_1 = \frac{K_s}{K_s - K_y(0)} \quad (14)$$

into equation (12), we can obtain x_1 from:

$$- \tanh bx_1 = \frac{b(I_l - K_s x_1)}{K_s} \quad (15)$$

The current is sketched in Fig. 4 for two different values I_{l_1} and I_{l_2} of the load current and under the assumption that the diode connection ranges over the

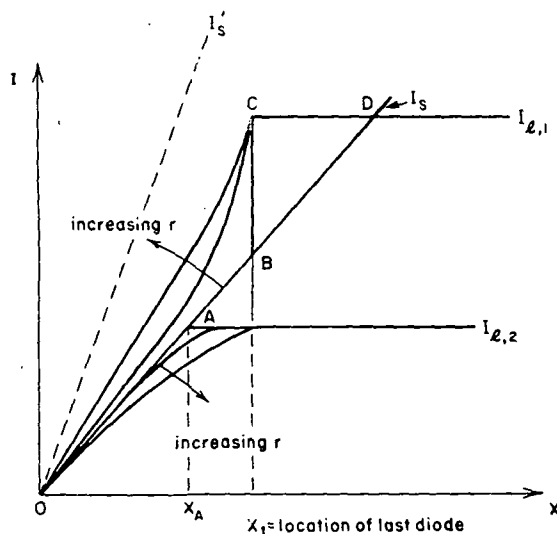


Fig. 4. Buildup of channel current in the inlet connection.

interval Ox_1 . We consider first the case of 'high' load current $I_{L,1}$. In the absence of ballast resistors ($r = 0$), the current builds up along the broken line OBC . Each diode carries the same current, except the last conducting diode which carries the additional current BC .

The current distribution becomes more uniform when ballast resistors are inserted. The higher the resistance r , the smoother the distribution. The whole region of the channel between O and D absorbs power.

Next we consider the case of 'low' load current $I_{L,2}$. In the absence of ballast resistors ($r = 0$), only the diodes in the interval Ox_A conduct; all carry the same current. Those between x_A and x_1 are blocking. With finite resistors ($r = 0$) more diodes become conducting and with increasing values of r , the current becomes more evenly distributed. The whole section of the channel between O and x_1 generates power.

Of course, the term 'high' or 'low' load current relates to the section of I_s cut-off by x_1 , i.e. the extent of the connection region. With a higher conductivity or a steeper magnetic field rise (e.g. line I'_s in Fig. 4) and the same $I_{L,1}$ and x_1 , the channel would behave as

in the 'low' load current case and there would be no power absorbing section.

VI. COMPARISON WITH EXPERIMENTAL DATA

The effect of the ballast resistors was checked during the fourth test in the U-25 B facility. Run #1998 was performed with ballast resistors of 0.5Ω (corresponding to $p = 0.014 \Omega \cdot m$) connected in series with the diodes and run #1999 with the resistors short-circuited. The current distribution in the inlet connection is shown in Fig. 5. A comparison with Fig. 4 demonstrates good quantitative agreement between theory and experiment, with particular reference to the smoothing effect of the ballast resistors.

Since none of the diodes blocks, the extent of the collecting region appears to be inadequate. The channel operates in the 'high' current regime and, with short-circuited diodes, the last conducting diode carries the difference between I_L and I_s . Therefore, under the conditions prevailing in the test, the inlet connection should have been moved downstream or more diodes added.

Alternatively, the short-circuit current I_s should have been increased by raising the conductivity, as explained in the previous section. Indeed, the general performance of the channel gives evidence that the effective conductivity never attained the design value. As it turned out, this low conductivity was caused by water and cold air leaks and by inhomogeneities in the plasma originating in the combustor and seed injector.

It follows that the quantitative analysis lends further support to the one-dimensional theory of power take-off. Nevertheless, the current in the outer diodes cannot be accurately predicted, especially in the outlet connection. The reason is that equation (1) was derived under the assumption that over the channel cross section A , the flow velocity u is constant and both the currents carried by the plasma and by the diagonal links are uniformly distributed.

These conditions, however, are not satisfied in the outer portions of the collection regions.

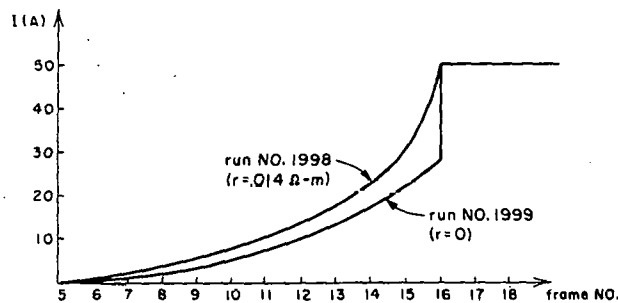


Fig. 5. Current distribution in the inlet connection of the U-25 B #1 channel.

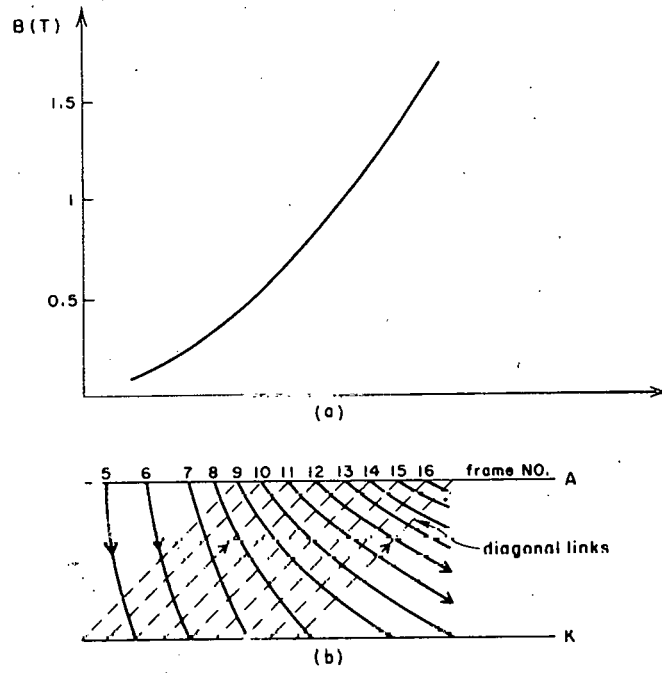


Fig. 6. Inlet connection for U-25 B #1 channel; (a) Magnetic field profile; (b) Current streamlines for $E_x = 0$.

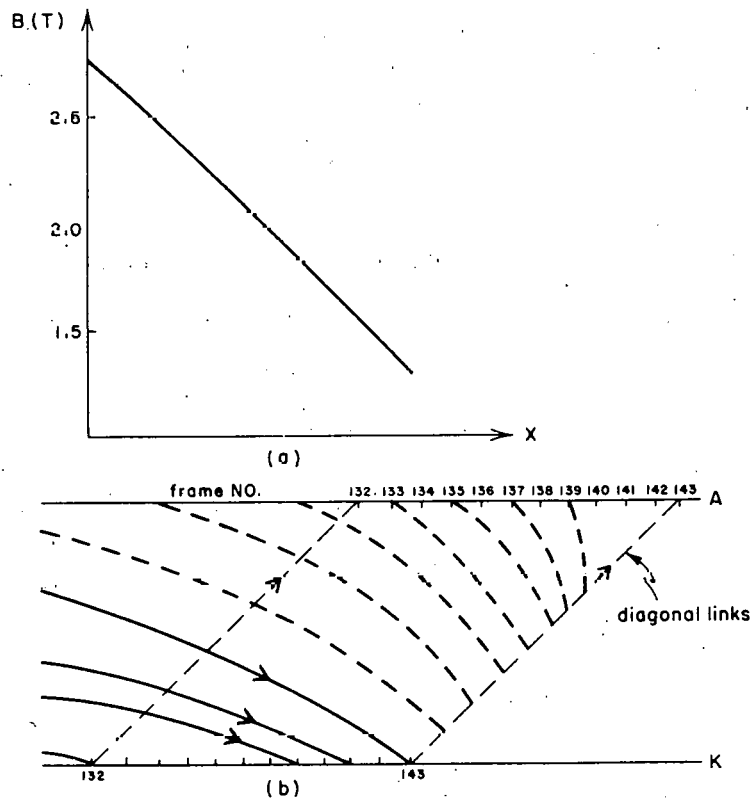


Fig. 7. Outlet connection for U-25 B #1 channel; (a) Magnetic field profile; (b) Current streamlines for $E_x = 0$.

When the ballast resistors are short circuited ($E_x = 0$), the x, y components of current density J satisfy the relation

$$J_x = \Omega J_y \quad (16)$$

and the current streamlines can be easily drawn. Two-dimensional plots of the current distribution in the U-25 B channel are shown in Figs 6 and 7. It is seen that with the inlet connection spanning frames 5 to 16, the diagonal links of the first six frames carry no current. In contrast, at the outlet, with the current being drawn from frames 132 to 143, very little current is carried by the plasma. The broken streamlines in Fig. 7 denote current filaments flowing near the side walls and turning in the z -direction towards the diagonal links. It was found that this three-dimensional effect of current collected by the sidebars could be accounted for, by increasing the collecting area A_k of the cathodes by 20%.

Under the assumption that the voltage drops in adjacent cathodes are equal, and hence compensate one another, the currents collected at the outer cathodes and carried by the diagonal links to the outer diodes under short circuit conditions can be determined as

$$I_n = 1.2 A_k J_y = 1.2 A_k \frac{\sigma u B}{1 + \Omega^2} \quad (17)$$

As seen from Fig. 7, the currents collected by these cathodes flow in the proximity of the wall. Therefore, the values of σ and u should be representative of the local conditions, i.e. they should characterize the boundary layer. When the measured values of I_n are introduced in equation (17), the product σu assumes a

value equal to about one quarter of the value presumed to prevail in the core.

It must be mentioned that u and Ω were calculated from measured values of the static pressure which were not too reliable. These uncertainties make further effort aimed at validating the theory unwarranted at this time.

In conclusion, it can be said that guidelines for the preliminary design of the diode scheme of power take-off for DCW channels have been established. A very conservative approach in terms of the number of diodes and value of ballast resistors is recommended, because at the present state-of-the-art in MHD, the plasma parameters are likely to depart significantly from the design conditions.

REFERENCES

- [1] A. de Montardy, *Proc. Int. Symp. MHD Electrical Power Generation*, Sept. 6-8, 1962, Newcastle-upon-Tyne, England. Paper No. 19. (1962).
- [2] J. B. Dicks, *Proc Fifth Symp. Engineering Aspects of MHD*, April 1-2, 1964, MIT Cambridge, Mass. (1964).
- [3] T. R. Brogan, J. A. Hill *et al.*, *Fourth U.S.-U.S.S.R. Colloquium on MHD Power Generation*, October 5-6, 1978, Washington, D.C. pp. 221-246 (1978).
- [4] V. A. Kirillin, A. E. Sheindlin *et al.*, *17th Symp. Engineering Aspects of Magnetohydrodynamics*. March 27-29, 1978, Stanford, Calif. pp. F1.1-F1.12 (1978).
- [5] Y. C. L. Wu, J. B. Dicks *et al.*, *AIAA JI* **6**, 1651-1657 (1968).
- [6] M. Ishikawa and Y. Hattoi, *Energy Conversion* **18**, 155-161 (1978).
- [7] A. Solbes and A. Lowenstein, *15th Symp. Engineering Aspects of Magnetohydrodynamics*. Philadelphia, Pa. (1976).
- [8] Y. C. L. Wu, *AIAA JI* **14**, 1362-1368 (1976).



AIAA 80-4051

Electrical Nonuniformities in Diagonally Connected Generators

S. Kuo, B. Cheo, and E. Levi

Reprinted from

Journal of Energy

Volume 4, Number 2, March-April 1980, Page 88

Copyright American Institute of Aeronautics and Astronautics, Inc., 1980. All rights reserved

Electrical Nonuniformities in Diagonally Connected Generators

S. Kuo,* B. Cheo,† and E. Levi‡

Polytechnic Institute of New York, Farmingdale, N. Y.

Experimental data show that stationary nonuniformities may occur at much longer wavelengths than the unstable ones predicted by the linear theory. A nonlinear analysis shows that the mechanism of mode coupling may be responsible for this occurrence. It is found that the instability regime extends over a much wider parameter range than previously determined. Analyses also show that over sections of the channel, the Hall field may diminish or even reverse.

Nomenclature

h	= width of the channel
h'	= $h \tan \theta$
H	= electrode length along magnetic field
I_0	= background dc current
P	= electrode segmentation pitch
x	= longitudinal coordinate
y	= transverse coordinate
θ	= angle of the diagonal link

I. Introduction

IT has been known for some time that the distribution of Hall potential along an MHD channel is not uniform.¹⁻⁴ This effect is due to the uneven distribution of current among the electrodes and leads to overvoltages between adjacent electrode segments. The result is a degradation in the performance of the MHD channel, with particular reference to its durability.

Solbes and Lowenstein¹ have performed a two-dimensional linear stability analysis of the MHD channel and have been able to explain the development of these spatial fluctuations in the Hall field in terms of the arc-mode transfer of current from the core region of the plasma to the electrodes. Their analysis determines the conditions for which the negative volt-ampere characteristics of the arc overcomes the ballasting resistance of the plasma and leads to current concentrations.

The eigenvalues characterizing the resistance of the freestream plasma are dependent upon the wavelength of the fluctuations. For long wavelengths, typically on the order of the generator length, the ballasting resistance is large, and, hence, the current distribution is linearly stable. As the wavelength decreases, however, the ballasting effect becomes weaker and the fluctuations grow with time. The fastest growing modes have wavelengths on the order of the segmentation pitch, and Solbes and Lowenstein have been able to show good agreement with the experimental evidence obtained in their diagonally connected Faraday channels.

In contrast, the diagonal conducting wall channels of the U-25 and U-25B facilities seem to be affected by spatial nonuniformities which may extend over a wavelength as large as the width of the channel.⁴ This type of channel is likely to

Received Oct. 19, 1979; revision received Feb. 11, 1980. Copyright © American Institute of Aeronautics and Astronautics, Inc., 1980. All rights reserved. Reprints of this article may be ordered from AIAA Special Publications, 1290 Avenue of the Americas, New York, N.Y. 10019. Order by Article No. at top of page. Member price \$2.00 each, nonmember, \$3.00 each. Remittance must accompany order.

Index categories: MHD; Boundary Layers and Convective Heat Transfer—Turbulent; Plasma Dynamics and MHD.

*Research Assistant Professor, Dept. of Electrical Engineering.

†Professor, Dept. of Electrical Engineering.

‡Professor, Dept. of Electrical Engineering, and Director of Power Engineering Institute.

be more prone to instability because the link connecting anode and cathode does not contain a ballasting resistance, as in the case of Faraday channels. Nevertheless, according to the linear analysis, the fastest growing modes are still those corresponding to the shortest wavelengths. Therefore the presence of longer and nearly stationary wavelengths is an indication that the mechanism of mode coupling, resulting from nonlinearities, is at play.

In this paper the nonlinear problem is considered. Of many nonlinearities in the governing equations, the nonlinear volt-ampere characteristic of the arc $V = \alpha I^{-1/2}$ is singled out for attention, because the arc is the most likely source of the instability. Following Solbes and Lowenstein,¹ we assume that the currents in the freestream plasma are rotation and divergence free. The currents flow from the plasmas to the electrodes through a nonlinear arc. A nonlinear differential-integral equation which governs the time evolution of a current perturbation at the electrode walls is formulated. In Sec. II, we demonstrate that a short wavelength linearly unstable mode may transfer energy into a long wavelength linearly stable mode, confirming the mode coupling mechanism mentioned earlier. In Sec. III, the time evolution of an initial current burst with a Gaussian spatial distribution is analyzed numerically using the nonlinear governing equation. A close form of the kernel which is different from that given in Ref. 1 is obtained by performing a contour integration in the k plane. The procedure is given in the Appendix. Numerical results show that within certain range of parameters a localized perturbation can spread and evolve into relatively long wavelength instabilities causing sections of the wall current at the electrodes to vanish. In Sec. IV the effect on the Hall field is studied. It is shown that the form of the instability arrived at in Sec. III may cause the Hall field to decrease and even to change signs at some places in the channel. Section V summarizes the main findings.

II. Coupling between Two Modes

The nonlinear analysis takes off from the Solbes and Lowenstein effort¹ and the same notation is used. Their Fig. 1 showing the dimensions of the generator and the external connection is repeated here for convenience.

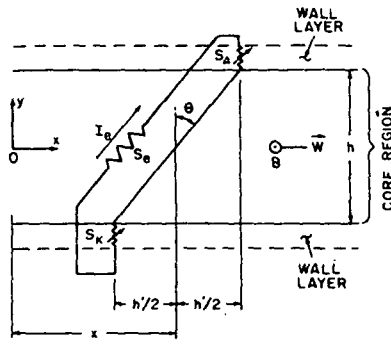
The equation governing the time evolution of the perturbation $\tilde{I}(x)$ in the load current distribution is

$$L \frac{\partial \tilde{I}}{\partial t} = \Delta \tilde{V} + \alpha \left(\frac{1}{\sqrt{I_0}} - \frac{1}{\sqrt{I_0 + I}} \right) \quad (1)$$

where

$$-\Delta \tilde{V} = \int_{-\infty}^{+\infty} \int_{-\infty}^{+\infty} \frac{\tilde{I}(x', t) \cos k(x-x') [\cosh(kh) - \cos(kh')]}{\pi \sigma H P k \sinh(kh)} \times dk dx'$$

Fig. 1 Two-dimensional channel model for study of nonuniformities.



is the ohmic voltage drop along the diagonal path in the freestream plasma resistance caused by the current fluctuation $\bar{I}(x')$. The second term in Eq. (1) represents the idealized nonlinear characteristics of the anode and cathode arcs which serves as sources for the instabilities. The other symbols are as shown in the Nomenclature.

To show how transfer of energy occurs from the short wavelength unstable modes to the long wavelength modes, we focus our attention on two modes only. We thus assume that the fluctuation current is

$$\bar{I} = \bar{I}_1(k_1) + \bar{I}_2(k_2)$$

where \bar{I}_1 is a long wavelength fluctuation ($k_1 \approx 0$) and \bar{I}_2 is a linearly unstable fluctuating mode. In general, it may represent a whole ensemble of unstable modes and k_2 represents its central wavenumber.

If we expand the second term of Eq. (1) to include the first nonlinearity, the coupled mode equations for \bar{I}_1 and \bar{I}_2 are obtained as:

$$L \frac{\partial \bar{I}_1}{\partial t} = - \left(S_1 - \frac{\alpha}{2\bar{I}_0^{3/2}} \right) \bar{I}_1 - \frac{3}{8} \frac{\alpha}{\bar{I}_0^{3/2}} (\bar{I}_1^2 + \langle \bar{I}_2^2 \rangle) \quad (3)$$

and

$$L \frac{\partial \bar{I}_2}{\partial t} = \left(\frac{\alpha}{2\bar{I}_0^{3/2}} - S_2 \right) \bar{I}_2 - \frac{3}{4} \frac{\alpha}{\bar{I}_0^{3/2}} \bar{I}_1 \bar{I}_2 \quad (4)$$

where

$$S_1 = h/\sigma HP (1 + \tan^2 \theta) = \text{freestream resistance for mode 1}$$

$$S_2 = 2/k\sigma HP = \text{freestream resistance for mode 2}$$

$$S_2 \langle \frac{1}{2} \alpha \bar{I}_0^{-3/2} \rangle \langle S_1 \rangle$$

$\langle \rangle$ = spatial average

where:

$$K(x-x') = \ell_n \left[\frac{\cosh \pi \left(\frac{x-x'}{h} \right) + \cosh(\pi \tan \theta)}{\cosh \left(\pi \frac{x-x'}{h} \right) - 1} \right]$$

$$- \pi \left(\frac{x-x'}{h} + \tan \theta \right) + \ell_n \left[\frac{\cosh \pi \left(\frac{x-x'}{h} \right) + \cosh(\pi \tan \theta)}{\cosh \left(\pi \frac{x-x'}{h} \right) - 1} \right]$$

$$+ \pi \left(\frac{x-x'}{h} - \tan \theta \right) + \ell_n \left[\frac{\cosh \pi \left(\frac{x-x'}{h} \right) + \cosh(\pi \tan \theta)}{\cosh \left(\pi \frac{x-x'}{h} \right) - 1} \right]$$

$$\ell_n \left[\frac{\cosh \left(\pi \frac{x-x'}{h} \right) + \cosh(\pi \tan \theta)}{\cosh \left(\pi \frac{x-x'}{h} \right) - 1} \right]$$

$$\text{for } \frac{x-x'}{h} < -\tan \theta$$

$$\text{for } -\tan \theta < \frac{x-x'}{h} < 0$$

$$\text{for } 0 < \frac{x-x'}{h} < \tan \theta$$

$$\text{for } \tan \theta < \frac{x-x'}{h}$$

We now observe that the term $\langle \bar{I}_2^2 \rangle$ in Eq. (3) provides a source of excitation for the long wavelength mode 1. As the amplitude \bar{I}_2 of the linearly unstable mode grows with time, \bar{I}_1 is excited to a negative value. This, in turn couples into mode 2 and enhances its growth rate, since the last term of Eq. (4) becomes positive. This explosive growth can be explained by noting that \bar{I}_1 causes the space invariant current to decrease. The lower value of current shifts the operating point of the arc toward a region in which the slope is more negative.

In order to show how the instability settles down to a stationary value, one might be tempted to include higher order nonlinear terms. However, if one did take those higher order nonlinear terms into account, the result would be the same, both \bar{I}_1 and \bar{I}_2 would grow absolutely. When they reach the levels

$$\bar{I}_1 \approx - [I_0 + \ell - \sqrt{\ell^2 + 2\ell I_0}] \quad (5)$$

and

$$I_{r0} \approx -\ell + \sqrt{\ell^2 + 2\ell I_0} \quad (6)$$

(where $\ell = 8(S_1 - \frac{1}{2}\alpha \bar{I}_0^{-3/2}) \bar{I}_0^{3/2} / 3\alpha$ and I_{r0} is the amplitude of \bar{I}_2), the polynomial expansion of the arc terms in Eq. (1) ceases to converge. Beyond this point, one should go back and re-examine the arc term $(1/\sqrt{I_0} - 1/\sqrt{I_0 + \bar{I}})$ in Eq. (1). Since \bar{I}_1 tends to suppress I_0 , one can contemplate a limiting situation in which $|I_0 + \bar{I}_1| \rightarrow 0$. In this case one has:

$$(I_0 + \bar{I})^{-1/2} \approx \bar{I}_2^{-1/2} \approx I_{r0}^{-1/2} \exp(-jk_2 x/2) \quad (7)$$

i.e., the k_2 mode loses energy to a subharmonic of double wavelength through this arc term. This implies that the instability may reach a stationary value before $|I_0 + \bar{I}_1| \rightarrow 0$.

The above discussions have not taken into consideration the effect of the positive slope region at low arc currents. This effect is accounted for by the numerical analysis of the dynamics of the nonuniformities, as is presented in the next section.

III. Time Evolution of Localized Nonuniformity

A more rigorous analysis must consider the whole spectrum of modes. By performing a contour integration in k (see the Appendix), the ohmic drop of the free plasma in Eq. (1) can be expressed as:

$$-\Delta \bar{V} = \frac{I}{\pi \sigma HP} \int_{-\infty}^{\infty} dx' K(x-x') \bar{I}(x') \quad (8)$$

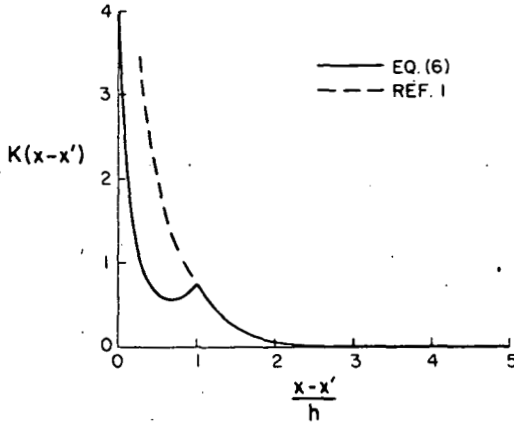


Fig. 2 Plots of kernel for freestream voltage current functional relation.

We observe that the kernel $K(x-x')$ is an even function. Also, this kernel differs from the one given in Ref. 1, since it contains an additional term in the range $-\tan\theta < (x-x')/h < \tan\theta$, where one of the contours must be closed below the real k axis. The kernels of Eq. (8) and of Ref. 1 are plotted for the case $\theta = 45$ deg in Fig. 2. The effect of the additional term is to reduce the ballasting effect of the freestream in the region between $(x-x')/h = 0$ and $(x-x')/h = \pm \tan\theta$. The current nonuniformity in one frame has little effect on the voltage drop in the neighboring frames and, therefore, tends to remain localized.

The kernel is too complex to allow an analytical solution of Eq. (1). In order to obtain numerical solutions, the variables are normalized as follows:

$$t' = \frac{\alpha}{L I_0^{3/2}} t = \frac{t}{\tau}, \quad \frac{x-x'}{h} = \xi - \xi' = \eta, \quad \frac{\bar{I}(x,t)}{I_0} = I(\xi, t'),$$

$$\tau = \frac{L}{R}, \quad R = \frac{\alpha}{I_0^{3/2}} \quad (9)$$

So that Eq. (1) takes the form:

$$\frac{\partial}{\partial t'} I(\xi, t') = -\frac{A}{2} \left\{ \pi \int_0^\infty d\eta (\eta - \tan\theta) [I(\xi - \eta, t') + I(\xi + \eta, t')] + \int_0^\infty d\eta \left[\ln \left(\frac{\cosh \pi \eta + \cosh \pi \eta \tan\theta}{\cosh \pi \eta - 1} \right) \right] \times [I(\xi - \eta, t') + I(\xi + \eta, t')] \right\} + \left[1 - \frac{1}{\sqrt{1 + I(\xi, t')}} \right] \quad (10)$$

where

$$A = \frac{2h}{\pi \sigma H P} \frac{I_0^{3/2}}{\alpha}$$

is the normalized ballasting resistance.

We are addressing the problem of determining the time evolution of a "bursting" type of current fluctuation, as may be caused by turbulence or combustion inhomogeneities. The initial perturbation is assumed to have a Gaussian distribution in space. We vary its width and the parameter A for a channel with $\tan\theta = 1$.

The results for an initial negative perturbation of width $0.32h$ are summarized in Fig. 3. The following conclusions can be drawn:

1) For $A < 1$, the channel is unstable and the initial perturbation will develop and spread over the rest of the channel. It must be noted that the linear analysis predict absolute

instability only in a much narrower range, $A < 1/[\pi(1 + \tan^2\theta)] (\sim 0.15)$.

2) For $1 < A < 1.5$, the channel is marginally stable and the perturbation will remain stationary. This seems to be the parameter range prevailing in the Soviet experiments.

3) For $A \geq 1.5$, the channel is stable and the initial perturbation will decay.

In the above discussion we have defined the term "marginally stable" in the following sense. The perturbation remains more or less constant as shown in the special case of Fig. 3c (width = $0.32h$, $A = 1.2$). If this perturbation grows or decays, it does so at a very slow rate, since the amplitude of the initial perturbation remains practically constant until the normalized time reaches 10^3 at which time the computation is terminated.

Positive wide perturbations are stable for lower values of A . This could be expected, because the slope of the arc characteristic becomes less negative as the current increases.

The time evolution of narrowly localized current nonuniformities requires much more computer time and is investigated for the unstable case only. The results for an initial negative perturbation of width $0.1h$ are summarized in Fig. 4. Apparently perturbations are spreading all over the channel, longer wavelength nonuniformities are developing, and the overall output current is decreasing.

IV. Effect of Current Fluctuation on the Hall Field

As shown in Sec. III, when the channel is unstable, the current distribution along the wall will develop into long wavelength nonuniformities. It is of interest to correlate this current nonuniformity with the nonuniformity of Hall field since this is the quantity that has been recorded in several experiments.¹⁻⁴ The Hall field is related to the current density distribution by the following relation

$$E_x = E_{x0} + \frac{1}{\sigma} (\bar{J}_x + \beta \bar{J}_y) = E_{x0} + \bar{E}_x \quad (11)$$

where $E_{x0} = (1/\sigma) (J_{x0} + \beta J_{y0})$ is the unperturbed Hall field.

Using the notation of Ref. 1, one can show that

$$\bar{J}_y \left(x - \frac{h'}{2}, -\frac{h}{2} \right) = -\frac{\bar{I}(x)}{HP} \quad (12)$$

$$\bar{J}_x \left(x - \frac{h'}{2}, -\frac{h}{2} \right) = -\frac{1}{HP h} \left\{ \int_0^\infty dy [\bar{I}(x-y) - \bar{I}(x+y)] \times \frac{1}{e^{\pi y/h} - 1} + \int_0^\infty dy [\bar{I}(x-y-h') - I(x+y-h')] \frac{1}{1 + e^{\pi y/h}} \right\} \quad (13)$$

and hence

$$\bar{E}_x \left(x - \frac{h'}{2}, -\frac{h}{2} \right) = -\frac{1}{\sigma H p} \left\{ \beta \bar{I}(x) + \frac{1}{h} \int_0^\infty dy [\bar{I}(x-y) - \bar{I}(x+y)] \frac{1}{e^{\pi y/h} - 1} + \int_0^\infty dy [\bar{I}(x-y-h') - \bar{I}(x+y-h')] \frac{1}{1 + e^{\pi y/h}} \right\}$$

The last equation gives the Hall field at the plasma boundary, where the experimental data were acquired.

In order to study the relation between current and voltage nonuniformities, we use two specific examples by assuming \bar{I} in forms shown in Fig. 5. These waveforms are seen to be

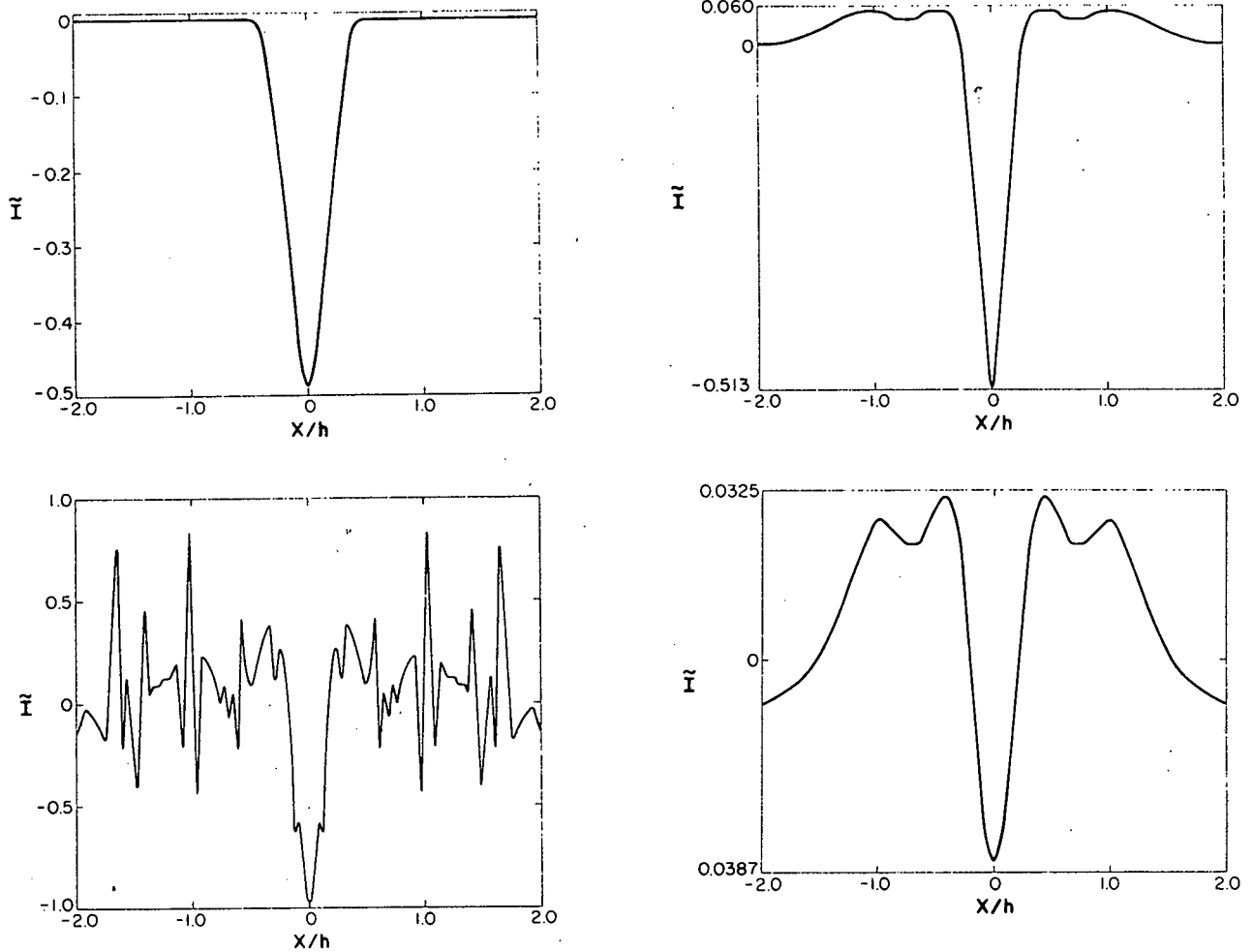


Fig. 3 Initial perturbation pulse shape and time evolved results for several cases: a) initial pulse (width $\approx 0.32 h$), b) $A = 0.9 t_j' = 0.4 \times 10^4$, c) $A = 1.2 t_j' = 0.4 \times 10^3$, d) $A = 20 t_j' = 0.5 \times 10^2$.

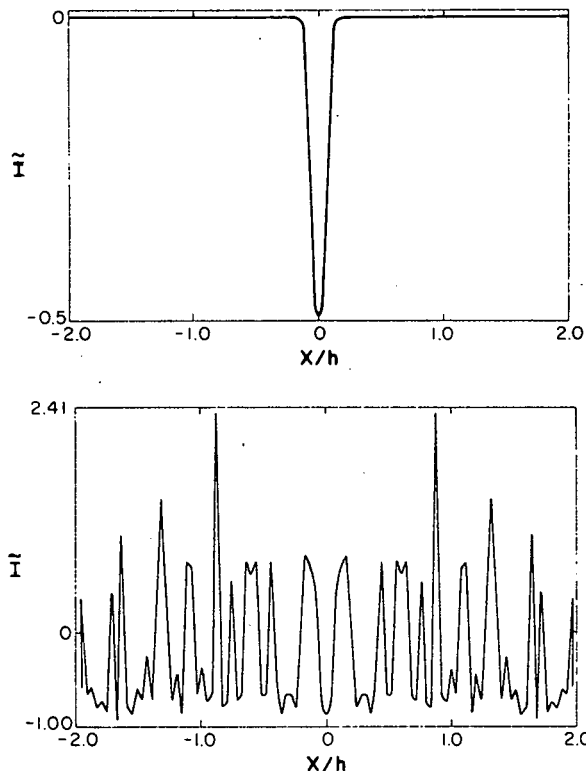


Fig. 4 Evolution of narrow initial perturbation for unstable case: a) initial pulse (width $\approx 0.1 h$), b) $A = 0.9 t_j' = 0.67 \times 10^4$.

typical of the unstable current nonuniformities obtained in the nonlinear analysis (Fig. 4). The corresponding \bar{J}_x and \bar{J}_y and hence \bar{E}_x derived through Eqs. (12-14) are calculated as:

Case 1

$$\bar{J}_y \left(x - \frac{h'}{2}, -\frac{h}{2} \right) = \begin{cases} (I_1/Hp) & |x| < a \\ 0 & |x| > a \end{cases} \quad (15)$$

$$\bar{J}_x \left(x - \frac{h'}{2}, -\frac{h}{2} \right) = \frac{I_1}{Hp\pi} F(x, a) \quad (16)$$

where

$$F(x, a) = \begin{cases} \ln \frac{(1 + e^{-\pi(h'+a-x)/h})(1 - e^{-\pi(a+x)/h})}{(1 + e^{-\pi(h'-a-x)/h})(1 - e^{-\pi(a-x)/h})} & x < -a \\ \ln \frac{(1 + e^{-\pi(h'+a-x)/h})(1 - e^{-\pi(a+x)/h})}{(1 + e^{-\pi(h'-a-x)/h})(1 - e^{-\pi(a-x)/h})} & -a < x < a \\ \ln \frac{(1 - e^{-\pi(a+x)/h})(1 + e^{-\pi(h'+a-x)/h})}{(1 - e^{-\pi(x-a)/h})(1 + e^{-\pi(h'-a-x)/h})} & a < x < \alpha - a \\ \ln \frac{(1 - e^{-\pi(a+x)/h})(1 + e^{-\pi(h'+a-x)/h})}{(1 - e^{-\pi(x-a)/h})(1 + e^{-\pi(a+x-h')/h})} & \alpha - a < x < \alpha + a \\ \ln \frac{(1 - e^{-\pi(a+x)/h})(1 + e^{-\pi(h'+a-x)/h})}{(1 - e^{-\pi(x-a)/h})(1 + e^{-\pi(a+x-h')/h})} & x > \alpha + a \end{cases} \quad (17)$$

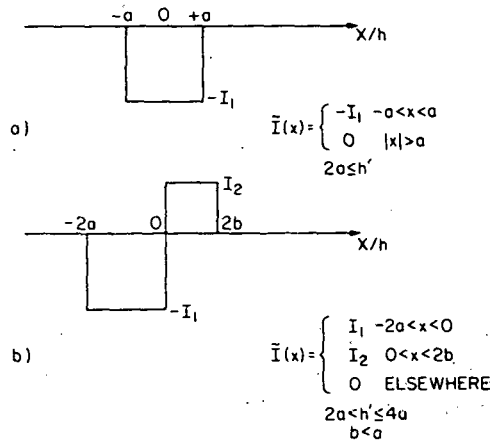


Fig. 5 Typical shapes of current fluctuations in unstable cases.

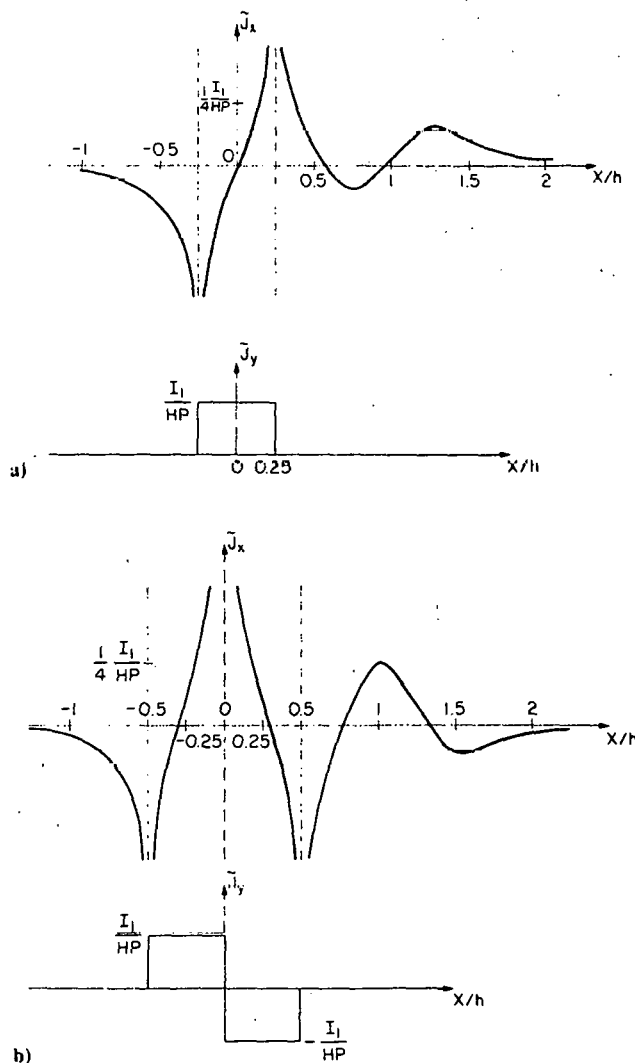


Fig. 6 Fluctuating current densities used in determination of Hall field.

Case 2

$$\bar{J}_y \left(x - \frac{h'}{2}, -\frac{h}{2} \right) = \begin{cases} (I_1/HP) & -2a < x < 0 \\ -(I_2/HP) & 0 < x < 2b \\ 0 & \text{elsewhere.} \end{cases} \quad (18)$$

$$\bar{J}_x \left(x - \frac{h'}{2}, -\frac{h}{2} \right) = \frac{I_1}{Hp\pi} F(x+a, a) - \frac{I_2}{Hp\pi} F(x-b, b) \quad (19)$$

where F is given by Eq. (17).

Plots of \bar{J}_x and \bar{J}_y as given by Eqs. (15-19) are shown in Fig. 6 for the case $a=b=0.25h$, $I_2=I_1$, $h'=h$. It appears that there exists a region in which both \bar{J}_x and \bar{J}_y are positive. As follows from Eq. (11), the value of the Hall field is less negative and may even become positive in that region. For example if we assume $I_1=0.8I_0$ as in the case of Fig. 4b, $J_{x0}=0$, and $\beta=1$, then Fig. 6b shows a region which extends over about $0.2h$ having a positive Hall field. It must be noted that Fig. 4b depicts a situation in which steady state has not been attained and the wavelength of the current nonuniformities is still increasing. Therefore, one can expect that the nonuniformities in Hall field may eventually reach the even larger wavelength recorded in the experimental data of Ref. 4.

For the square wave current distributions used here, there appears in \bar{J}_x a mild logarithmic singularity as shown in Fig. 6. Since the real current fluctuation will not be in peak sharp steps, these singularities are not expected to occur.

V. Conclusions

We have presented a nonlinear analysis of the nonuniformities which occur in a diagonal MHD channel. The criterion of stability characterized by the parameter $A=2hI_0^{3/2}/(\pi\sigma Hp\alpha)$ is established by the results of examples which use a negative Gaussian pulse as the initial perturbation. For sufficiently large A (≈ 20 for instance), the evolution of an initial perturbation as shown in Fig. 3d indicates that long wavelength modes damp away and only short wavelength modes remain in agreement with the linear stability analysis. This is because for long wavelength modes the ballasting effect of the plasma dominates over the destabilizing effect of the arc. As A decreases, the system tends to become unstable. The nonlinear mechanism of mode-mode coupling becomes significant, and balances the linear damping of long wavelength modes. This is demonstrated in Fig. 3c, where the linearly stable modes do not damp away; hence, linear stability analysis breaks down for the corresponding values of A . As A decreases further (< 1), the system becomes unstable. Not only do all the modes become unstable, but also an initially localized perturbation spreads over the whole channel. The domain of stability extends over a much narrower range than predicted by the linear theory.

As already mentioned the kernel presented in Sec. III is different from the one obtained in Ref. 1 when $h' \neq 0$. The new kernel shown in Fig. 2 for $h'=h$ is more localized at the center and has a peak at each side. This can be viewed as a long-range effect across the plasma in the Faraday direction produced by the diagonal bar connection. We therefore expect the spreading of the perturbation to occur in discrete steps, since the kernel will transport each induced perturbation from one step to another h' distance away. If the system is unstable, these perturbations will grow simultaneously at different locations, and eventually form the long wavelength nonuniformities as shown in Figs. 3b and 4b.

The analysis of the effect of the current nonuniformities on the Hall field (Fig. 6b) indicates that the Hall field can decrease and even change sign at some place in the channel, as has been observed in Ref. 4.

At this point it will be appropriate to comment on the time-scaling factor $\alpha/LI_0^{3/2}$. Here L is the inductance of the path consisting of the shorting bars of the diagonal channel and the arcs at the electrodes, and the path of the fluctuating current in the freestream plasma. Taking $H=h=1$ m, the value of L is about 10^{-6} H. $\alpha/I_0^{3/2}=V_0/I_0$, where V_0 is the arc drop at the operating current I_0 , is approximately 1Ω . The time constant $L/(V_0/I_0)$ is thus estimated to be on the order of 1

μ s. Hence 1000 time units in our computation correspond to only 1 ms. The pattern of the current distribution shown in Fig. 4b is obtained after about 6000 time units, and thus in real time corresponds to only 6 ms. Furthermore, in the computation, one can see noticeable changes of the fine grain details from frame to frame in steps of about 100 time units. Therefore these fluctuations at any point of space will correspond to oscillations at about 10 KHz.

It is to be noted that the present analysis does not include wall leakage effects, which are under investigation.

Appendix

To proceed from a double integration to an expression of Eq. (8), a contour integration in k is performed as follows:

$$\int_{-\infty}^{+\infty} \frac{\cos k(x-x') [\cosh(kh) - \cos(kh')]}{k \sinh(kh)} dk = \frac{1}{2} \left\{ \oint_{x-x'>0} dk \frac{e^{ik(x-x')} \cosh(kh)}{k \sinh(kh)} + \oint_{x-x'>0} dk \frac{e^{-ik(x-x')} \cosh(kh)}{k \sinh(kh)} \right. \\ - \frac{1}{2} \oint_{x-x'+h'>0} dk \frac{e^{ik(x-x'+h')}}{k \sinh(kh)} - \frac{1}{2} \oint_{x-x'-h'>0} dk \frac{e^{-ik(x-x'-h')}}{k \sinh(kh)} - \frac{1}{2} \oint_{x-x'-h'>0} dk \frac{e^{ik(x-x'-h')}}{k \sinh(kh)} \\ \left. - \frac{1}{2} \oint_{x-x'+h'>0} dk \frac{e^{-ik(x-x'+h')}}{k \sinh(kh)} + (\text{contributions from } < 0 \text{ parts}) \right\} \tag{A1}$$

where \odot (or \ominus) stands for a contour closed in the upper (or lower) plane as shown in Fig. A1. Since there is no singularity at $k=0$ in the original integrand [LHS of Eq. (A1)], we concern ourselves only with the pole contributions at $\pm in\pi/h, n=1,2,\dots$. Hence each contour integration becomes a summation of residues of the poles, and Eq. (A1) becomes

$$= \sum_{n=1}^{\infty} \left\{ \frac{2e^{-n\pi|x-x'|/h}}{n} - (-1)^n \frac{e^{-n\pi|x-x'+h'|/h}}{n} - (-1)^n \frac{e^{-n\pi|x-x'-h'|/h}}{n} \right\} \tag{A2}$$

Furthermore, this summation can be expressed as

$$\left. \begin{aligned} & \left[\frac{\cosh\left(\pi \frac{x-x'}{h}\right) + \cosh(\pi \tan\theta)}{\cosh\left(\pi \frac{x-x'}{h}\right) - 1} \right] && \frac{x-x'}{h} < -\tan\theta \\ & -\pi \left(\frac{x-x'}{h} + \tan\theta\right) + \left[\frac{\cosh\left(\pi \frac{x-x'}{h}\right) + \cosh(\pi \tan\theta)}{\cosh\left(\pi \frac{x-x'}{h}\right) - 1} \right] && -\tan\theta < \frac{x-x'}{h} < 0 \\ & \pi \left(\frac{x-x'}{h} - \tan\theta\right) + \left[\frac{\cosh\left(\pi \frac{x-x'}{h}\right) + \cosh(\pi \tan\theta)}{\cosh\left(\pi \frac{x-x'}{h}\right) - 1} \right] && 0 < \frac{x-x'}{h} < \tan\theta \\ & \left[\frac{\cosh\left(\pi \frac{x-x'}{h}\right) + \cosh(\pi \tan\theta)}{\cosh\left(\pi \frac{x-x'}{h}\right) - 1} \right] && \tan\theta < \frac{x-x'}{h} \end{aligned} \right\} \tag{A3}$$

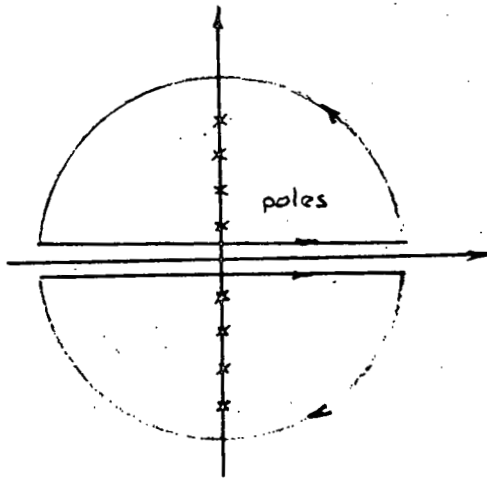


Fig. A1 k plane.

with the aid of Eq. (A1-A3), $\Delta \bar{V}$ reduces to the expression of Eq. (8).

Acknowledgment

This work was supported in part by the Department Energy under Contract ET-78-C-01-3084.

References

¹Solbes, H. and Lowenstein, A., "Electrical Non-Uniformities in Linear MHD Channels," *Proceedings of the 15th Symposium, Engineering Aspects of Magnetohydrodynamics*, Philadelphia, 1976, pp. 1-7.

²Hutonov, B. M., Biturin, V. H., et al., "Studies of MHD Generator Loading," *Proceedings of Fourth US-USSR Colloquium on HMD Power Generation Conference*, Oct. 5-6, 1978, Washington, D.C.

³US/USSR Cooperative Program in Open-Cycle MHD Electrical Power Generation, ANL-IVTAN/MHD-78-J71.

⁴Buznikow, A. E., Kovbasiuk, V. I., Pishikov, S. I., and Shumiatski, B. Y., "Electrical Non-Uniformities in U-25 MHD Channels," *Proceedings of the 18th Symposium on Engineering Aspects of Magnetohydrodynamics*, Butte, Mont., 1979, pp. ES1-ES6.

Two-dimensional Power Take-off Analysis
in
Diagonal Conducting Wall Channels

S. Kuo and E. Levi

Polytechnic Institute of New York
Route 110
Farmingdale, NY 11735

ABSTRACT

A true two-dimensional analysis of diagonal-conducting-wall MHD channels leads to design principles for the power take-off and good quantitative agreement with experimental data. The effect of power take-off schemes on the output power level is investigated analytically. It is found that it is possible to design the electrical circuit of the channel with passive elements in the take-off region, and, achieve a fairly even lead current distribution under changing load conditions without loss of power output.

Nomenclature

$h_{i,o,m}$	= width of the channel in inlet, outlet and middle regions respectively
H	= electrode length along magnetic field
P	= electrode segmentation pitch
A	= cross sectional area of the channel
I_s	= local short circuit current
I	= current in the channel
i	= $\frac{dI}{dx}$
I_n	= $P i$ = current in the nth lead
R_n	= $R(x_n)$ = resistance in the nth electric lead
β	= Hall parameter
σ	= conductivity
u	= flow velocity
V_f	= forward voltage drop
x, y	= Cartesian coordinates
W	= $x + (y - h/2) \tan \theta$
θ	= angle of the diagonal link
B	= magnetic field
E	= electric field
h'	= $h \tan \theta$
ν	= collision frequency between electron and neutral gas

I. Introduction

Over the years, a large effort has been devoted to the development of economic and durable MHD power generators. Among the channel types, the Diagonal Conducting Wall (DCW) channel offers the advantage of a simple design for the power take-off. The diagonal connection permits the use of a single load, hence, the power take-off in a DCW channel should, in principle, be a simple scheme. Several problems however, still remain to be solved. If ballasting resistors are not used in the power take-off connection, or are not properly chosen, dangerous current concentrations may appear in the leads when operating under off-design condition and in the case of faults. Moreover, the Hall field may change sign over a certain range and have the same direction as the load current. This so called Hall field reversal causes that section of the channel to absorb rather than deliver power. Hence reliable and/or efficient operation of the channel cannot be achieved. Therefore, the main design problem in the power take-off is to determine the distribution of the resistors so as to establish a uniform current distribution under design conditions and avoid dangerous current concentrations under off-design and fault conditions. Effective utilization of the power take-off region of the channel, so as to avoid the loss of output power due to the field reversal should also be considered simultaneously.

In a previous analysis, Levi¹ developed a one-dimensional model to describe the performance characteristics of the power take-off schemes used in DCW channels,^{2,3} analytically. He only dealt with the case of uniform resistance distributions (short circuit or constant resistance).

Pan and Doss^{4,5} derived a similar model in which the parameters were averaged over the second dimension instead of simply assuming to be uniform as in Levi's model. A numerical investigation of several cases of electrical loading was made. They extended Levi's work to include non-uniform resistance distributions: (1) monotonic increasing (2) monotonic decreasing (3) peak or trough in the middle. They, however, considered the problem only from the point of view of analysis. This can be inferred from their figures which show that their typical resistance distributions, when carrying evenly distributed currents, result in different profiles for the short circuit currents. Since the short circuit current reflects the profile of the magnetic field impressed on the channel, it must, instead, be considered as a fixed specification for the design of the power take-off.

In this paper, a true two-dimensional model has been developed for the analysis and design of the ballasting resistances in the power take-off regions of the DCW channel. The results show that, even if the plasma parameters are constant along a cross-section of the channel, the one-dimensional analysis falls short of giving an accurate picture, because in the power take-off regions, the current density is not uniformly distributed along a normal cross-section. Moreover, it is shown that it is not enough to aim at a uniform current distribution under design conditions, because unsafe current concentrations can arise under overcurrent situations. It is also shown that, with the proper design of the ballasting resistors, these passive elements will not cause any loss of output power from the channel. The reason is that the proper resistance distribution makes available to power generation an additional section of the power take-off region, so that

this additional generated power exactly balances the joule loss in the resistors. The paper also considers the power take-off in the immediate region in a different manner from Pan and Doss⁴.

In Section II fundamental relations are derived. The effect of the power take-off schemes on the output power is considered in Section III, and guiding principles for choosing resistors in the light of efficiency considerations are obtained. In Section IV, the equations derived in Section II and the results of Section III are applied to specific designs. Comparisons with U-25B experiments are made in Section V, and Section VI presents a summary and conclusions.

II. Fundamental Relations:

Consider the configuration and vector orientation of Fig. 1. The electric field \vec{E} , and the current density \vec{J} in the channel are related as follows:

$$E_x = \frac{1}{\sigma} (J_x + \beta J_y) \quad (1)$$

$$E_y = uB + \frac{1}{\sigma} (J_y - \beta J_x) \quad (2)$$

where the electric field \vec{E} satisfies the Maxwell equation:

$$\vec{z} \cdot \nabla \times \vec{E} = \frac{\partial}{\partial x} E_y - \frac{\partial}{\partial y} E_x = 0 \quad (3)$$

and the relation established by the diagonal bar connection⁶:

$$E_y = -\tan\theta E_x \quad (4)$$

thus Eq. (3) becomes:

$$(\tan\theta \frac{\partial}{\partial x} + \frac{\partial}{\partial y}) E_{x,y} = 0 \quad (3a)$$

The solutions have the functional dependence:

$$E_x(x,y) = E_x(x-y\tan\theta) \text{ and } E_y(x,y) = E_y(x-y\tan\theta) \quad (5)$$

Thus one obtains from Eqs. (1) and (2),

$$J_y = \frac{\sigma}{1+\beta^2} [(\beta\tan\theta)E_x - uB] \quad (6)$$

$$J_x = \frac{\sigma}{1+\beta^2} [(1+\beta\tan\theta)E_x + \beta uB] \quad (7)$$

Since $\nabla \cdot \vec{J} = 0$ in the channel, one can relate the current flowing in the channel $I(x)$ to the current density \vec{J} in the channel by integrating the current flow through the cross section cut along the diagonal bar as shown in Fig. 1:

$$I(x) = \int \vec{J} \cdot \hat{n} da = \frac{A}{h} \int_{-h/2}^{h/2} dy [J_x(W, y) - J_y(W, y)\tan\theta] \quad (8)$$

where $A=Hh$ is the cross sectional area of the channel and

$W=x+(y-h/2)\tan\theta$ is defined.

Substituting Eqs. (6) and (7) into Eq. (8), the latter becomes

$$I(x) = A (1+\tan^2\theta) E_x(x-h'/2)\alpha(x) + A[\xi(x)+\tan\theta \eta(x)] \quad (9)$$

where

$$\alpha(x) = \frac{1}{h} \int_{-h/2}^{h/2} dy \frac{\sigma(W, y)}{1+\beta^2(W, y)} \quad (10)$$

$$\eta(x) = \frac{1}{h} \int_{-h/2}^{h/2} dy \left\{ \frac{\sigma(W, y)}{1+\beta^2(W, y)} u(W, y)B(W, y) \right\} \quad (11)$$

$$\xi(x) = \frac{1}{h} \int_{-h/2}^{h/2} dy \left[\frac{\sigma(W,y) \beta(W,y) u(W,y) B(W,y)}{1 + \beta^2(W,y)} \right] \quad (12)$$

E_x can now be expressed as

$$E_x(x-h'/2) = \frac{I(x) - I_s(x)}{A(1 + \tan^2 \theta) \alpha(x)} \quad (13)$$

where

$$I_s(x) = A[\xi(x) + \tan \theta \eta(x)] \quad (14)$$

is the short circuit current corresponding to ($E_x = 0$).

A second relation is obtained by applying the Kirchhoff's voltage relation to the circuit external to the channel as shown in Fig. 2. In the limit of vanishing electrode pitch, this relation becomes:

$$\frac{d}{dx} [R(x) \frac{d}{dx} I(x)] = \frac{E_x(x-h'/2)}{P} = \frac{I(x) - I_s(x)}{PA(1 + \tan^2 \theta) \alpha(x)} \quad (15)$$

where the relations $R_n = R(x_n)$ and $I_n = P i(x_n) = P dI/dx|_{x=x_n}$ are employed. Equation (15) constitutes the fundamental equation for the power take-off within the framework of a two-dimensional analysis. Evidence for the major differences between the one-dimensional analyses of Ref. 1 and 4 and the two-dimensional analysis is given by the different expressions for the x dependence in Eqs. (10), (11) and (12). This implies that even if the parameters σ , β , and B are independent of the y variable, the results of the one-dimensional analysis are still different from those of the two-dimensional analysis.

Eq. (13) provides a relation between the Hall field E_x and the channel flowing current I . Since $\alpha(x)$ is a positively definite function, as it appears from its definition in Eq. (10), the sign of the Hall field depends on the sign of the difference of I and I_s . If the

channel current $I(x)$ at any point x is larger than the local short circuit current $I_s(x)$, E_x lies in the same direction as the flow. When such a Hall field reversal occurs, the plasma in that region operates in the motoring, or accelerating mode, thus reducing the net output power level. Three typical Hall field distributions along the channel are shown in Fig. 3 for three different loadings connected to the nozzle and diffuser. Fig. 3a corresponds to the minimum loading case (open circuit). Since $I=0$, no field reversal occurs in the whole region. With finite load, the field distribution acquires the shape shown in Fig. 3b. Field reversal does occur in the inlet and outlet regions due to the weak magnetic field and hence low I_s . When the channel is short circuited, the field distribution is shown in Fig. 3c. One observes that the channel region which generates power, i.e. the region between the positive and negative extremes in Hall potential decreases with increasing loading. In order to optimize the output power level for each given load (or operating point), field reversal regions must be reduced in extent or completely avoided, so that the load voltage corresponds to the Hall potential difference between its positive and negative extremes. This can be achieved by optimizing the positions of the inlet and outlet connections and by designing the power take-off arrangement (i.e. the distribution of the resistance) properly.

In the following, $\alpha(x)$, $\eta(x)$ and $\xi(x)$ are presented in explicit expression for two typical magnetic field profiles. To simplify the analysis, σ , u , and v , are kept constant, while full variability in J_x and J_y is retained.

Case I: $B(x) = B_0 + B_1 x$ and hence $\beta = \beta_0 + \beta_1 x = a B$, where

$$\beta_0 = a B_0 \text{ and } a = e/\mu u$$

$$\alpha(x) = \frac{\sigma}{h\beta_1 \tan\theta} \tan^{-1} \frac{\beta_1 h \tan\theta}{1 + [\beta_0 + \beta_1(x - h \tan\theta/2)]^2 - (\beta_1 h \tan\theta/2)^2} \quad (16)$$

$$\eta(x) = \frac{\sigma u}{2ah\beta_1 \tan\theta} \ln \left\{ \frac{1 + (\beta_0 + \beta_1 x)^2}{1 + [\beta_0 + \beta_1(x - h \tan\theta)]^2} \right\} \quad (17)$$

$$\xi(x) = \frac{\sigma u}{a} (1 - \alpha(x)/\sigma) \quad (18)$$

Case II: $B(x) = B_0 (x_0 + x)^2$ and $\beta(x) = aB(x) = \beta_0 (x_0 + x)^2$

$$\alpha(x) = \frac{\sigma}{h\sqrt{\beta_0} \tan\theta} \left\{ \frac{1}{4\sqrt{2}} g(x) + \frac{1}{2\sqrt{2}} f(x) \right\} \quad (19)$$

$$\eta(x) = - \frac{\sigma u}{ah\sqrt{\beta_0} \tan\theta} \left[\frac{1}{4\sqrt{2}} g(x) - \frac{1}{2\sqrt{2}} f(x) \right] \quad (20)$$

$$\xi(x) = \frac{\sigma u}{a} (1 - \alpha(x)/\sigma) \quad (21)$$

where

$$f(x) = \tan^{-1} \frac{\beta_0 \sqrt{2\beta_0} \tan\theta \{1 + \beta_0 [(x - h \tan\theta/2 + x_0)^2 - h^2 \tan^2\theta/4]\}}{\{1 + \beta_0 [(x - h \tan\theta/2 + x_0)^2 - h^2 \tan^2\theta/4]\}^2 - 2\beta_0 [(x - h \tan\theta/2 + x_0)^2 + h^2 \tan^2\theta/4]} \quad (22)$$

$$g(x) = \ln \frac{\{\beta_0 [(x - h \tan\theta/2 + x_0)^2 - h^2 \tan^2\theta/4] - \sqrt{\beta_0/2} h \tan\theta\}^2 + (1 + \sqrt{\beta_0/2} h \tan\theta)^2}{\{\beta_0 [(x - h \tan\theta/2 + x_0)^2 - h^2 \tan^2\theta/4] + \sqrt{\beta_0/2} h \tan\theta\}^2 + (1 - \sqrt{\beta_0/2} h \tan\theta)^2} \quad (23)$$

One should bear in mind that the value B_0 in Case I or x_0 in Case II are determined by the chosen positions of the inlet and outlet connections.

III. Effect of Power Take-off Schemes on Output Power

The power take-off affects the distribution of Hall potential and, hence the output power. It is therefore worthwhile to examine, in general, how the output level is affected by the presence of resistors in the power take-off leads.

In the absence of resistors, consider the general loading model shown in Fig. 1. The inlet and outlet sections in which the diodes are not blocking are short circuited; no power is generated in those sections of the channel but there is no joule loss in the loading scheme either. The available power generating region of the channel is confined between the last conducting diode in the inlet region and the first conducting diode in the outlet region; the output power is V_o^2/R_o . However, if resistors are connected in series with the diodes, it is conceivable to shape the profile of the Hall potential, so that the power take-off regions are also made available for power generation. The additional generated power, for example in the inlet region, can be calculated as follows:

$$\begin{aligned}
 P_{\text{add}} &= - \int \vec{j} \cdot \vec{E} \, dv \\
 &= - H \int_0^{x_f} dx \int_{-h/2}^{h/2} dy \{ J_x(W, y) E_x(x-h'/2) + J_y(W, y) E_y(x-h'/2) \} \\
 &= - \int_0^{x_f} dx I(x) \cdot E_x(x-h'/2) \\
 &= - P R(x_f) I(x_f) i(x_f) + P \int_0^{x_f} dx R(x) i^2(x) \quad (24)
 \end{aligned}$$

where use has been made of Eqs. (8), and (15), $i(x) = dI(x)/dx$ is defined as before, and x_f corresponds to the position of the last con-

ducting diode. Since resistors are now connected in series with the diodes, additional joule loss is also expected. This loss is calculated as follows:

The external resistances in the power take-off leads are smeared into an equivalent volume distribution, and a volume current density distribution $J_{yA} = \frac{i(x)}{H}$ and an equivalent resistivity $\rho(x)$ are introduced. Thus $J_{yA} = E_{yA}/\rho(x)$ and $R(x) = \rho(x) \frac{\ell}{HP}$, where E_{yA} is the electric field intensity inside the resistors and ℓ is the physical length of the resistors.

The power dissipation in the volume of resistance is then defined as

$$\begin{aligned}
 P_{\text{loss}} &= \int J_{yA} E_{yA} dv = H\ell \int_0^{x_f} dx J_{yA} E_{yA} \\
 &= P \int_0^{x_f} dx R(x) i^2(x) \quad (25)
 \end{aligned}$$

Introducing the expression in Eq. (25), one obtains the following relation

$$P_{\text{add}} = P_{\text{loss}} - PR(x_f) I(x_f) i(x_f) \leq P_{\text{loss}} \quad (26)$$

It follows that, at best, the additional generated power covers the loss in the ballasting resistors. Therefore, the condition for obtaining maximum output when resistors are deemed necessary in order to even out the current distribution, is to let the resistances be zero in the last conducting lead of the inlet region and in the first lead of the outlet region.

IV. Guiding Principles for the Design:

The resistors in the power take-off should be chosen, so as to establish a uniform current distribution under design conditions and avoid dangerous current concentrations under off-design and fault conditions. Case I, in which the magnetic field profile varies linearly in space, is considered. Equations (15) through (18) are applied to determine current and resistance distributions for the #2 channel in the U-25B facility. The dimensions and the operating conditions used in the calculations are given in Table 1. The leads in the inlet and outlet regions, contain a diode as well as a resistor while the leads in the mid-channel have resistors but no diodes. Several cases are analyzed for the inlet connection, symmetrical distributions are obtained for the outlet. The first two cases deal with a channel designed for maximum output, the other two for a high efficiency channel.

Case 1a: Inlet in a channel designed for high output with all diodes conducting (no spare diodes.)

The distribution of resistors needed to achieve a uniform design current distribution is shown in Fig. 4a and the current distributions corresponding to design conditions (curve I), reduced load current (curve II), and enhanced load current (curve III and IV) are shown in Fig. 4b. One observes from curve II that with reduced current, part of the diodes are blocking. The load current is distributed among the remaining leads without exceeding the design value.

Undercurrent, therefore, presents no problem and since this is always the case, undercurrent will not be discussed further. With higher currents than the design value, instead, curve III shows that the excess current is carried mainly by the last lead; thus creating a potentially dangerous current concentration. This appears as a δ - function in curve III, because of the initial assumption of vanishingly small electrode pitch. Adding equal resistances in all leads (.14 Ω in curve IV of Fig. 4b) would leave curve I and II unchanged and reduce somewhat the current concentration (See curve IV.) This, however, would violate the condition derived in the previous section; it would result in additional joule losses and reduce the output power. It becomes clear that allowance should be made for overcurrent in the design stage by concentrating the current over a fraction of the take-off leads. This consideration, therefore, guides the design in all the following cases.

Case 1b: Inlet in channel designed for high output with spare blocking diodes.

It is now clear that, for the same load current, the fewer conducting leads are called upon to carry a higher current than in the preceding case. For a take-off region extending over $1.5 h_1$, rather than $2 h_1$, the current i is 30% larger. The corresponding distribution of resistors is shown in Fig. 5a. The value of the resistors has decreased by one order of magnitude. The current distribution with 14% overcurrent is shown in Fig. 5b. In this design, no current concentration will occur for load current below 308.6A. With over-

current, additional leads start conducting. Since these leads contain no resistances, the current $I(x)$ in the channel attains the local value of the short circuit current $I_s(x)$ and the distribution of current i is governed by the slope of $I_s(x)$. As long as the load current is less than the value attained by the short circuit current at the location of the last lead, this will carry no particularly high current. Overcurrents are expected to be more dangerous in channels designed for high efficiency, and, therefore, for load currents which are a smaller fraction of the short-circuit current. This situation is considered in the next cases.

Case 1c: Inlet in channel designed for high efficiency with most of the diodes conducting.

As in the previous case, the channel is designed with the leads extending beyond $1.5 h_1$ having blocking diodes, but with a load current about 30% lower. As Fig. 6a shows, higher value resistors are needed. For this reason, when higher than design current is called for, the current collected in the resistive leads is below the level of the short circuit current. This level is attained in the first nonresistive lead, as shown in curve I of Fig. 6b. This lead therefore must carry excess current. Again this discontinuity in the current flowing in the channel cause a δ - function to appear in its derivative, curve II of Fig. 6b, which represents the distribution of current in the leads, because of the initial assumption of vanishing electrode pitch. To ward against the occurrence of such current concentration an attempt is made to restrict further the number of leads which are conducting under design conditions.

Case 1d: Inlet in channel designed for high efficiency with half of the diodes conducting.

The needed distribution of resistors is shown in Fig. 7a. As expected from the more limited extent of the conducting region, the value of the resistor is smaller. However, it is not possible to obtain a smooth transition with the non-resistive leads. For this reason, in order to avoid the small loss of power output due to the finite value of $R(x_f)$, as explained in Sec. II, one should make sure that, also under design conditions, the first non-resistive lead is conducting. As the load current increases, more non-resistive loads become conducting, until none of the diodes is blocking, as shown in Fig. 7b. No current concentration occurs even up to 55% overcurrent. Further increases in the load current will be forced upon the last conducting diode. If a channel is expected to operate under such conditions for a long time, either more diodes should be added, or the whole take-off region moved towards higher magnetic fields, so that the load current remains lower than the short circuit current.

Case 2: Mid-channel take-off

It is advantageous to be able to tap the current in midchannel in order to gain operational flexibility. For uniform current distribution the resistances should increase in value monotonically when the current is taken out, as shown in Fig. 8a and decrease monotonically in a similar fashion when current is fed in. Therefore, when the direction of the current is not known, a priori variable resistances should

be used. The effect of a 20% variation of the load current from a design value, on the distribution of the lead current for a fixed current withdrawn (10% of the design value) is shown in Fig. 8b. It appears that in the overcurrent case most of the current is withdrawn from the first lead and in the undercurrent case from the last lead. An attempt was also made to study the case of equal resistances to allow drawing current in both direction. The results are shown in Fig. 9 for two cases corresponding to two leads having equal resistances of 5 and 10 ohms respectively. As expected, the high resistance reduces the amount of circulating current between the two leads.

V. Comparisons with Experiments:

Since data from the seventh test on the U-25B facility are available, it is possible to check the two-dimensional theory with the experimental observations. In these experiments equal resistances of .5 Ω were connected in series with all diodes in the inlet and outlet power take-off regions. A total of twelve leads in each region were connected. The general features of the profile of the current distribution in the inlet region may be classified into two distinct categories:

1. Low efficiency, high operating load current, with field reversal in the region of the last two or three electrodes. For instances, tests # 5361, 5495, 5586, 5656, 5784, 5797, 5886 etc.

2. High efficiency, lower operating load current, without field reversal. For instances, test # 5368, 5542, 5621, 5686, 5805, 5881, etc.

The outlet profile is much more irregular. This may be due to the presence of an oblique shock near the channel exit, but data on lead currents and interelectrode voltages give consistent evidence (over many tests) of short circuited resistances and loose contacts.

Tests #5797 and 5804 are chosen for the comparisons, since the profiles of current distributions in the inlet region are typical and can represent the general features of each category respectively. Besides these two tests have significant output power: In test #5797 the load current was 399A and the power output was 1386W. In test #5805 the load current was 264A and the power output was 1296W. These operating conditions were probably close to the design expectations. The time separation between the two tests was about 14 minutes. This also leads one to assume that most of the parameters (for instance, the conductivity and the temperature, etc.) remained the same for the two tests. The only difference between the two tests was a slight variation in background pressure, and hence, the collision frequency and Hall parameter. Consideration of this slight difference in pressure was indeed needed to obtain the very good agreement with the experimental data on the inlet current distribution, as shown in Figs. (10) and (11). This sensitivity of the results on slight pressure variation attests to the accuracy of the analytical procedure.

Reasonably good agreement between theory and experiment can also be observed for the outlet current distribution as shown in Fig. 12. Four data of points of test #5797 had to be discarded for the reasons mentioned above and the rapid oscillatory trend observed in test #5805 could not be duplicated.

VI. Summary and Conclusions:

1. An exact two dimensional formulation for the analysis of power take-off problems is obtained by integrating the current flow through the cross section cut along the diagonal bar instead of the conventionally used normal cross section. The result of the formulation indeed demonstrates that the one-dimensional analysis can only provide a qualitative description of the power take-off problems. This is because in the power take-off regions the current distribution in the channel varies in both x and y .
2. The effect of power take-off schemes on output power level is investigated. If only passive elements are used, the scheme in which the leads contain no resistances provides maximum output power level. However, properly designed resistance distributions can also give the same output level. The analysis shows that when the resistances in series with the last conducting diode in the inlet region, or with the first diode in the outlet region are finite, the output power is always reduced. Therefore, if resistors are deemed necessary, in order to even out the current distribution, the last conducting lead in the inlet region

and the first lead in the outlet region should have zero resistance, in order to maximize the output power. In this case the additionally generated power in the power take-off region balances the joule loss in the series resistors exactly.

3. Guiding principles for the design are provided by examples which show how to determine the resistance distribution, so that uniform current distribution is obtained under design condition and no current concentrations occur in the allowable range of off-design conditions. Moreover, the power absorbed by the ballast resistors is withdrawn from the channel, without reduction in the level of power delivered to the load.
4. Mid-channel power take-off (two leads only) is also analyzed. The effect of 20% variation of the load current from the design value on the distribution of the lead current for a fixed current withdrawn (10% of the design value) is examined. It appears that, in the overcurrent case most of the current is withdrawn from the first lead, and in the undercurrent case, from the last lead.
5. The results of this two-dimensional analysis are compared with the U-25B experimental data. Good agreement is observed.

Acknowledgement

This work was supported in part by the Department of Energy under Contract ET-78-C-01-3084.

Table I: U25B Channel Operating Conditions

Channel Dimensions:

Width: $h_i = 0.168\text{m}, h_o = 0.253\text{m}, h_m = 0.19\text{m}$

Height: $H = h$

Length: 5m

Magnetic Field: 5T maximum

Conductivity σ : inlet $9 \text{ } \nu/\text{m}$, outlet $7 \text{ } \nu/\text{m}$

Flow Velocity u : 1000 m/sec

Collision Frequency: $v_{in} = 1.94 \times 10^{11}/\text{sec}, v_{out} = 3.23 \times 10^{11}/\text{sec}$

References:

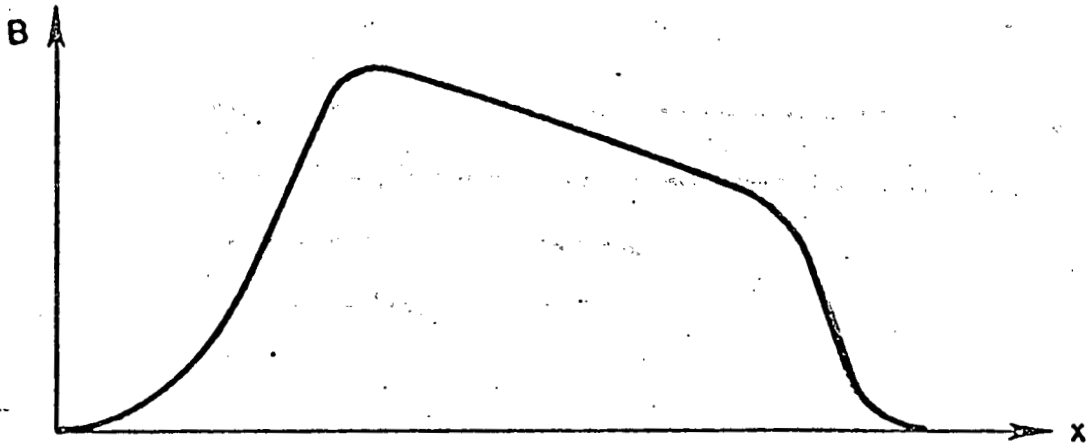
1. Levi, E., "Preliminary Design for the Power Take-Off of Singly-Loaded Magnetohydrodynamic Channels," Energy Conversion Management, 20, 1980, pp. 33-39
2. Brogan, T.R., Hill, J.A., et al., "Design of a Single Output MHD Generator for the U.S.S.R. U25 Installation," Fourth U.S. - U.S.S.R. Colloquium on MHD Power Generator October 5-6, 1978, Washington, D.C., pp. 221-246
3. Kirillin, V.A., Sheindlin, A.E., et al., "The U-25B Facility for Studies in Strong Magnetohydrodynamic Interaction," 17th Symposium, Engineering Aspects of Magnetohydrodynamics March 27-29, 1978, Stanford, CA, pp. F1.1 - F1.12
4. Pan, Y.C. and Doss, E.D., "Power Take-Off Analysis for Diagonally Connected MHD Channels," Paper No. 80-0253, AIAA 18th Aerospace Sciences Meeting, January, 1980
5. Pan, Y.C. and Doss, E.D., "Analyses of the Power Take-Off Regions of the U-25 Bypass and the U.S. U-25 Channels," Seventh International Conference on MHD Electrical Power Generators, June 16-20, 1980, pp. 178-186
6. Wu, Y.C.L., "Performance Theory of Diagonal Conducting Wall MHD Generators," AIAA Journal, 14, 10, 1976, pp. 1362-1368

THIS PAGE
WAS INTENTIONALLY
LEFT BLANK

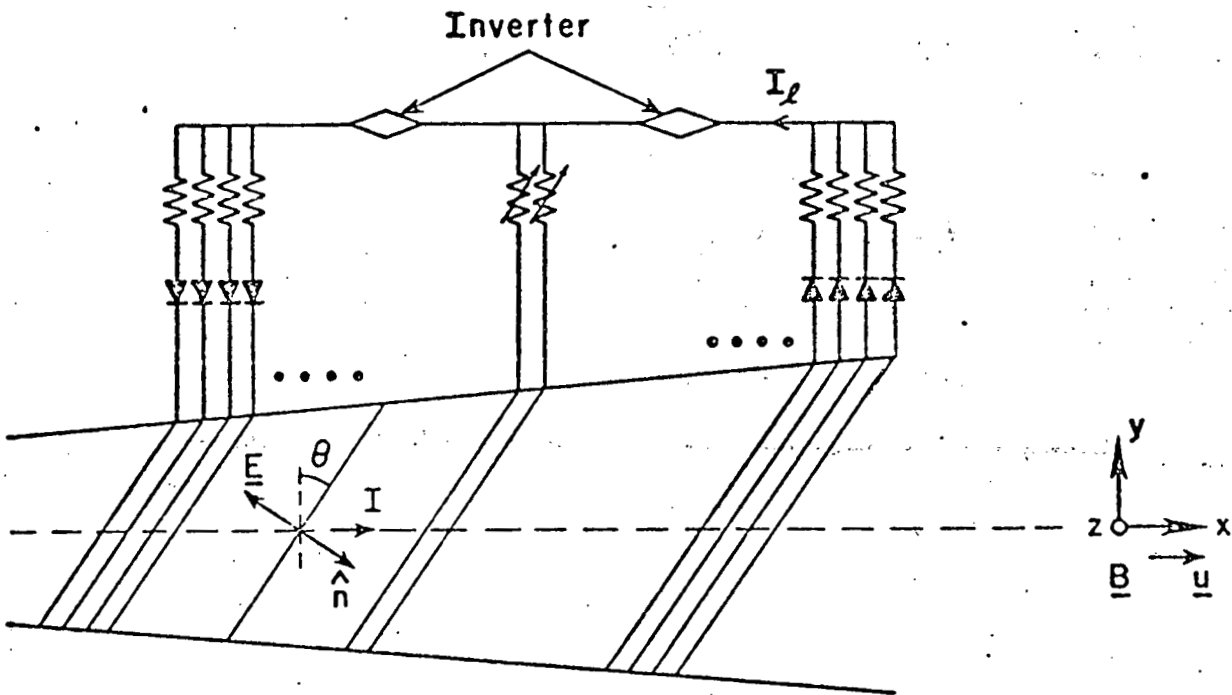
Figure Legends:

- Fig. 1 DCW channel configuration:
(a) Magnetic field profile;
(b) Power take-off and coordinate system.
- Fig. 2 Inlet connection.
- Fig. 3 Typical profiles of the Hall potential distributions for different loadings: (I) Open circuit; (II) Finite load; (III) Short circuit.
- Fig. 4 (a) Distribution of resistance for uniform current distribution under design conditions: $\tan \theta = 1$, $\beta_1 h_i = 0.7$, $\beta_o = 0.287$, $I_\ell = 278A$, $i_p = 23.2A$
(b) Lead current distribution: (I) Design case; (II) Undercurrent; (III) Overcurrent; (IV) Overcurrent with augmented resistors.
- Fig. 5 (a) Distribution of resistance for uniform current distribution with 25% spare blocking diodes under design conditions: $I_\ell = 270A$, $i_p = 30A$
(b) Lead current distribution with 14% overcurrent.
- Fig. 6 (a) Resistance distribution for uniform current distribution with 30% spare blocking diodes under high efficiency design conditions: $I_\ell = 198.5A$, $i_p = 23.2A$
(b) Distribution of current flowing in the channel (I) and in the leads (II) under overcurrent condition: $I_\ell = 308.6A$.
- Fig. 7 (a) Resistance distribution for uniform current distribution with 50% spare blocking diodes under high efficiency design conditions: $I_\ell = 198.5A$, $i_p = 33.1A$.
(b) Lead current distributions under design and overcurrent conditions.
- Fig. 8 (a) Resistance distribution for uniform current distribution in mid-channel leads. The design conditions are: $I_\ell = 214.5A = \frac{1}{2}I_s$, $i_p = 10.725A$, $\beta_o = 3.2$, $\beta_1 h_i = 0.149$.
(b) Distributions of the lead currents for a 20% variation of the load current.
- Fig. 9 Mid-channel lead current distributions for equal resistances (5 and 10 Ω). $I_\ell = 214.5A$.

- Fig. 10 Current distribution at the inlet power take-off region of the U-25B channel. $I_{\varrho} = 399\text{A}$, Power output = 1386W, Test 7, #5797.
- Fig. 11 Current distribution at the inlet power take-off region of the U-25B channel. $I_{\varrho} = 264\text{A}$, Power output = 1296W, Test 7, #5805.
- Fig. 12 Current distribution at the outlet power take-off region of the U-25B channel. $I_{\varrho} = 399\text{A}$, Power output = 1386W, Test 7, #5797.



(a)



(b)

Fig. 1 DCW channel configuration:
 (a) Magnetic field profile;
 (b) Power take-off and coordinate system.

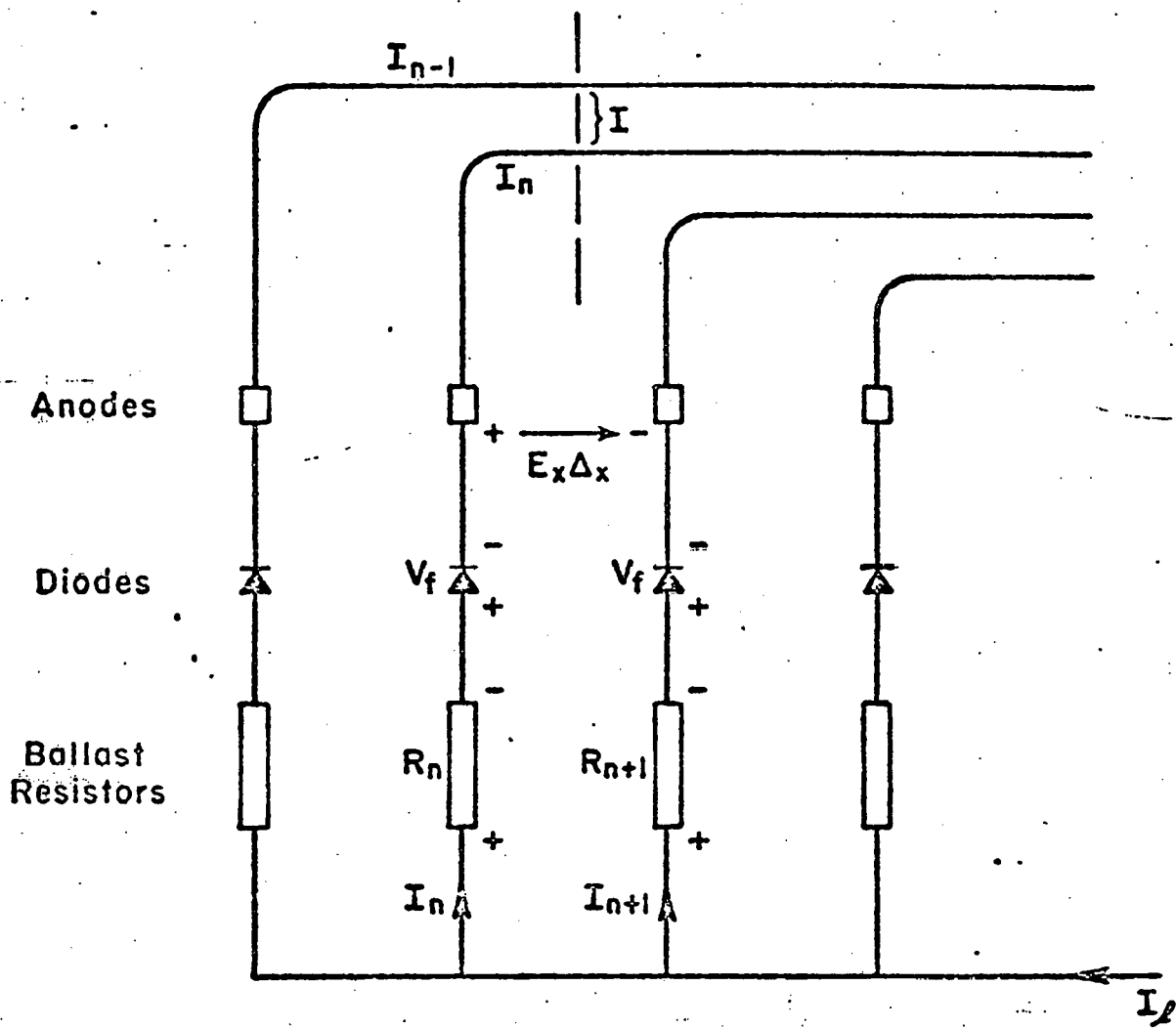


Fig. 2 Inlet connection.

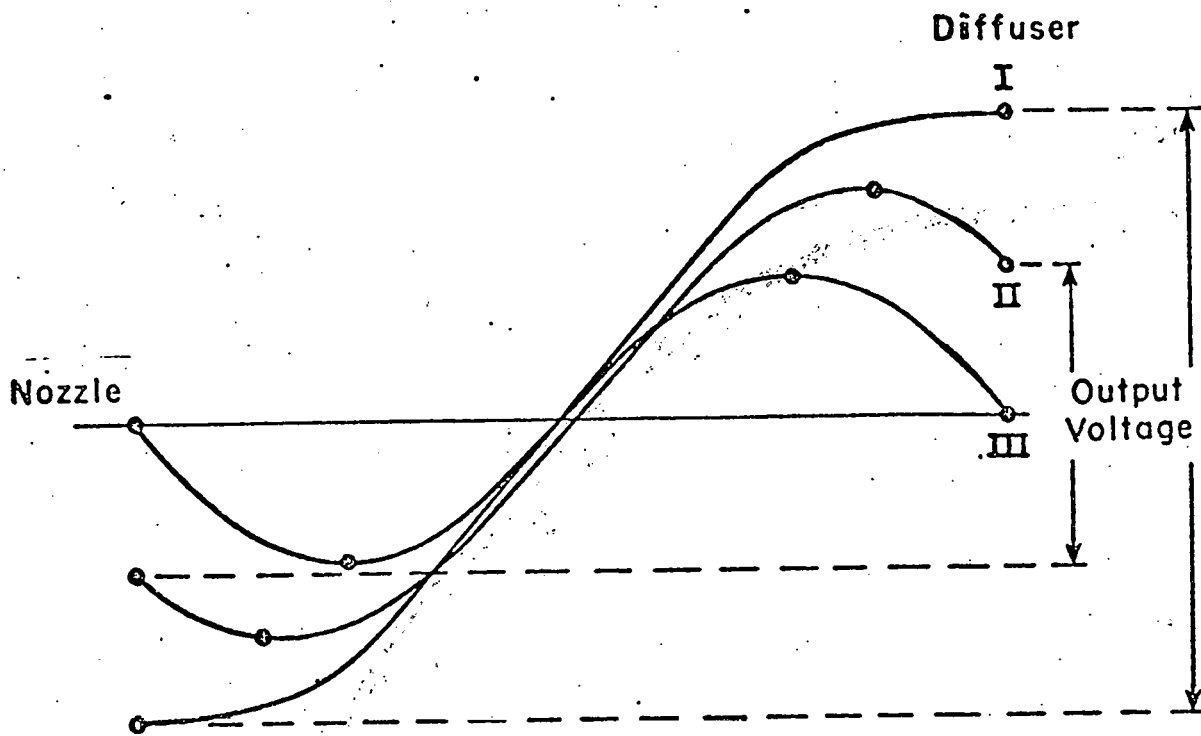
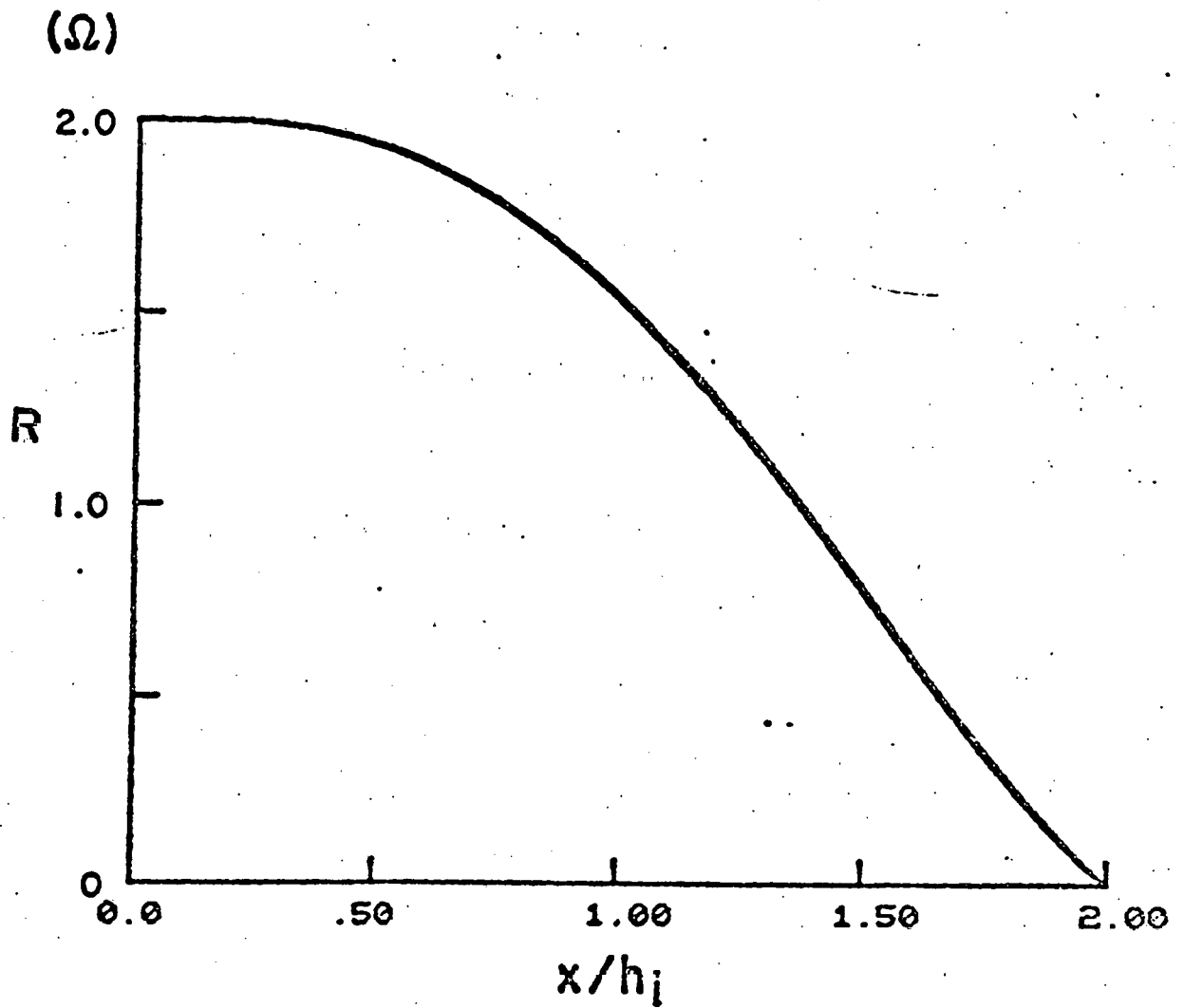


Fig. 3 Typical profiles of the Hall potential distributions for different loadings: (I) Open circuit; (II) Finite load; (III) Short circuit.



(a)

Fig. 4 (a) Distribution of resistance for uniform current distribution under design conditions: $\tan \theta = 1$, $\beta_1 h_i = 0.7$, $\beta_0 = 0.287$, $I_g = 278\text{A}$, $i_p = 23.2\text{A}$

(b) Lead current distribution: (I) Design case; (II) Undercurrent; (III) Overcurrent; (IV) Overcurrent with augmented resistors.



QUEENS GUARD

RUTGERS, The State University

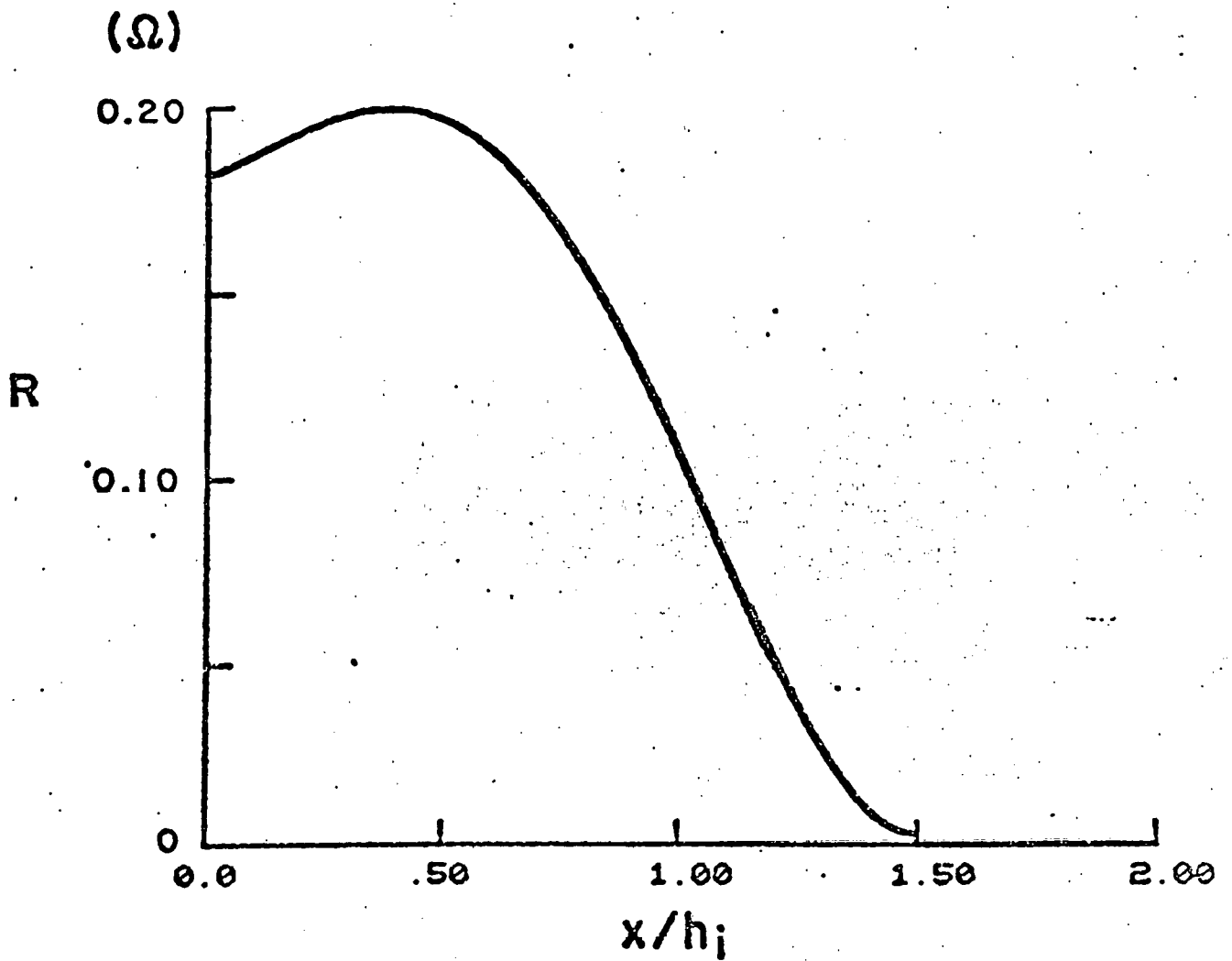
BOX 85
RUTGERS STUDENT CENTER
126 COLLEGE AVENUE
NEW BRUNSWICK, NEW JERSEY
08903

A short history of the Queens Guard

The Queens Guard Trick Drill Team from Rutgers, the State University of New Jersey was formed in 1957 under guidance from the Air Force ROTC program. During the 1960's the team represented New Jersey in the 1961 and 1965 Presidential Inaugural Parades for John F. Kennedy and Lyndon B. Johnson. In addition the Queens Guard won the national parade championship in 1963 and the national drill championships in 1961 and 1965. Then, in 1968 the team went overseas for its first international performance in the Edinburgh Military Tattoo in Edinburgh, Scotland. In 1969 and 1970 the Queens Guard and the Scarlet Rifles (Rutgers' Army ROTC drill team) merged to form the present day Queens Guard, a student run organization.

In 1973 the Queens Guard went on to take first place at the national championship competition during the National Cherry Blossom Festival in Washington, D.C. During the summer of that same year the team returned for its second performance at the Edinburgh Tattoo. Since then the Q.G. has participated in the 1976 and 1980 tattoos in Melbourne and Hobart, Australia; the 1980 Edinburgh Military Tattoo; the 1977 NATO Musik Festival in Kaiserslautern, West Germany and the 1974 Canadian National Exposition Scottish World Festival in Ontario, Canada. This summer the Queens Guard looks forward to participating in the 3rd Annual Durban Military Tattoo in the Republic of South Africa.

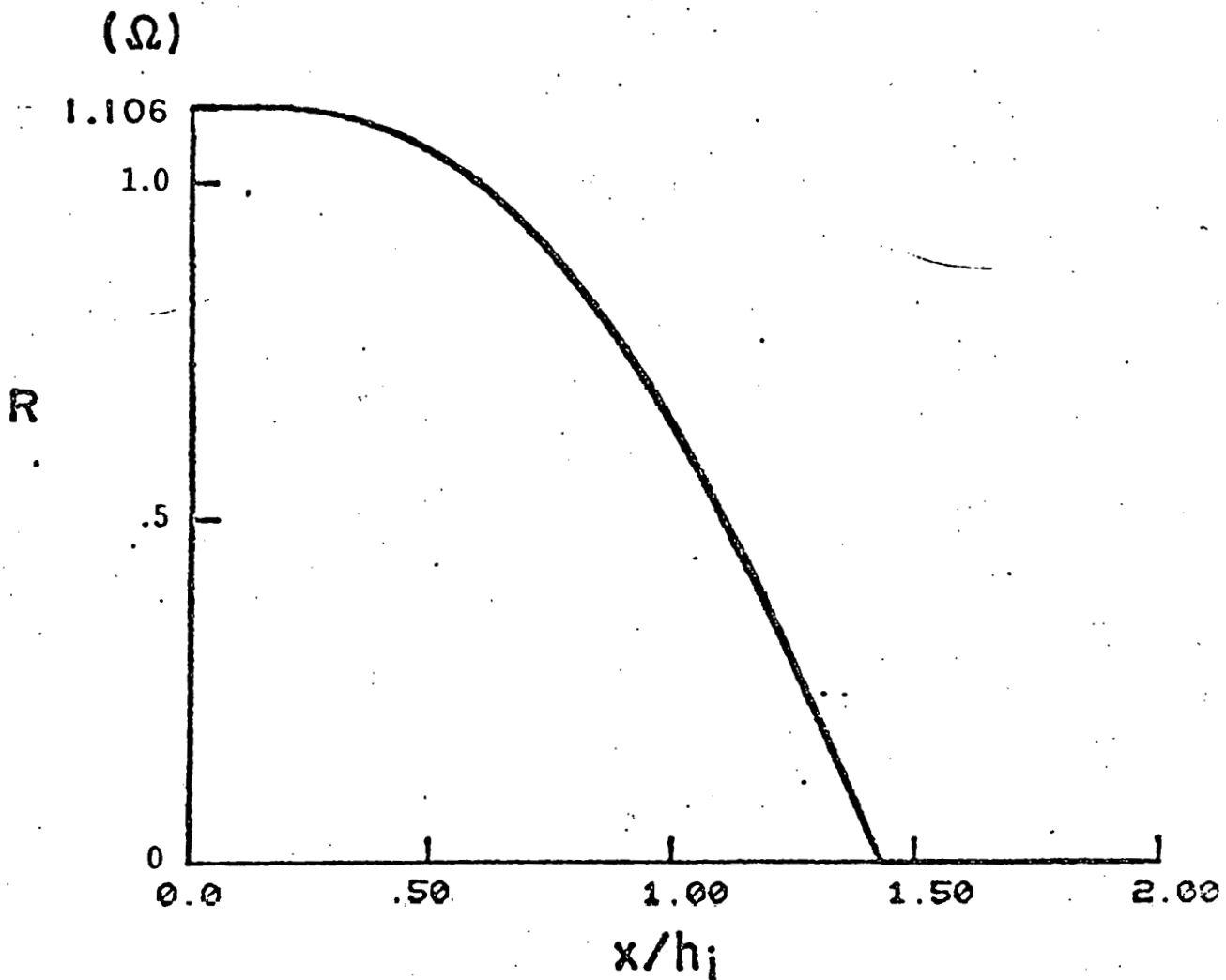
This year the 17 member team is under the guidance and leadership of its commander Verne A. James, Jr.; Jeff D. Dunne its executive commander and Captian Richard Comisso its advisor. Other team members include: Tom Barrale; Lewis Brooks; Christopher Buhner; Richard Crosta; Kenneth Danielson; John Dick; Donald Dubois; Richard Harsell; Gregory Lehman; Brian Mortensen; Alan Moryan; Robert Plano; Terry Trepel; Patrick Woody and John Young.



(a)

Fig. 5 (a) Distribution of resistance for uniform current distribution with 25% spare blocking diodes under design conditions: $I_g = 270A$, $i_p = 30A$

(b) Lead current distribution with 14% overcurrent.

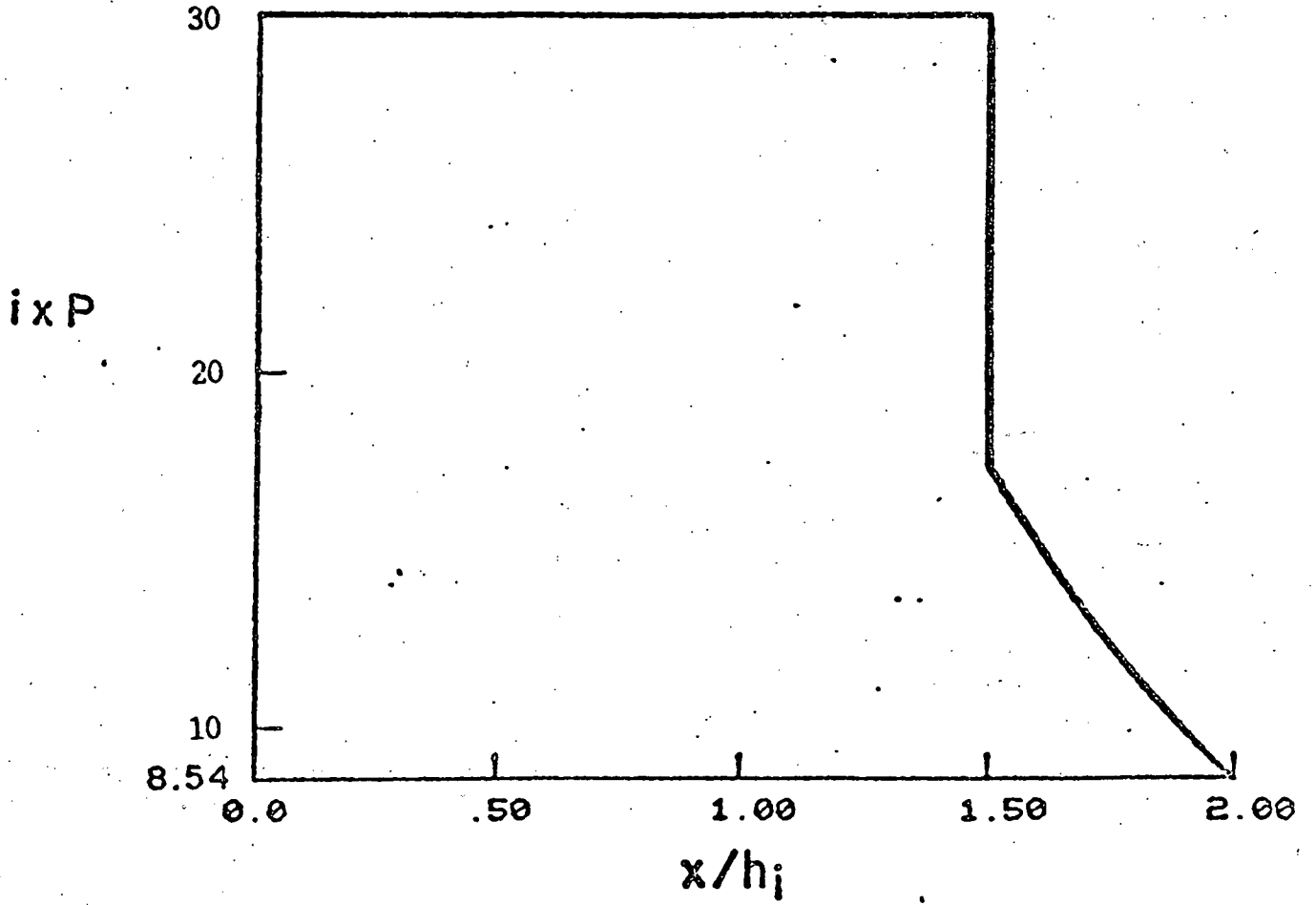


(a)

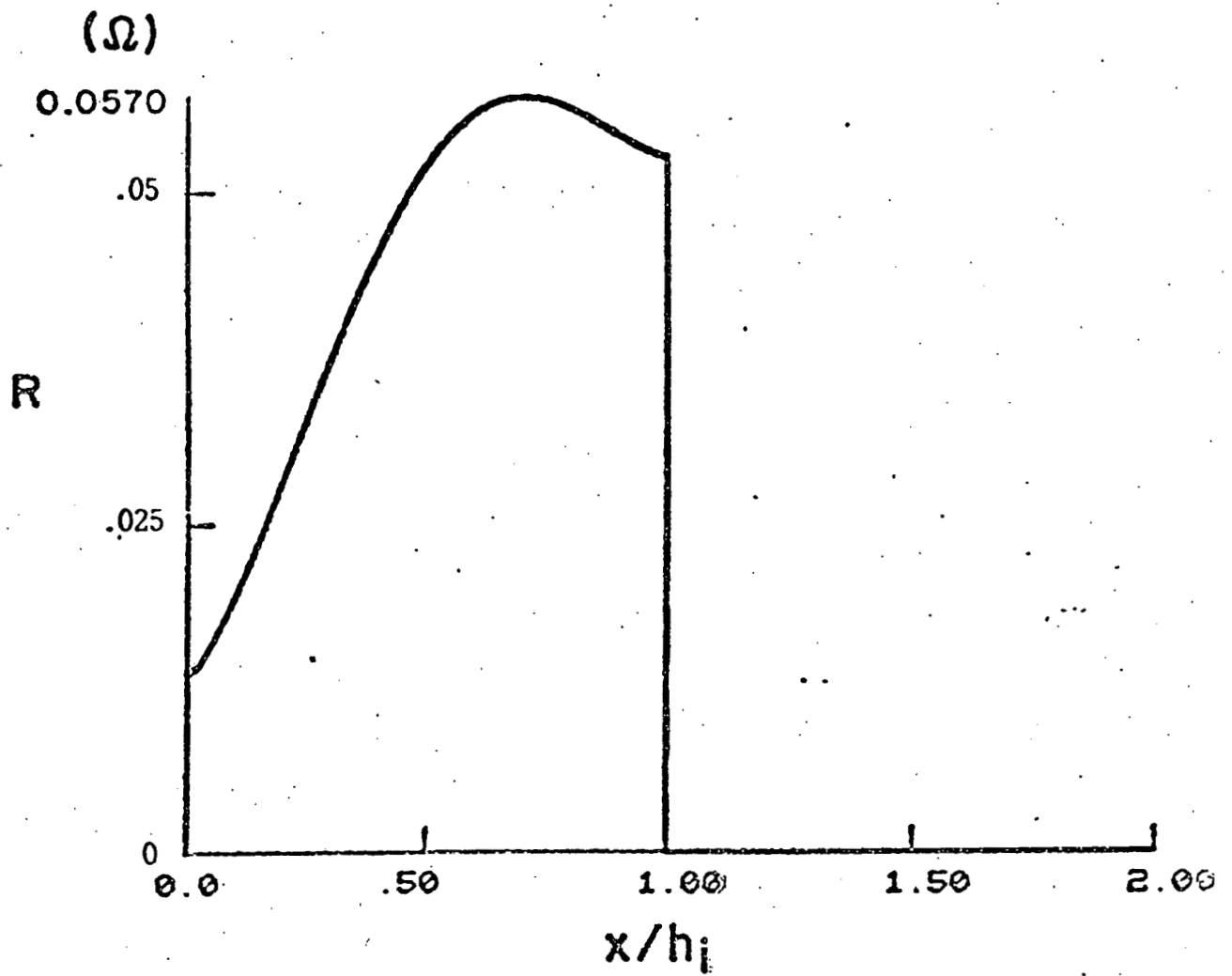
Fig. 6 (a) Resistance distribution for uniform current distribution with 30% spare blocking diodes under high efficiency design conditions: $I_\ell = 198.5\text{A}$, $i_p = 23.2\text{A}$

(b) Distribution of current flowing in the channel (I) and in the leads (II), under overcurrent condition: $I_\ell = 308.6\text{A}$.

(A)

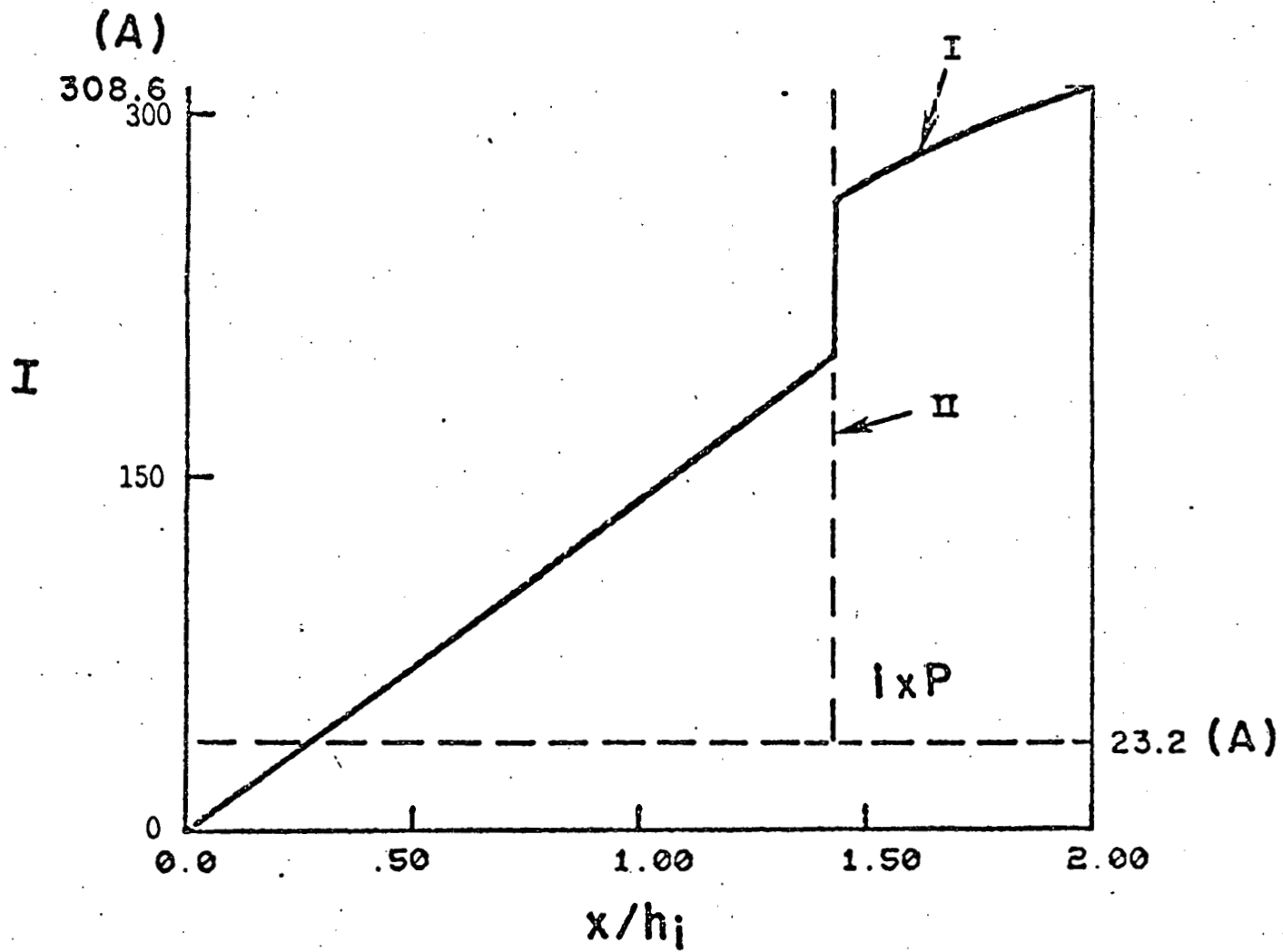


(b)

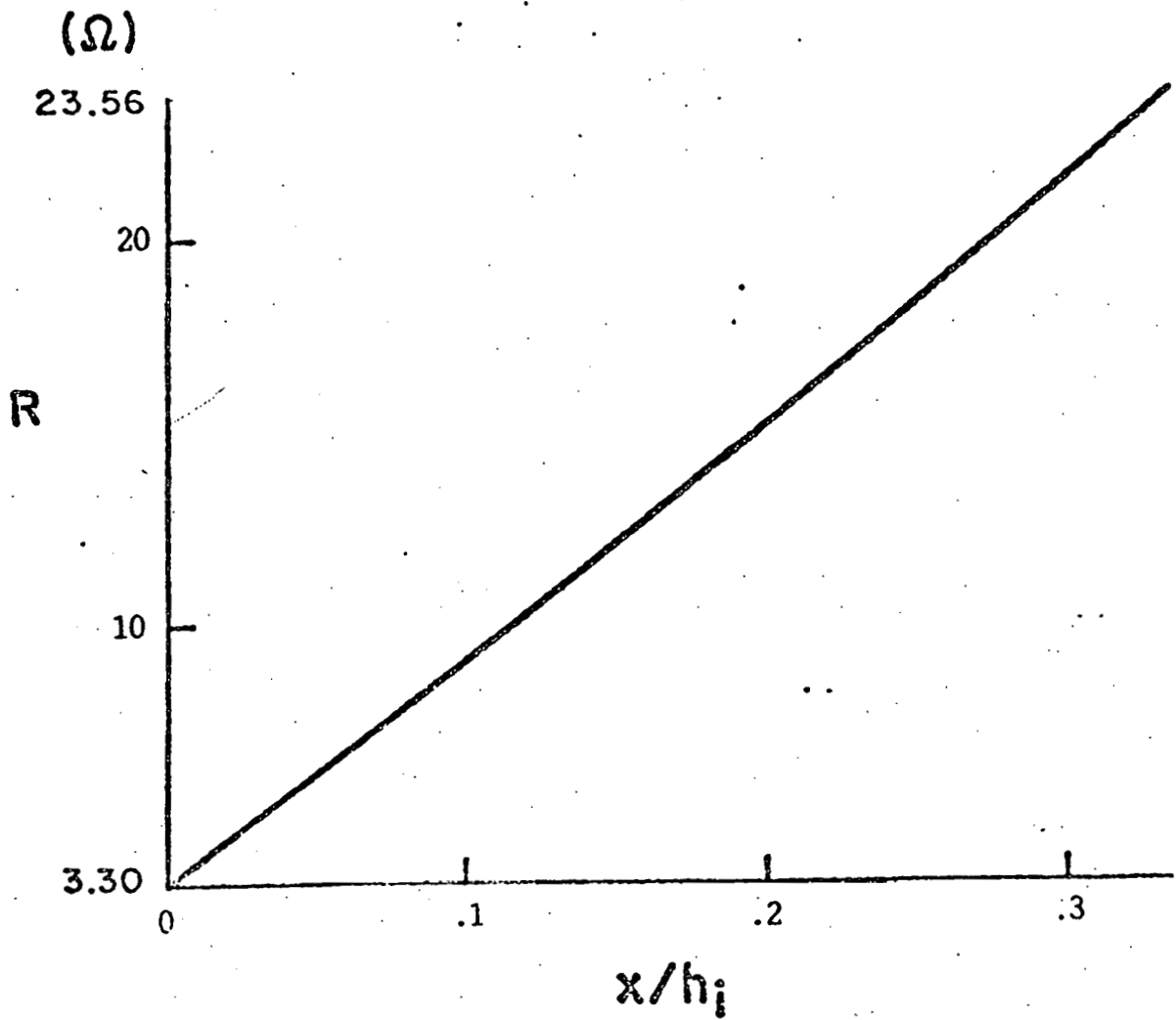


(a)

Fig. 7 (a) Resistance distribution for uniform current distribution with 50% spare blocking diodes under high efficiency design conditions: $I_p = 198.5A$, $i_p = 33.1A$.
 (b) Lead current distributions under design and over-current conditions.



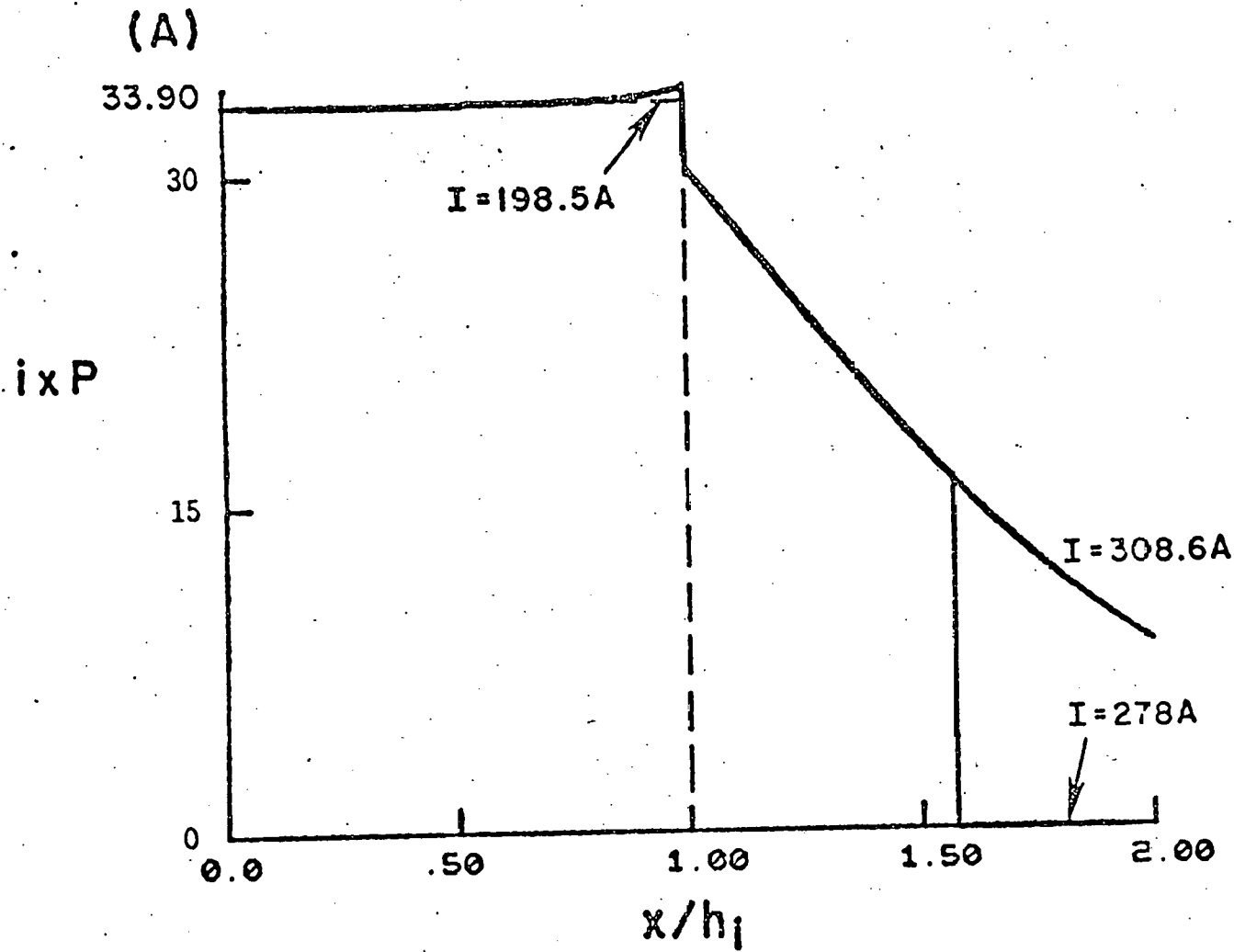
(b)



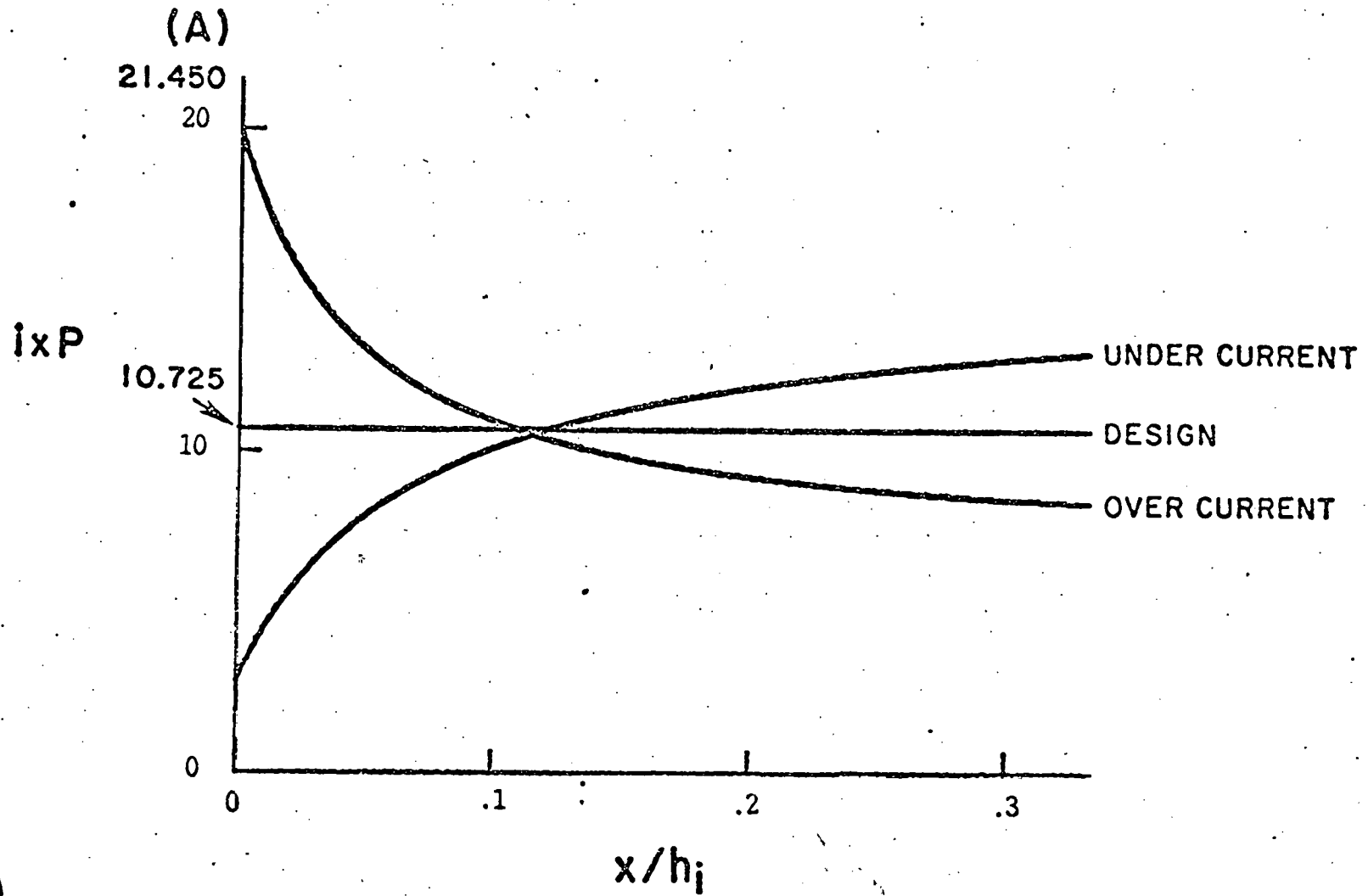
(a)

Fig. 8 (a) Resistance distribution for uniform current distribution in mid-channel leads. The design conditions are:
 $I_0 = 214.5A = \frac{1}{2}I_s$, $i_p = 10.725A$, $\beta_0 = 3.2$,
 $\beta_1 h_i = 0.149$.

(b) Distributions of the lead currents for a 20% variation of the load current.



(b)



(b)

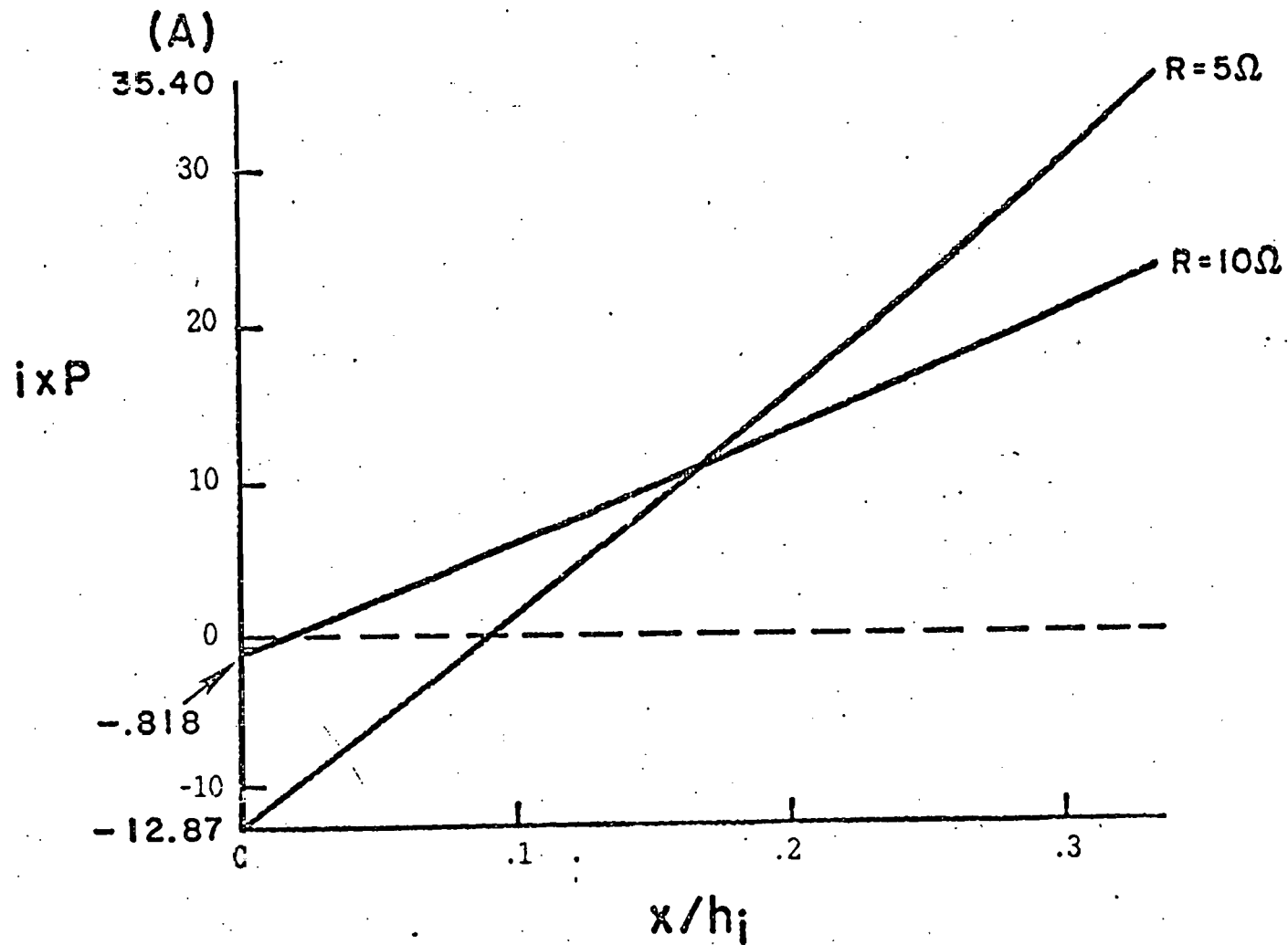


Fig. 9 Mid-channel lead current distributions for equal resistances (5 and 10 Ω). $I_0 = 214.5A$.

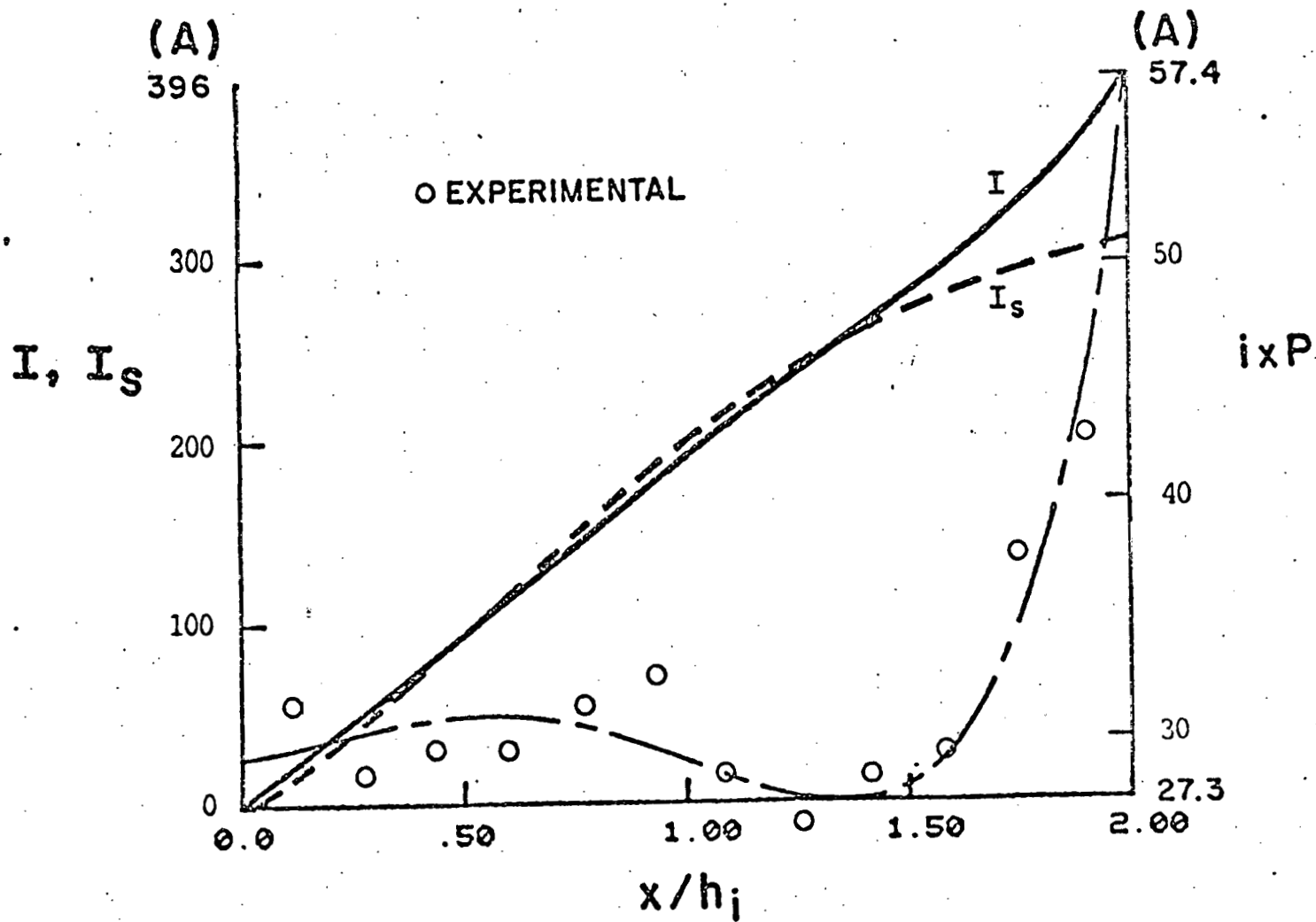


Fig. 10 Current distribution at the inlet power take-off region of the U-25B channel. $I_2 = 399A$, Power output = 1386W, Test 7, #5797.

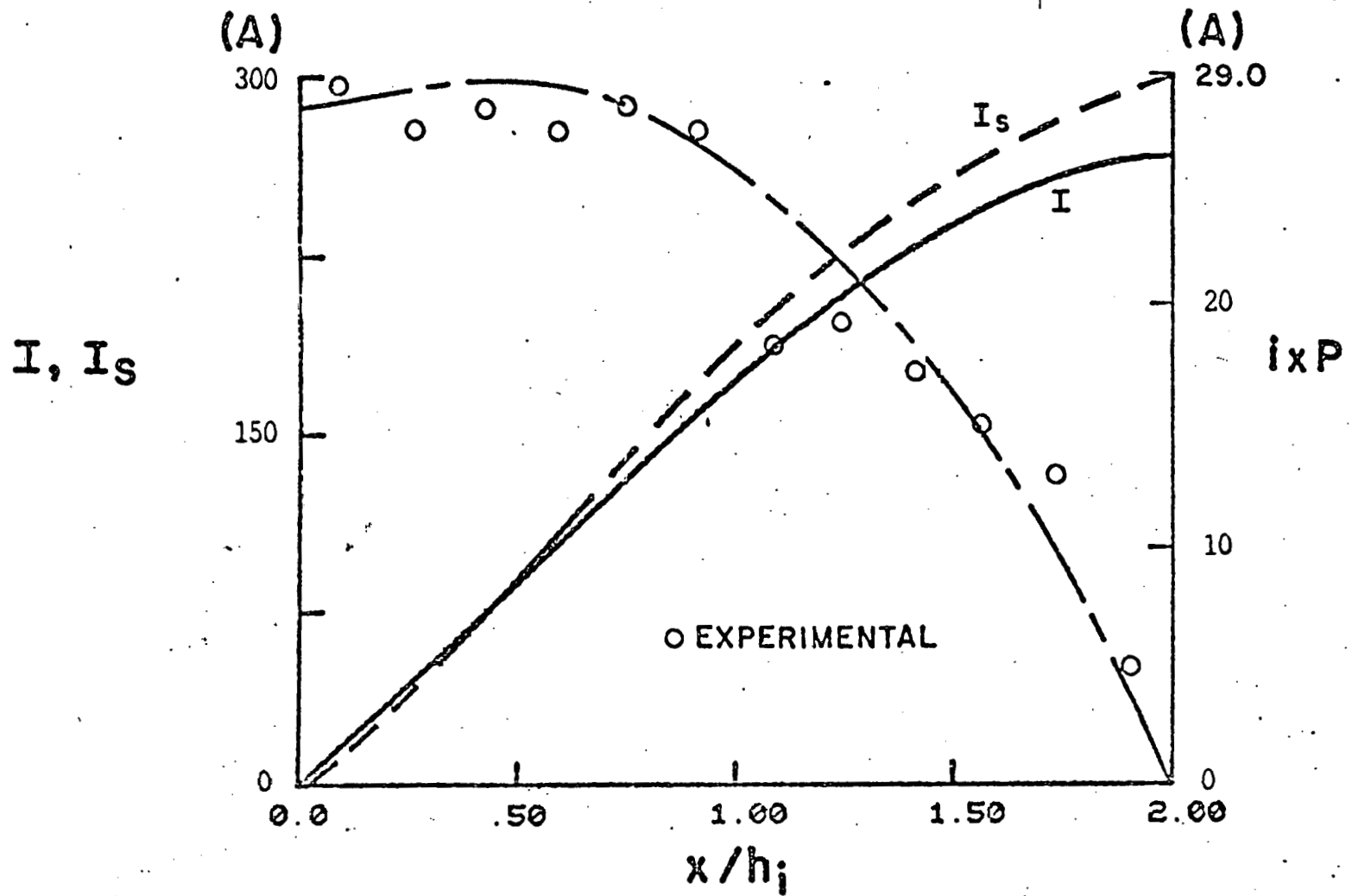


Fig. 11 Current distribution at the inlet power take-off region of the U-253 channel. $I_\ell = 264\text{A}$, Power output = 1296W, Test 7, #5805.

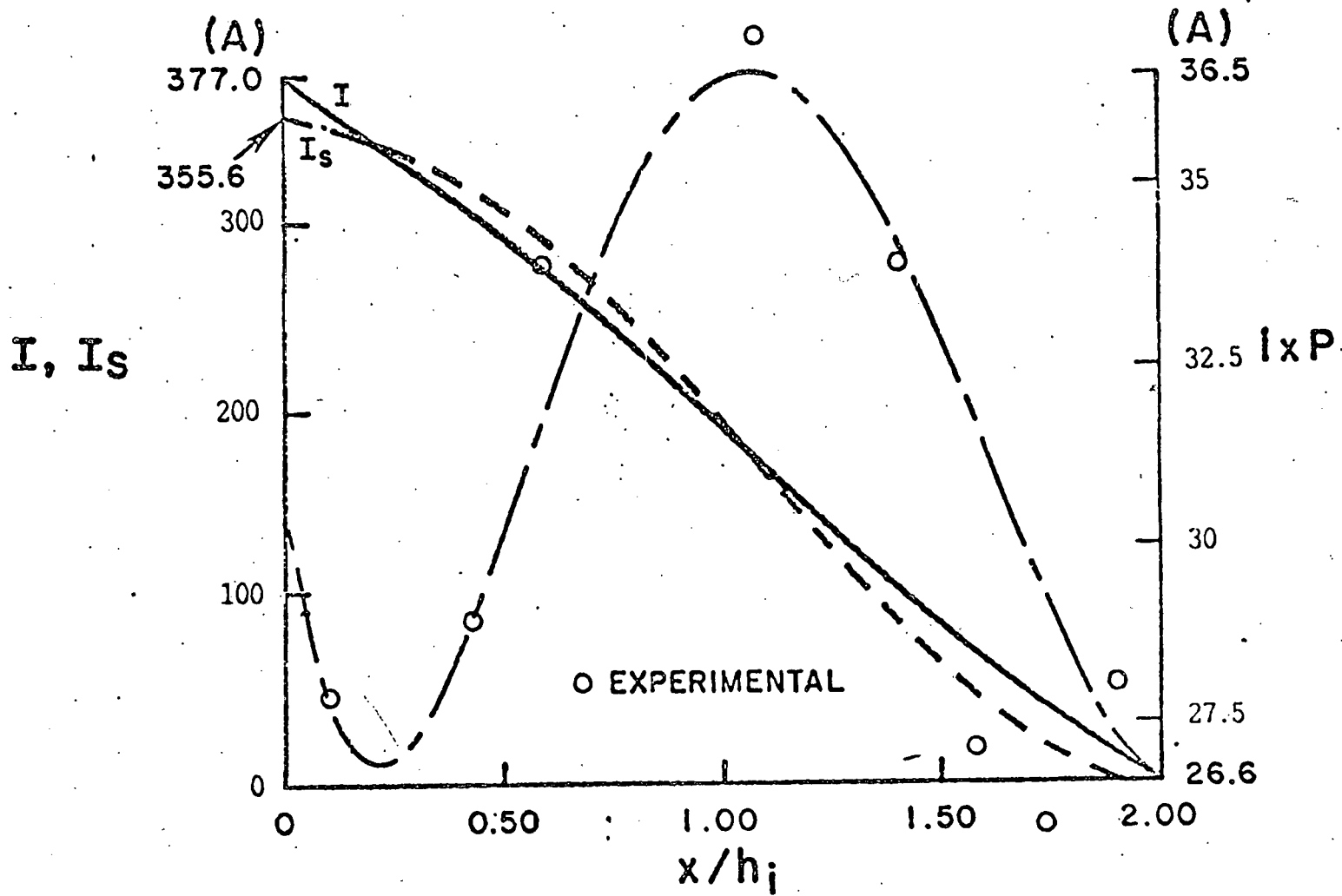


Fig. 12 Current distribution at the outlet power take-off region of the U-25B channel. $I_2 = 399A$, Power output = 1386W, Test 7, #5797.

WALL LEAKAGE EFFECT ON NON-UNIFORMITIES IN
DIAGONAL MHD-CHANNELS

S. Kuo, E. Levi, and B. Cheo

Polytechnic Institute of New York
Route 110
Farmingdale, NY 11735

ABSTRACT

The effect of wall leakage, symmetric as well as asymmetric is examined in the linear and nonlinear regimes. It is found:

1. The range of wavelength in the nonuniformities is reduced and in the asymmetric case splits into two separate pass-bands.
2. Depending on the wave length, forward waves can propagate both upstream and downstream, backward waves only upstream.
3. The growth rate is minimal when the leakage at the cathode wall is four times that of the anode wall.
4. In all cases, a resistance introduced in the diagonal bars reduces the growth rate by a constant.

1.1 Introduction

Recently, experimental results in the U-25 and U-25B Soviet facilities have shown that the performance characteristics of MHD channels may be strongly degraded by the presence of large scale electrical nonuniformities in the current distribution. The stability of the channel with regard to these nonuniformities, then, becomes one

of the most important factors in achieving economic and reliable generation of electric power by magnetohydrodynamic means. For this reason much effort has been devoted in trying to understand the origin of these fluctuations. Solbes and Lowenstein¹ have performed a two-dimensional linear stability analysis of the MHD channel and have been able to explain the development of the observed spatial fluctuations in the Hall field in terms of the arc-mode transfer of the current to the electrodes. Their analysis determines the conditions for which the negative voltage-ampere characteristic of the arc overcomes the ballasting resistance of the plasma and leads to the development of electrical nonuniformities. Since the ballasting resistance becomes smaller as the wavelength decreases, their theory predicts that the fastest growing modes have shortest possible wavelengths, in the order of the segmentation pitch. This is in good agreement with the experimental observations obtained in their diagonal Faraday channels.

In contrast, Kuo et al² have focused on the subject of the development of large scale nonuniformities observed in the experiments of U-25 and U-25B^{3,4} facilities. They have presented a nonlinear analysis of the nonuniformities in the diagonal MHD channel, and concluded that nonlinear mode-mode coupling is the mechanism responsible for the transfer of energy from the short wavelength linearly unstable modes to the long wavelength modes. The temporal evolution studies of the nonlinear instabilities enabled them to establish a stability criterion expressed in terms of a normalized ballasting resistance. Their numerical results have also demonstrated that the diagonal bar connections are responsible for the spread of the localized stationary nonuniformities. Although the theory provides good

agreement with the experimental observations of U-25 and U-25B facilities, the analysis did not include the effect of wall leakage, and hence of the coupling between frames.

In the following, the stability problem of an MHD channel having arbitrary wall characteristics is considered. A general set of coupled nonlinear equations is formulated from the circuit model shown in Fig. 1. The procedure of formulation is presented in Sec. 2. Section 3 deals with the linear stability analysis. An equivalent circuit for the original model of the channel is derived. This equivalent circuit provides great insight about the stability behavior of the channel and the effects of wall leakage on the instabilities. Moreover, the neutral stability boundaries are also established. Nonlinear coupled mode equations are derived in Sec. 4 for the two limiting cases of complete symmetry and asymmetry at the cathode and anode. The effect of wall leakage on the nonlinear development of large scale nonuniformities is discussed. The main finds are summarized in Sec.5.

2. Formulation With Wall Leakage

In the absence of current leakage along the walls of the channel the current in each frame does not depend on the interframe voltage and the temporal evolution of the current fluctuations is governed by a single rate equation. The wall leakage, however, introduces a coupling between the frames and more equations are needed. These are obtained in the limit of vanishing electrode pitch by applying Kirchhoff's voltage and current laws to the channel model shown in Fig. 1.

Current continuity leads to:

$$\tilde{I}_A(x) = \tilde{I}_e(x) - P \frac{\partial}{\partial x} \tilde{I}_{WA}(x+h'/2) \quad (1)$$

$$\tilde{I}_K(x) = \tilde{I}_e(x) + P \frac{\partial}{\partial x} \tilde{I}_{WK}(x-h'/2) \quad (2)$$

where $\tilde{I}_A(x) = -HP \tilde{J}_A(x+h'/2)$ and $\tilde{I}_K(x) = -HP \tilde{J}_K(x-h'/2)$, and voltage loops lead to:

$$P\tilde{E}_X(x+h'/2, h/2) = \tilde{I}_{WA}S_{WA} + P\alpha_A \frac{\partial}{\partial x} \left(\frac{1}{\sqrt{I_0 + \tilde{I}_A}} - \frac{1}{\sqrt{I_0}} \right) \quad (3)$$

$$P\tilde{E}_X(x-h'/2, -h/2) = \tilde{I}_{WK}S_{WK} - P\alpha_K \frac{\partial}{\partial x} \left(\frac{1}{\sqrt{I_0 + \tilde{I}_K}} - \frac{1}{\sqrt{I_0}} \right) \quad (4)$$

$$L \frac{\partial}{\partial t} \tilde{I}_e = \Delta\tilde{V}_1 + \Delta\tilde{V}_2 - S_e \tilde{I}_e + \alpha_A \left(\frac{1}{\sqrt{I_0}} - \frac{1}{\sqrt{I_0 + \tilde{I}_A}} \right) + \alpha_K \left(\frac{1}{\sqrt{I_0}} - \frac{1}{\sqrt{I_0 + \tilde{I}_K}} \right) \quad (5)$$

where

$$\Delta\tilde{V}_1 = -\iint \frac{[\tilde{I}_e(x') - P \frac{\partial}{\partial x'} \tilde{I}_{W-}(x')] \cos k(x-x') [\cosh(kh) - \cos(kh')]}{\pi\alpha H k P \sinh(kh)} dx' dk$$

and

$$\Delta\tilde{V}_2 = \iint \frac{[\frac{\partial}{\partial x'} \tilde{I}_{W+}(x')] \sin(x-x')}{\pi\alpha H k} \left[\beta - \frac{\sin(kh')}{\sinh(kh)} \right] dx' dk$$

are the ohmic voltage drops across the free stream plasma resistance from cathode to anode resulting from the current fluctuations. The last terms to the right in Eqs. (3), (4) and (5) are the idealized nonlinear characteristic of the anode and cathode arcs which serve as sources for the instabilities. Also the definition $\tilde{I}_{W\pm}(x) = \frac{1}{2} [\tilde{I}_{WA}(x+h/2) \pm \tilde{I}_{WK}(x-h/2)]$, has been used in $\Delta\tilde{V}_1$ and $\Delta\tilde{V}_2$. The assumption of vanishing pitch may be justified if the wave lengths of the fluctuations under consideration are longer than several electrode pitch. Equations (3) and (4) can be reexpressed by subtracting and adding one another and become:

$$\tilde{I}_{W+} S_{W-} + \tilde{I}_{W-} S_{W+} = P [L \frac{\partial}{\partial t} \frac{\partial}{\partial x} \tilde{I}_e + S_e \frac{\partial}{\partial x} I_e] \quad (6)$$

$$\tilde{I}_{W+} S_{W+} + \tilde{I}_{W-} S_{W-} = - \frac{2\beta}{\sigma H} (\tilde{I}_e - P \frac{\partial}{\partial x} \tilde{I}_{W-}) - P \frac{\partial}{\partial x} \left[\frac{\alpha_A}{\sqrt{I_0 + \tilde{I}_A}} - \frac{\alpha_K}{\sqrt{I_0 + \tilde{I}_K}} \right] + \frac{2P}{\sigma} \tilde{I}_x(x) \quad (7)$$

where the relation $\tilde{E}_x(x+h/2, h/2) - \tilde{E}_x(x-h/2, h/2) = \frac{\partial}{\partial x} (\Delta\tilde{V}_1 + \Delta\tilde{V}_2)$ and the x derivative of Eq. (5) have been employed to obtain Eq. (b), Generalized Ohm's law has been used to derive Eq. (7),

$$\tilde{I}_x(x) = - \frac{1}{HP} \iint \left\{ \frac{[P \frac{\partial}{\partial x'} \tilde{I}_{W+}(x')] \text{sink}(x-x') [\cosh(kh) + \cos(kh')]}{2\pi \sinh(kh)} + \frac{[\tilde{I}_e(x') - P \frac{\partial}{\partial x'} \tilde{I}_{W-}(x')] \cos k(x-x') \sin(kh')}{2\pi \sinh(kh)} \right\} dx' dk$$

is the averaged fluctuating current density along the core boundaries and $S_{W\pm} = S_{WA} \pm S_{WK}$. Equations (1), (2), (5), (6) and (7) provide a complete description of the effect of wall leakage within the framework of the circuit model. With no wall leakage, Eq. (5) reduces to the rate equation of Ref. (1) and (2). The rate equation (5) clearly

shows that the fluctuating current \tilde{I}_e is coupled to the fluctuating wall leakage currents through both the plasma and the arcs. To study the effect of wall leakage on the stability of the fluctuations, the nonlinear Eqs. (5), (6) and (7) have to be solved simultaneously. The linear regime will be considered first, since in this case each mode k can be considered separately.

3. Linear Stability Analysis

The nonlinear arc terms are linearized by keeping only the first expansion term, so that Eqs. (1), (2), (5), (6) and (7) can be combined to obtain a single rate equation for the k mode of the fluctuation current \tilde{I}_e . Since the ballasting effect of the free stream is wavelength dependence, only the short wavelength modes are linearly unstable, and are of interest in the linear regime. For the short wavelength mode k , the rate equation governing $\tilde{I}_e(k)$ is:

$$L \frac{\partial}{\partial t} \tilde{I}_e(k) = - \left\{ S_e + \frac{S'_{WK} \left[S_K + \frac{|S_p| + i\beta S_p}{2} \right]}{S'_{WK} + S_K + \frac{|S_p| + i\beta S_p}{2}} + \frac{S'_{WA} \left[S_A + \frac{|S_p| - i\beta S_p}{2} \right]}{S'_{WA} + S_A + \frac{|S_p| - i\beta S_p}{2}} \right\} \tilde{I}_e(k) \quad (8)$$

where $S_p = \frac{2}{\sigma H P k}$ is the ballasting resistance of the free stream, $S'_{WK} = S_{WK}/k^2 P^2$, $S'_{WA} = S_{WA}/k^2 P^2$ are the effective resistances of cathode and anode wall respectively, and $S_K = -\alpha_K/2I_0^{3/2}$ and $S_A = -\alpha_A/2I_0^{3/2}$ are the negative cathode and anode arc resistances serving as sources for the instabilities.

Without wall leakages, Eq. (8) reduces to the previous result.^{1,2} Eq. (8) can be represented by the equivalent circuit of Fig. 2. It is seen that when leakage is present, the wall leakage impedances are essentially shunting the arcs and the plasma. The Hall effect introduces reactances of opposite sign at the anode and cathode. Unless there is complete symmetry in the arcs and leakages at the anode and cathode, these reactances cause the fluctuations to oscillate in time as well as space. It should be noted at this point that, whereas the ballast resistance of the plasma $|S_p|$ is always positive, the signs of the reactances βS_p change with the sign of k . The Hall effect also

enhances the overall ballasting effect of the free stream, as will be shown later. The solution of Eq. (8) indicates that the fluctuations oscillate at the complex frequency $\omega = \omega_0 + i\gamma$, the growth rate and the oscillation frequency ω_0 of the k mode are obtained from Eq. (9) as:

$$\gamma L = -\left\{ S_e + \frac{S'_{WK} [(S'_K + |S_p|/2)(S'_{WK} + S'_K + |S_p|/2) + \beta^2 S_p^2/4]}{(S'_{WA} + S'_A + |S_p|/2)^2 + \beta^2 S_p^2/4} + \frac{S'_{WA} [(S'_A + |S_p|/2)(S'_{WA} + S'_A + |S_p|/2) + \beta^2 S_p^2/4]}{(S'_{WA} + S'_A + |S_p|/2)^2 + \beta^2 S_p^2/4} \right\} \quad (9)$$

$$\omega_0 L = \frac{\beta S_p}{2} \left\{ \frac{S'^2_{WK}}{(S'_{WK} + S'_K + |S_p|/2)^2 + \beta^2 S_p^2/4} - \frac{S'^2_{WA}}{(S'_{WA} + S'_A + |S_p|/2)^2 + \beta^2 S_p^2/4} \right\}$$

$$= \frac{2\beta S_p \{ (S_- + S'_{W-})(S'^2_{W+} + S'^2_{W-})(S'_{W+} + S'_+ + |S_p|) - S'_{W-} S'_{W+} [(S'_{W+} + S'_+ + |S_p|)^2 + (S'_{W-} + S'_-)^2 + \beta^2 S_p^2] \}}{[(S'_{W+} + S'_+ + |S_p|)^2 + \beta^2 S_p^2 - (S_- + S'_{W-})^2]^2 + [2\beta S_p (S_- + S'_{W-})]^2} \quad (10)$$

where $S_{\pm} = S_A \pm S_K$ and $S'_{W\pm} = S'_{WA} \pm S'_{WK}$.

By setting $\gamma \leq 0$ the following stability criterion is obtained:

$$\begin{aligned} & [(S_+ + |S_p| + S'_{W+})^2 + \beta^2 S_p^2 - (S_- + S'_{W-})^2] \left\{ (S_+ + |S_p| + S'_{W+})(S_+ + |S_p| + \frac{S_e S'_{W+}}{S_e + S'_{W+}}) \right. \\ & \left. + \beta^2 S_p^2 - S'^2_{W-} - \frac{S'_{W-}}{S'_{W+} + S_e} [2S_- S_e + S'_{W-} (S_+ + |S_p| + S_e)] \right\} \\ & + \frac{4\beta^2 S_p^2 (S'_{W-} + S'_-)[S_e (S'_{W-} + S'_-) + S'_{W+} S'_-]}{(S_e + S'_{W+})} \geq 0 \quad (11) \end{aligned}$$

This criterion is, in general, different from that obtained by Solbes and Lowenstein¹. For symmetric wall characteristics ($S'_{W-} = 0 = S'_-$), Eq. (11) reduces to

$$(S_+ + |S_p| + S_{W+}') (S_+ + |S_p| + \frac{S_e S_{W+}'}{S_e + S_{W+}'}) + \beta^2 S_p^2 > 0 \quad (12)$$

the neutral stability boundary in the $(-S_+/|S_p|, S_{W+}'/|S_p|)$ plane is then given by the two curves:

$$\begin{aligned} -S_+/|S_p| = \frac{1}{2} \{ (2 + S_{W+}'/|S_p| + S_{W+}' S_e / (S_{W+}' + S_e) |S_p|) \\ \pm \sqrt{[S_{W+}'^2 / (S_{W+}' + S_e) |S_p|]^2 - 4\beta^2} \} \end{aligned} \quad (13)$$

The boundary given by Eq. (13) agrees with the result of Solbes and Lowenstein¹, except that they found an additional oscillatory domain. This cannot exist, as can be seen by introducing symmetric conditions in Fig. 2 and Eq. (10), which reduces to $\omega_0 L = 0$.

In a channel with asymmetric wall leakage, there are, instead, two unstable regions separated by one stable region. These are best studied starting with the case of the most practical interest when the wall leakage is weak:

3.1 Weak wall leakage

In the limit of weak leakage, $S_{W+}'/|S_p| \gg 1$, the Hall effect terms $\beta^2 S_p^2/4$ in Eqs. (9) and (10) can be neglected and Eq. (11) reduces to four asymptotes described by the following straight lines:

$$-S_+/|S_p| = 1 + (S_e/|S_p|) \quad (14)$$

$$-S_+/|S_p| = \frac{1-a}{1-b} \frac{S_{W+}'}{|S_p|} \quad (15)$$

$$-S_+/|S_p| = \frac{(1-a^2)S_{W+}'/|S_p| + (a-b)^2 S_e/|S_p|}{1-b^2} \quad (16)$$

$$-S_+ / |S_p| = \frac{1+a}{1+b} \frac{S'_{W+}}{|S_p|} \quad (17)$$

where $a = S'_{W-}/S'_{W+}$ and $b = S_-/S_+$ represent indexes of the degree of asymmetry in the channel. In the analysis, they are assumed to be parameters varying between -1 and +1. As S'_{W+} decreases the Hall effect terms must be considered; these straight lines curve to connect (14) and (15), and (16) and (17), thus limiting the extent of the instability domains, as shown in Fig. 3 for the particular case of $b=0$ and $a=0.6$. In order to assess the effect of asymmetry, one should start from the symmetric condition. In this case, the lines given by Eq. (15), (16) and (17) reduce to the single line $-S_+ = S'_{W+}$, which connects with (14) to form the single neutral stability curve represented by Eq. (13). As asymmetry appears between the cathode and anode walls, the straight lines (15), (16) and (17) split up. A new stable region appears between lines (15) and (16) and the extent of the stable region above line (17) is decreased.

This peculiar behavior on the stability of the channel is due to the shunting effects of the wall leakage reactances on the sources of the fluctuations, the arcs. In the symmetric case, the presence of leakage modifies the source impedance from $S_+ + |S_p|$ into $S'_{W+}(S_+ + |S_p|) / (S'_{W+} + S_+ + |S_p|)$. This expression changes sign twice as the negative arc impedance S_+ increases. It is positive as long as $|S_+| < |S_p|$. A further increase in $|S_+|$ makes the source impedance sufficiently negative to overcome the ballasting effect of the resistance S_e of the diagonal bar. The channel then becomes unstable. Stability is regained, however, when $|S_+|$ is sufficiently large to render negative the denominator, as well as the numerator of the source impedance.

As the denominator $S'_{W+} + S_+ + |S_p|$ approaches zero from the positive side the growth rate which is given by

$$\gamma_L = -S_e + \frac{S'_{W+} \{ (S_+ + |S_p|) (S'_{W+} + S_+ + |S_p|) + \beta^2 S_p^2 \}}{(S'_{W+} + S_+ + |S_p|)^2 + \beta^2 S_p^2} \quad (19)$$

would increase without bound if it were not held in check by the Hall effect term $\beta^2 S_p^2$. This may result in a growth rate having a larger value, than in the absence of leakage, as can be seen from Fig. 4a.

In the case of asymmetric wall characteristics, the source impedance has two components

$$\frac{S'_{WA} (S_A + |S_p|/2)}{S'_{WA} + S_A + |S_p|/2} + \frac{S'_{WK} (S_K + |S_p|/2)}{S'_{WK} + S_K + |S_p|/2}$$

instead of one. They change signs for different values of $S_+ = S_A + S_K$. Since the term which undergoes a change in sign in the denominator becomes infinitely large, and hence dominant, the sign of the combined source impedance changes four times. As $|S_+|$ is increased along the vertical line I of Fig. 3, one crosses four stability boundaries.

3.2 Strong Wall Leakage, Hall Effect

The stability of the channel is increasingly affected by the Hall reactances, as the wall leakage becomes stronger. It was already mentioned that they have a stabilizing effect. The reactances connected in series with the arc sources reduce the growth rate, and in the limit $S'_{W+} \ll -(S_+ + |S_p|)$, they completely prevent the onset of instability, as can be seen from Eq. (18) and Fig. 3.

In addition the Hall effect causes oscillations to appear, whenever the anode and cathode walls have dissimilar characteristics.

If, for instance, seed deposition completely short-circuits the cathode ($S_{WK}=0$), while the anode retains good insulation ($S_{WA} \rightarrow \infty$), Eqs. (9) and (10) become

$$\gamma L = -[S_e + \frac{1}{2}(S_+ + |S_p|)] \quad (19)$$

$$\omega_o L = -\frac{\beta S_p}{2} \quad (20)$$

A comparison with the value of γ when no leakage is present on either side, shows that the source value is halved, as can be expected, since only one side of the channel is functioning. Moreover, the absence of a Hall effect term in Eq. (19) shows that the stabilizing effect of the Hall reactances depends on the degree of asymmetry. Figures 4a and b show that it is maximum around $|a| \sim .6$.

Equation (20) for the oscillation frequency shows that the Hall term, which couples with the loop inductance L , represents an equivalent capacitance of value $2/\beta S_p \omega_o$.

3.3 Wavelength Dependence

3.3.1 Growth Rate

Both the free-stream plasma-resistance S_p and the normalized wall leakage resistances S'_w are functions of the wavenumber $|k|$ of the fluctuations. The ballasting effect of the plasma resistance decreases in proportion to the wavelength and leads to the onset of the instability at a certain value of $|k|$. The growth rate increases, then, with k . Beyond a certain value, however, the damping provided by the wall leakage effects, which are quadratic in k , takes

over and rapidly quenches the instability. This band-pass behavior is clearly shown in Figs. 4 and 5 which portray the growth rate of a channel with high and low anode wall resistance respectively, and with varying cathode wall leakage.

Figure 4a clearly shows that, as the cathode wall leakage increases, the growth rate decreases. In fact for intermediate values of asymmetry the unstable band ($\gamma > 0$) splits into two bands separated by a stable band $\gamma < 0$. This could be expected from the discussion of the stability boundaries, since for the channel of given characteristics a variation in k corresponds to the tracing of a hyperbole in the $S_+ / |S_p| - S_- / |S_p|$ plane. Curve II and III in Fig. 3 represent a channel having the dimensions and operating points of the U-25B channel #1, under conditions of weak and strong wall leakage respectively.

The general trend is more graphically displayed in the 3-dimensional plot of Fig. 4b.

A comparison of Figs. 4 and 5 shows that, the greater the anode wall leakage, the smaller the value of k at which the instability is cut-off. In the common range of wavelength, the curves for the limiting cases of $a=0$ and $a=1$ almost overlap.

3.3.2 Frequency

The dependence of the frequency on the wavelength of the fluctuations is depicted in Fig. 6 for the case of high anode wall resistance. (Similar trends are obtained in the case of strong anode wall leakage.) Again, the degree of asymmetry (a) serves as a parameter. Starting with the symmetric case represented by the top line ($a=1$), one observes that ω_0 is zero in the whole range of k .

However, with the smallest degree of asymmetry, regions with positive and negative frequencies can be detected. A comparison between Figs. 6 and 4b shows that: the maximum in the range of positive frequency occurs at the peak of the growth rate, and the minimum in the range of negative frequency occurs at the instability cut-off value of k . These extremes in frequency, as well as the zero crossing, divide the wavelength domain into modes having group and phase velocities in the same and opposite directions. Starting from the longer wavelength end (small k) one finds that both phase (ω/k) and group velocity ($\partial\omega/\partial k$) are positive. This is a forward wave-mode propagating in the direction of the diffuser. Beyond the peak in γ the phase velocity is still positive, but the group velocity becomes negative. This is a backward wave-mode propagating towards the nozzle. Beyond the zero cross-over point in ω , both group and phase velocities are negative. This is again a forward wave mode, but propagating towards the nozzle. The mode beyond the instability cut-off point ($\gamma=0$) is of no interest, since it is damped.

3.4 Effect of the Diagonal Bar Resistance

The diagonal bar resistance S_e has a stabilizing effect. Equation (9) shows that S_e reduces the growth rate by a constant. Therefore all that is needed to account for S_e is a shift in the zero lines of Figs. 4 and 5. Also according to Eq. (14) and (16) and Fig. 3 the main effect of S_e on the stability boundaries, is to increase the extent of the stable regions.

4. Nonlinear Mode-Mode Coupling

To examine the possibility of transfer of energy from the short wavelength unstable modes to the long wavelength modes, one extends the procedure outlined in the previous paper². Namely, one considers two current-fluctuation modes:

$$\tilde{Y}_e = \tilde{Y}_1(k_1) + \tilde{Y}_2(k_2) \quad \text{and} \quad \tilde{I}_W = \tilde{I}_{W1}(k_1) + \tilde{I}_{W2}(k_2) \quad (21)$$

where \tilde{Y}_1 and \tilde{I}_{W1} are the linearly stable long wavelength fluctuations ($k_1 \sim 0$) and \tilde{Y}_2 and \tilde{I}_{W2} are linearly unstable short wavelength current fluctuation modes centered around the wavenumber k_2 . Again, as before two extreme cases are considered:

4.1 Symmetric Characteristics ($S_- = 0 = S_{W-}$)

In this case $\tilde{I}_{W-} = 0$. By letting $\tilde{I}_{W+} = \tilde{I}_W$ and $S_e = 0$, introducing Eq. (21) into Eqs. (5), (6), and (7), and then expanding the nonlinear terms to include the first nonlinearity, one finds that the coupled mode equations for \tilde{Y}_1 and \tilde{Y}_2 are:

$$L \frac{\partial}{\partial t} \tilde{Y}_1 = - [S_1 + S_+ + \frac{S_p^2(\beta^2 - \tan^2\theta)}{(S_{W+} + 2S_p/k_2h)}] \tilde{Y}_1 + \frac{3}{4} \frac{S_+}{I_0} (\tilde{Y}_1^2 + [2AS_{W+}' (\Lambda^2 + \beta^2 S_p^2)^{-1} - 1] \langle \tilde{Y}_2^2 \rangle) \quad (22)$$

$$L \frac{\partial}{\partial t} \tilde{Y}_2 = S_{W+}' [A S_{W+}' (\Lambda^2 + \beta^2 S_p^2)^{-1} - 1] \tilde{Y}_2 \quad (23)$$

where $A = S_{W+}' + [|S_p| + S_+ (1 - \frac{3}{2} \tilde{Y}_1 / I_0)]$, $\tan\theta = h'/h$, $S_p = S_p(k_2)$, $S_{W+}' = S_{W+}'(k_2)$, $\langle \rangle$ stands for spatial average, and $S_1 = h(1 + \tan^2\theta) / \sigma_{HP}$ is the free stream plasma resistance for mode 1. Equations (22) and (23) reduce to the previous result of Ref. 2, in the limiting case of no wall leakage ($S_{W+}' \rightarrow \infty$).

It was mentioned before that the effective arc sources display a singular behavior when leakage is present. Even though the leakage may increase the growth rate of the short wavelength unstable modes in a narrow k interval around k_2 , the rest of the modes is stabilized. This significant reduction in the extent of the instability range, leads to a reduction of the total current \tilde{I}_2 carried by the short wavelength fluctuations and thereby of the transfer of energy from the short wavelength unstable modes to large scale nonuniformities. Equation (22) shows that leakage, as represented by $S'_{W+}(k_2)$, adds both negative damping and forcing terms which enhance the large scale nonuniformities only if $\beta^2 < \tan^2\theta$ and

$$S'_{W+} > \frac{\beta^2 S_p^2 + [|S_p| + S_+ (1 - 3\tilde{I}_1 / 2I_0)]^2}{-2[|S_p| + S_+ (1 - 3\tilde{I}_1 / 2I_0)]}, \text{ where } |S_p| + S_+ (1 - 3\tilde{I}_1 / 2I_0) < 0$$

by definition.

4.2 Extremely Asymmetric Wall Leakage Characteristics

($S_{WK}=0$, $S_{WA}=\infty$, and $S_- = 0 = S_e$)

In this case $\tilde{I}_{WA} = 0$. By letting $\tilde{I}_{WK} = \tilde{I}_W$ and, hence, $\tilde{I}_{W+} = \tilde{I}_{W-} = \tilde{I}_W / 2$, and using the same approach as in the previous case, one obtains the coupled mode equations for \tilde{I}_1 and \tilde{I}_2

$$L \frac{\partial}{\partial t} \tilde{I}_1 = - [S_+ + h(1+\beta^2)/\sigma_{HP}] \tilde{I}_1 + 3S_+ \tilde{I}_1^2 / 4I_0 \quad (24)$$

$$L \frac{\partial}{\partial t} \tilde{I}_2 = - \frac{1}{2} (S_+ + |S_p| - i\beta S_p) \tilde{I}_2 + 3S_+ \tilde{I}_1 \tilde{I}_2 / 4I_0 \quad (25)$$

Obviously, \tilde{I}_1 is not coupled to the linearly unstable modes \tilde{I}_2 and the process of energy transfer from the short wavelength unstable modes to the long wavelength modes will not occur. Equation (25) is also consistent with the results (19) and (20) of the linear analysis, namely

that the growth rates of the unstable modes are reduced by half and instabilities will oscillate at frequency $\omega_0 = -\beta S_p/2L$.

5. Summary and Conclusions

Wall leakage affects the performance of an MHD channel in a very complex way. Considerable insight can be gained by first considering the excitation of current-distribution nonuniformities, having short-wavelength and small amplitude. The channel can then be modeled by the equivalent circuit of Fig. 2.

It appears that the anode and cathode wall resistances S_W shunt the series combinations of a negative arc resistance S , which is the source of the instability, the resistance of the plasma free stream $|S_p|$, and a reactance $\pm j\beta S_p$, due to the Hall effect. The most significant result of this parallel arrangement of positive and negative resistances is the occurrence of a "parallel resonance" phenomenon which leads to a sudden change from negative to positive damping of the nonuniformities.

With increasing magnitude of the negative arc resistance S , instability is excited when the arc overcomes the ballasting effect of the free-stream plasma resistance $|S_p|$. Rapid restoration of stability occurs, however, when with further increase in $|S|$, the wall leakage path draws more current than can be supplied by the arc source. The remainder, then, must come from the external circuit by discharging whatever magnetic energy happens to be stored in L .

It follows that the domain of instability in the S - S_W plane is bounded. The stabilizing effect resulting from the reduction in the extent of the unstable domain is, in the case of wall leakage, counterbalanced by an increase in the growth rate γ , above the value it would have in the complete absence of wall leakage (see Fig. 4a). This increase is restricted to the neighborhood of the "parallel resonance" condition.

If the anode and cathode have dissimilar characteristics, such "parallel resonance" cut-off does not occur simultaneously at the anode and at the cathode, so that the domain of instability splits into two regions separated by a stable one, as shown in Fig. 3.

The ballasting effect of the free stream plasma is linearly dependent on the wavelength, while the shunting effect of the wall leakage is quadratic in the wavelength. It follows that the unstable domains in the $S_+ / |S_p| - S_{W+} / |S_p|$ plane of Fig. 3 transform into band pass filter characteristics in the $\gamma - k$ plane of Fig. 4. With increasing wall leakage the cut-off point shifts toward smaller k , thus stabilizing an increasing range of short wavelengths, until instability is eliminated completely (see Figs. 5 and 3).

As long as symmetry prevails at the anode and cathode, the effect of the opposite signs in the Hall effect reactances, balances out and the non-uniformities remain stationary. The slightest asymmetry, however, is sufficient to introduce a temporal dependence. Therefore the non-uniformities become traveling waves which propagate toward the diffuser or the nozzle, depending on their wavelength. Moreover, both forward and backward waves may be excited.

As the amplitudes of the fluctuations increases, energy is transferred from the short to the long wavelength modes by the nonlinear mechanism of coupling. This mechanism becomes less efficient, as the wall leakage increases and, in particular, for the case of asymmetry.

How do these theoretical findings stand up against experimental evidence? Unfortunately there is a dearth of reliable data. As was mentioned before, nonuniformities extending over a wavelength as large as the width of the channel were observed in the U-25 and

U-25B Soviet channels^{3,4}. The absence of the fast growing short wavelength modes can now be explained either by the mode coupling mechanism, in the case of weak wall leakage, or by the wall leakage effect if significant. It is interesting to note that the U-25 channel was loaded by connecting each frame to a resistive voltage divider which duplicated the effect of strong asymmetry in the wall leakage. This arrangement evened out the interelectrode voltages at the expense of strong current nonuniformities which caused the blowing of fuses in the frame leads. As for the #1 channel in the U-25B facility, there was plenty of leakage, symmetric or otherwise.

In both facilities the sweep rate of the data acquisition system was too slow to detect temporal fluctuations. It is hoped that this analysis will stimulate more experimentation performed with better instrumentation.

Without the backing of experimental evidence it would be presumptuous to draw from this analysis guiding principles for the design of MHD channels. A few comments, however, are in order. A certain amount of wall leakage and its asymmetry due to preferential deposition of seed at the cathode seems to be a reality to be reckoned with. Two methods for the control of the nonuniformities in the diagonal conducting wall channels have been tried out. AVCO introduced nonlinear resistors S_e in the diagonal link. The Soviets introduced what in effect amounted to an artificial and asymmetric wall leakage. Even though both methods should eventually develop into dynamically adjustable and nondissipative controls, the present analysis can provide some clues on their relative merits in specific situations.

Acknowledgement

This work was supported in part by the Department of Energy Under Contract ET-78-C-01 3084.

References:

1. Solbes, H. and Lowenstein, A., "Electrical Non-Uniformities in Linear MHD Channels," Proceedings of the 15th Symposium, Engineering Aspects of Magnetohydrodynamics, Philadelphia, 1976, pp. 1-7.
2. Kuo, S., Cheo, B. and Levi, E., "Electrical Non-Uniformities in Diagonally Connected Generators," Accepted for the publication in Journal of Energy, AIAA Journal.
3. Antonov, B.M., Bitiurin, V.H., et al., "Studies of MHD Generator Loading," Fourth US-USSR Colloquium on MHD Power Generation Conf.-781009, October 5-6, 1978, Washington, D.C.
4. Buznikow, A.E., Kovbasiuk, V.I., Pishikov, S.I., and Shumiatski, B.Y., "Electrical Nonuniformities in U-25 MHD Channels," Proceedings of the 18th Symposium on Engineering Aspects of Magnetohydrodynamics, Butte, Mont., 1979, pp. ES1-ES6.

Figure Legends:

Fig. 1 Two-dimensional model of MHD channel for studying the effect of wall leakage on the nonuniformities.

Fig. 2 Equivalent circuit of the two-dimensional channel model.

$$S_p = 2/(\sigma h k P), \quad S'_{WK} = S_{WK}/k^2 P^2, \quad S'_{WA} = S_{WA}/k^2 P^2, \\ S_K = -\alpha_K / (2I_0^{3/2}), \quad S_A = -\alpha_A / (2I_0^{3/2}), \quad \beta = \text{Hall parameter.}$$

Fig. 3 Stability boundaries for generator with asymmetric wall leakage. $a=0.6$, $\beta=2$ and $0 \leq S_e \leq 8\Omega$.

Fig. 4 (a) Growth rate vs. normalized wave number in channel with weak anode wall leakage: $\beta=2$, $-S_+ = 4\Omega$, $S_e = 0$, $khS_p = 2h/\sigma h P = 8\Omega$, $0 < a < 1$, and $S_{WA} h^2/P^2 = 1000\Omega$.
(b) Three-dimensional plot of Fig. 4(a).

Fig. 5 Growth rate vs. normalized wave number in channel with strong anode wall leakage: $\beta=2$, $-S_+ = 4\Omega$, $S_e = 0$, $khS_p = 2h/\sigma h P = 8\Omega$, $0 < a < 1$ and $S_{WA} h^2/P^2 = 300\Omega$.

Fig. 6 Frequency vs. normalized wave number in channel with weak anode wall leakage of the case of Fig. 4(a).

Nomenclature

I_0	= background dc current
H	= electrode segmentation pitch
h	= width of the channel
θ	= angle of the diagonal link
h'	= $h \tan \theta$
x	= longitudinal coordinate
y	= transverse coordinate
S_e	= externally connected resistance in the diagonal bars
$\tilde{I}_e(x)$	= total fluctuating current in the diagonal bars
$\tilde{I}_e(k)$	= k mode component of the fluctuating current
k	= wave number

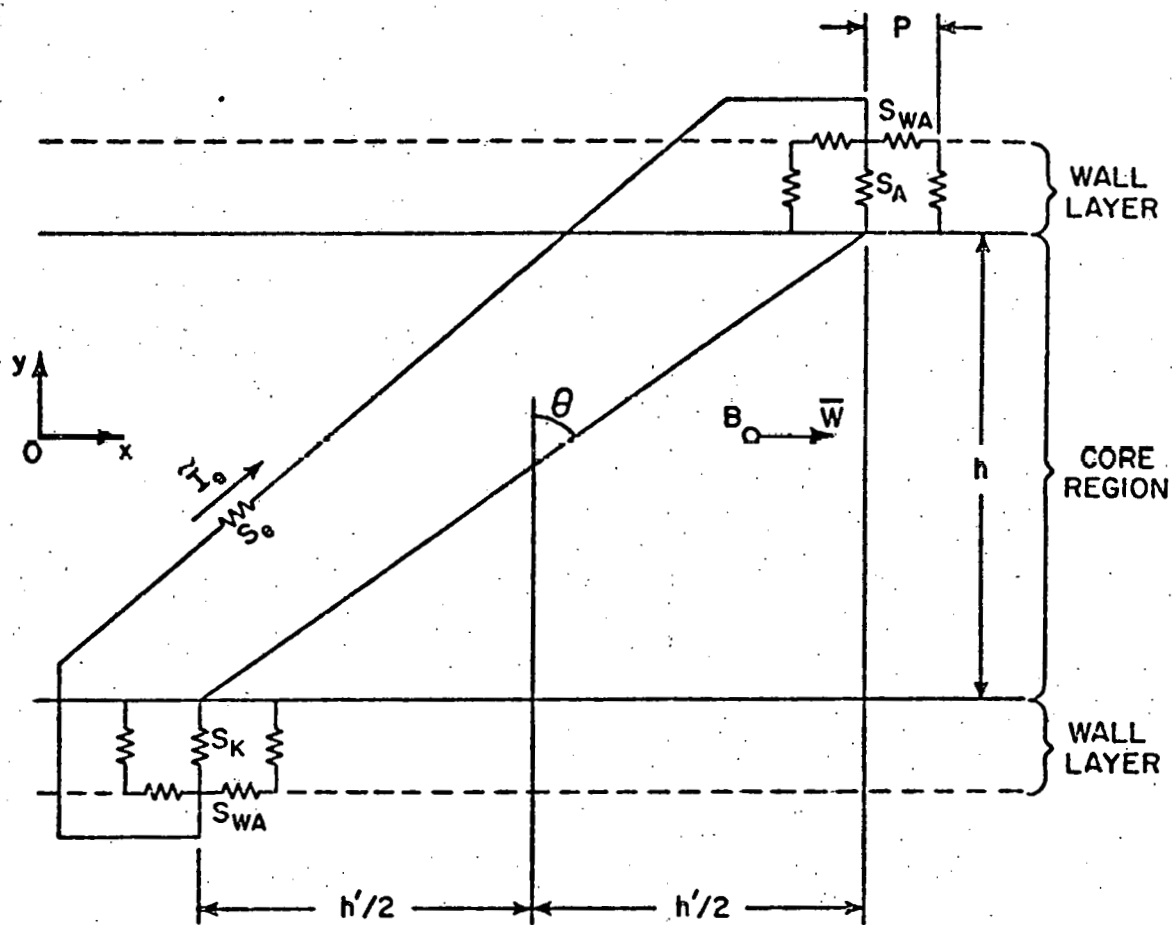


Fig. 1. Two-dimensional model of MHD channel for studying the effect of wall leakage on the nonuniformities.

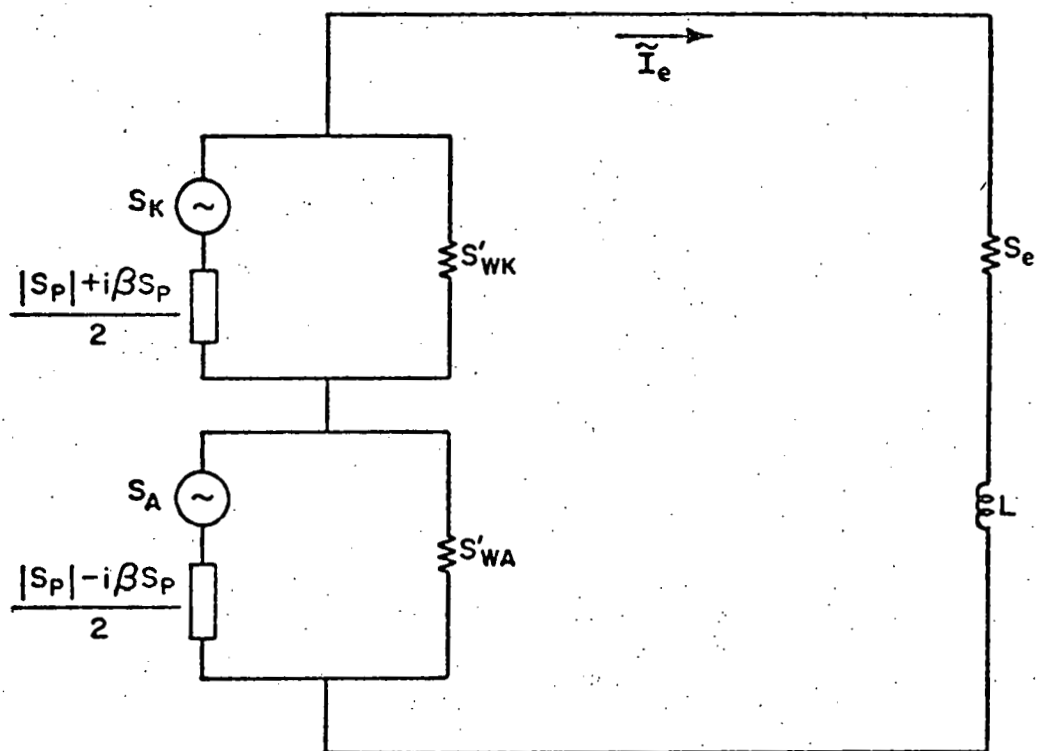


Fig. 2. Equivalent circuit of the two-dimensional channel model.

$$S_P = 2 / (\sigma H k P), \quad S'_{WK} = S_{WK} / k^2 P^2, \quad S'_{WA} = S_{WA} / k^2 P^2, \\ S_K = -\alpha_K / (2I_o^{3/2}), \quad S_A = -\alpha_A / (2I_o^{3/2}), \quad \beta = \text{Hall parameter.}$$

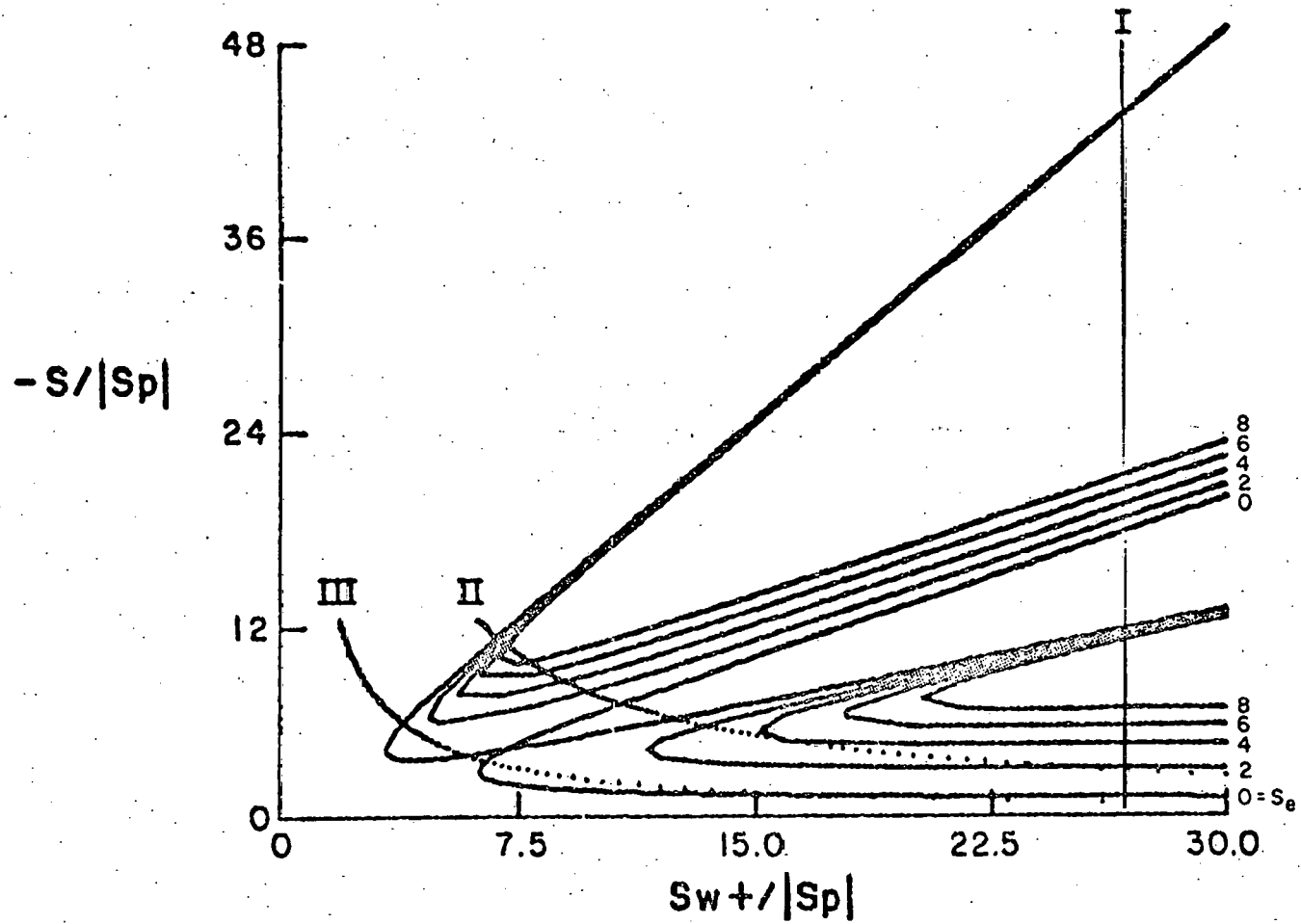


Fig. 3. Stability boundaries for generator with asymmetric wall leakage. $a = 0.6$, $\beta = 2$ and $0 < S_e < 8\Omega$.

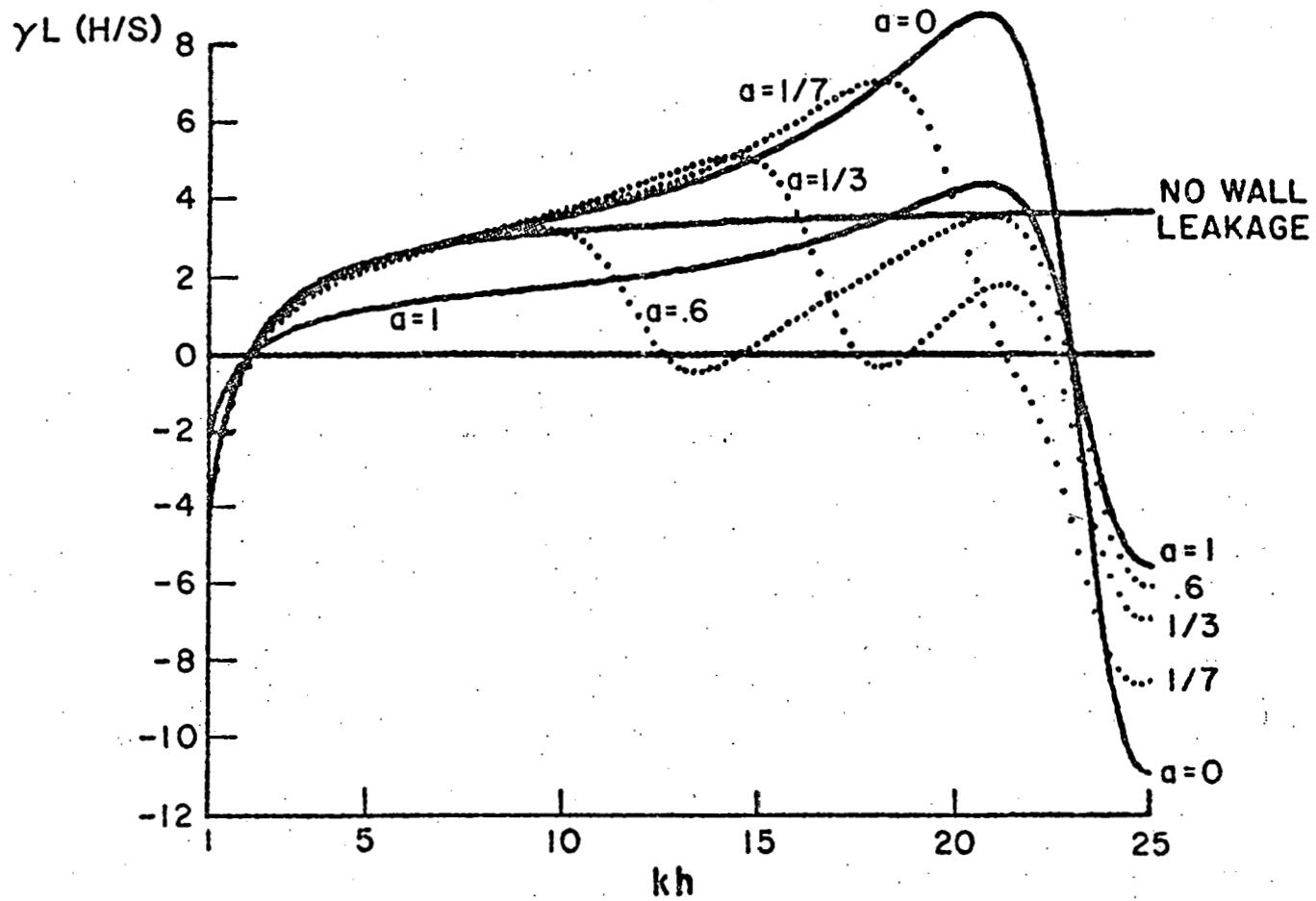
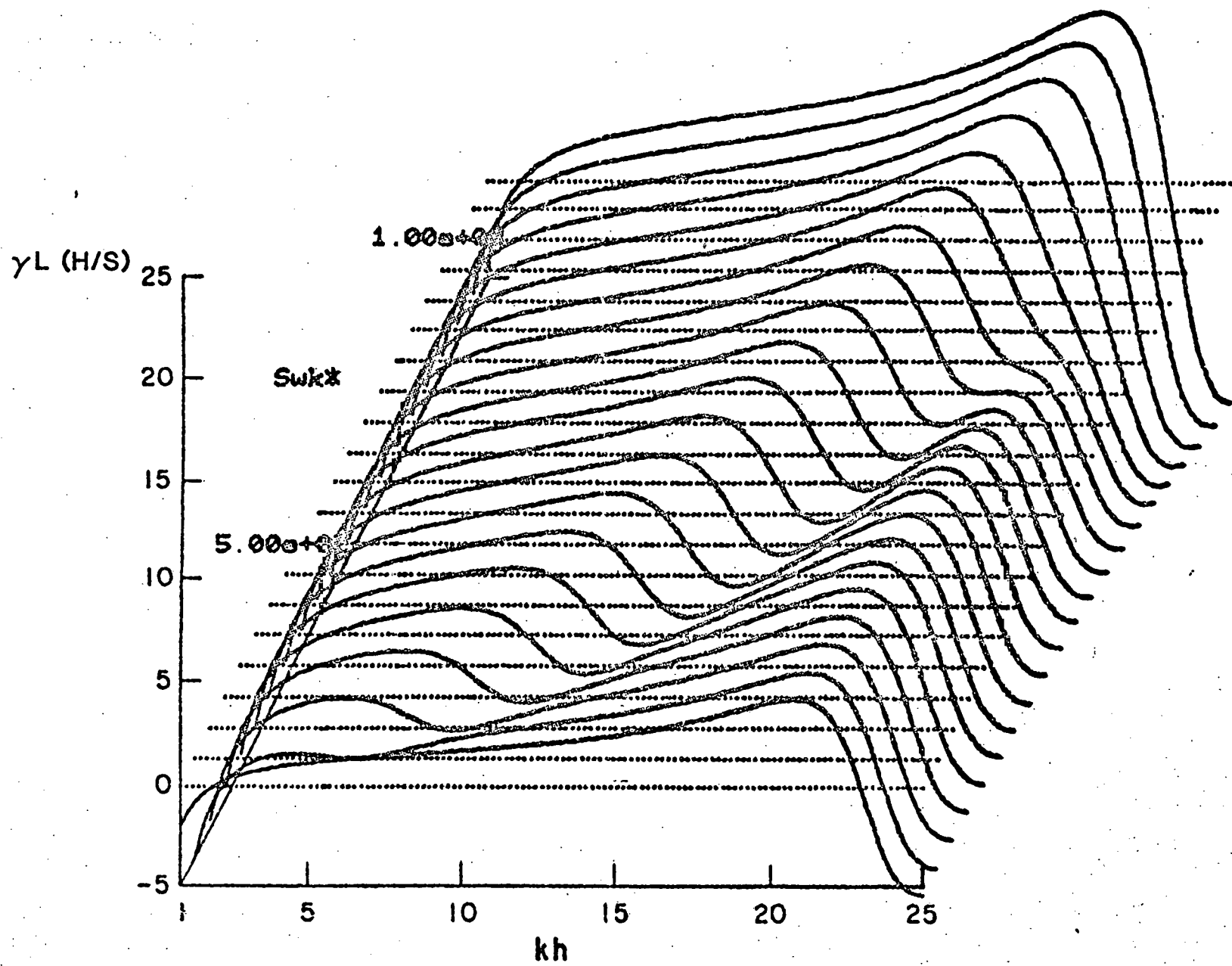


Fig. 4. (a) Growth rate vs. normalized wave number in channel with weak anode wall leakage: $\beta = 2$, $-S_+ = 4\Omega$, $S_e = 0$, $khS_p = 2h/\sigma HP = 8\Omega$, $0 \leq a \leq 1$, and $S_{WA} h^2/P^2 = 1000\Omega$.



(b) Three-dimensional plot of Fig. 4(a).

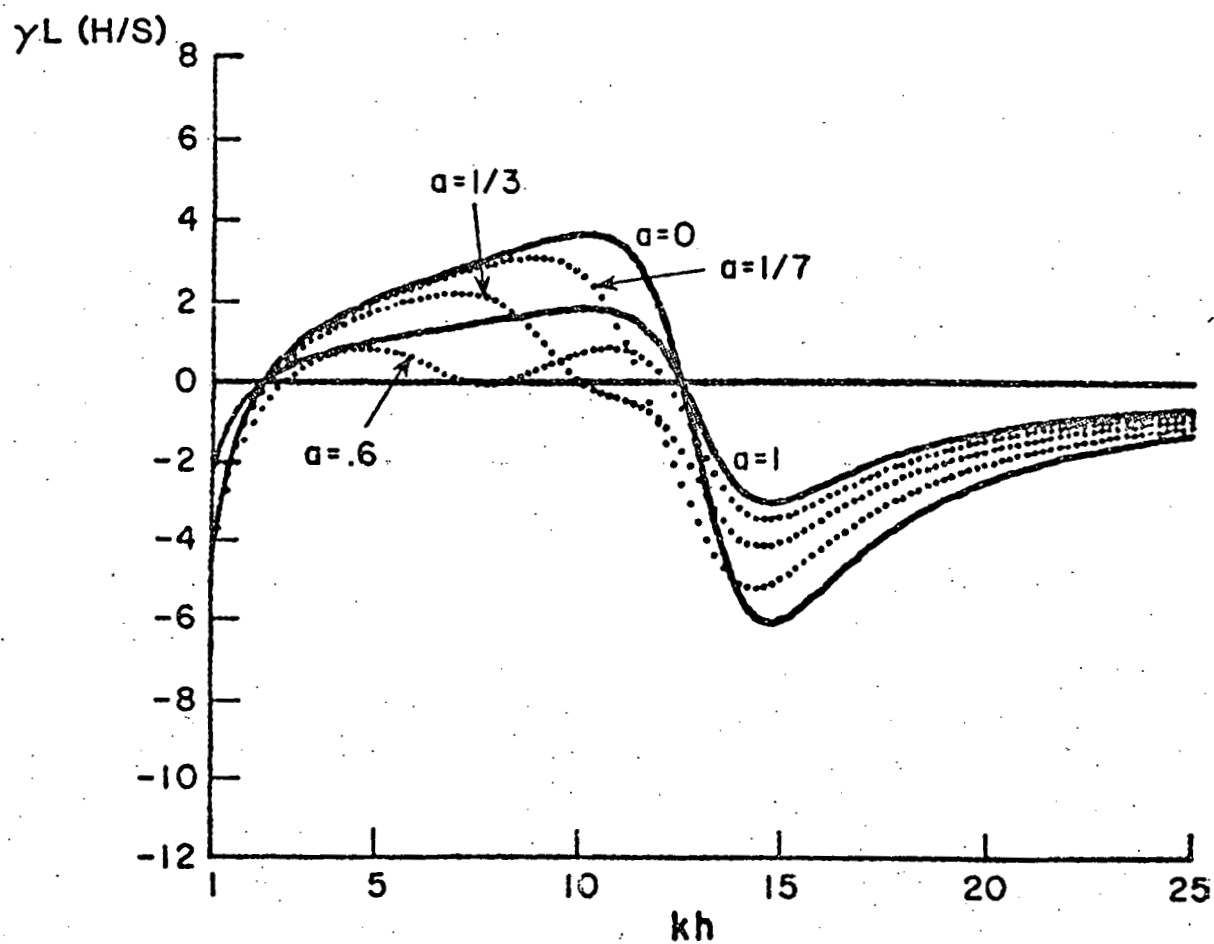


Fig. 5. Growth rate vs. normalized wave number in channel with strong anode wall leakage: $\beta = 2$, $-S_+ = 4\Omega$, $S_e = 0$, $khS_p = 2h/\sigma hP = 8\Omega$, $0 \leq a \leq 1$ and $S_{WA} h^2/P^2 = 300\Omega$.

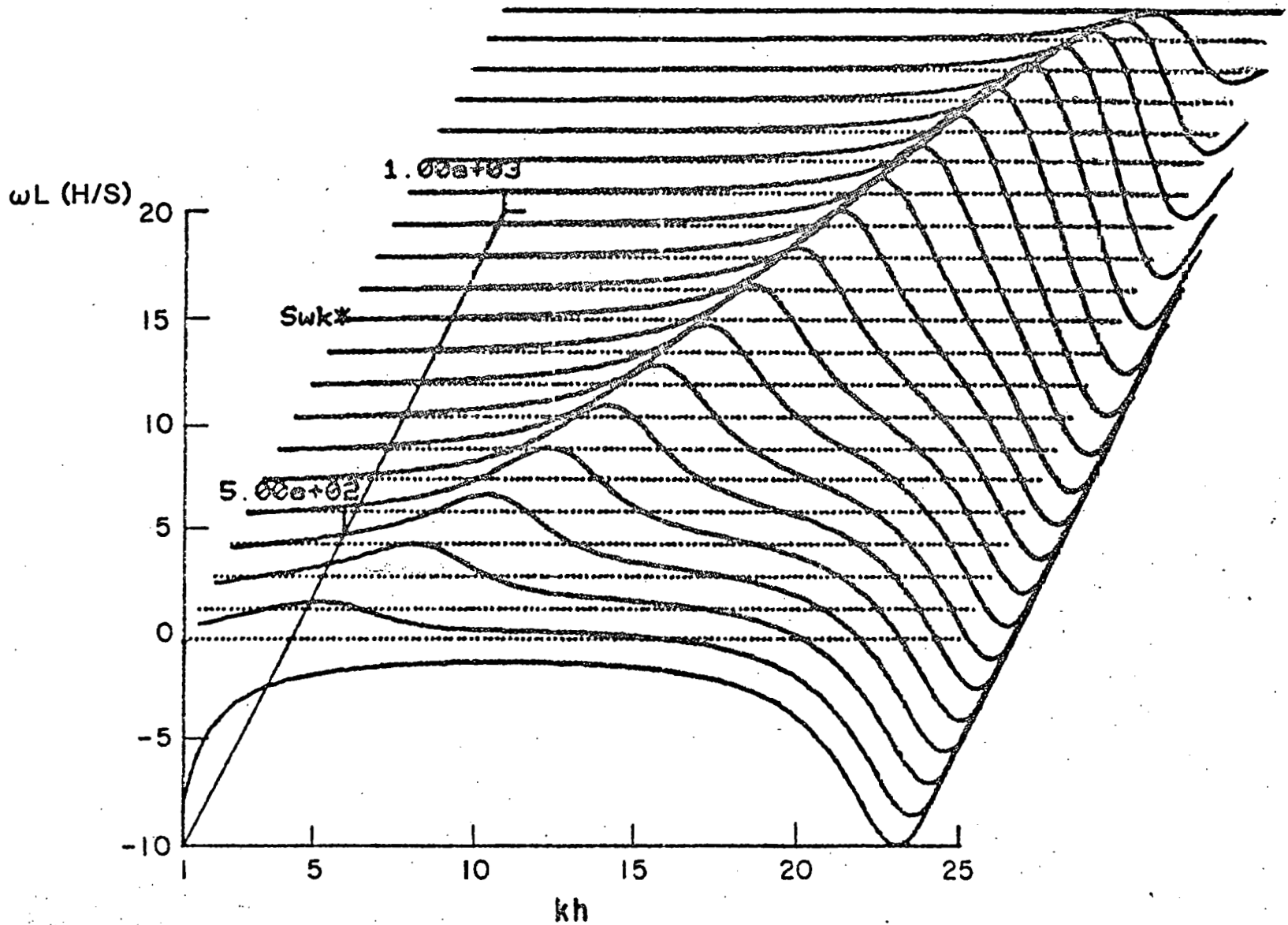


Fig. 6. Frequency vs. normalized wave number in channel with weak anode wall leakage of the case of Fig. 4(a).

Polytechnic Institute of New York

AERODYNAMICS
LABORATORIES

X

DEPARTMENT OF MECHANICAL
and
AEROSPACE ENGINEERING

DEVELOPMENTS IN LASER-BASED DIAGNOSTICS

By S. Lederman

JULY 1979

Contract No. F-49620-78-C-0020
Project No. 2307-AI

AFOSR-TR-80-0517
ADA 086904

ET-78-C-01-3084

N00014-75-C-1143
Subcontract No. 8960-5

POLY M/AE Report #79-23

Approved for public release;
distribution unlimited.

SHOCK TUBES AND WAVES

*Proceedings of the 12th International Symposium
on Shock Tubes and Waves*

ירושלים, כ"א—כ"ד בתמוז תשל"ט
Jerusalem, July 16-19, 1979

Edited by

ASSA LIFSHITZ

The Hebrew University of Jerusalem

JOSEF ROM

Israel Institute of Technology, Haifa

JERUSALEM 1980

THE MAGNES PRESS, THE HEBREW UNIVERSITY

DEVELOPMENTS IN LASER BASED DIAGNOSTIC TECHNIQUES

S. LEDERMAN

*Aerodynamics Laboratories, Department of Mechanical and Aerospace Engineering
Polytechnic Institute of New York
Farmingdale, New York 11735, USA*

Several laser based diagnostic techniques, applicable to fluid dynamic and combustion research consisting of the spontaneous Raman effect, coherent anti-Stokes Raman scattering, coherent Raman gain spectroscopy, laser induced fluorescence and the laser Doppler velocimeter are discussed. Characteristic features of each of these techniques are brought forth. It is shown that these modern, laser based diagnostic techniques are capable of measuring most of the variables of interest in fluid dynamics and combustion research. Among these are the temperature, species concentration, velocity, turbulent intensity temperature and concentration fluctuation as well as a number of correlation and crosscorrelation parameters. Practical examples of the applicability to flow fields and combustion diagnostics are presented.

INTRODUCTION

The appearance of the laser and its introduction into the field of spectroscopy was a turning point in the development of light scattering diagnostic techniques. In a relatively short period of time, laser based diagnostic techniques emerged as major investigative tools in a number of branches of the physical sciences. Since in this work the application of laser based diagnostic techniques to the investigations of flow fields and combustion systems are of interest, only some of the techniques which have been successfully applied, and which present some potential promise in the future for those investigations will be discussed.

Some of these techniques as mentioned previously are based on light scattering. A number of scattering processes have been considered for diagnostic purposes of flow fields and combustion systems. Among these the elastic scattering processes such as Rayleigh¹⁻³ and Mie⁴ and the inelastic scattering processes represented by Raman,⁵⁻¹⁷ near-resonant Raman^{6,7} and fluorescence¹⁸⁻²⁰ have been extensively investigated. Other processes which could be utilized in combustion and flow field diagnostics are the absorption and nonlinear optical processes. The latter are represented by coherent anti-Stokes Raman²¹⁻²⁷ and stimulated Raman scattering.²⁸⁻³⁰ From this list of potential diagnostic techniques applicable to flow fields and combustion, the Mie and spontaneous Raman scattering techniques are the most versatile. The Mie scattering phenomenon has been utilized in Laser Doppler Velocimetry³¹⁻³² capable of providing non-intrusively velocity, turbulent intensity, and particle size distribution in

flow fields. The spontaneous Raman effect can provide simultaneously, remotely and instantaneously species concentration and temperature of a flow field consisting of any number of species. When properly used it can provide, in addition, local turbulence properties, correlation and cross-correlation parameters and the so called mixedness parameters in reactive flows.³³ However, due to the very low equivalent scattering cross-section under certain conditions occurring in hydrocarbon turbulent combustors, difficulties may develop in securing reliable measurements. These difficulties are related to the very high noise level, generally attributable to carbon emissions. The signal to noise ratio under those conditions may become unacceptably low thus making the utilization of the spontaneous Raman technique very difficult. Here the coherent anti-Stokes Raman spectroscopy appears to fill the gap. The equivalent scattering cross-section in conjunction with the coherence of the radiation combine to provide signals 5 to 6 orders of magnitude higher than the spontaneous Raman effect. Its coherent character permits, in addition to the collection of the total generated signal, the simultaneous suppression of the collected interference signals, resulting in high signal to noise ratios in very hostile environments. One of the major drawbacks of CARS is its nonlinear character which may cause difficulties in a number of situations encountered.

A process which holds out great promise for flow field and combustion diagnostics has been recently demonstrated.²⁸ This process known as stimulated Raman spectroscopy, [SRS] has been known for over a decade³⁴⁻³⁵ and applied in the first practical demonstration of a collinear CARS system. It has been used with high power pulsed lasers and CW low power lasers.²⁹ Being of a coherent nature, the SRS signals under certain conditions may exceed the signal strength of the CARS signals, with the added advantage of being linear and the fact that the technique is self-phase matched and thus requires no great effort in this respect.

In terms of high signal response, a technique which has been known for several decades is the fluorescent diagnostic method. Here the major interfering phenomenon of the spontaneous Raman technique is being utilized as a diagnostic technique. This technique, in spite of its very high signal levels, has not been until recently very successfully applied. The major obstacle being the strong collisional quenching process associated with fluorescence, which is competing with the radiative decays, and thus makes the measured fluorescent intensities ambiguous.

The cited possible nonintrusive diagnostic techniques are discussed at length in this work. A description and evaluation of these new techniques, the accomplishments to date and their potential applicability to flow fields and combustion systems is presented here.

THE RAMAN EFFECT

The Raman effect is the phenomenon of light scattering from a material medium, whereby the light undergoes a wavelength change and the scattering molecules undergo an energy change in the scattering process. The Raman scattered light has no phase relationship with the incident radiation. Based on quantum theoretical considerations, the incident photons collide elastically or inelastically with the molecules to give Rayleigh and Raman lines respectively with the inelastic process much less probable than the elastic. The process of light scattering can be visualized, as the process of absorption of an incident photon of energy E by a molecule of a given initial state, rising the molecule to a virtual state, from which it immediately returns to a final stationary state emitting a photon of the difference energy between the two stationary states and incident energy E . This is seen graphically in the schematic diagram of Fig. 1, where vibrational and rotational transitions are indicated corresponding to the appropriate vibrational and rotational selection rules which are $\Delta J = 0, \pm 2$ and $\Delta V = \pm 1$. Since the anti-Stokes lines must originate in mole-

cules of higher energy level, which are less abundant at normal temperatures, the anti-Stokes lines would be expected to be much weaker than the Stokes lines. This qualitative description of the Raman effect is obviously very superficial. For a more rigorous and complete discussion of this effect one must consult the cited references.

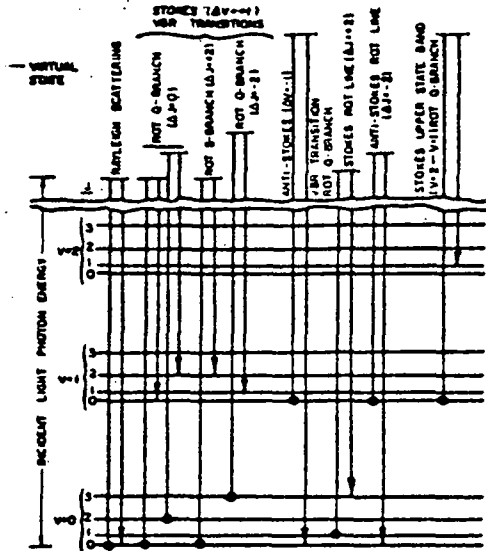


FIG. 1 SCHEMATIC DIAGRAM OF MOLECULAR TRANSITION⁴⁰

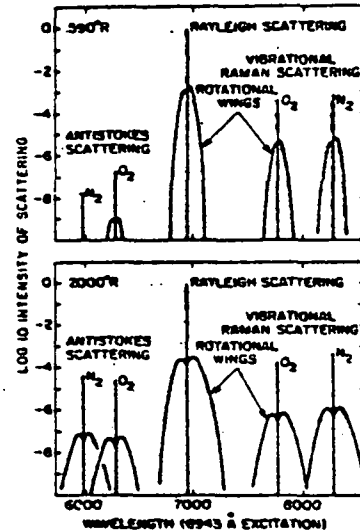


FIG. 2 RAMAN AND RAYLEIGH SCATTERING FROM AIR⁴⁶

An inspection of Fig. 1 reveals that the incidence of a photon on a molecule, if Raman active, may result in the excitation of vibrational as well as rotational transitions. Fig. 2 presents an approximate Raman and Rayleigh scattering response from air illuminated by a Ruby laser. It is evident that the Rayleigh as well as the vibrational spectra have closely associated rotational wings. Since, for our purposes, the vibrational scattering is of direct interest, it is worthwhile to examine the vibrational Raman response. It consists essentially of three branches: (1) the intense Q-branch for which $\Delta J = 0$, (2) the much weaker O-branch for which $\Delta J = -2$, and (3) the S-branch for which $\Delta J = +2$ of approximately the same intensity as the O-branch. The O and S branches are much weaker than the Q-branch and represent only about 1% of the intensity of the Q-branch. They are therefore of minor importance as far as the present applications to fluids are concerned. The Q-branch, if a high dispersive instrument is used, can be resolved into components corresponding to the energy levels characterized by the quantum numbers $v = 1, 2, 3$, etc. These of course will appear at elevated temperatures, and may be used to determine temperatures, Fig. 3. Since in fluids the orientation of the molecules cannot be fixed, the scattering will correspond to an average overall molecular orientation, and the vibrational Raman scattered intensity as derived using the Placzek polarizability theory may be expressed as

$$I_{S,A} = CNI_0 \frac{(v_0 \pm v)^4 f(\alpha', \gamma')}{(1 - \exp\{-\frac{hcv}{kT}\})}$$

Laser Based Diagnostic Techniques

and from the relative intensity of the Stokes and anti-Stokes lines, taking account of the Boltzmann factor, the temperature is given by

$$T = \frac{h\nu}{k} \left[\ln \frac{I_s}{I_A} + 4 \ln \left(\frac{\nu_0 + \nu}{\nu_0 - \nu} \right) \right]^{-1}$$

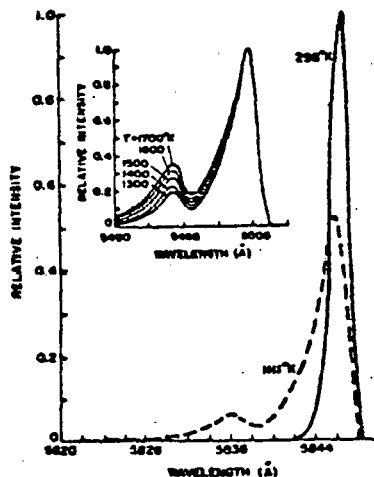


FIG. 3 THE RESOLVED Q-BRANCH⁹

It should be noted that the scattered intensity is proportional to the fourth power of the frequency and to the incident intensity and, of course, to the number density of a given species. It is well-known that the pure rotational Raman spectra appearing near the exciting radiation frequency can be quite intense. However the very small wavelength separation of the lines particularly in a mixture of gases makes the pure rotational spectra very difficult to use for diagnostic purposes as defined here in spite of its stronger signals. The weakness of the Raman scattering technique is its low scattering cross-section. Consequently, the signal obtainable is a major factor in determining the applicability of the technique to a given problem. The number of photoelectrons contributing to the signal, may be written

$$n_s = E_0 N \sigma \Omega \eta_o \eta_g E_p^{-1}$$

where E_p is the energy per photon, η_o is the optical efficiency of the collecting optics, and η_g is the quantum efficiency of the photocathode. The last equation may also be written in terms of an output voltage from a photomultiplier tube across a load R, with a gain G and laser pulse duration t,

$$V_s = E_0 N \sigma \Omega \eta_o \eta_g \cdot G \cdot eR \cdot (E_p \cdot t)^{-1}$$

where e is the electron charge in coulombs and V_s the signal voltage. The last two equations permit the evaluation of the achievable voltage signal or photon count in a given situation, if not exactly, at least to a first reasonable approximation. (The laser pulse in the above approximation is assumed to have a rectangular shape whereas in actuality the laser pulse has generally a Gaussian distribution in intensity). The voltage signal or photon count must exceed the signals due to background noise or other disturbing signals, if the measurement is to be useful.

Some features of the Raman diagnostic technique

At this point it is clear that, in principle at least, instantaneous and simultaneous data for the determination of species concentration and temperature can formally be obtained. The former because the Raman transition takes place in a time of the order of fractions of picoseconds for most Raman active molecules, if illuminated by light in the visible range; and the second because one may record the Stokes and anti-Stokes intensity at the same time, the number of data points depending on the number of receiving channels one has available. The vibrational Raman system, which generally permits clear identification of species involved, is generally used. An obvious difficulty in performing Raman intensity measurements is the extremely small equivalent Raman scattering cross-section. Typically, this cross-section may vary between 10^{-29}cm^2 and 10^{-31}cm^2 , depending on the molecule under investigation and the frequency of the primary light. Since the frequency dependence is of overriding importance here (fourth power), and is essentially the only parameter which is at the disposal of the experimentalist, one would tend to automatically chose the laser operating at the highest frequency. While this choice might be desirable in one respect, other aspects of this choice might be less favorable.

The line separation of the resulting Raman spectra is greater as a result of longer wavelength lasers, than shorter wavelength sources of primary radiation. This feature may become important in cases where several species are involved and their measurement and resolution are desired, in particular when narrow bandpass filters are contemplated. Figs. 4 and 5 illustrate this problem

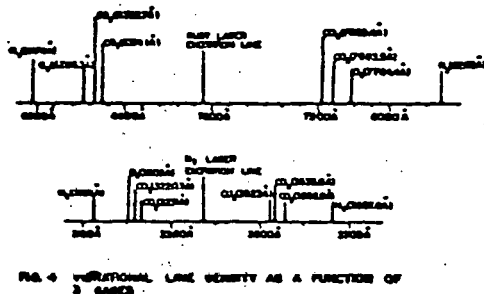


FIG. 4 ROTATIONAL LINE DENSITY AS A FUNCTION OF WAVELENGTH

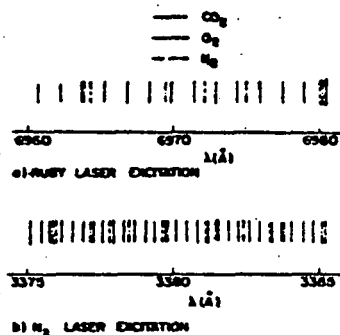


FIG. 5 ROTATIONAL LINE DENSITY OF A MIXTURE OF 3 GASES

very clearly, both in terms of concentration measurements of a mixture of gases and the preference of using the ratio of the vibrational Stokes to anti-Stokes intensity for the determination of temperature, as opposed to the rotational spectra. It should also be pointed out that the use of a nitrogen laser at the conventional energy (1mj) levels available, requires the utilization of photon counting techniques and generally mean values of the measured variables are obtained, while with a Ruby laser, due to its much higher energy (4 joules) per pulse (several orders of magnitude), single pulse operation is possible and therefore instantaneous values can be obtained. The latter is also true for a doubled neodymium yag laser operating at 5320\AA available at a repetition rate of 10pps at energy levels in excess of 0.5 joules.

In addition to these pulsed lasers, C-W lasers are being utilized to perform Raman measurements. In particular the argon ion laser operated at 5145\AA or 4880\AA is very useful in steady state systems where mean concentration and temperature are desired. C-W lasers would, of course, be ideal for time re-

Laser Based Diagnostic Techniques

solved Raman measurements of fluctuating flow fields and combustion systems. However, the available commercial lasers are of insufficient power to provide useful data concerning fluctuating systems.

It is therefore apparent from the above that spontaneous laser Raman scattering has all the desired features of an ideal probe. There are, however, problems associated with this diagnostic method.

In discussing the feasibility of diagnostics by means of monitoring the intensity of radiation, and particularly scattered radiation resulting from the Raman effect, one must consider the background radiation which may interfere with the desired signal and render it useless. There are a number of sources which may contribute to the undesired background radiation. In order of significance they are: Rayleigh scattering, scattering of the incident beam by viewing port windows, walls and large particles in the flow, gas particle and surface fluorescence, ambient light, detector dark current, electrical noise and detector shot noise.

The first two, being of the same frequency as the incident beam and thus spectrally separated from the desired signal, can be filtered out using proper interference filters or spectrographs used for the selection of the desired signals. The fluorescence problem can be a very serious problem. Careful selection of the materials and surface coatings may eliminate this problem. In some cases by proper choice of the primary laser this problem can be avoided. In this respect, the use of a Ruby laser has not caused any significant fluorescent problem in this laboratory. The detector dark current and electrical noise can generally be coped with by using photomultiplier coolers, which serve a dual purpose of decreasing the dark current and shielding the photomultiplier from electrical interferences. As far as the shot noise is concerned, this problem must be dealt with at the data processing level.

In general the larger the signal-to-noise ratio the better the system. As has been pointed out,¹⁴ a very convenient parameter to assess the capability of a system is the "feasibility index". This index was defined as $X = NL\sigma_0\Omega\epsilon$ where N is the number density of the scatterers per cm^3 , L is the length of the sample in the direction of the laser beam, σ_0 reference cross-section, and Ω and ϵ the solid angle and optical efficiency, respectively. The minimum feasibility index for a 1 joule Ruby laser in a single pulse operation is approximately 10^{15} . Thus, for a situation where this index is below 10^{15} a 1 joule single pulse laser would not provide the desired information. An increase in the laser energy or any of the other factors may be necessary. There is, however, a limit on the laser energy one may apply. The laser energy density should be below the breakdown threshold which for Ruby and air appears to be around 10^{10}W/cm^2 .

The choice of the proper method of spectral analysis can be very important. There are basically three methods available. The standard monochromators, interference filters and Fabry-Perot interferometers. Each has a range of applicability and its positive as well as negative features. The interested reader may consult standard texts or some of the references cited.^{10,15,24}

The detection of the scattered photons of interest is best accomplished by photomultipliers. They are the most sensitive low level light detectors available at present, applicable in the wavelength range from u.v. to near infrared or from about 3-10 thousand Angström wave length. The output of the photomultiplier may be used in one of several ways: a) as an input to a d.c. amplifier, b) as an input to a photon counter, c) as an input to a phase sensitive detector, or as a combination or modification of the above basic schemes.

In general photon counting is more accurate than a direct reading of the photomultiplier current. The reasons are: 1. the d.c. level caused by leak-

age currents of photomultiplier tubes cannot be detected by photon counters, 2. the statistically varying heights of the detector output pulses are replaced by standard height pulses, 3. the photon counting rate with proper care can be made insensitive to power supply voltage fluctuations. However, at high photon count rates photon counting may present some difficulties particularly if the detection rate exceeds about 10^7 counts sec^{-1} .

Recently a new detection system has been introduced. It offers a number of advantages over photomultiplier tubes. It is supposed to be capable of providing simultaneous measurements of the Raman scattering signals of a multiplicity of species at many spatial points, during a single laser pulse. It would therefore be capable in conjunction with proper computational facilities to provide in addition to concentration and temperature, data necessary for the determination of spacial correlation functions.

Two commercial versions are now on the market, the first and most known is the optical-multichannel analyser OMA and the more recent entree, the DAARS. Both claim a photon sensitivity as high as the best available photomultiplier. One claims one signal count for two detected photons, the other one count per photon. I have not been able to confirm that with either. Be it as it may, this kind of a detector represents a major advance in the laser scattering diagnostic technology. At this point it must be mentioned that, due to the simultaneous and instantaneous response of the spontaneous Raman signals, the correlation and crosscorrelation parameters defined in the following³² can be obtained. Thus:

$$\overline{C_a C_b} = \frac{1}{n} \sum_{i=1}^k f_i (C_{a_i} - \bar{C}_a) (C_{b_i} - \bar{C}_b)$$

$$\overline{C_a^2 C_b} = \frac{1}{n} \sum_{i=1}^k f_i (C_{a_i} - \bar{C}_a)^2 (C_{b_i} - \bar{C}_b)$$

and

$$\overline{C_a C_b^2} = \frac{1}{n} \sum_{i=1}^k f_i (C_{a_i} - \bar{C}_a) (C_{b_i} - \bar{C}_b)^2$$

where f_i is the frequency of occurrence of the joint values C_{a_i} and C_{b_i} , and $n = \sum_{i=1}^k f_i$ and \bar{C}_a and \bar{C}_b are the concentrations of species a and b .

CARS

Coherent anti-Stokes Raman scattering has been receiving a great deal of attention since its introduction in 1973 by Regnier, Moya and Taran. It became popular among the researchers in the field of combustion and particularly combustion in systems with excessive soot. As discussed previously, the spontaneous Raman techniques cannot easily handle this type of flow field. It has been shown^{21,23,24,33} that the coherent anti-Stokes Raman scattering system can provide signals several orders of magnitude higher than the Spontaneous Raman signals for the same initial driving laser intensity. In addition, the coherent character of the signal beam allows the collection of the total beam and at the same time minimize the collection of the interfering radiation.

Theory

When an incident photon of fixed frequency ω_1 , interacts with a tunable photon ω_2 (Stokes photon of the given specie of interest) through the third order nonlinear Raman susceptibility it generates a polarization field which is responsible for coherent radiation of frequency $\omega_3 = 2\omega_1 - \omega_2$. If $\omega_1 - \omega_2$ is of or near a Raman resonance line the intensity of the coherent radiation becomes

very large, in fact several orders of magnitude larger than the intensity of the spontaneous Raman radiation, and it occurs at the Raman anti-Stokes line with respect to the incident radiation ω_1 . In Fig. 6 an energy level and the corresponding phase matching diagrams are shown, which are self-explanatory. The CARS radiated power for the case of collinear diffraction limited beams, can be shown to be:

$$P_3 = \left(\frac{\omega_1}{\omega_d}\right)^2 \left(\frac{4\pi^2 \omega_3}{c}\right)^2 P_1^2 P_2 |\chi|^2$$

where P_1 , P_2 and P_3 are the incident, Stokes and anti-Stokes powers respectively and $|\chi|$ is the absolute Raman nonlinear susceptibility given by

$$\chi = K_j \Gamma_j (2\Delta\omega_j - i\Gamma_j)^{-1}$$

where $\Delta\omega_j = \omega_j - (\omega_1 - \omega_2)$ = the detuning frequency and

$$K_j = 4\pi C^4 (\hbar\omega_2^4 \Gamma_j)^{-1} N \Delta_j g_j (\partial\sigma/\partial\Omega)$$

ω_j is the frequency of a particular possible transition from $V, J+V, J^-$; Δ_j = the normalized population difference between the levels involved in the transition, g_j = line strength factor equal to $(V+1)$ when at resonance $\Delta\omega_j = 0$ and $|\chi| = K_j$ and Γ_j is Raman line width. The interaction of this type of CARS system will occur in a beam diameter d of length l given by:

$$d = 4\lambda f/\pi D \quad l = \pi d^2/2\lambda$$

where f , λ and D are the focal length of the lens, the wavelength of the incident beam and the beam diameter at the lens respectively.

As is evident from the above, the CARS technique is a nonlinear technique, unlike the spontaneous Raman technique. It is a double ended technique. It is therefore necessary to traverse the sample and obtain the desired signal at the opposite side of the signal input to the sample. CARS can resolve only one specie at a time. The resolved specie corresponding to the applied Stokes beam. Spontaneous Raman as pointed out previously can resolve simultaneously as many species as there are in a mixture providing the acquisition system is capable of resolving the acquired spectra.

In applying CARS to a system, one must exert caution if the flow-field is very turbulent and extensive. Beam steering may cause difficulties in phase matching and relating the signals to actual concentrations and temperatures as obtained by this method.

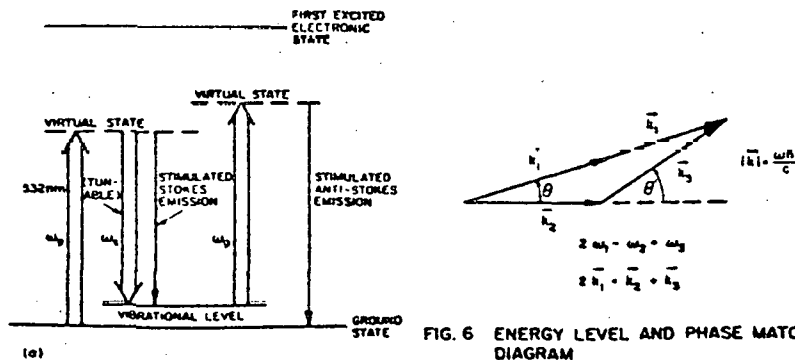


FIG. 6 ENERGY LEVEL AND PHASE MATCHING DIAGRAM

COHERENT RAMAN GAIN TECHNIQUE

A technique as old as CARS which provides a coherent signal beam of considerable strength has until recently been completely neglected as a diagnostic tool. This technique is based on stimulated Raman spectroscopy SRS. Recently it has been reported²⁸⁻³⁰ that sensitivities comparable or exceeding those of CARS under similar conditions can be obtained. The added attraction of this new technique is the possible utilization of two low power C-W lasers, and the linear response of the technique.

Theory

The idea behind the direct SRS technique using C-W sources is as follows. A linearly polarized pump beam of a frequency ω_1 is -using an electro-optical modulator - modulated and combined coaxially through a dichroic mirror with a probe beam of frequency ω_2 . The combined beam is focussed through the sample. The modulated pump beam produces a modulated Raman gain at the Stokes frequency or Raman loss at the anti-Stokes frequency which is then detected by the probe beam Fig. 7. If the probe and pump beams are focussed collinearly

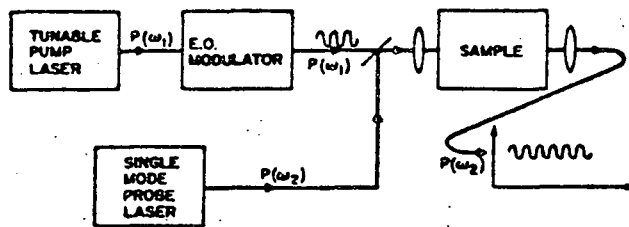


FIG. 7 SRS CONFIGURATION

through the sample, it can be shown that the fractional power gain $\delta P(\omega_2)/P(\omega_2)$ at the probe frequency ω_2 induced by the pump beam of a frequency ω_1 is given approximately by³⁰

$$G = \delta P(\omega_2)/P(\omega_2) = 384\pi^4 \lambda^{-2} c^{-1} n^{-1} \text{Im}\chi_3(-\omega_2, \omega_2, -\omega_1, \omega_1) \cdot P(\omega_1)$$

where n is the refractive index at frequency ω_2 , $P(\omega_2)$ and $P(\omega_1)$ are the probe and pump powers respectively $\lambda^2 = (2\pi c)^2/\omega_1\omega_2$ and $\text{Im}\chi_3$ is the imaginary part of the third order nonlinear susceptibility and is given by:

$$\text{Im}\chi_3(-\omega_2, \omega_2, -\omega_1, \omega_1) = \pi N c^3 (24\hbar\omega_2^4)^{-1} L(\omega_1 - \omega_2) d\sigma/d\omega_1 d(1/\lambda)$$

where $L(\omega_1 - \omega_2)$ is the line shape function equal to unity at the line center. Since both CARS and SRS depend on the nonlinear susceptibility χ_3 it is worth pointing out that SRS is linearly dependent on χ and the pump power $P(\omega_1)$, whereas CARS's dependence on these parameters is quadratic. One other property of SRS is the fact that the SRS technique is self-phase matched and therefore requires only an overlap of the two beams to proceed with the interaction, similar to the collinear CARS system. The technique is insensitive to slight depolarization of the beams, and offers high resolution.

As an example of the signal strength of SRS, Owyong cites the following: the 992 cm^{-1} mode of liquid benzene for which $\text{Im}\chi_3 = 15.9 \cdot 10^{-14} \text{ cm}^3/\text{erg}$, a pump power of 100mw yields an SRS signal $\delta P(\omega_2)/P(\omega_2) = 3.5 \cdot 10^{-5}$ which is about 6 orders of magnitude larger than that obtained at comparable power levels in CARS.

There are, however, certain problems associated with this diagnostic technique. The most serious of them being the required probe laser stability, and mode purity.

As of now, experimental data in liquids and dense media have been obtained. The application to gaseous media have been limited as of now to molecular hydrogen²⁹ at 1/4 to 14 atm. of pressure.

LASER INDUCED FLUORESCENCE

A technique which holds out great promise as a diagnostic tool in flames, combustors and combustion driven MHD generators is laser induced fluorescence. The great attraction of this technique is the relatively very high scattering cross-section, compared to any of the thus far discussed techniques. It is a very sensitive, spacially precise technique for determination of the species concentration in difficult environments. Fluorescence occurs when a light beam which is in resonance with a particular absorption line of an illuminated molecule, excites it into a higher energy level which, after a time delay of the order of 10⁻⁸ sec, radiatively decays to the original or intermediate energy level with the spontaneous emission of a corresponding photon. This process is illustrated in the simple energy level diagram Fig. 8. This process could

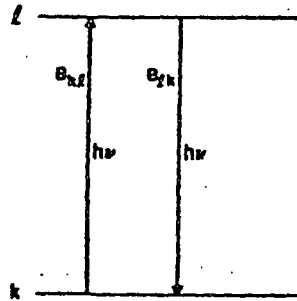


FIG. 8 ENERGY LEVEL DIAGRAM FLUORESCENCE

therefore be used for diagnostic purposes, provided that this spontaneous emission is the only deexcitation process active. This however is not the case. Since at STP the collision rate is of the order of 10¹⁰ sec⁻¹, collisional deexcitation of the excited molecules may occur without radiative emission. This phenomenon known as collisional quenching is essentially a very complicated process depending on a number of properties of the gas under investigation such as density, temperature etc. Since those are the properties one is trying to measure, the computation of the quenching effects, effecting the measurement of some of those properties is generally very difficult.

Theory

Recently, Daily³⁶ proposed a technique which may result in a very sensitive and useful method of obtaining concentrations. It is based on the so called saturation condition given by

$$N_l = N_k B_{kl} / B_{lk}$$

where N_l and N_k are the upper and lower state number densities. This condition requires that:

$$B_{lk} I_{\nu} \gg Q_l + A_l$$

where B_{jk} and B_{kj} are the Einstein coefficients for stimulated emission and absorption. A_j is the total Einstein coefficient for spontaneous emissions summed over all transitions, Q_j is the total quenching probability, and $I = P/\Delta v$ is the laser beam energy density of the wavenumber interval Δv and finally P and A are the incident power and cross-sectional area of the focal volume of the sample, respectively.

Assuming that the saturation condition is satisfied and N_2 is saturated, the fluorescent intensity can be written:

$$I_1 = hv\lambda_L (4\pi)^{-1} \Omega_c V_c N_k R_{kj} / B_{jk}$$

where Ω_c is the solid angle of the collecting optics and V_c is the excited volume. In the simplest case of a two level system N_0 the total number density is given by

$$N_0 = N_k + N_l = N_1 + N_2$$

$$I_1 = I_2 = hv\lambda_2 (4\pi)^{-1} \Omega_c V_c \cdot N_0 (1 + g_1/g_2)^{-1}$$

with $R_{kj}/B_{jk} = g_1/g_k = g_2/g_l$ resulting in the total number density

$$N_0 = I_2 (g_2 + g_1) 4\pi (hv\lambda_2 \Omega_c V_c g_2)^{-1}$$

For multi-level system, assuming that the lines can be separated, similar expression for the total number density can be found. The complexity, however, increases greatly particularly the separation of the fluorescence spectrum of the various levels. In principle this technique requires the illumination of a gas volume with the intensity I and the collection of the fluorescence radiation at 90° to the laser beam. From the last equation it is apparent that the concentration can be measured without any knowledge of the quenching probabilities when the saturation technique is used. However not all species are suitable for fluorescent diagnostics. First of all the specie must have its first excited electronic energy level located such that the absorption transitions are in a portion of the spectrum that can be covered with a laser. Second, the rotational spectrum must be sufficiently wide spaced such that the individual absorption and emission lines can be easily isolated. The last requirement might be difficult to satisfy with more complex molecules, whose rotational vibrational structure can be very complicated. It is therefore clear that while this technique can provide very strong signals in hostile environments, the range of applicability is limited to a selected group of species. In addition, only one specie at a time can be measured, with a given laser wavelength, in contrast to spontaneous Raman, where all the species present can be identified simultaneously using only one laser. In addition the temperature can be determined simultaneously with the concentration using spontaneous Raman, whereas the fluorescence technique cannot provide the temperature.

Laser Doppler Velocimeter

Laser Doppler Velocimetry is the best known laser based diagnostic technique. Mie scattering in conjunction with the Doppler effect provides the theoretical basis of the LDV. The laser Doppler velocimeter has been in use for over a decade. Its development has reached a point where most laboratories use it as a standard measuring device. The theoretical and operational background is described in References 31, 32 where most aspects of LDV technology have been treated and additional references can be found.

The operation of an LDV is predicated on the assumption that particles suspended in the flow, move with the same velocity as the fluid whose velocity

one is attempting to measure. Furthermore, in the case of a turbulent flow, it is assumed that the frequency spectra of the scattering particles, provide the required information regarding the turbulent structure of the flow field. The latter is associated with particle dynamics. The effect of particle dynamics on the performance of LDV has been considered by a number of researchers.³⁸⁻⁴¹ They all came to the conclusion that the size of the scattering particle has an effect on the frequency resolution of the spectrum. This is shown in Fig. 9.

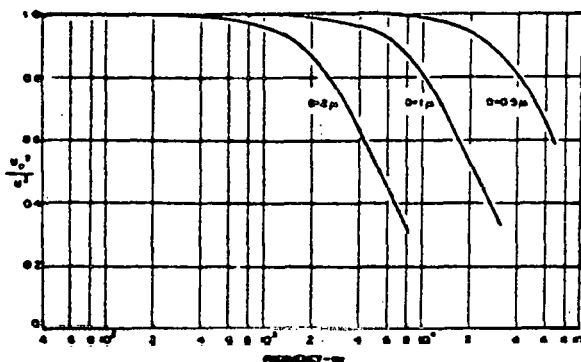


FIG. 9 RESPONSE OF ALUMINUM OXIDE PARTICLES TO TURBULENT FLUCTUATIONS

It is evident from the above, that the relationship of the frequency spectra from an LDV, to the turbulence spectra of a flow field is limited to the lower frequency region, that limitation being a function of the size of the majority of the scattering particles. This puts also a restriction on the use of naturally occurring particulates, because their sizes are generally unknown. The above suggests that for a more meaningful interpretation of the LDV measurements, a monitoring of the sizes of the particulates should be carried out and incorporated in the data reduction process. Careful choice, however, of the size and number of scatterers does permit one, within limits, to determine the velocity of the fluid and its turbulent intensity. The major problem in laser Doppler velocimetry is the acquisition, processing, and handling of the acquired data not the principle itself. Of the many optical arrangements possible, the one most frequently used is the dual scatter or sometimes known as the differential scatter systems. A schematic diagram of this type of an arrangement is shown in Fig. 10. The reason for its popularity is the fact that it can be operated in the forward as well as backward

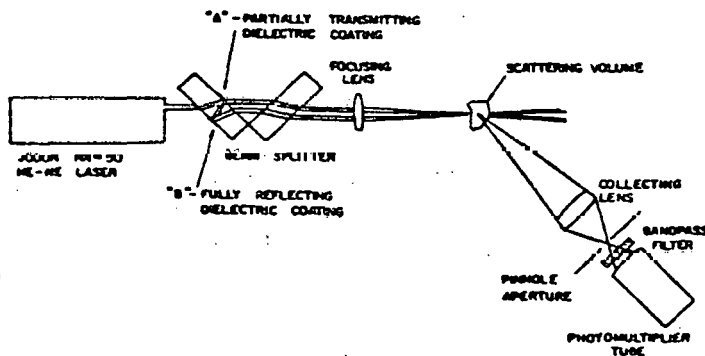


FIG. 10 SCHEMATIC DIAGRAM OF THE DUAL SCATTERER LDV SYSTEM

scatter mode. The acquired signals are independent of the angle of observation, and the alignment process is very simple. The translation of the signals into velocity and turbulent intensity of a one dimensional dual scatter LDV³³ is essentially reduced to the measurement of frequency. Since frequency can be measured with very high precision, extreme care is required in acquisition, processing, seeding and control of the LDV system to obtain precise velocity information.

At this point it should be mentioned that one of the very important parameters in combustion research is the droplet or particle size distribution in the flow field. Besides the standard sampling probe methods, optical methods based on the Mie scattering have been developed over the years. It has been found that for spheres the scattered light intensity is a complicated function of the scattering angle, of the size parameter $a = \pi d/\lambda$, the refractive index and the polarization. Durst⁴² using two photomultipliers on both sides of optical axis of a forward scattering LDV was able to show that under certain conditions the phase difference between the two signals could be related to the particle size. Farmer⁴³ on the other hand, using fringe spacings larger than 100 μ m, was able to measure particles whose diameter was less than 100 μ m using the visibility concept. Youle et al⁴⁴ using a dual scatter LDV was able to measure particle sizes between 30-240 μ m. The particles had to be transparent, spherical and larger than the fringe spacing. They found that under those conditions, the peak LDV signal increased monotonically with the diameter of the particles. As of now there appears to be no satisfactory diagnostic technique based on Mie scattering, holography, or diffusion correlated spectroscopy capable of providing unambiguous measurements of size and concentration of particulates in a flow remotely and nonintrusively. Most of the techniques mentioned are under development and further research is needed to develop particle diagnostics for combustion flows.

Applications: Experimental Results

The previously discussed, laser based diagnostic techniques have been and are still being developed for the most part for a unique purpose. That is, to provide a reliable, nonintrusive, nondisturbing probe for the measurement of the relevant parameters of fluid dynamics and combustion. It is obvious that the spontaneous Raman and LDV techniques would fit that purpose completely if all the encountered practical systems would be ideal, that is, free from interfering radiation and noise. As has been pointed out previously, the equivalent scattering cross section of the spontaneous Raman technique is relatively very low and subsequently this technique is not universally applicable. However in systems where this technique can be applied, it, in conjunction with an LDV, presents a very unique diagnostic system. As an example, the system utilized in our laboratories and shown in Fig.11 is capable of providing simultaneous measurements of concentration of 4 species, or 2 species and their respective temperatures, the velocity, the turbulent intensity, the correlations and crosscorrelations of species and velocities and in reacting flows the mixedness parameters. In addition the probability density functions (PDF) which is of importance in combustion modeling can be obtained easily.

The system shown in Fig.11 is self-explanatory. The number of receivers is by no means limited to four. Any number required for a given system may be incorporated without affecting the system's performance. In the next several figures examples of measurements performed on turbulent diffusive flames are given. Thus Fig.12 shows the normalized axial velocity and temperature distribution in a flame with the corresponding turbulence intensity and temperature fluctuation. Fig.13 shows the normalized nitrogen, carbon dioxide and oxygen concentration distribution and the corresponding fluctuations in the same flame. Fig.14 represents the first and second order correlations between oxygen, nitrogen and carbon dioxide. Finally some histograms of the N_2 species in the flame are shown in Fig.15 at several points. It must be emphasized that all these data have been taken simultaneously with the apparatus shown in Fig.11.

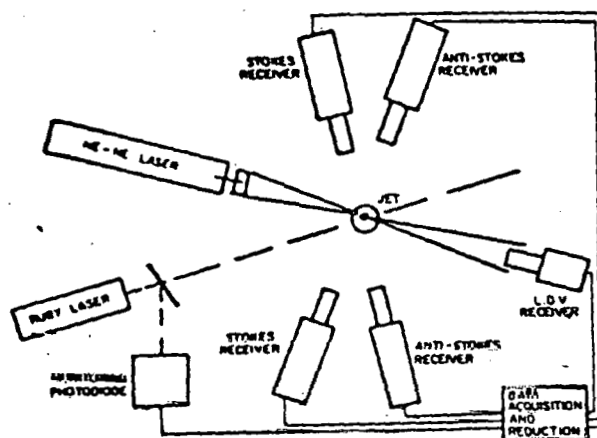


FIG. 11 BLOCK DIAGRAM OF EXPERIMENTAL APPARATUS

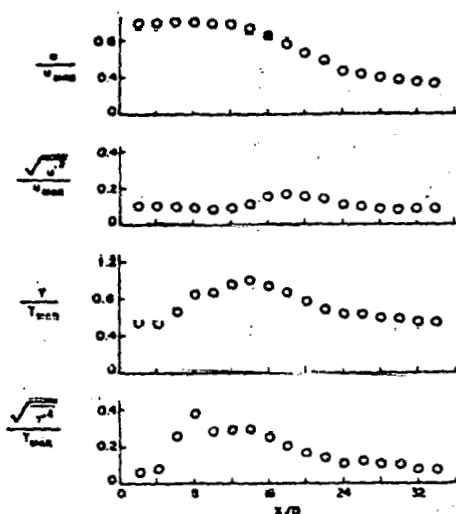


FIG. 12 VELOCITY AND TEMPERATURE, AXIAL PROFILES IN A FLAME

As discussed previously, under certain conditions the spontaneous Raman technique becomes inapplicable. Under those conditions, attempts have been made to utilize CARS. While CARS cannot replace spontaneous Raman, it is capable of providing information concerning density and temperature of a single specie in a hostile environment. There are essentially two types of optical arrangements utilized in CARS. They are both shown in Fig.16. The first one is the so called collinear one. The other is the so called "boxcars".²⁴ Both are essentially self-explanatory. The reason for the "boxcar" is the desire to improve the spacial resolutions, with a possible sacrifice in the anti-Stokes intensity. One should remark that the collinear type is self-phase matching, whereas the "boxcar" requires some delicate adjustments. The collinear system can be quite simple if one uses a stimulated Raman cell to generate the necessary Stokes line.^{22,32}

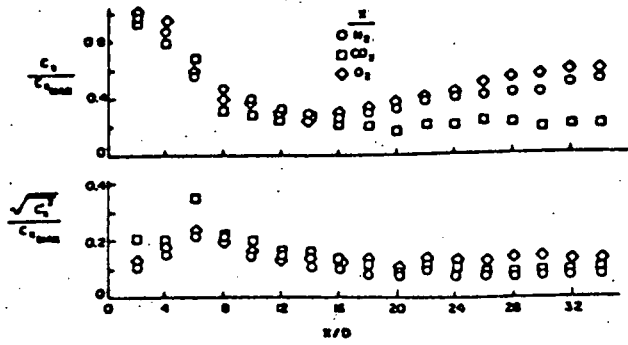
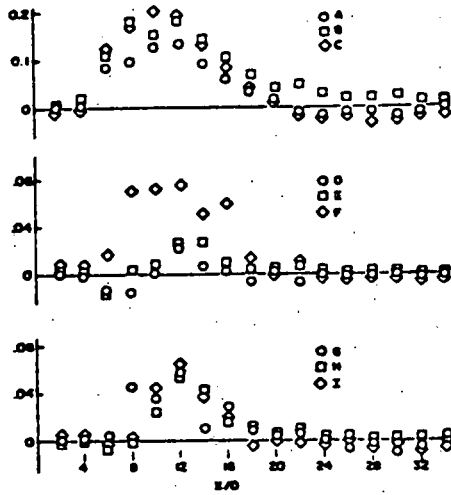


FIG. 13 CONCENTRATION, AXIAL PROFILES IN A FLAME



$$\begin{aligned}
 A &= \frac{\overline{C_x C_y}}{\overline{C_x} \overline{C_y}} & B &= \frac{\overline{C_x C_z}}{\overline{C_x} \overline{C_z}} & C &= \frac{\overline{C_y C_z}}{\overline{C_y} \overline{C_z}} \\
 D &= \frac{\overline{C_x^2 C_y}}{\overline{C_x^2} \overline{C_y}} & E &= \frac{\overline{C_x^2 C_z}}{\overline{C_x^2} \overline{C_z}} & F &= \frac{\overline{C_y^2 C_z}}{\overline{C_y^2} \overline{C_z}} \\
 G &= \frac{\overline{C_x C_y^2}}{\overline{C_x} \overline{C_y^2}} & H &= \frac{\overline{C_x C_z^2}}{\overline{C_x} \overline{C_z^2}} & I &= \frac{\overline{C_y C_z^2}}{\overline{C_y} \overline{C_z^2}}
 \end{aligned}$$

FIG. 14 FIRST AND SECOND ORDER CORRELATION WITH $x = N_2$, $y = CO_2$, $z = O_2$

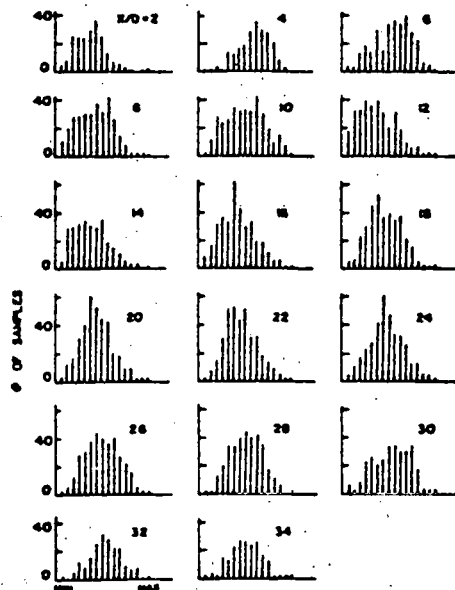


FIG. 15 HISTOGRAM OF N_2

Laser Based Diagnostic Techniques

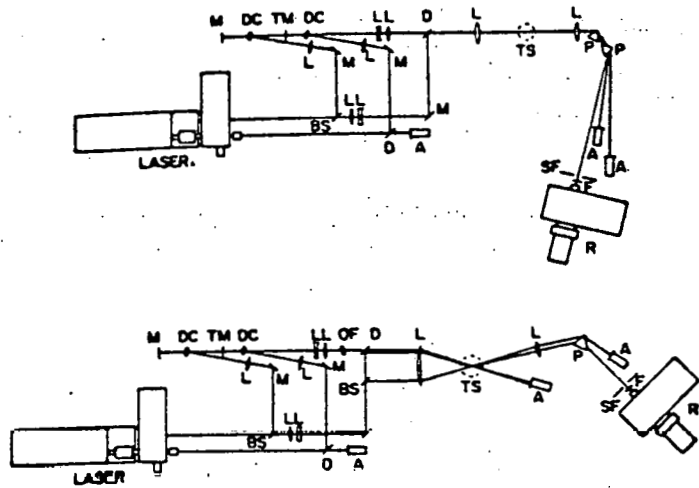


FIG. 16 COLLINEAR AND BOXCAR SCHEMATICS OF CARS

Some examples of data obtained using CARS are shown in the next few figures. Thus Fig. 17 shows the concentration of unburned methane in a sooty flame, obtained with a collinear system and a stimulated cell,³² while Fig. 18 the radial temperature profiles in a laminar propane diffusion flame²⁵ obtained using the so called "boxcar" system. It would be emphasized again that CARS, unlike spontaneous Raman, can supply only temperature and concentration of one specie at a time with a given set of lasers. It is not generally applicable to provide fluctuation information or correlation parameters.

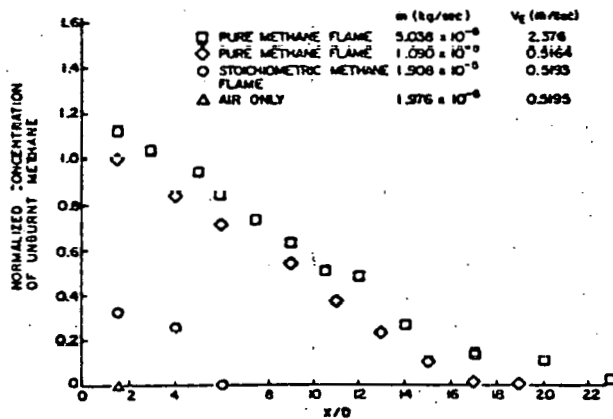


FIG. 17 CONCENTRATION OF UNBURNT METHANE

The practical application of laser fluorescence is still very limited, The available data in the open literature are scarce and of limited scope. The same is true of the stimulated Raman technology. Both of these techniques as discussed previously hold out great promise for the future, by virtue of their great radiation transfer efficiency and their pointwise resolution capability. Both techniques need further development.

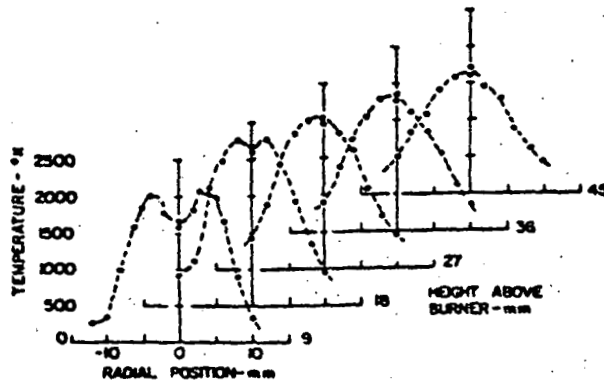


FIG. 18 TEMPERATURE PROFILE IN A PROPANE FLAME

TABLE I - SUMMARY

	Raman	CARS	SRS	Fluorescence	LDV
Specificity	Yes	Yes	Yes	Yes	X
Linearity	Yes	No	Yes	No	Yes
Independent					
Response	Yes	Yes	Yes	No	X
Spacial Resolution	Yes	Yes	Yes	Yes	Yes
Remoteness	Yes	Yes	Yes	Yes	Yes
Single Endedness	Yes	No	No	Yes	Yes
Instantaneity	Yes	Yes	Yes	Yes*	Yes*
Nonintrusiveness	Yes	Yes	Yes	Yes	Yes*
Simultaneity	Yes	No	No	No	Yes
General Applicability	Yes	Yes	No	No	Yes
Applicability to Fluctuation Meas.	Yes	No	No	No	Yes
Auto and Crosscorrelation	Yes	No	No	No	Yes*

*conditionally

ACKNOWLEDGEMENT

This research was sponsored by the Air Force Office of Scientific Research under Contract No. F-49620-78-C-0020, Project No. 2307-A1, the Department of Energy under Contract No. ET-78-C-01-3084 and the Office of Naval Research under Contract No. N00014-75-C-1143, Subcontract No. 8960-5.

REFERENCES

1. G. Placzek: Handb. Radial. Akademie-Verlagsgesellschaft VI (1939).
2. C.M. Sadowski and Y.E.H. Vanoverschelde, CARDE TN 1764167.
3. F. Robben: Project Squid ONR PU-R1-76 1975.
4. H.C. Van de Hulst: Light Scattering by Small Particles, Wiley N.Y. (1957).
5. G. Herzberg: Spectra of Diatomic Molecules, Van Nostrand, NY 1963.
6. H.A. Szymanski ed.: Raman Spectroscopy Theory and Practice, Plenum Press, 1967.
7. A. Anderson ed.: The Raman Effect, Bekker, N.Y. 1971.
8. B.P. Stoicherff: High Resolution Raman Spectroscopy, Adv. Spectr. I, pp. 91-174, Interscience (1959).
9. M. Lapp, C. Penny eds.: Laser Raman Gas Diagnostics, Plenum Press, NY, London 1974.

Laser Based Diagnostic Techniques

10. W. Lapp, C. Penny: *Infr. and Raman Spectr.*, 3, p. 204 (1977).
11. C. Widhopf, S. Lederman: *AIAA J.*, 9, 1971.
12. S. Lederman, M.H. Bloom, J. Bornstein, P.K. Khosla: *Int. J. Heat and Mass Transfer*, 17, p. 1479 (1974).
13. T. Yoshino, H.J. Bernstein: *J. Mol. Spectr.*, 2, p. 213 (1958).
14. R. Coulard: *Quant. Spectrosc. Rad Transfer*, 14, p. 969 (1974).
15. S. Lederman: *Prog. Energy Comb. Sci.*, Pergamon Press, 3, pp. 1 (1977).
16. S. Lederman: *AIAA Paper No. 76-26* (1976).
17. S. Lederman: *AIAA Paper No. 76-21* (1976).
18. E.L. Baardsen, R.W. Terhune: *Appl. Phys. Lett.*, 21, p. 209 (1972).
19. A.C. Gaydon: *The Spectroscopy of Flames*, Chapman & Hall, London (1974).
20. A.P. Baranowski, J.R. McDonald: *J. Chem. Phys.*, 66, p. 3300 (1977).
21. P.R. Regnier, J.P.E. Taran: *Appl. Phys. Lett.*, 23, p. 240 (1973).
22. P.R. Regnier, F. Moya and J.P.E. Taran: *AIAA J.*, 12, 826 (1974).
23. A.B. Harvey, J.R. McDonald, W.M. Tolles: *Progr. in Anal. Chem.*, 8, Plenum, (1976).
24. A.C. Eckbreth, P.A. Bonczyk, J.F. Verdick: *Appl. Spectr. Rev.*, 13, (1), 15 (1978).
25. J.W. Nibler, J.R. McDonald, A.B. Harvey: *Opt. Comm.*, 18, 371 (1976).
26. J.J. Berret, R.F. Begley: *Appl. Phys-Lett.*, 27, p. 129 (1975).
27. A. Owyong, E.D. Jones: *Opt. Lett.*, 1, p. 152 (1977).
28. A. Owyong: *Opt. Lett.*, 2, p. 91 (1978).
29. A. Owyong: *IEEE Journal of Quantum Electronics*, QE, 14, 3, p. 192 (1978).
30. W.H. Stevenson, H.D. Thompson: *Proceedings of a Workshop Project SQUID* (1972).
31. H.D. Thompson, W.H. Stevenson: *Proc. of a Workshop*, 1, & 2, Proj. SQUID (1974).
32. S. Lederman, A. Celentano, J. Glaser: *Phys. of Fluids*, 22, 1965 (1979).
33. P. Lallemand, P. Simova and G. Brer: *Phys. Rev. Letters*, 17, 1239 (1966).
34. W. Werncke, A. Lau, M. Pfeiffer, H.J. Weigmann, G. Hunsaly, K. Leur: *Opt. Comm.*, 16, 128 (1976).
35. A.C. Eckbreth: *AIAA*, 79-0083, p. 9 (1979).
36. J.W. Daily: *Applied Optics*, 16, 3, p. 568 (1977).
37. P.A. Bonczyk, J.A. Shirley: *Combustion and Flame*, 34, p. 253 (1979).
38. F. Durst: *Journal of Appl. Math. & Phys.*, 24, (1973).
39. W.J. Yantre: *AIAA*, 73-705 (1973).
40. S.L. Soo: *Fluid Dyn. of Multiphase Systems*, Blaisdell (1972).
41. P.K. Khosla, S. Lederman: *PIBAL Rep. No. 73-22* (1973).
42. F. Durst and M. Zere: *SFB 80-TM-63 U. Karlsruhe* (1975).
43. W.M. Farmer: *Appl. Opt.*, 13, p. 610 (1974).
44. A.J. Youle, N.A. Chigier, S. Atakan, A. Ungut: *AIAA 77-214* (1977).
45. A.C. Eckbreth, R.J. Hall, J.A. Shirley: *AIAA 79-0083* (1979).
46. M. Lapp, C.M. Penney, J.A. Asher: *ARL 73-0045* (1973).

UNCLASSIFIED

SECURITY CLASSIFICATION OF THIS PAGE (When Data Entered)

REPORT DOCUMENTATION PAGE		READ INSTRUCTIONS BEFORE COMPLETING FORM
1. REPORT NUMBER AFCSR-TR- 30-0517	2. GOVT ACCESSION NO. ADA026904	3. RECIPIENT'S CATALOG NUMBER
4. TITLE (and Subtitle) DEVELOPMENTS IN LASER BASED DIAGNOSTIC TECHNIQUES		5. TYPE OF REPORT & PERIOD COVERED INTERIM
		6. PERFORMING ORG. REPORT NUMBER
7. AUTHOR(s) S. LEDERMAN		8. CONTRACT OR GRANT NUMBER(s) F49620-78-C-0020
9. PERFORMING ORGANIZATION NAME AND ADDRESS POLYTECHNIC INSTITUTE OF NEW YORK MECHANICAL & AEROSPACE ENGINEERING FARMINGDALE, NY 11735		10. PROGRAM ELEMENT, PROJECT, TASK AREA & WORK UNIT NUMBERS 2307A1 61102F
11. CONTROLLING OFFICE NAME AND ADDRESS AIR FORCE OFFICE OF SCIENTIFIC RESEARCH/NA BLDG 410 BOLLING AIR FORCE BASE, DC 20332		12. REPORT DATE 1980
		13. NUMBER OF PAGES 19
14. MONITORING AGENCY NAME & ADDRESS (if different from Controlling Office)		15. SECURITY CLASS. (of this report) UNCLASSIFIED
		15a. DECLASSIFICATION/DOWNGRADING SCHEDULE
16. DISTRIBUTION STATEMENT (of this Report) Approved for public release; distribution unlimited		
17. DISTRIBUTION STATEMENT (of the abstract entered in Block 20, if different from Report)		
18. SUPPLEMENTARY NOTES Proceedings of the International Symposium on Shock Tubes and Waves, 12th The Hebrew University, Jerusalem 16-19 July 1979, The Magnes Press 1980, pp. 48-65.		
19. KEY WORDS (Continue on reverse side if necessary and identify by block number)		
SPONTANEOUS RAMAN CARS COHERENT RAMAN GAIN SPECTROSCOPY TEMPERATURE	TURBULENCE CORRELATION CROSS-CORRELATION FLUORESCENCE	VELOCITY LDV
20. ABSTRACT (Continue on reverse side if necessary and identify by block number) Several laser based diagnostic techniques, applicable to fluid dynamic and combustion research consisting of the spontaneous Raman effect, coherent anti-Stokes Raman scattering, coherent Raman gain spectroscopy, laser induced fluorescence and the laser Doppler velocimeter are discussed. Characteristic features of each of these techniques are brought forth. It is shown that these modern, laser based diagnostic techniques are capable of measuring most of the variables of interest in fluid dynamics and combustion research. Among		

DD FORM 1 JAN 73 1473

UNCLASSIFIED

SECURITY CLASSIFICATION OF THIS PAGE (When Data Entered)

these are the temperature, species concentration, velocity, turbulent intensity temperature and concentration fluctuation as well as a number of correlation and crosscorrelation parameters. Practical examples of the applicability to flow fields and combustion diagnostics are presented.

APPENDIX F

A UNIFIED SPONTANEOUS RAMAN AND CARS SYSTEM*

S. Lederman and C. Posillico

Polytechnic Institute of New York
Aerodynamics Laboratories
Farmingdale, N.Y.

ABSTRACT

A novel arrangement which permits the utilization of a single Q-switched high power Ruby laser to obtain simultaneously CARS, and spontaneous Raman signals is described. With the two versions indicated one has the additional option to chose between two operating frequency ranges as may be required due to possible inteference of ambient radiation. With this system upon incorporating, in addition, a LDV as indicated in Ref. 6, a most versatile diagnostic apparatus for flow fields and combustion research is made available.

* This work was supported by the Department of Energy under Contract No. ET-78-C-01-3084.

INTRODUCTION

A hope of every experimentalist involved in fluid-dynamics or combustion research has been to find a universal probe capable of providing with reasonable accuracy parameters of interest, nonintrusively, instantaneously, simultaneously and remotely. It appeared for a while that such a probe can be provided by the utilization of the spontaneous Raman scattering techniques. As is well known (Ref.1-3) these techniques can provide almost all of the important measurables in a flow field or flame. Particularly, if the short time duration high power laser pulse technique is utilized, some of the derived parameters, of major importance, in turbulent combustion modeling or chemically reacting flows, can easily be obtained.

While the above is still true for clean flow fields and flames (Ref. 4-6) in cases where carbon particles or soot is present the appearance of fluorescence, incandescence and other interfering radiation may make the utilization of the spontaneous Raman scattering techniques very difficult. While certain data acquisition techniques, such as gating, utilization of some field polarization properties etc. may help in improving the signal to noise ratio under difficult conditions, the basically low scattering crosssection of the spontaneous Raman effect, has made it necessary to reach into the nonlinear wave mixing phenomena to develop a technique based on the Raman effect, which is capable of providing a diagnostic probe several orders of magnitude more efficient in terms of signal strength. This technique the Coherent anti-Stokes Raman scattering technique or CARS, while providing larger signals, is not capable of re-

placing the spontaneous Raman scattering technique in terms of generality. In addition it generally requires two lasers to provide a single specie or temperature measurement. In order to provide a more universal diagnostic apparatus using as a prototype the integrated system of Ref. 7 L.D.V. and spontaneous Raman, a novel arrangement is being described here. This arrangement in its simplest variety utilizes a Q-switched Ruby laser and a Raman cell filled with a gas of particular interest, whereby stimulation of the Stokes line of the particular gas is caused, and when collinearly mixed with the primary beam generates a CARS signal in a given flow field. The part of the incident Ruby laser is simultaneously utilized to obtain spontaneous Raman signals. Thus, one is able to avail himself of the advantages of both the spontaneous and CARS techniques utilizing only one Ruby laser. The system can also be operated using a doubler on the Ruby laser, a broadband dye laser pumped with part of the doubled laser and a spontaneous Raman systems centered on 6943\AA and a CARS system based on the 3471\AA as the driving wavelength. These systems are described and some preliminary data are shown.

THEORETICAL BACKGROUND

The basic theoretical background of the formulation and operation of both the spontaneous Raman techniques and CARS have been discussed abundently in the literature. It is therefore sufficient here just to cite some of the references, (1-7) and point out only some of the major differences between the spontaneous Raman and the coherent anti-Stokes Raman scattering (CARS) systems. Thus, spontaneous Raman is single ended, CARS

is not.

Spontaneous Raman can resolve any number of Raman active species in a mixture simultaneously, CARS can not.

Spontaneous Raman can provide the temperatures of any number of Raman active species in a mixture simultaneously and simply, CARS can not.

Spontaneous Raman can provide a measure of the fluctuation of a number of species in a flow field and thus a measure of turbulent intensity, CARS can not.

Spontaneous Raman can provide a measure of the mixedness parameters, autocorrelation or correlation of parameters of importance in a flow field, CARS can not.

Spontaneous Raman is linear, CARS is not.

Those are some of the advantages of spontaneous Raman scattering over CARS.

However, one of the major drawbacks of spontaneous Raman is its extremely low differential scattering crosssection. This feature is responsible for very low signal levels and therefore limits the application of spontaneous Raman scattering diagnostics to well behaved, clean, low noise systems, particularly systems containing essentially no carbon particles or carbon soot. In those cases which are most important in a majority of combustion systems, CARS with its coherent signals, several orders of magnitude higher than the spontaneous Raman signal, is highly preferred in spite of its other limitations.

Experimental Apparatus

To take advantage of the positive properties of both systems, a unified diagnostic system utilizing a single Q-switched Ruby

laser has been designed, built and tested. A schematic diagram of the system is shown in Fig. 1. Here the Stoke line of the specie of interest is generated in a stimulated Raman cell, which together with the primary pumping wave (6943\AA) is co-linearly focussed on the flow field under investigation. The primary power of the Ruby laser is sufficient here to provide the necessary power for the CARS and in addition to provide sufficient intensity to provide the excitation for the spontaneous Raman signals, from the same point in the flow field.

Fig. 2 indicates a different version of the same apparatus. Here a doubler converts part of the Ruby pulse at 6943\AA to a 3471\AA which is then separated by a dichroic mirror from the fundamental. Part of the 3471\AA laser energy is used to pump a broadband dye laser, which is then combined coaxially with the rest of the 3471\AA laser energy and focussed at a point in the working fluid to obtain CARS. The total energy of the second harmonic (3741\AA) is approximately 500 mj. Since the original Ruby laser pulse energy was over 3 joules, well over 2 joules of laser light is available after separation by the dichroic mirror to be focussed on the working fluid to be used to excite spontaneous Raman scattering.

Experimental Results and Conclusions

Preliminary experiments using these systems have been conducted on a methane diffusion flame. The purpose of these experiments was the demonstration of its feasibility, practicality and advantages in terms of making this a more universal diagnostic system.

As is well known, the concentration of the unburned methane in a air methane flame is generally very low, and its measurement

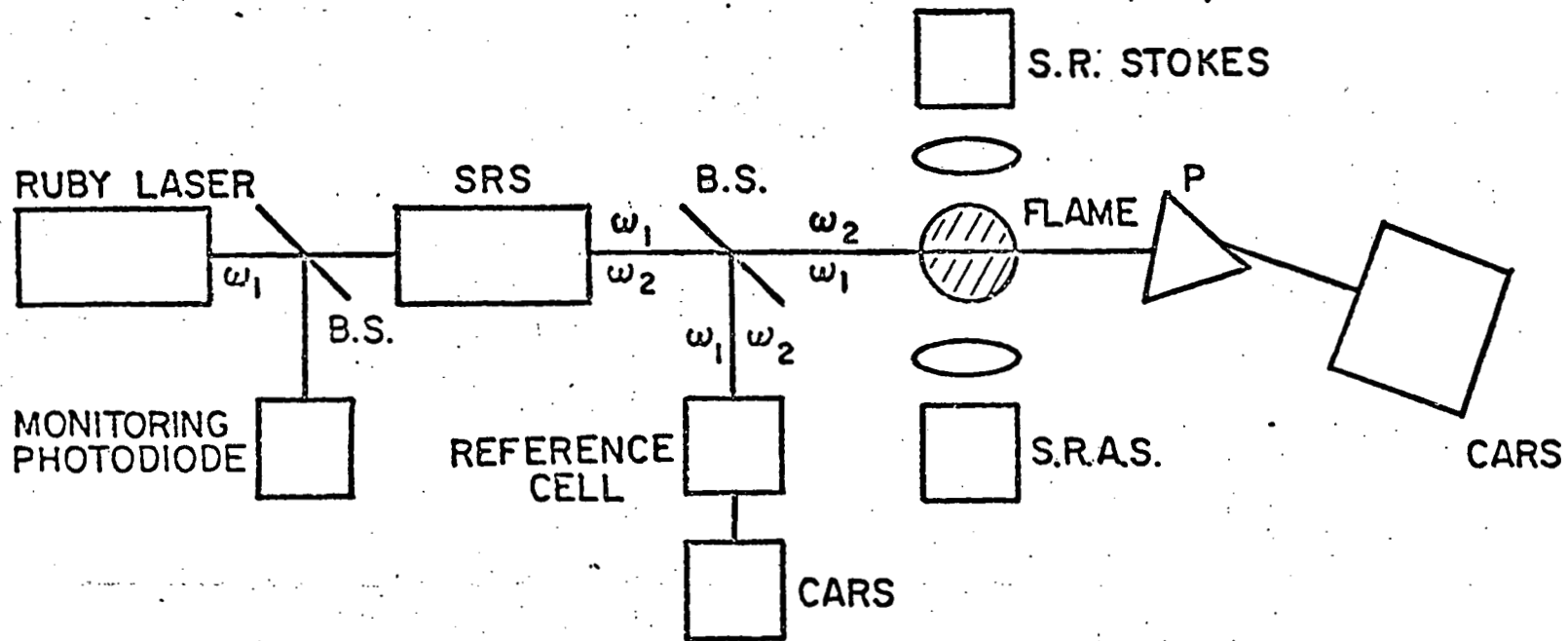
at a point of about 1mm cubed is almost impossible using spontaneous Raman scattering. On the other hand, the concentration of the products of combustion as well as heated nitrogen and their temperature, simultaneously is impossible using CARS. This combined apparatus permits a complete diagnosis of the flame simultaneously and instantaneously.

Fig. 3 indicates a preliminary survey of the concentration of the unburned methane using CARS. Figure 4 shows the concentration of nitrogen, and Figure 5 the temperature of the nitrogen in the flame using spontaneous Raman.

It is clear from the above that this system with the addition of the LDV capability which has been included previously into the diagnostic system using only spontaneous Raman (Ref. 7) fulfills the requirements for a universal diagnostic system. It can provide data on most practical flow fields of interest, be they "clean", or "contaminated", be they environmentally "friendly" or "hostile". A system like this portable and adjustable with respect to the flow field of interest should be very useful.

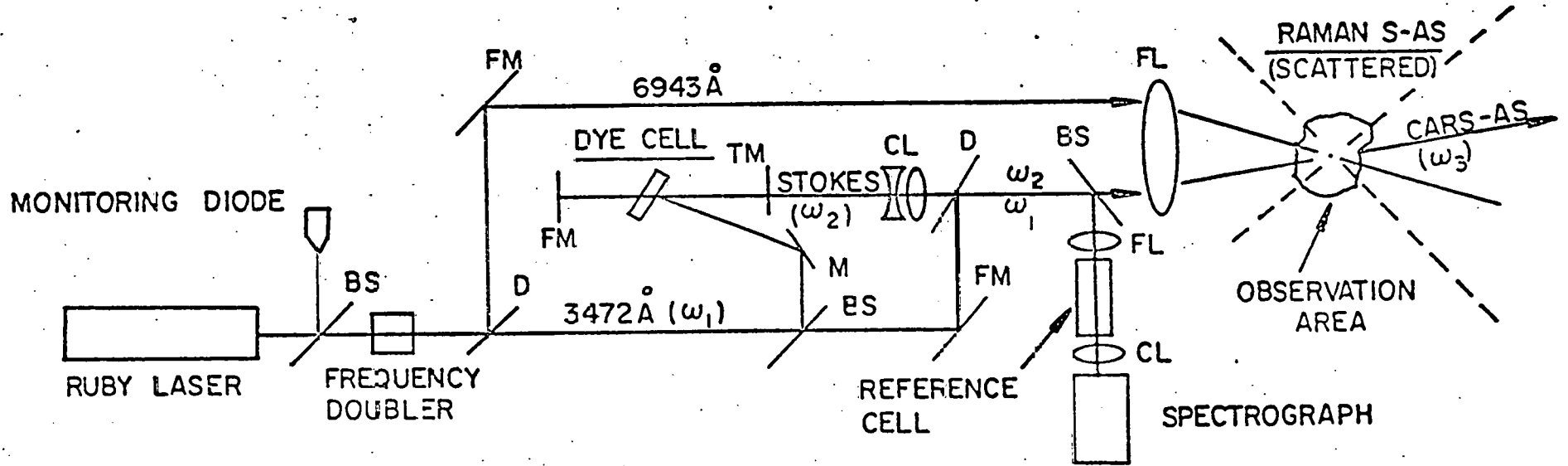
References

1. M. Lapp, C. Penny, eds.: Laser Raman Gas Diagnostics. Plenum Press N.Y., London 1974.
2. A. C. Eckbreth, P. A. Bonchyk and Y. F. Verdick: Laser Raman and Fluorescence Techniques for Practical Combustion Diagnostics. Applied Spectroscopy Reviews, 13, (1), 15-164, (1978).
3. S. Lederman: The Use of Laser Raman Diagnostics in Flow Fields and Combustion. Prog. in Energy and Combustion Sci, 3, 1-34, 1977.
4. M. Lapp, C. Penny: Infr. and Raman Spectroscopy. Vol. 3, 204, 1977.
5. S. Lederman: Developments in Laser Based Diagnostic Techniques. Shock Tubes and Waves, Proceedings of the 12 Int'l Symposium on Shock Tubes and Waves, A. Lifshitz, J. Rom, eds. The Magnes Press, Jerusalem, 48-65, 1980.
6. S. Lederman, A. Celentano, J. Glaser. Phys. of Fluids, 22, 1965, (1979).
7. S. Lederman. Some Applications of Laser Diagnostics to Fluid Dynamics. AIAA Paper No. 76-21, (1976).



B. S. - BEAM SPLITTER
 S. R. - SPONTANEOUS RAMAN
 P. - PRISM

FIG. 1 SPONTANEOUS RAMAN - CARS CONFIGURATION UTILIZING A STIMULATED RAMAN SCATTERING CELL (SRS)



BS - BEAM SPLITTER
 D - DICHOIC
 FM - FULL MIRROR
 TM - TRANSMITTING MIRROR
 M - MIRROR
 FL - FOCUSING LENS
 CL - COLLIMATING LENS

FIG. 2 SPONTANEOUS RAMAN - CARS CONFIGURATION UTILIZING DOUBLER AND DYE CELL

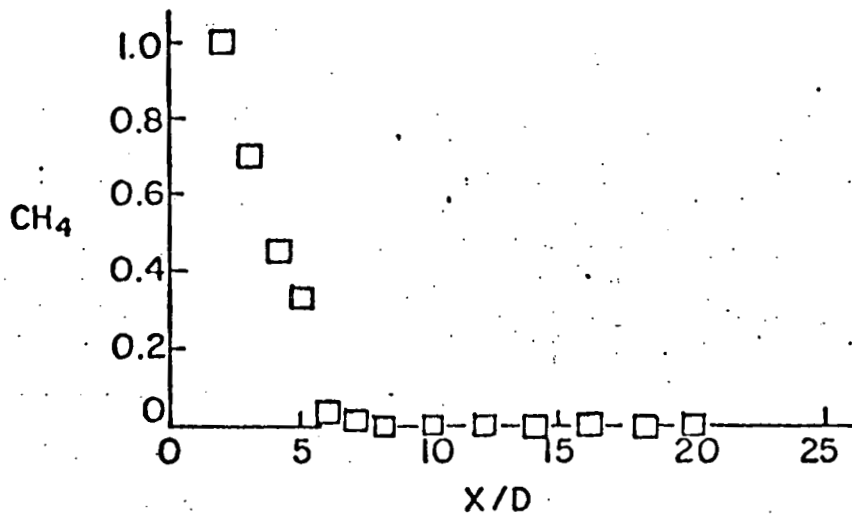


FIG. 3 NORMALIZED AXIAL METHANE CONCENTRATION PROFILE USING CARS

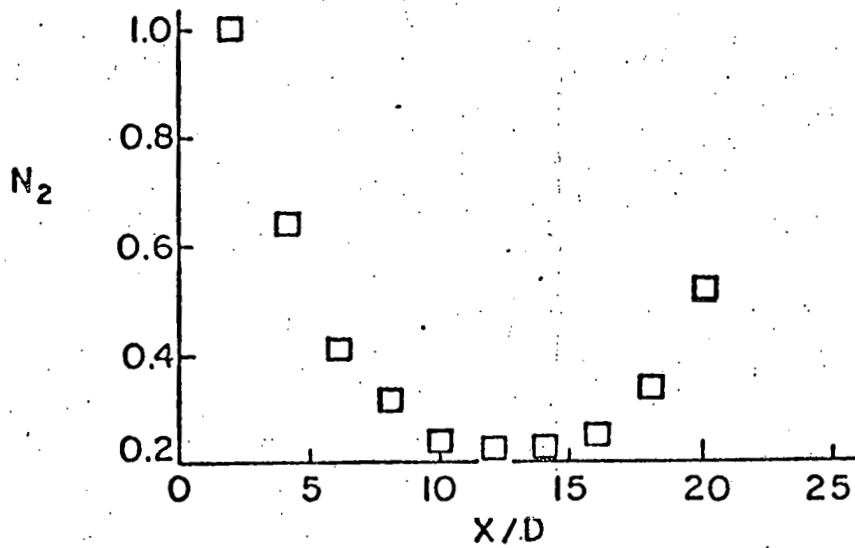


FIG. 4 NORMALIZED AXIAL NITROGEN CONCENTRATION USING SPONTANEOUS RAMAN

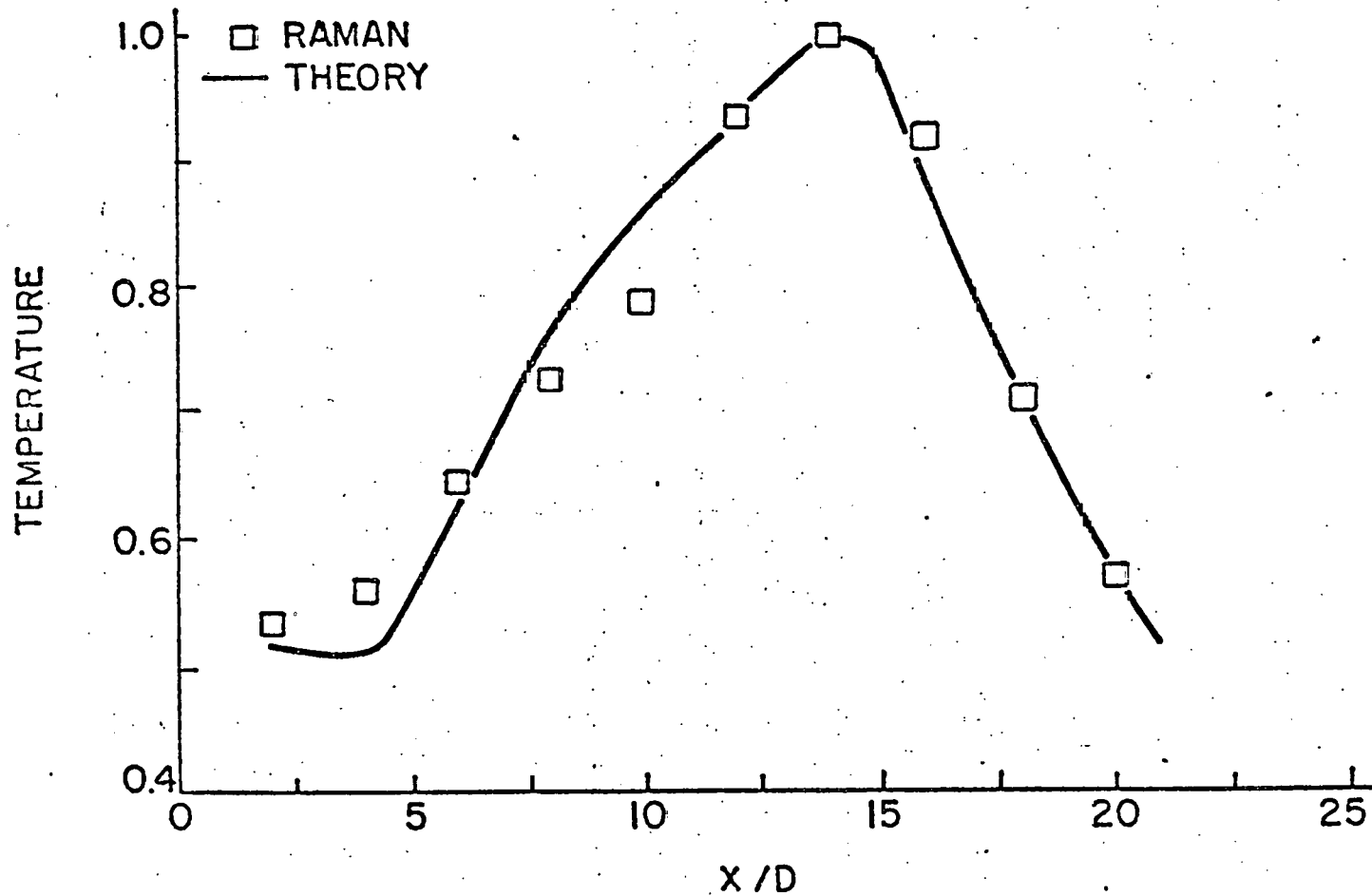


FIG. 5 NORMALIZED SPONTANEOUS RAMAN AXIAL TEMPERATURE PROFILE

APPENDIX G

ABSTRACT

ONE-DIMENSIONAL FLOW MODEL

FOR

COAL COMBUSTORS

by

Walter O. Peter

Advisor: Dr. Pasquale M. Sforza

Submitted in Partial Fulfillment of the Requirements for the
Degree of Master of Science (Mechanical Engineering)

June 1980

A quasi-one-dimensional approach to the analysis of a high temperature coal combustor is presented. The results obtained with these equations are compared to present analyses. An existing chemical equilibrium code is then utilized to improve the accuracy of the required input data to this analysis. An operating MHD combustor is modelled assuming a specified chemical heat release. Both adiabatic and radiative heat loss cases are examined. Results obtained are shown to be in agreement with the present-day literature.

TABLE OF CONTENTS

<u>Section</u>	<u>Page</u>
I. Introduction.	1
II. Derivation of the Basic One-Dimensional Flow Equations.	3
1. Equation of State	4
2. Speed of Sound.	4
3. Mach Number	5
4. Conservation of Mass.	5
5. Conservation of Energy.	8
6. Conservation of Momentum.	12
7. Equations of Motion in Standard Form.	13
III. Argonne Case Study.	15
1. First Stage of a Two-Stage Combustor.	17
2. Single-Stage Combustor.	21
IV. Chemical Equilibrium Code	24
V. PERC Case Study	29
1. Combustor Description	29
2. Model Assuming Adiabatic Process.	31
3. Model Including Radiative Heat Losses	36
VI. Conclusions and Discussion.	39
References.	42

LIST OF TABLES AND FIGURES

<u>Title</u>	<u>Page</u>
Table I. Influence Coefficients for Quasi-One-Dimensional Flow.44
Table II. First Stage Gasifier Exit Gas Compositions.45
Table III. Second Stage Combustor Exit Gas Compositions.46
Fig. 1 Argonne Case: First Stage of a Two-Stage Combustor47
Fig. 2 Argonne Case: First Stage of a Two-Stage Combustor48
Fig. 3 Argonne Case: Single-Stage Combustor49
Fig. 4 Argonne Case: Single-Stage Combustor50
Fig. 5 PERC Case: Two-Stage Combustor51
Fig. 6 PERC Case: Adiabatic Case with Chemical Heat Release52
Fig. 7 PERC Case: Adiabatic Case with Chemical Heat Release53
Fig. 8 PERC Case: Chemical Heat Release with Radiative Heat Loss.54
Fig. 9 PERC Case: Chemical Heat Release with Radiative Heat Loss.55
Fig.10 PERC Case: Second Stage of a Two-Stage Combustor56
Fig.11 PERC Case: Second Stage of a Two-Stage Combustor57

NOMENCLATURE

a	Speed of sound
A	Surface area
A_w	Channel wetted area
B_1	Constant appearing in Eq. (43)
B_2	Constant appearing in Eq. (43)
c	Molar concentration
C_f	Skin friction coefficient
c_p	Specific heat at constant pressure
c_v	Specific heat at constant volume
D	Hydraulic diameter
dF_z	Net external force
dH	Energy term defined by Eq. (28)
dh_T	Change in the total enthalpy per unit mass
dQ	Net heat added to the flow from external sources
dW_k	Work per unit mass removed from the flow
h	Enthalpy per unit mass
HV	Fuel heating value
k	Ratio of total specific heats
m	Mass flow rate
M	Mach number
n	Total number of moles
\hat{n}	Surface area unit outward normal vector
N	Total number of species
p	Pressure
Q	Radiative heat loss given by Eq. (45)
r	Radial coordinate

R	Gas constant on a molar basis
R_u	Universal gas constant
T	Temperature
T_{AF}	Adiabatic flame temperature
T_o	Initial temperature
V	Local flow speed
V_c	Combustor volume
W	Mixture molecular weight
z	Axial coordinate
z_l	Location of complete combustion
γ	Ratio of sensible specific heats
Δh_f°	Heat of formation per unit mass
ϵ_g	Gas emissivity
ϵ_w	Wall emissivity
ζ	Term defined by Eq. (44)
η	Efficiency
η_t	True (or actual) efficiency
θ	Azimuthal coordinate
π	3.1415927
ρ	Density
τ	Shear stress
$\%$	Percent coal consumed

SUBSCRIPTS AND SUPERSSCRIPTS

f	Fuel
i	Counter used for a total of N species
o	Oxidant

r Radial component
S Constant enthalpy process
T Constant temperature process
w Component occurring at the chamber wall
z Axial component
' Reactants
" Products

I. INTRODUCTION

Much time and effort is currently being spent on new ways of producing electrical energy to meet the ever-increasing energy demands of today's society. One area presently being explored is that of magnetohydrodynamic power generation.

The magnetohydrodynamic generator, like the electrical generators currently being used, produces a current by moving a conductor through a magnetic field. In the conventional turbogenerator, the conductor is an armature driven by a steam turbine. In the magnetohydrodynamic generator, the conductor is a stream of hot ionized gas that has been seeded with metal particles to improve its electrical conductivity. This plasma is accelerated through a rocket-like nozzle and sent through a channel lined with electrodes, where its electrical power is drawn off. There are many advantages claimed with this system. Since there are no moving parts and you are dealing with much higher temperatures than in present-day electrical generation, up to 50 percent more power from the same fuel, with lower pollution, is claimed [1].

With the projected construction of open-cycle magnetohydrodynamic power generation systems utilizing coal as the primary fuel, interest has arisen in recent years in the design of efficient coal combustors which would satisfy the requirements of such a system. (For a more complete description of existing large-scale test facilities, see the works presented by Jackson [2] and Dicks, et. al. [3]). The demands of this system on the coal combustor are to produce combustion products on the order of 3000 °K, yet at a sufficient rate to meet the power require-

ment. The flue gas must also contain only a small fraction of the original ash content of the coal, so as not to damage the electrodes in the generator channel.

Coal has been perhaps the most commonly used fuel for power generation in the past, and much information can be found on its properties and use. With the rising interest in coal-fired magnetohydrodynamic generators, however, there is a need to understand the behavior of the coal under these highly elevated and stringent operating conditions. The basic properties of coal which dictate the ignition, combustion, and slag formation at these high temperatures are not well known. Nevertheless, there is a need to model these coal combustors in view of the current design work being performed in this area.

The purpose of this work is to construct a viable model for these high temperature coal combustors and to accurately predict their overall behavior. Commensurate with the degree of accuracy of the data currently available on the properties of coal and existing coal combustors, this model will be developed using a simplified flow-field configuration.

II. DERIVATION OF THE BASIC ONE-DIMENSIONAL FLOW EQUATIONS

The equations of motion which describe the flow through a combustor within the constraints of a quasi-one-dimensional approximation will be developed in this section. These equations are particularly simple to deal with yet they are commonly acknowledged as being reasonably accurate, even for rather complex problems, such as the one considered here. The analysis will take into account the following parameters:

- (i) changes in the combustor's cross-sectional area,
- (ii) chemical reaction,
- (iii) variations in the molecular weight and specific heat of the mixture due to combustion,
- (iv) exchange of heat with the surroundings,
- (v) drag caused by internal bodies or solid particles within the flow,
- (vi) losses due to friction along the combustor walls.

These equations will be developed in such a manner that close correspondence with the combustor problem at hand will be maintained, without significant loss of generality. These equations could, therefore, be applied to other problems such as rocket nozzles, ramjets, and combustion chambers for gas turbines or turbojet and turbofan engines.

The necessary flow-field equations will be treated individually in the development that follows. They will be expressed in logarithmic differential form, following the format used by Shapiro [4].

II.1 Equation of State

We assume that the mixtures flowing through the combustor behave as ideal gases and are well-described by the perfect gas law:

$$p = \frac{\rho R_u T}{W} \tag{1}$$

where p , ρ , and T denote the mixture pressure, density, and temperature, respectively. W represents the mixture molecular weight, and R_u is the universal gas constant. The presence of liquid or solid particles in the flow will be neglected in the general development of these equations. The effects due to these particles will be treated individually, as they arise. Taking the logarithm of the state equations, we obtain:

$$\log p = \log \rho + \log R_u + \log T - \log W$$

Rewriting this in differential form, we have:

$$\frac{dp}{p} = \frac{d\rho}{\rho} + \frac{dT}{T} - \frac{dW}{W} \tag{2}$$

II.2 Speed of Sound

For a semiperfect gas, the sound speed may be written as:

$$a^2 = \frac{k R_u T}{W} \tag{3}$$

where k is the ratio of total specific heats, which are those specific heats which include heats of formation, heats of vaporization, etc. For flows of nonreacting perfect gases the quantity k reduces to γ , the ratio of sensible specific heats. In differential form, Eq. (3) becomes:

$$\frac{da}{a} = \frac{1}{2} \left[\frac{dk}{k} + \frac{dT}{T} - \frac{dW}{W} \right] \tag{4}$$

II.3 Mach Number

In general, the Mach number is defined as the ratio of the local flow speed to the local sonic velocity, or:

$$M = \frac{V}{a} \quad (5)$$

Casting this equation in terms of M^2 , for convenience in the manipulations of these equations to follow, and recalling the expression given for the sonic velocity, we obtain the following equations in differential form:

$$\frac{dM^2}{M^2} = \frac{dV^2}{V^2} + \frac{dW}{W} - \frac{dk}{k} - \frac{dT}{T} \quad (6)$$

II.4 Conservation of Mass

The basic concept of mass conservation, for a steady flow, may be expressed by the integral equation:

$$\int_A \rho \bar{V} \cdot \hat{n} \, dA = 0 \quad (7)$$

where \bar{V} is the velocity vector, A is the surface area of a control volume, fixed in space and enclosing all or part of the flowing fluid, and \hat{n} is the unit outward normal vector of that surface. If the fluid can be considered a continuum, this equation can be written in cylindrical polar coordinates as:

$$\frac{\partial}{\partial r} (\rho r V_r) + \frac{\partial}{\partial \theta} (\rho V_\theta) + \frac{\partial}{\partial z} (\rho r V_z) = 0 \quad (8)$$

where r , θ , z are the radial, azimuthal, and axial coordinates, respectively; and V_r , V_θ , V_z are their associated velocity components. Assuming that the flow is axisymmetric, there are no changes occurring with respect to θ , and Eq. (8) simplifies to:

$$\frac{\partial}{\partial r} (\rho r V_r) + \frac{\partial}{\partial z} (\rho r V_z) = 0 \quad (9)$$

Multiplying this equation by 2π and integrating with respect to r between the limits of 0 and $r_w(z)$ we obtain, using the Leibniz rule:

$$\frac{\partial}{\partial z} \left[2\pi \int_0^{r_w(z)} \rho V_z r dr \right] - \rho V_{z,w} r_w \left[\frac{dr_w}{dz} - \frac{V_{r,w}}{V_{z,w}} \right] = 0 \quad (10)$$

where $r_w(z)$ is the radial coordinate of the wall bounding the flow, $V_{r,w}$ is the radial component of velocity at the wall, and $V_{z,w}$ is the axial component of velocity at the wall.

For an inviscid flow, we can write the following expression:

$$\frac{dr_w}{dz} = \frac{V_{r,w}}{V_{z,w}} \quad (11)$$

This describes the fact that the flow follows the shape of the wall exactly. Even for viscous flow, this is generally a good approximation as long as a well-developed boundary layer exists at the wall, and there is no evidence of separation. For the combustor case being considered here such conditions will, in general, be satisfied. Eq. (10) may therefore be rewritten as:

$$\frac{\partial}{\partial z} \left[2\pi \int_0^{r_w(z)} \rho V_z r dr \right] = 0 \quad (12)$$

where the quantity enclosed by the square brackets represents the mass flow rate, m . Thus we have:

$$m = 2\pi \int_0^{r_w(z)} \rho V_z r dr = \text{constant} \quad (13)$$

Since we are developing a quasi-one-dimensional flow analysis, the values of ρ and V_z are assumed to vary little with respect to r so that they may be replaced by constant mean values and removed from under the integral sign. Eq. (13) then

becomes:

$$m = \rho V \pi r^2 = VA = \text{constant} \quad (14)$$

where ρ now denotes the mean value for the density at any axial station, V is the mean axial velocity at that station, and A is the cross-sectional area normal to the z -axis associated with that same axial location. The assumption made for ρ and V_z is a reasonable one, provided that the variation in flow cross-sectional area along the axial direction is small. This provision can be expressed as:

$$\frac{dr_w}{dz} \ll 1 \quad (15)$$

For most problems concerning combustors, including the case studies of magnetohydrodynamic combustors which follow, this requirement is met. There are certain systems, however, that contain large cross-sectional area differentials or abrupt turns in the flow path. Such configurations would suggest that the quasi-one-dimensional approximation would fail locally for some distance downstream of these abrupt changes. One such example would be a two-stage magnetohydrodynamic coal combustor where a vertical gasifier and slag removal stage is mated to a horizontal combustor stage, thereby causing the flow to change direction by ninety degrees. In more conventional combustor designs, such abrupt changes in the flow would not be present. With these constraints in mind, we can rewrite the mass conservation equation, Eq. (14), in the differential form:

$$\frac{dm}{m} = \frac{d\rho}{\rho} + \frac{dV}{V} + \frac{dA}{A} = 0 \quad (16)$$

II.5 Conservation of Energy

As was noted previously for our quasi-one-dimensional flow analysis, we may assume that the quantities of interest vary only with axial location and are constant across any section of the combustor. With this in mind, we may apply the principle of energy conservation quite readily. Considering a control volume beyond any mixing region that may occur, we may write:

$$m \left[dQ - dW_k \right] = m dh_T \quad (17)$$

where dQ is the net heat added to the stream from external sources by way of conduction, radiation, or convection, measured on a unit mass basis. The variable dW_k represents the work per unit mass removed from the flow, and dh_T is the change in the total enthalpy per unit mass of the fluid flowing through the control volume. This equation may be rewritten as:

$$m \left[dQ - dW_k \right] = m \left[dh + \frac{dV^2}{2} \right] \quad (18)$$

where h is the enthalpy of the mixture per unit mass, and m represents the mass flow rate of the entire mixture. Therefore, m is the sum of the oxidant and fuel mass flow rates and may be represented as:

$$m = m_o + m_f \quad (19)$$

On a mass basis, the enthalpy may be defined as:

$$h = \sum_{i=1}^N \rho_i h_i \quad (20)$$

where ρ_i is the mass density of species i , and N is the total number of species present in the mixture. The quantity h_i is

the enthalpy of species i , and is given by:

$$h_i = \Delta h_{f_i}^{\circ} + \int_{T_r}^T c_{p_i} dT \quad (21)$$

where $h_{f_i}^{\circ}$ is the heat of formation per unit mass of species i at the reference temperature, $T_r = 298.16^{\circ}\text{K}$; and c_{p_i} is the sensible specific heat per unit mass of species i . Differentiating Eq. (20), we obtain:

$$dh = \sum_{i=1}^N \rho_i dh_i + \sum_{i=1}^N h_i d\rho_i \quad (22)$$

and it is noted that:

$$dh_i = c_{p_i} dT \quad (23)$$

where the mixture sensible specific heat may be written as:

$$c_p = \sum_{i=1}^N \rho_i c_{p_i} \quad (24)$$

Therefore, Eq. (22) may be expressed as:

$$dh = c_p dT + \sum_{i=1}^N h_i d\rho_i \quad (25)$$

Recalling the energy conservation relation given by Eq. (18), and substituting the above result into that equation, we obtain:

$$dQ - dW_k - \sum_{i=1}^N h_i d\rho_i = c_p dT + \frac{dV^2}{2} \quad (26)$$

which can be rearranged to yield:

$$\frac{dQ - dW_k - dH}{c_p T} = \frac{dT}{T} + \frac{dV^2}{2c_p T} \quad (27)$$

where we have:

$$dH = \sum_{i=1}^N h_i d\rho_i \quad (28)$$

The last term in Eq. (27) may be put into the following form:

$$\frac{dv^2}{2c_p T} = \frac{a^2 M^2}{2c_p T} \frac{dv^2}{v^2} \quad (29)$$

Using the expression derived previously for the speed of sound:

$$a^2 = \frac{kR_u T}{W} \quad (3)$$

and noting the following relationships:

$$c_p - c_v = \frac{R_u}{W} \quad (30)$$

$$\gamma = \frac{c_p}{c_v} \quad (31)$$

we obtain:

$$\frac{dv^2}{2c_p T} = \frac{k}{\gamma} \left[\frac{\gamma - 1}{2} \right] M^2 \frac{dv^2}{v^2} \quad (32)$$

so that Eq. (27) now becomes:

$$\frac{dQ - dW_k - dH}{c_p T} = \frac{dT}{T} + \frac{k}{\gamma} \left[\frac{\gamma - 1}{2} \right] M^2 \frac{dv^2}{v^2} \quad (33)$$

It is noted here that the factor k/γ in Eq. (33) indicates the importance of the chemistry that is taking place in the flow; that is, that the speed of sound is altered due to the presence of chemical reactions. This difference is rarely described in previous applications of the quasi-one-dimensional equations to reacting flows, and, as will be seen subsequently, can be quite important.

The term defined by Eq. (28) can be written in molar

form as:

$$dH = \sum_{i=1}^N H_i dc_i \quad (34)$$

where H_i is the enthalpy on a molar basis and c_i is the molar concentration of species i . For a reaction between ideal gases, we would have:

$$\sum_{i=1}^N c_i' A_i + \sum_{i=1}^N c_i'' A_i \quad (35)$$

where c_i' and c_i'' denote the number of moles of species i in the reactants and the products, respectively, and A_i denotes a general chemical species. Penner [5] shows that the heat of reaction for a given temperature and pressure is:

$$\begin{aligned} \Delta H(T) = & \sum_{i=1}^N c_i'' \left[\Delta H_{f_i}^{\circ} + \int_{T_r}^T c_{p_i} dT \right] \\ & - \sum_{i=1}^N c_i' \left[\Delta H_{f_i}^{\circ} + \int_{T_r}^T c_{p_i} dT \right] \end{aligned} \quad (36)$$

which may be rewritten as:

$$\Delta H(T) = \sum_{i=1}^N [c_i'' - c_i'] H_i(T) \quad (37)$$

We see that this is the equivalent of Eq. (34) in the case of finite, rather than infinitesimal, chemical changes. Therefore, the dH term in Eq. (28) is actually the heat of reaction for the fuel and oxidizer under consideration. The details of how this equation will be manipulated for the problem at hand appear in

a later section.

II.6 Conservation of Momentum

For this equation, we will employ Newton's second law, which equates the rate of change of momentum of the fluid in a fixed control volume to the net force acting on that fluid. For the cases considered here we may formulate this as:

$$m dV = - A dp - \tau_w dA_w - dF_z \quad (38)$$

where A is again the cross-sectional area of the channel, τ_w is the wall shear stress which acts to retard the flow, A_w is the wetted area of the channel, and dF_z is the net external force, such as the drag of stationary bodies in the flow or body forces which act on the flow. The shear stress may be expressed in coefficient form by noting that:

$$C_f = \frac{\tau_w}{\frac{1}{2}\rho V^2} \quad (39)$$

where C_f is the skin friction coefficient, which of course may vary with axial location. The wetted area may be related to the cross-sectional area by means of the hydraulic diameter:

$$D = \frac{\text{cross-sectional area}}{\text{wetted perimeter}}$$

as follows:

$$\frac{dA_w}{A} = \frac{4dz}{D} \quad (40)$$

Substituting these expressions into the conservation of momentum relation, Eq. (38), and rearranging terms yields:

$$\frac{dp}{p} + \frac{1}{2}kM^2 \frac{dv^2}{v^2} + \frac{1}{2}kM^2 \left[4C_f \frac{dz}{D} + \frac{dF_z}{\frac{1}{2}kpAM^2} \right] = 0 \quad (41)$$

II.7 Equations of Motion in Standard Form

The independent variables in the preceding development may be chosen to be:

$$\frac{dA}{A}$$

$$\frac{dQ - dW_k - dH}{c_p T}$$

$$\left[\frac{4C_f dz}{D} + \frac{dF_z}{\frac{1}{2}kpAM^2} \right]$$

$$\frac{dW}{W}$$

$$\frac{dk}{k}$$

while the dependent variables are selected as:

$$\frac{dM^2}{M^2}$$

$$\frac{dT}{T}$$

$$\frac{dv}{v}$$

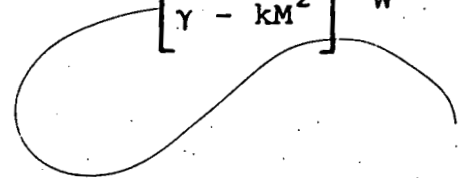
$$\frac{dp}{p}$$

$$\frac{da}{a}$$

$$\frac{dp}{p}$$

Of course additional dependent variables could have been chosen, but the six above are sufficient for our purposes. Manipulation of the governing equations reduces them to a standard form which is best reported in the form of a table of influence coefficients as shown in Table I. The equation for any of the dependent variables in the first column is formed by the sum of the products of the influence coefficients and

the respective independent variables in the first row of the table, for example:

$$\begin{aligned}
\frac{dp}{P} = & \left[\frac{\gamma k M^2}{\gamma - k M^2} \right] \frac{dA}{A} - \left[\frac{\gamma k M^2}{\gamma - k M^2} \right] \left[\frac{dQ - dW_k - dH}{c_p T} \right] \\
& - \left[\frac{k M^2 (\gamma + (\gamma - 1) k M^2)}{2(\gamma - k M^2)} \right] \left[\frac{4C_f dz}{D} + \frac{dF_z}{\frac{1}{2} k P A M^2} \right] \\
& + \left[\frac{\gamma k M^2}{\gamma - k M^2} \right] \frac{dW}{W}
\end{aligned}
\tag{42}$$


III. ARGONNE CASE STUDY

To utilize the equations of motion, as they appear in Table I, one must first understand the combustion process that will be taking place. Typical operating conditions for existing magnetohydrodynamic (MHD) combustors can be found in the analysis done by Chung and Smith [6]. In the case of either a two-stage or single-stage combustor, it is noted that a precipitous rise in the temperature of the mixture occurs soon after entering the combustor. This characterizes the ignition of the coal particles within the combustor due to the presence of intense radiative heat flux. To model this jump in temperature, an S-shaped exponential curve was used. Thus, the chemical heat released within the combustor is given by:

$$dH = H(\exp(-B_1\zeta^{B_2})) \quad (43)$$

where:

$$\zeta = \left| \frac{z}{z_1} - 1 \right| \quad (44)$$

and z is the axial location as you march down the combustor, while z_1 is the location of complete combustion. B_1 and B_2 are constants which can be varied to obtain the desired curve shape. (In this case, the distribution of chemical heat release due to reaction as a function of z). H , in this case, represents the total amount of chemical heat released, while dH would be the amount released at each z location. The term H , as we will see, can be expressed as some fraction of the total heating value of the fuel used.

When examining the high temperatures present in the MHD combustor, it is noted that radiation would be the predominant

mode of heat transfer. Depending on the flow configuration, convective heat transport through the wall boundary layers may not be negligible. Chung and Smith state, however, that the simple radiative relationship based on the gas and wall temperatures and emissivities would tend to overestimate the heat transfer. In any case, the uncertainties in the gas and wall emissivities would not warrant the inclusion of the convective heat loss. While both the solid particles and gaseous species within the flow interchange heat with the combustor wall, we will deal with the flow as if it were composed purely of gases to simplify the analysis. Much work has been carried out on the radiative transport properties of the gaseous combustion products. For further discussions on this topic, see the publications of Petrick and Shumyatsky [7] and Palmer and Beer [8].

Haywood and Womack [9] have developed the following equation to describe the radiative heat loss from a cylindrical combustor:

$$Q = \left[4.77 \times 10^5 \right] \left[\frac{A}{V_c} \right] \left[\epsilon_g \left(\frac{T}{100} \right)^4 - \epsilon_w \left(\frac{T_w}{100} \right)^4 \right] \quad (45)$$

where: $\epsilon_g = (1.53 \times 10^{-5}) T \sqrt{D}$ (46)

and: $\epsilon_w \approx 0.8$ (47)

The temperatures in this case are in °R; while D, A, and V_c are dimensioned in ft., ft.², and ft.³ respectively. The radiative heat loss of the gas, Q, will then have the units of Btu per ft.³-sec. (Since the flow-field equations were employed using metric units, the above equations can be multiplied by the proper conversion factors for consistency in units). The above heat loss equations are valid when the combustor contains only the gaseous species. Of course, a more accurate heat transfer analysis

could be performed based on a detailed concentration distribution of the radiating gaseous species; however, the above analysis will be sufficient for our purposes.

These two quantities, the chemical heat released due to chemical reaction and the radiative heat loss to the combustor walls, define the parameters which will have the greatest affect on the temperature of the gas as we proceed along the combustor length. While losses due to friction will be nominal, they will also be included since Heywood and Womack provide tables of friction factors for various combustor configurations. Drag losses will not be considered here since we are assuming the flow to be gaseous. With this in mind, we are now ready to utilize the quasi-one-dimensional equations derived in Section II.

III.1 First Stage of a Two-Stage Combustor

Chung and Smith model a two-stage combustor, whose first stage has a diameter of 0.19 m. The first stage operates at a pressure of 8 atm. and an air inlet temperature of 1866 °K. It burns approximately 1 kilogram of coal per second at a stoichiometric ratio of 0.3951. Plots of velocity, gas temperature, and percent combustible coal consumed versus z location were also available for this case. These served to furnish the initial data required for the one-dimensional equations. For lack of more complete chemical data, the gaseous mixture's specific heat (at constant pressure) and molecular weight were assigned constant global values. The ratio of total specific heats and sensible specific heats were assumed equal and constant for this case as well.

The purpose of this first stage, as is typical with most two-stage MHD combustors, is to gasify the pulverized coal with either oxygen or air to form a hot fuel gas. This fuel-rich mixture is then sent to the second stage of the combustor, where additional oxidant is added to complete combustion. The details of a typical two-stage combustor will be shown in a later section. We are primarily interested, in this section, in comparing the results obtained using the one-dimensional equations to the work done by Chung and Smith.

Utilizing Eqs.(43) - (47), we now have a means of distributing the chemical heat release and radiative heat loss along the combustor length, without going into the details of a chemical reaction analysis. The use of the radiative heat loss equations is self-explanatory when it is noted that Chung and Smith list the combustor wall temperature as 2089 °K. The chemical heat release equation, however, requires some explanation. To use the S-shaped exponential curve shown in Eqs.(43) - (44), we have to determine the variables z_1 , B_1 , and B_2 . Since a plot of percent combustible coal consumed versus z location was available for this case; z_1 was originally set equal to 1.5 m., the total combustor first-stage length, since only 78% of the combustible coal was consumed at this location. Chung and Smith noted that this two-stage configuration would have trouble consuming all of the combustible coal in a finite length, since only 80% would be consumed if the first stage were extended to 2.4 m. Now, with z_1 determined, B_1 and B_2 were originally taken as 2 and 12 respectively. (These values were chosen to yield the required distribution after an analysis was performed to determine their affect on the

results obtained). Values for the total chemical heat released, H , were then chosen which would lead to the desired temperature, pressure, and velocity at the exit, as stated by Chung and Smith. The value yielding the best results was:

$$H = 376.53 \frac{\text{cal.}}{\text{gm.}}$$

Chung and Smith give a heating value for the coal of:

$$HV = 10262 \frac{\text{Btu.}}{\text{lb. coal}} = 5705 \frac{\text{cal.}}{\text{gm. coal}}$$

This seems to be a reasonable value, after checking the works by Smith and Stinson [10] and Wilson and Wells [11]. Since Chung and Smith claim that only 30 percent of the flow through the combustor is comprised of coal, we can determine a combustor efficiency as follows:

$$H = HV (0.30)\eta \quad (48)$$

For this case, we obtain:

$$\eta = 0.22$$

Since only a percentage of the combustible coal is consumed, a more accurate value for the combustor efficiency could be obtained as follows:

$$H = HV (0.30) (\% \text{ coal consumed}) (\eta_t) \quad (49)$$

where, in this case, 78% of the combustible coal is consumed for the combustor length specified. This yields a true efficiency for the combustor of:

$$\eta_t = 0.283$$

Thus, a true efficiency of only 28.3 percent was obtained. While this value seems very low for a combustor efficiency, it is noted here that the purpose of this first stage was not to completely burn the coal and air entering. Rather, it was to serve as a

gasifier stage to form a hot fuel gas to be completely burned in the second stage of the combustor. (Recall the rather low equivalence ratio given by Chung and Smith for this fuel-rich mixture).

Even though the one-dimensional solutions obtained were in agreement with the results given by Chung and Smith; the temperature and velocity distributions as functions of z obtained did not closely match their results. To obtain the initial jump undergone by the temperature, z_1 was varied while maintaining B_1 , B_2 , and H constant. A final value of z_1 equal to 0.15 m. was chosen to best match the results given by Chung and Smith. Recall that z_1 specifies the position of complete combustion. It is noted here, that while only 78% of the combustible coal was consumed at the combustor total length of 1.5 m., 60% was already consumed at 0.15 m. Even though the combustor configuration chosen has difficulty in consuming all of the available coal within a given length, it is seen that the majority of the reaction occurs within the first 0.15 m.

With z_1 and H now determined, B_1 and B_2 were varied slightly to determine their affect on the solutions obtained. Varying B_1 and B_2 would result in changes to the final velocity, pressure, temperature, and density of less than 10 percent. The distributions of temperature, and velocity as functions of z , on the other hand, could be brought closer to the results of Chung and Smith in this manner. The final results were obtained with the values:

$$B_1 = 2 \quad B_2 = 8 \quad z_1 = 0.15 \text{ m.}$$

Temperature and velocity profiles comparing the results obtained using our quasi-one-dimensional analysis with the results obtained by Chung and Smith (using a complete chemical reaction analysis) appear on pages 47 and 48, respectively.

III.2 Single-Stage Combustor

Chung and Smith also give results for a typical single-stage combustor. This combustor has a diameter of 0.56 m. and an overall length of 1.5 m. It also operates at a constant pressure of 8 atm. with an air inlet temperature of 1866 °K. While likewise consuming approximately 1 kilogram of coal per second, this combustor operates with a nearly stoichiometric fuel to air mixture. The stoichiometric ratio is given as 0.9491. As with the first-stage case, Chung and Smith provide curves of gas temperature, velocity, and percent coal consumed versus axial distance along the combustor. The above figures and information yield the initial variables needed for our quasi-one-dimensional equations; namely, the initial pressure, temperature, velocity, area, and change in area. The properties involving the chemistry of the problem, that is, the values for k , γ , W , and c_p were again chosen as constant global values.

Chung and Smith state that the single-stage combustor seems to burn most of the coal within the finite combustor length, due to the rapid devolatilization of the coal particles possible at such high temperatures. Therefore, the variable z_1 (which is the location of total combustion) was chosen as the combustor total length of 1.5 m. The constants in the exponential distribution curve, B_1 and B_2 , were again chosen to yield variations in temperature and velocity versus axial position along the combustor which were similar to the results of Chung and Smith. The values yielding the best results in this case were:

$$B_1 = 6 \quad B_2 = 20 \quad z_1 = 1.5 \text{ m.}$$

The value for the total chemical heat released which yielded results closest to that of the reference is:

$$H = 382.69 \frac{\text{cal.}}{\text{gm.}}$$

For this single-stage combustor case, we are given that the flow initially contains 12 percent coal. Therefore, a combustor efficiency can be found to be:

$$H = HV (0.12)\eta \quad (50)$$

where we obtain:

$$\eta = 0.56$$

Since 100% of the combustible coal is consumed by the end of the combustor, we have:

$$\eta_t = \eta = 0.56$$

Yielding an overall efficiency for the combustor of 56 percent.

Temperature and velocity profiles obtained utilizing the one-dimensional equations as they appear in Table I (and the chemical heat distribution and radiative heat loss equations as defined above), can be found on pages 49 and 50, respectively. For this combustor, the flow-field calculations were also performed assuming zero heat loss (adiabatic case), to see the affects that radiative heat transfer would have on the final solutions. These results also appear on the temperature and velocity curves. For this single-stage combustor, Chung and Smith list an outlet temperature of 2856.8 °K assuming heat losses due to radiation. The program developed using the quasi-one-dimensional approach obtains an exit temperature of 2877.9 °K when the radiative heat loss equation given by Heywood and Womack, Eq.(45), is employed. When assuming the combustor operates

adiabatically, the exhaust temperature is given as 3001.8 °K. Thus, we can see that the radiative heat losses incurred do not severely degrade the efficiency of the combustor, even for such large diameter combustors as the one modelled here.

When examining Figs.(1) - (4), we note that the final conditions obtained are close to those values given by Chung and Smith. The results obtained also follow the basic trends shown in the reference. It is noted, however, that there are difficulties in using the S-shaped distribution curve to model the energy released due to chemical reaction. No matter how B_1 , B_2 , and z_1 are varied, it is extremely difficult to model the thermal shock which occurs initially when the coal particles and oxidant ignite. This can be seen as the dramatic jump that occurs in the temperature and velocity of the gas over the first 0.2 m. of combustor length. It can be found, when examining the literature, that it is generally the case that the majority of the reaction occurs over a very small time (and space) interval. Therefore, to model this phenomenon within the combustor more precisely, a chemical equilibrium code was employed. This code was used to provide more precise information on the values of k , γ , W , and c_p , and their changes with respect to axial location. The heat of reaction term, H , could now also be calculated in a more precise manner. A description of this program appears in the next section.

IV. CHEMICAL EQUILIBRIUM CODE

The reactants for a coal-fired MHD combustor fall into the same category as those required for standard electrical power generation. A hydrocarbon fuel, in this case coal, with a given chemical analysis and heating value is burned in a preheated air or air/oxygen mixture. For MHD applications, a small amount of potassium seed, usually in the form of K_2CO_3 , is also injected into the flow. For particular combustors, this fuel, air, and seed mixture may also be accompanied by some given amount of water.

Coal, upon analysis, is found to be an extremely complex chemical compound. Therefore, an existing chemical equilibrium code was employed to obtain a detailed account of the chemical species resulting from the combustion of coal. This equilibrium code will be described in this section. For a more complete discussion of the equations used by this code, the reader is directed to the reports by Gordon and McBride [12], and Svehla and McBride [13].

This Fortran IV computer program has the ability of calculating the thermodynamic and transport properties of rather complex mixtures. Thermodynamic data for a large number of ideal gases and condensed species are provided with the program for a temperature range of 300 to 5000 °K. Transport data are also provided; and for many cases, over a wider range. Some of the calculations which this code is capable of performing are:

- (i) chemical equilibrium for assigned thermodynamic states,
- (ii) theoretical rocket performance for both equi-

librium and frozen compositions during expansion,

- (iii) incident and reflected shock properties,
- (iv) Chapman-Jouguet detonation properties.

Condensed species, as well as gaseous species, are considered in the thermodynamic calculations. Only gaseous species, however, are considered in the transport property calculations. When using this program, it is noted that the range of applicability of these thermodynamic calculations is approximately described by the limits of applicability of the ideal gas law. In all of these cases, this program utilizes the international systems of units (SI units). To apply this program to our one-dimensional study on coal combustion we will primarily be interested in the code's chemical equilibrium capabilities.

Chemical equilibrium can be described by either specifying equilibrium constants or the minimization of free energy. This code has chosen to use the free-energy minimization formulation. The conditions for equilibrium may be stated in terms of any of several thermodynamic functions such as the minimization of the Gibbs free energy or Helmholtz free energy or the maximization of entropy. Thermodynamic states may be specified by assigning any of the following pairs of thermodynamic state functions:

- (i) temperature and pressure,
- (ii) enthalpy and pressure,
- (iii) entropy and pressure,
- (iv) temperature and volume or density,
- (v) internal energy and volume or density,
- (vi) entropy and volume or density.

The two equilibrium processes that would substantially aid in our flow-field calculations are the constant temperature and pressure (TP) and constant enthalpy and pressure (HP) processes.

For the TP process, a schedule of one or more assigned temperatures and pressures may be specified. Chemical equilibrium is then allowed to occur at each of these specified temperature and pressure positions. Such a process could be very useful in constructing a Mollier diagram.

When the program is run in the HP mode, the heat of formation of each reactant (as input or as computed) is multiplied by its specified mole fraction. These terms are then summed to yield the total enthalpy for the reactants. Chemical equilibrium is then calculated for that total enthalpy term and each specified pressure. This calculation is valuable, in that it defines the adiabatic flame temperature for the given pressure and initial reactants.

The thermodynamic properties which result from these processes are printed out in tabular form. They include the mixture's pressure, temperature, density, enthalpy, entropy, molecular weight $(\partial \ln V_c / \partial \ln p)_T$, $(\partial \ln V_c / \partial \ln T)_p$, specific heat at constant pressure, isentropic exponent, sonic velocity, and composition. The calculated transport properties are viscosity and thermal conductivity. The specific heat and thermal conductivity are calculated for both frozen and equilibrium conditions. Prandtl and Lewis numbers are also included.

The intended purpose of this section was not to cover in detail the equations and numerical techniques used in the calculations of

these thermodynamic properties; but rather to give a brief description of this equilibrium code and show its usefulness in the MHD combustor problem at hand. The following equations, however, have been reproduced here in an attempt to clarify some of the terms derived in Section II. Gordon and McBride define the velocity of sound, a , as follows:

$$a^2 = \left(\frac{\partial p}{\partial \rho} \right)_S = \frac{p}{\rho} \left(\frac{\partial \ln p}{\partial \ln \rho} \right)_S = \frac{-p}{\rho} \left(\frac{\partial \ln p}{\partial \ln V_c} \right)_S \quad (51)$$

where all of these terms have previously been explained. From standard Bridgman tables, it can be shown that:

$$\left(\frac{\partial \ln p}{\partial \ln V_c} \right)_S = \frac{c_p}{c_p \left(\frac{\partial \ln V_c}{\partial \ln p} \right)_T + \frac{pV_c}{T} \left(\frac{\partial \ln V_c}{\partial \ln T} \right)_p^2} \quad (52)$$

This may be rewritten as:

$$\left(\frac{\partial \ln p}{\partial \ln V_c} \right)_S = \frac{c_p}{c_v \left(\frac{\partial \ln V_c}{\partial \ln p} \right)_T} \quad (53)$$

where:

$$c_v = c_p + \frac{\frac{pV_c}{T} \left(\frac{\partial \ln V_c}{\partial \ln T} \right)_p^2}{\left(\frac{\partial \ln V_c}{\partial \ln p} \right)_T} \quad (54)$$

Using the symbols:

$$\gamma_S \equiv \left(\frac{\partial \ln p}{\partial \ln \rho} \right)_S \quad (55)$$

and:

$$\gamma \equiv \frac{c_p}{c_v} \quad (56)$$

Eq. (53) may be rewritten as:

$$\gamma_S = \frac{-\gamma}{\left(\frac{\partial \ln V_c}{\partial \ln p}\right)_T} \quad (57)$$

Using the equation of state, Gordon and McBride then express the sonic velocity as:

$$a = \sqrt{nRT\gamma_S} \quad (58)$$

where n is the total number of moles and R is the gas constant on a molar basis.

Comparing these equations to the ones derived in Section II, we note that here γ represents the ratio of sensible specific heats, just as it does in our one-dimensional equation development. The term γ_S defined by Gordon and McBride is seen to be the term k used in Section II. Therefore, we note that this equilibrium code will provide us with precise values of γ and k , along with the other required information related to chemical reaction, needed for our combustor analysis. The method in which this program will be utilized will be fully explained in the next section.

Others have utilized this chemical equilibrium code as well. For another approach in the use of this program to model combustor and heater components with MHD applications, see the work of Sacks, et. al. [14].

V. PERC CASE STUDY

In this section, the quasi-one-dimensional flow-field equations will be utilized, along with the chemical equilibrium code, to model a MHD coal combustor currently under test at the Pittsburgh Energy Research Center, Pittsburgh, Pennsylvania. This combustor is to eventually be installed in the Component Development and Integration Facility currently under construction in Montana. (Recall the report authored by Jackson describing this facility). A complete technical report containing the operating conditions of this combustor can be found by Kurtzrock and Bienstock [15]. A brief discussion of this combustor follows.

V.1 Combustor Description

PERC has advocated high slag rejection using staged combustion as a technique to assure high recoverability of potassium seed and reduce downstream design and material problems resulting from the presence of molten coal slag. Therefore, the degree of ash carryover in the PERC combustor is controlled by adjusting operating parameters, such as coal particle size range and air velocity.

The configuration chosen by PERC was that of a two-stage combustor. The first stage acts as a slagging gasifier, operating at 50 to 54 percent of stoichiometric air. This section is actually a vertical cyclone with an axially located slag tap and discharge throat (vortex finder). Preheated air at 2050 °K is fed into the gasifier through a scroll-shaped side entry in a path essentially tangent to the outer wall of the scroll. Pulverized coal at room temperature is fed into the scroll at a

rate of approximately 6000 kg./hr. inside the airstream; that is, on a shorter radius which could be considered as a secant referenced to the scroll diameter. Separation of the coal slag is obtained in this section by the cyclonic fluid motion, employing the vortex flow principle. Good separation (greater than 90 percent) is claimed by PERC to depend on a set of interrelated design parameters. They include the first-stage geometry, operating temperature, stoichiometry, fuel particle size, gas velocities, and viscosity-temperature characteristics of the slag.

The hot fuel gas created in the gasifier leaves through the gasifier throat and passes through an interstage connection which conducts the gas to the second stage horizontal combustor. PERC states that this combustor configuration was chosen for two reasons. First, as the gasifier stage is vertical, a turn had to be made to mate with the horizontal MHD generator. Second, this configuration was seen to provide a simple but effective way to mix the oxidant with the fuel gas while at the same time using the oxidant at a velocity ratio of 4 to 1 to straighten the swirling flow of the fuel gas from the first stage. The oxidant and any seed that may be used is injected at the bend, and PERC claims that mixing should be complete in less than 0.5 combustor diameters. Upon mixing with the oxidant, the hot fuel gas has entered the second stage at a temperature of approximately 2350 °K. This stage operates as a combustor at a pressure of 6 atm. and an overall system stoichiometry of 95 percent. It is approximately 1.45 m. long, with a cross-sectional diameter of 0.6 m. The resulting hot plasma exits this stage at a temperature of 2870 °K and Mach

number of 0.05. The flow is then accelerated through a nozzle to raise the Mach number to 0.3 before entering the generator channel. A sketch of this combustor drawn to approximate scale can be found on page 51. Again, it is noted here that the quasi-one-dimensional flow-field equations previously developed would fail locally in the mixing region. This is primarily due to the assumptions used when deriving these equations. They would, however, offer good results when applied in the combustion region, assuming that mixing of the hot fuel gas and oxidant is completed by this stage. With this in mind, we can proceed to model the second stage of this two-stage combustor.

V.2 Model Assuming Adiabatic Process

The PERC combustor was chosen for this case because of the extensive information available on its operating conditions. In beginning this calculation, it was necessary to determine the composition of the hot fuel gas entering the second stage elbow combustor. The PERC report provided information on the species concentrations of this hot fuel gas in terms of mole fractions. These values have been reproduced, and can be found in Table II, page 45. Knowing these initial values, and recalling that PERC states that the second stage operates at an overall system stoichiometry of 95 percent, we are now able to completely define the total initial reactants in terms of their mole fractions. Noting that the hot fuel gas enters the second stage at 2350 °K and the extra oxygen enters at 298 °K (room temperature), we are now prepared to use the chemical equilibrium code explained earlier.

Specifying the mole fractions of the total initial reactants at their given input temperatures, and an equivalence ratio at which the reaction is to occur; the equilibrium code was then run in the HP mode previously described. This calculation yielded the following result:

$$T_{AF} = 2908 \text{ }^\circ\text{K}$$

where T_{AF} represents the adiabatic flame temperature. This is the gas temperature that we would obtain if the following assumptions were made:

- (i) the velocity of the gases and condensed phases is small enough so that the contribution of kinetic energy to an overall energy balance is negligible (thereby representing the combustor energy as completely random thermal energy),
- (ii) the combustion occurs as an isobaric process,
- (iii) the combustion products are gases and, in particular, behave like perfect gases,
- (iv) the combustion process is adiabatic.

The first three assumptions are generally reasonable for a combustor problem of this type, while the fourth one is a more idealistic approximation. This assumption presumes that there is no heat transferred to or from the gas during reaction. Therefore, the entire enthalpy of reaction would be utilized in raising the temperature in the chamber. This value is useful since it represents a theoretical ideal with which to compare actual results.

Once this had been done, the chemical code was then run assuming a constant temperature and pressure process. While

the pressure was maintained constant at 6 atm., the temperature was varied from 2200 °K to 3400 °K in increments of 100 °K. The values obtained at these positions; that is, the mixture's molecular weight, specific heat, isentropic exponent, and $(\partial \ln V_c / \partial \ln p)_T$ were all stored on data files. Values for the individual species' enthalpies and mole fractions were also stored on data files. These values were to be used to furnish the detailed information necessary to determine the variables W , c_p , k , dk , γ , $H_i(T)$, and c_i' and c_i'' as functions of the combustor axial distance. (These variables were defined previously in Section II). With this information available, a more complete analysis of the actual chemical reaction undergone by the combustor could now be performed. Of course, the basic assumption made in using this chemical equilibrium code to model these combustor parameters is that the chemical reactions defining the combustion of these gases occur at infinitely fast rates. This is also assumed true for any recombination or dissociation that may take place. Therefore, the gases in the combustor are said to achieve chemical equilibrium instantaneously at each location along the combustor's length; and we will not concern this analysis with finite-rate reaction techniques.

Starting with the definition describing the adiabatic flame temperature, as given by Sforza [16], we have:

$$\Delta Q = \sum c_i'' H_i(T_{AF}) - \sum c_i' H_i(T_O) = 0 \quad (59)$$

where T_O is the initial temperature of the reactants, and the other variables are as previously defined. Subtracting the

following quantity from both sides of the above equation:

$$\sum c_i' H_i(T_{AF})$$

we obtain, with a little manipulation:

$$\sum (c_i'' - c_i') H_i(T_{AF}) = \sum c_i'' [H_i(T_0) - H_i(T_{AF})] \quad (60)$$

Noting that the right-hand side of this equation is equivalent to the expression given by Eq.(37), we obtain the final result:

$$\Delta H = \sum c_i' [H_i(T_0) - H_i(T_{AF})] \quad (61)$$

which defines the chemical heat release term. Referring back to Table II, we see that the c_i' have been given for this case. Therefore, this form of the equation will be used to describe the heat release due to chemical reaction.

In reviewing the existing literature on MHD combustors, it has been found that the majority of the reaction was seen to occur within finite distance down the combustor length. When comparing temperature or velocity profiles, as given by Figs.(1) - (4), we see that the majority of the change in these parameters occurs within 10 to 15 percent of the total combustor length. After this initial jump, these values gradually level off to their final results.

Using the information provided by Table II and the chemical equilibrium code, this combustor stage was then modelled utilizing the quasi-one-dimensional equations. In this case, since the adiabatic flame temperature had been calculated; and species enthalpies were known as a function of temperature, a global chemical heat release could be determined for this combustor utilizing Eq.(61). It is noted here that only the species enthalpies of the original nine reacting species were retained as functions of temperature. Therefore, they were the only species

considered when determining the chemical heat release. While other species had formed due to recombination and dissociation; their concentrations over the temperature range at hand were so small as not to warrant their inclusion. It was found that the change in concentration of the initial reactants was the predominant influence on the thermal aspects of the combustion problem. This total chemical heat release was then distributed in a linear fashion, over the first 10 percent of combustor length. Since this case assumed an adiabatic process, there were no radiative heat losses considered. Thus, we have defined the energy terms required to make use of our one-dimensional equations. Frictional losses were considered using the tables of friction factors supplied by Heywood and Womack. Changes due to drag and area change were assumed negligible for this case.

With this information, the one-dimensional equations were used to calculate new values for the dependent variables as they are listed in Table I. These calculations were continued, in an incremental fashion, along the entire combustor length. At each station new values of k , γ , and W were used, having been determined as functions of temperature by the chemical equilibrium code. The species mole fractions were also updated in this manner. Since the variations in these properties were smooth, a simple linear interpolation scheme was used to obtain the actual values for these variables at the temperature corresponding to each axial location. Since a large number of points were originally determined for these parameters utilizing the equilibrium code TP process, this linear scheme proved to be both accurate and efficient. It was found to be commensurate with the accuracy

obtained in employing the quasi-one-dimensional flow-field equations.

The results obtained utilizing this model can be seen as Figs.(6) - (7) on pages 52 and 53, respectively. These plots can be seen to follow existing trends. It is noted, that the chemical heat release was confined to the first 0.145 m. of the total 1.45 m. length. This along with the fact that no radiative heat losses were assumed, resulted in the "freezing" of the temperature and velocity after this short distance. That is to say, that the changes in W , k , γ , and c_p were very small from this point on, and could not alter the dependent variables appreciably after this point. This shows that the chemical heat released is a major factor that results in the greatest changes to these variables.

V.3 Model Including Radiative Heat Losses

The above analysis was repeated, this time assuming that after the chemical heat was released adiabatically, radiative heat losses would occur for the remaining length of the combustor. Since a wall temperature for this combustor was not specified, the radiative heat loss equation developed by Heywood and Womack (shown as Eq.(45)) was not used. Rather, PERC specified a total heat loss through this section of approximately 40 cal./gm. This value was distributed linearly along the combustor length. This represents only a small portion of the value obtained for ΔH , which is approximately 350 cal./gm. (Recall that ΔH represents the total heat released due to chemical reaction). Thus we see, as was the case with the Argonne combustor, that the total heat

loss due to radiation is only a small fraction of that heat liberated due to chemical reaction. This has been shown to be the case, even when the combustor diameter has approached one third to one half of the total overall length. This result lends credibility to the adiabatic process previously assumed.

The temperature and velocity plots obtained assuming radiative heat loss can be found on pages 54 and 55. A table comparing the species concentrations obtained at the end of the second stage combustor using the one-dimensional analysis with those values given by PERC appears on page 46. It can be seen that these values are close to those stated by PERC. Discrepancies arise since these concentration values are a function of temperature, and the one-dimensional analysis did not match the exit temperature given by PERC exactly. More will be said about these results in the section to follow.

Fig.(10), which appears on page 56, shows the concentrations of the major species as they vary along the combustor length. The trends shown by this figure are in agreement with the work performed by Chung and Smith.

Fig.(11), which can be found on page 57, was included to show the difference between the values of γ and k , which represent the ratio of sensible specific heats and the ratio of total specific heats, respectively. Thus, a difference between these two variables can be noted for the combustor problem at hand.

It is noted here, for the sake of uniformity, that all of the figures appearing in this work show the results obtained with this process versus axial location. The combustor axial location was denoted as z in the flow-field equation development. All

of the figures denote axial distance down the combustor as x .
These two variables are equivalent in this work.

VI. CONCLUSIONS AND DISCUSSION

In the Argonne case study, the quasi-one-dimensional analysis yielded results that were consistent with the operating conditions given. The method used in evaluating the overall chemical heat released due to reaction was rather cumbersome. While it was a simple task to have the flow-field equations yield the proper results by varying ΔH ; it was difficult to obtain values for B_1 , B_2 , and z_1 for the S-shaped curve that would accurately depict the required distribution of this heat release. Thus, while exit conditions could be obtained to match the values given in the literature, it was a formidable task to obtain the proper variation of these parameters as functions of axial location. To do this, a more accurate method was needed to determine the chemical heat release and any heat losses which might occur.

To improve this situation, an existing chemical equilibrium code was utilized. Now, given a known quantity of initial reactants, it was possible to obtain the required chemical properties needed to model the coal combustor with the flow-field equations developed.

For the PERC two-stage combustor case, it is recalled that an adiabatic flame temperature of 2908 °K was obtained with the equilibrium code. When the quasi-one-dimensional equations were utilized with a linear chemical heat distribution as described earlier; both the adiabatic and radiative heat loss cases resulted in a value of 2850 °K at this location. For the adiabatic case, this temperature remained constant until the end of the combustor. This was due to the fact that the chemical

heat release due to reaction was assumed complete and there were no heat losses to diminish this temperature. For the case allowing for radiative heat losses, the final temperature obtained at the combustor exit was 2806 °K. The exit temperature specified by PERC was 2870 °K.

PERC also listed an exhaust Mach number of 0.05 at a pressure of 6 atm. The results obtained for both the adiabatic and heat loss cases were 0.07 and 5.99 atm., respectively. Thus, it can be seen that the flow-field equations developed can accurately predict the actual results.

Upon examination of the one-dimension equations derived, it is seen that the variables dk and dH actually refer to differences between the final and initial values of these parameters. While these variables are required to determine the final temperature (for each increment over which the one-dimensional equations were applied), their actual final values are not known until this temperature is obtained. In the case of the term dk , the values used lagged the calculation by one increment. In other words, dk was represented as the initial k minus the final k of the previous step. This was viewed as acceptable since a curve of k versus temperature proved to be smooth, and the incremental step chosen was very small. For the dH term, a global chemical heat release was initially calculated assuming that the reaction proceeded to the adiabatic flame temperature within a specified distance down the combustor length. This value was chosen as being on the order of 10 percent of the total length. The total chemical heat release obtained, as calculated by Eq. (61), was then distributed

over this specified length. An adiabatic process, or one allowing for radiative heat losses was then assumed to occur from this specified length until the end of the combustor. The results obtained in this manner have been shown to conform well with expected exit parameters.

A possible way of improving on these results would be to set up some sort of prediction-correction iterative scheme. An initial value for the final temperature could be assumed. Exact values for dk and dH (making use of Eq.(34)) could then be obtained. These values could then be used by the flow-field equations to actually calculate the final temperature. This process could continue in an iterative fashion at each incremental step until the initially assumed value for the final temperature was within a given tolerance of the calculated final temperature.

REFERENCES

1. R.F. Grundy, Magnetohydrodynamic Energy For Electric Power Generation (New Jersey: Noyes Data Corporation, 1978).
2. W.D. Jackson, "Design of the Montana Magnetohydrodynamics Component Development and Integration Facility", Twelfth Intersociety Energy Conversion Engineering Conference, 988-995 (1977).
3. J.B. Dicks, K.E. Tempelmeyer, J.F. Martin, J.W. Muehlhauser, L.W. Crawford, Y.C.L. Wu, H.P. Markant, "A Description of the Direct Coal-Fired MHD Test Facility at the University of Tennessee Space Institute", Twelfth Intersociety Energy Conversion Engineering Conference, 995-1004 (1977).
4. A.H. Shapiro, The Dynamics and Thermodynamics of Compressible Fluid Flow (New York: Ronald Press, 1953).
5. S.S. Penner, Chemistry Problems in Jet Propulsion (New York: Pergamon Press, 1957).
6. P.M. Chung and R.S. Smith, "An Analysis of a High-Temperature Coal Combustor According To A One-Dimensional Flow Model", Argonne National Laboratory, Argonne, Illinois (1977).
7. M. Petrick and B. Ya. Shumyatsky, Open-Cycle Magnetohydrodynamic Electrical Power Generation (Illinois: Argonne National Laboratory, 1978).
8. H.B. Palmer and J.M. Beer, Combustion Technology: Some Modern Developments (New York: Academic Press, 1974).
9. J.B. Heywood and G.J. Womack, Open Cycle M.H.D. Power Generation (New York: Pergamon Press, 1969).
10. M.L. Smith and K.W. Stinson, Fuels and Combustion (New York: McGraw-Hill, 1952).
11. P.J. Wilson and J.H. Wells, Coal, Coke, and Coal Chemicals (New York: McGraw-Hill, 1950).
12. S. Gordon and B.J. McBride, "Computer Program for Calculation of Complex Chemical Equilibrium Compositions, Rocket Performance, Incident and Reflected Shocks, and Chapman-Jouguet Detonations", NASA SP-273, NASA Lewis Research Center, Cleveland, Ohio (1971).
13. R.A. Svehla and B.J. McBride, "Fortran IV Computer Program for Calculation of Thermodynamic and Transport Properties of Complex Chemical Systems", NASA TN D-7056, NASA Lewis Research Center, Cleveland, Ohio (1973).

14. R.A. Sacks, H.K. Geyer, S.J. Grammel, and E.D. Doss, "Modified NASA-Lewis Chemical Equilibrium Code for MHD Applications", Argonne National Laboratory, Argonne, Illinois (1979).
15. R.C. Kurtzrock and D. Bienstock, "50 MW(T) Coal-Fired MHD Combustor for Component Development and Integration Facility (CDIF) for the MHD Division of ERDA/Fossil Energy", Pittsburgh Energy Research Center, Pittsburgh, Pennsylvania (1977).
16. P.M. Sforza, "Lectures on Aerothermochemistry", course notes prepared at the Polytechnic Institute of New York, Farmingdale New York (1967).

TABLE I. INFLUENCE COEFFICIENTS FOR QUASI-ONE-DIMENSIONAL FLOW

	$\frac{dA}{A}$	$\frac{dQ - dw_k - dH}{c_p T}$	$\left[\frac{4C_f dz}{D} + \frac{dF_z}{\frac{1}{2}k\rho AM^2} \right]$	$\frac{dw}{w}$	$\frac{dk}{k}$
$\frac{dM^2}{M^2}$	$-2 \left[\frac{\gamma + \frac{1}{2}(\gamma - 1)kM^2}{\gamma - kM^2} \right]$	$\frac{\gamma(1 + kM^2)}{\gamma - kM^2}$	$\frac{kM^2 \left[\gamma + \frac{1}{2}(\gamma - 1)kM^2 \right]}{\gamma - kM^2}$	$\frac{-\gamma(1 + kM^2)}{\gamma - kM^2}$	-1
$\frac{dV}{V}$	$\frac{-\gamma}{\gamma - kM^2}$	$\frac{\gamma}{\gamma - kM^2}$	$\frac{\gamma kM^2}{2(\gamma - kM^2)}$	$\frac{-\gamma}{\gamma - kM^2}$	0
$\frac{da}{a}$	$\frac{(\gamma - 1)kM^2}{2(\gamma - kM^2)}$	$\frac{\gamma(1 - kM^2)}{2(\gamma - kM^2)}$	$\frac{-(\gamma - 1)k^2 M^4}{4(\gamma - kM^2)}$	$\frac{-\gamma(1 - kM^2)}{2(\gamma - kM^2)}$	$\frac{1}{2}$
$\frac{dT}{T}$	$\frac{(\gamma - 1)kM^2}{\gamma - kM^2}$	$\frac{\gamma(1 - kM^2)}{\gamma - kM^2}$	$\frac{-(\gamma - 1)k^2 M^4}{2(\gamma - kM^2)}$	$\frac{(\gamma - 1)kM^2}{\gamma - kM^2}$	0
$\frac{d\rho}{\rho}$	$\frac{kM^2}{\gamma - kM^2}$	$\frac{-\gamma}{\gamma - kM^2}$	$\frac{-\gamma kM^2}{2(\gamma - kM^2)}$	$\frac{\gamma}{\gamma - kM^2}$	0
$\frac{dp}{p}$	$\frac{\gamma kM^2}{\gamma - kM^2}$	$\frac{-\gamma kM^2}{\gamma - kM^2}$	$\frac{-kM^2 \left[\gamma + (\gamma - 1)kM^2 \right]}{2(\gamma - kM^2)}$	$\frac{\gamma kM^2}{\gamma - kM^2}$	0

TABLE II. FIRST STAGE GASIFIER EXIT GAS COMPOSITIONS

<u>Component</u>	<u>Mole Fraction</u>
N ₂	0.489
CO ₂	0.094
CO	0.232
H ₂ O	0.122
Ar	0.006
H ₂	0.054
H	0.001
SO ₂	<u>0.001</u>
	0.999

TABLE III. SECOND STAGE COMBUSTOR EXIT GAS COMPOSITIONS

<u>Component</u>	<u>Mole Fraction</u>	
	<u>PERC*</u>	<u>1-D</u>
N ₂	0.446	0.4653
CO ₂	0.221	0.2208
CO	0.082	0.0927
H ₂ O	0.176	0.1510
O ₂	0.025	0.0225
Ar	0.005	0.0058
H ₂	0.009	0.0093
H	0.003	0.0033
O	0.003	0.0033
OH	0.016	0.0152
NO	0.010	0.0097
KOH	0.005	--
K	0.003	--
SO ₂	<u>0.001</u>	<u>0.0009</u>
	1.005	0.9998

*NOTE: Second stage includes aqueous seed solution.

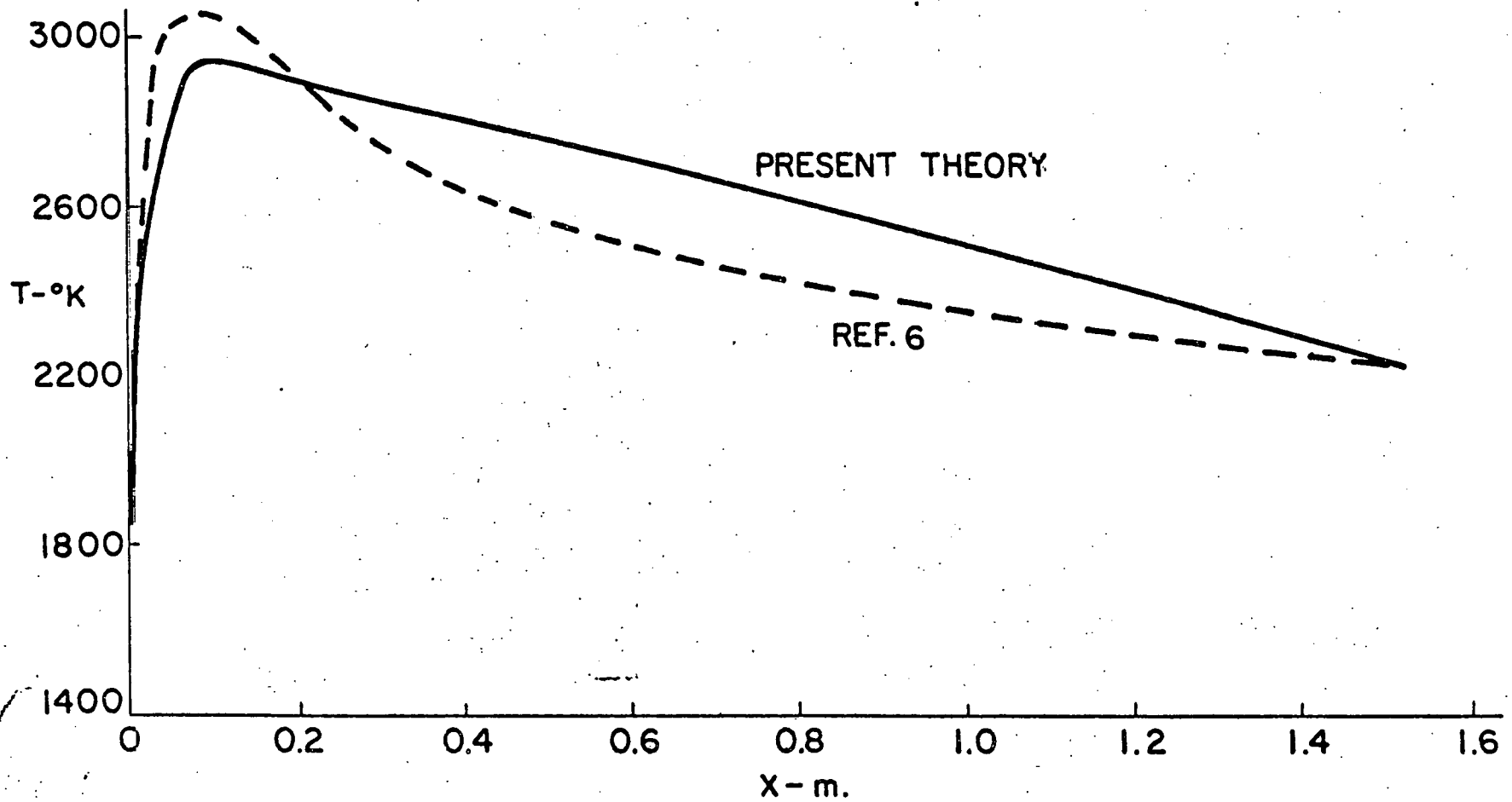


FIG. 1 ARGONNE CASE: FIRST STAGE OF A TWO-STAGE COMBUSTOR

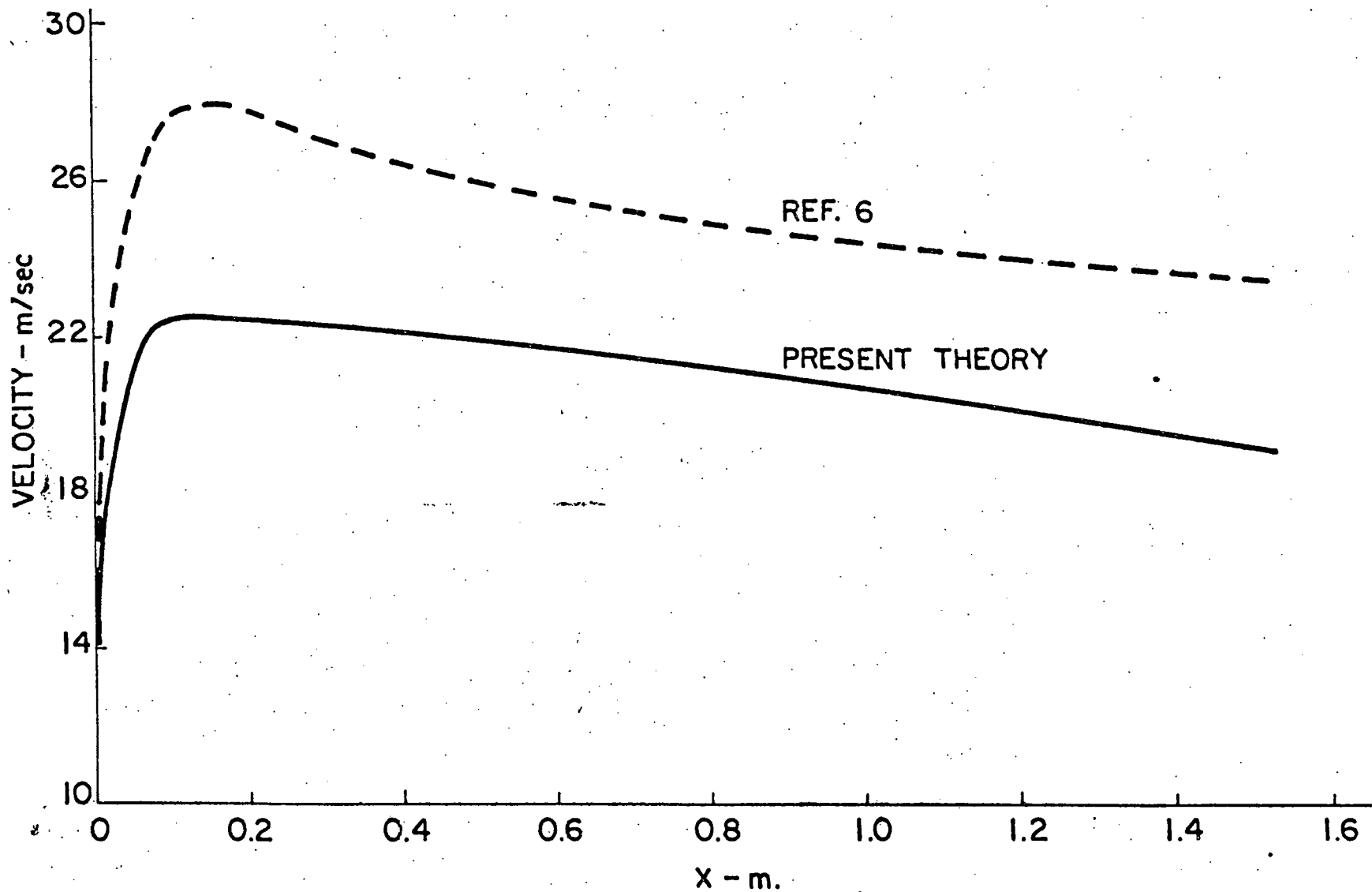


FIG. 2 ARGONNE CASE: FIRST STAGE OF A TWO-STAGE COMBUSTOR

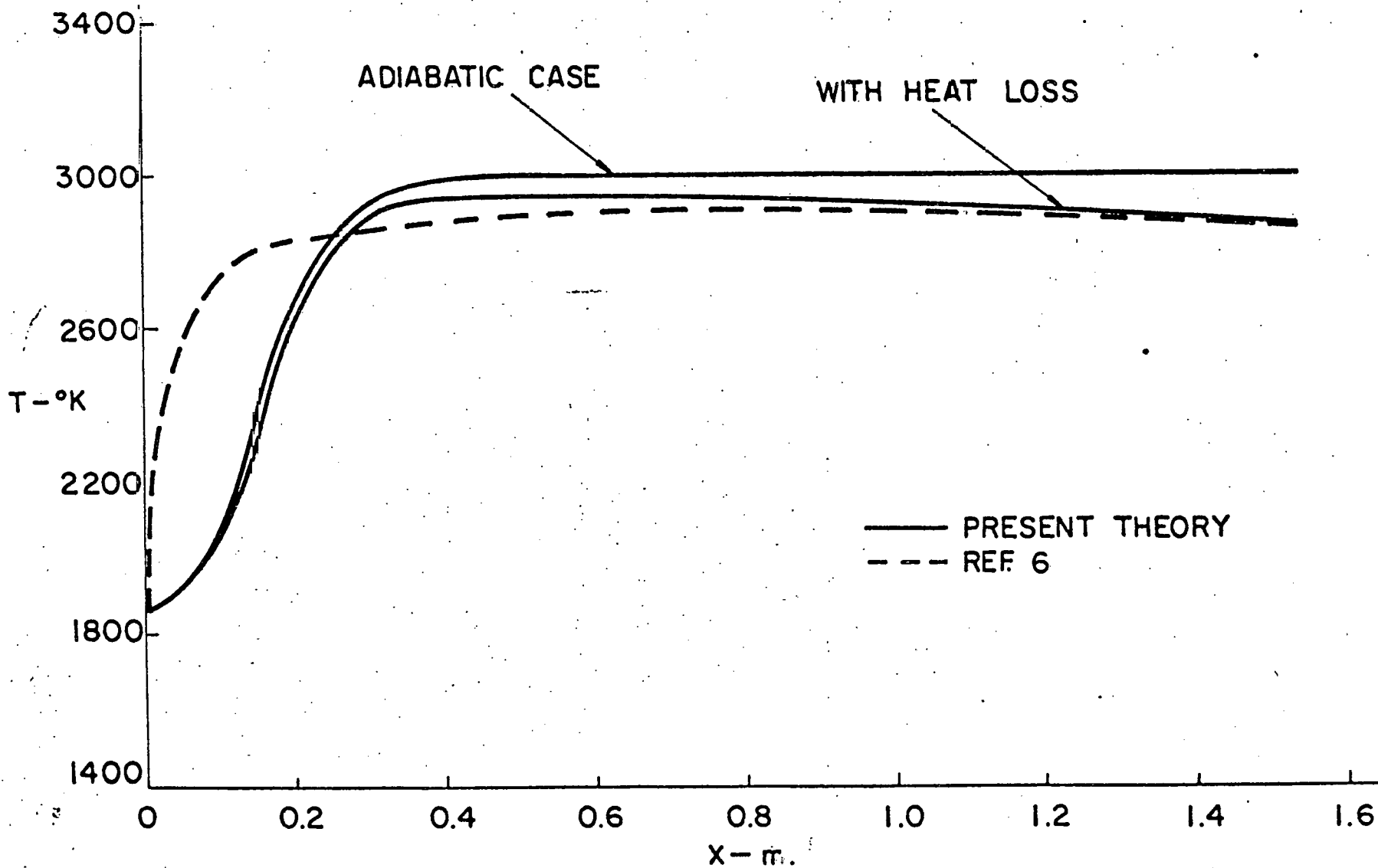


FIG. 3 ARGONNE CASE: SINGLE STAGE COMBUSTOR

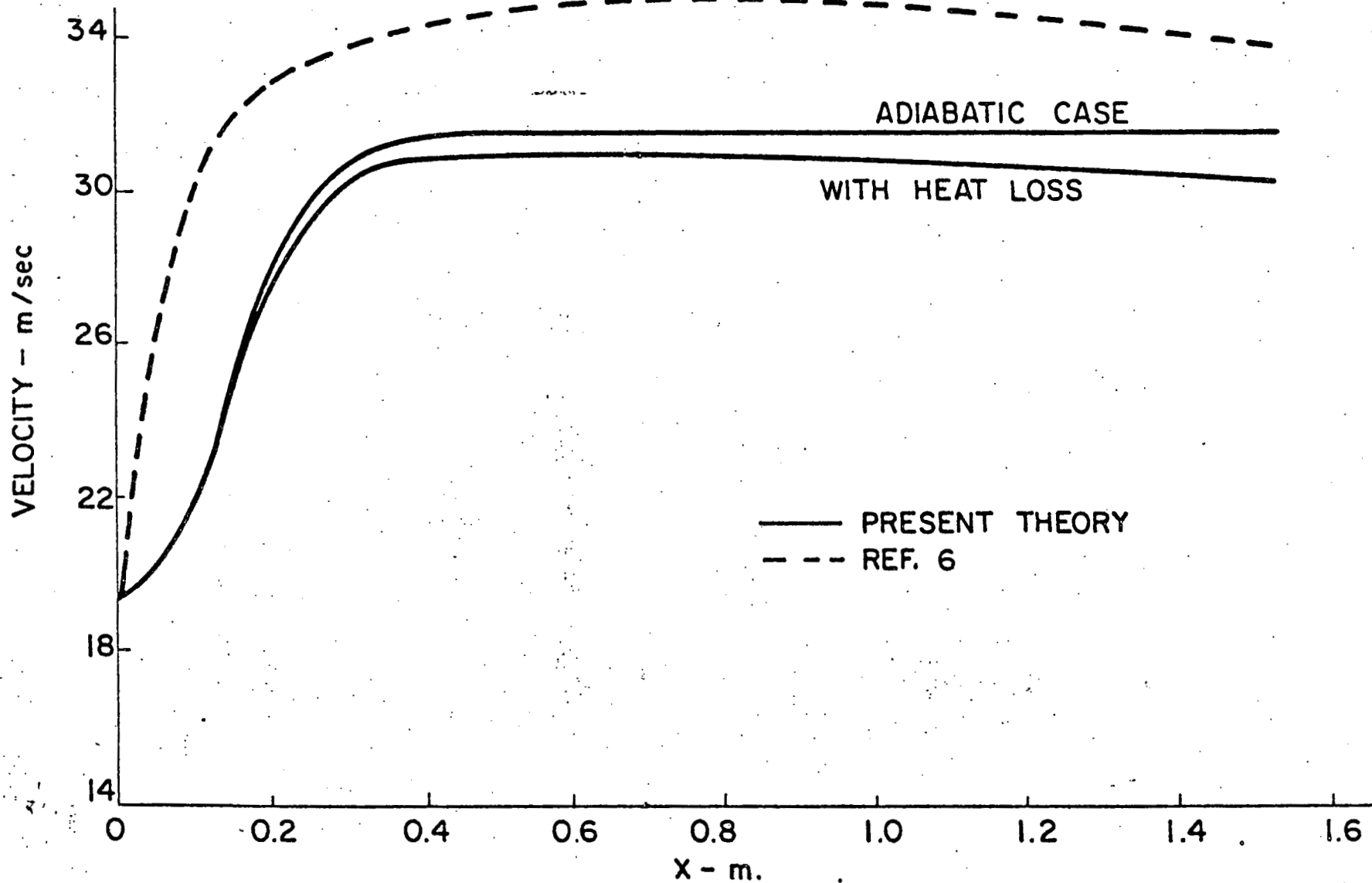


FIG. 4 ARGONNE CASE: SINGLE STAGE COMBUSTOR

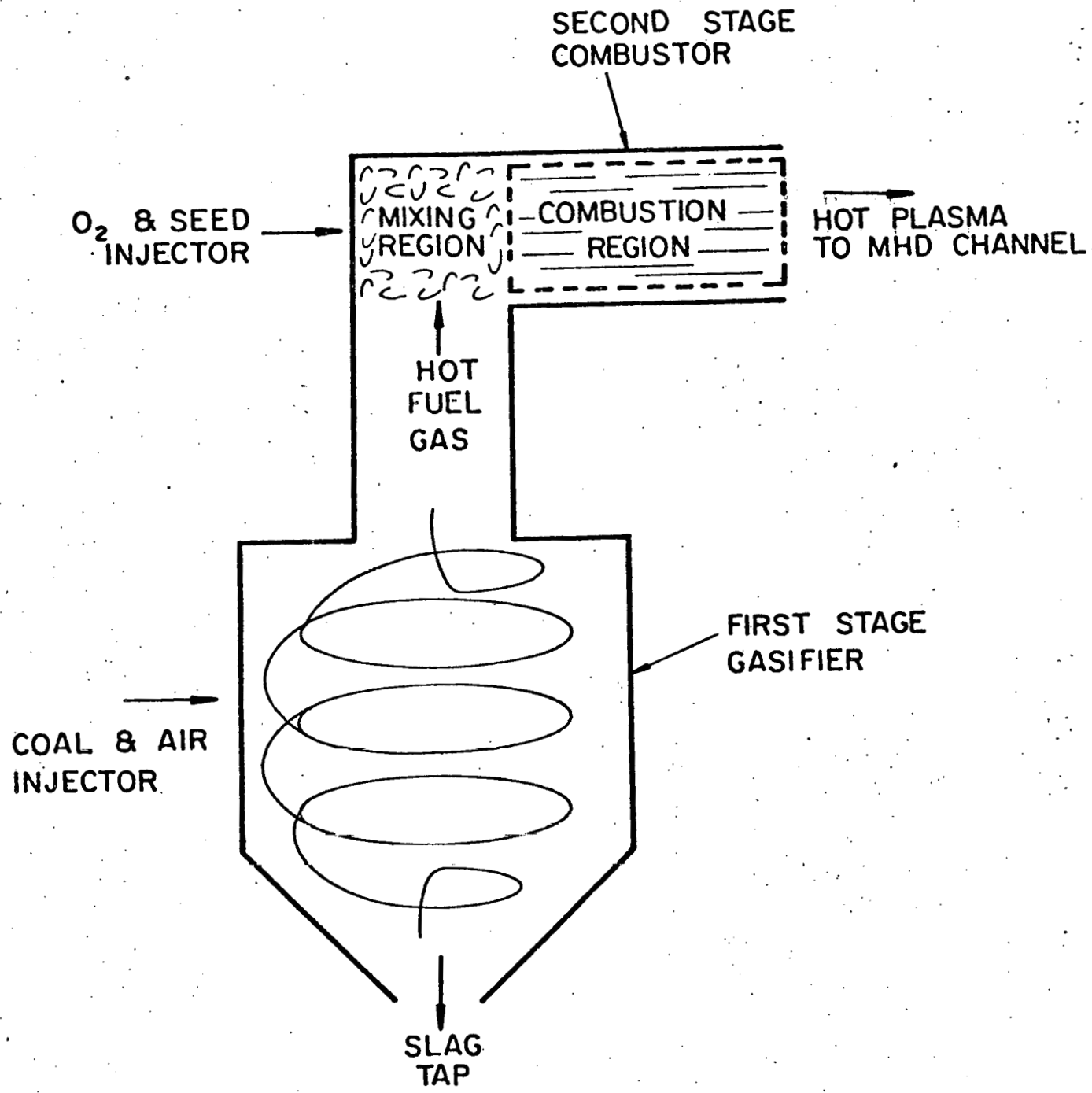


FIG. 5 PERC CASE : TWO-STAGE COMBUSTOR

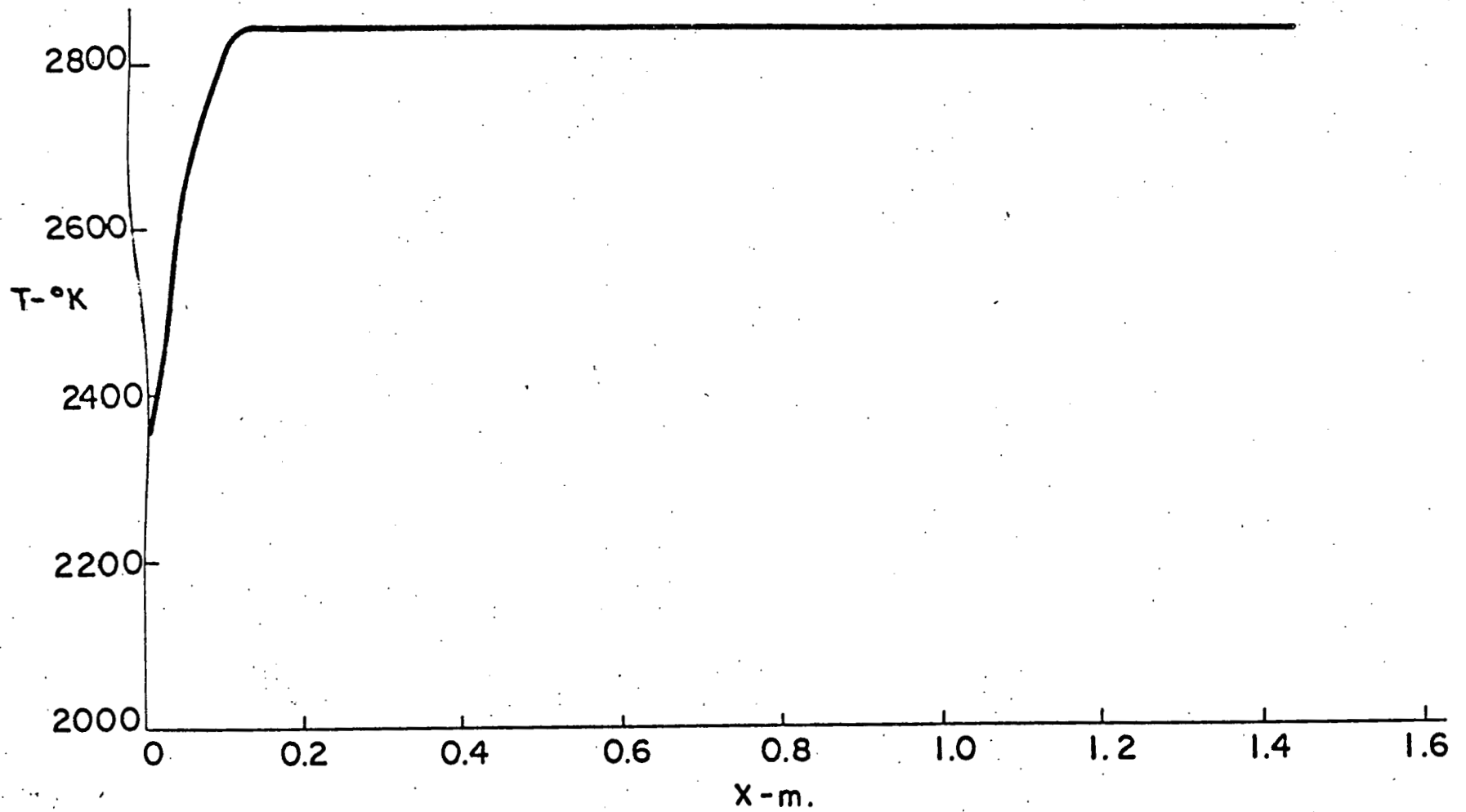


FIG. 6 PERC CASE: ADIABATIC CASE WITH CHEMICAL HEAT RELEASE

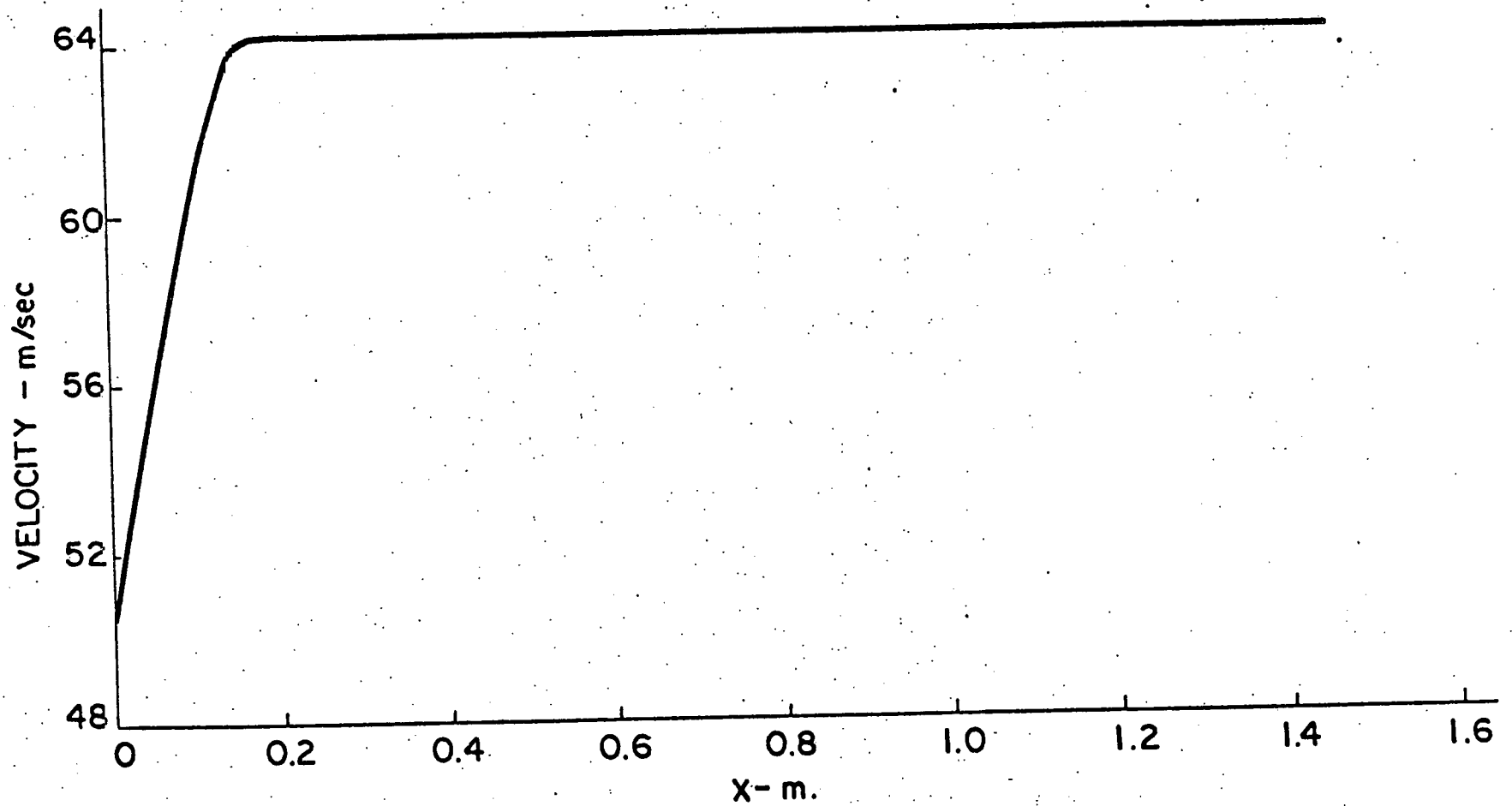


FIG. 7 PERC CASE: ADIABATIC CASE WITH CHEMICAL HEAT RELEASE

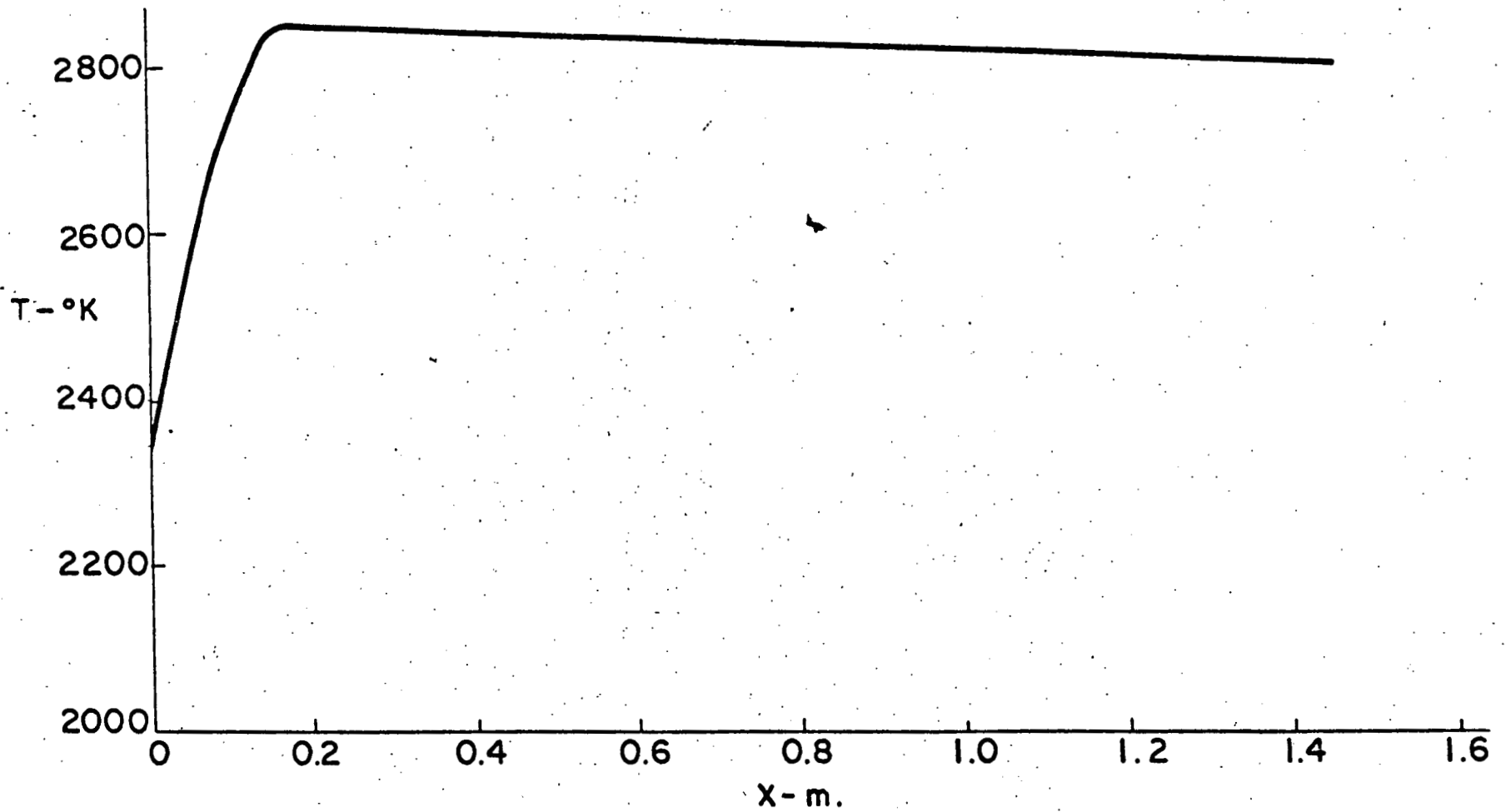


FIG. 8 PERC CASE: CHEMICAL HEAT RELEASE WITH RADIATIVE HEAT LOSS

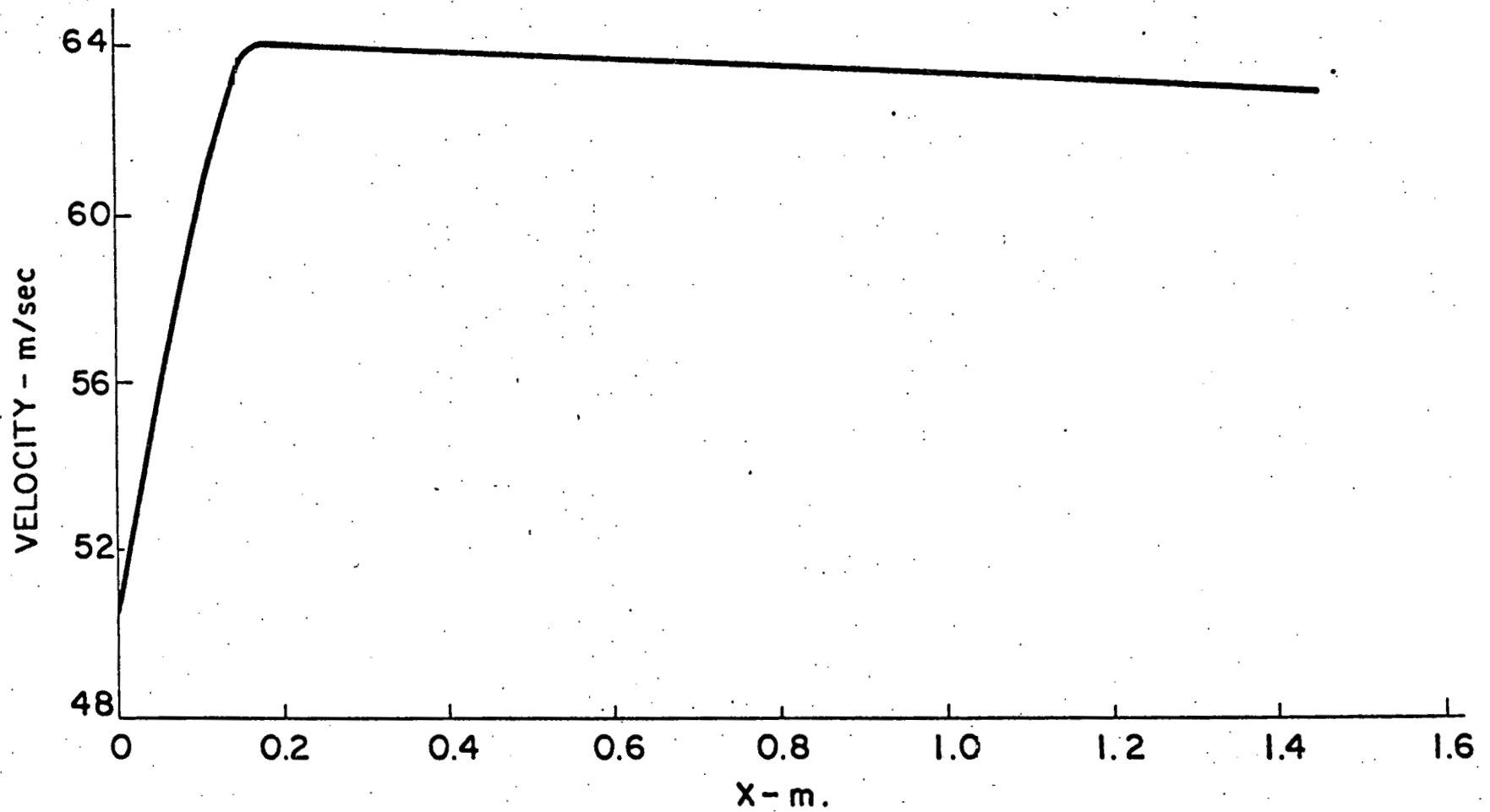


FIG. 9 PERC CASE: CHEMICAL HEAT RELEASE WITH RADIATIVE HEAT LOSS

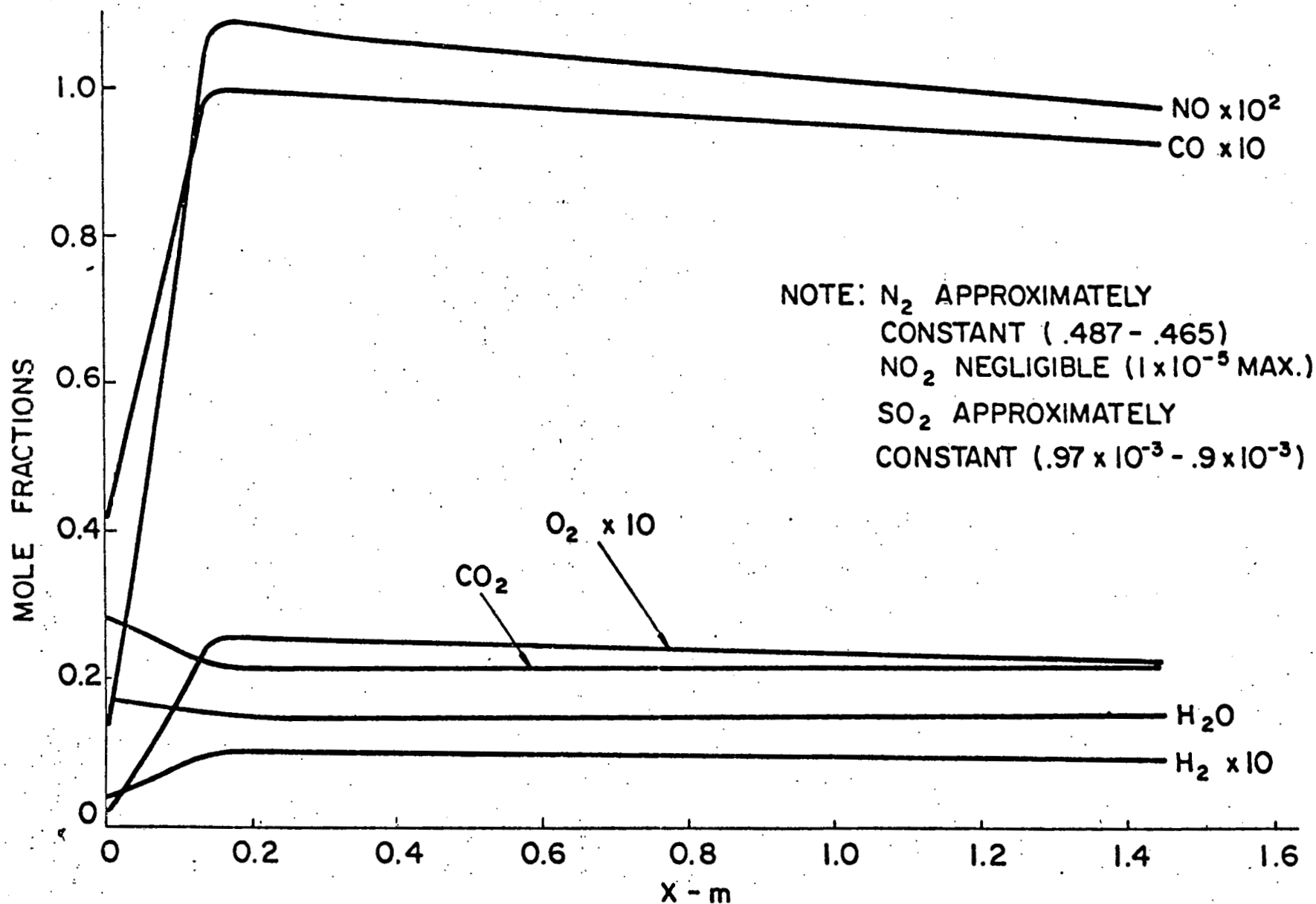


FIG. 10 PERC CASE: SECOND STAGE OF A TWO-STAGE COMBUSTOR

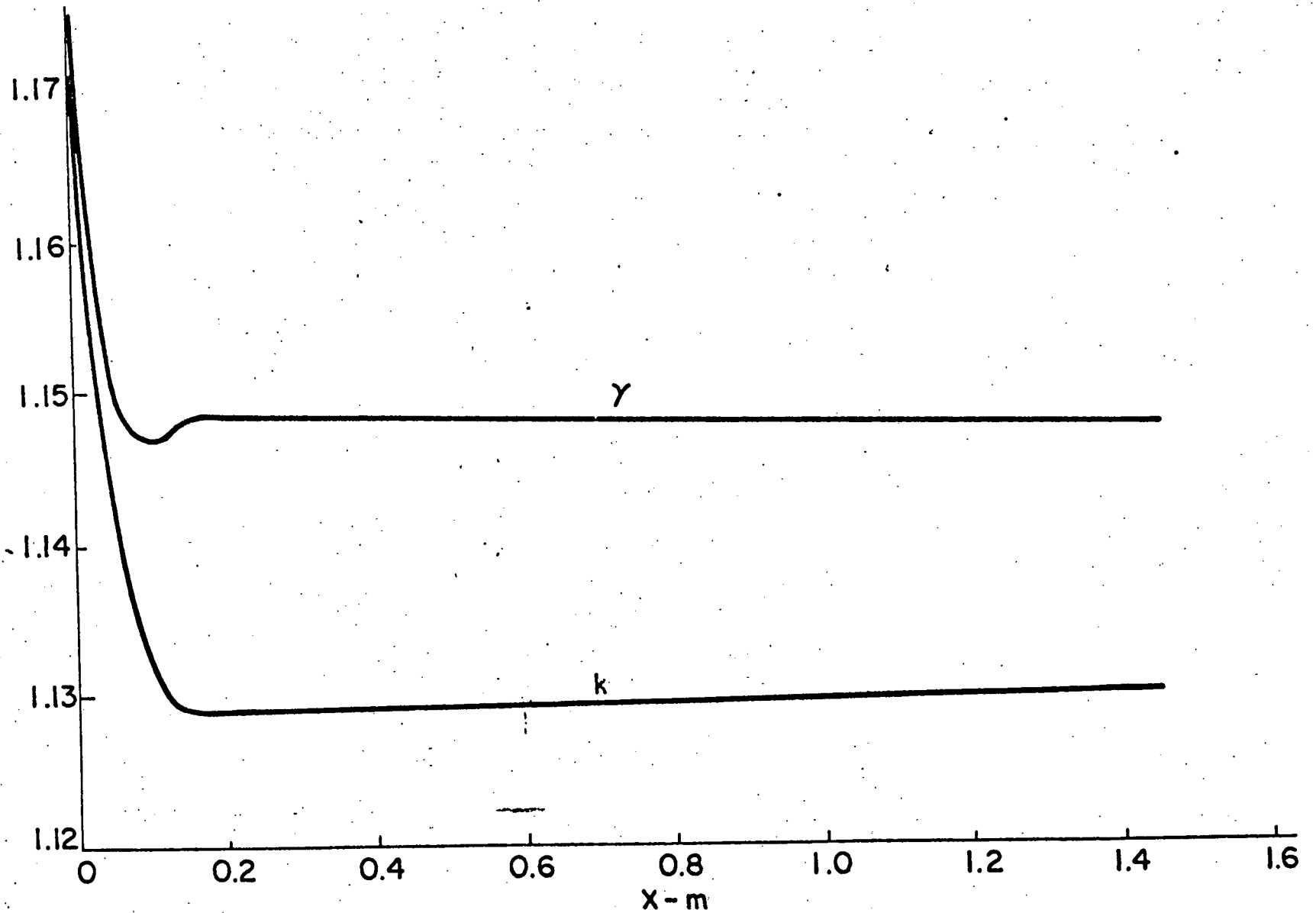


FIG. II PERC CASE: SECOND STAGE OF A TWO-STAGE COMBUSTOR

Polytechnic Institute of New York

Aerodynamics Laboratories

Department of Mechanical
and
Aerospace Engineering

COMPLETE BURNING AND EXTINCTION OF A
CARBON PARTICLE IN AN OXIDIZING ATMOSPHERE

By Moshe Matalon

MAY 1980

U. S. Department of Energy
Contract No. ET-78-C-01-3084

COMPLETE BURNING AND EXTINCTION OF A
CARBON PARTICLE IN AN OXIDIZING ATMOSPHERE

By

Moshe Matalon

Prepared for

U.S. Dept. of Energy
MHD Div. of Fossil Energy
Contract No. ET-78-C-01-3084

May 1980

Polytechnic Institute of New York
Aerodynamics Laboratories
Farmingdale, N.Y. 11735

POLY M/AE Report No. 80-16

TABLE OF CONTENTS

	<u>PAGE</u>
Abstract	i
Introduction	1
Formulation	4
The Reaction Rates	9
Flame at the Interior of the Gas Phase	12
Flame Structure	15
Flame Contiguous to the Particle	20
The Burning Rate	23
Conclusion	26
Appendix	28
References	30
List of Figures	32
Figures	33-42

Complete Burning and Extinction of a
Carbon Particle in an Oxidizing Atmosphere

Moshe Matalon
Aerodynamics Laboratories
Polytechnic Institute of New York
Farmingdale, N. Y., 11735

Abstract

The departure from an equilibrium gas phase behavior is described in order to obtain the rate of mass loss M of a pure carbon particle immersed in an oxidizing atmosphere over a wide range of Damköhler numbers D_g (representing either the particle size or the ambient pressure). Unlike the equilibrium limit ($D_g \rightarrow \infty$) in which M depends solely on the indirect oxidation $C+CO_2$, the present analysis allows a small leakage of oxygen through the flame so that M depends on the direct oxidation $C+O_2$ as well. Furthermore, the structure of a thin but finite flame where the CO oxidation takes place is analyzed and its influence on M is determined. It leads to a minimum value D_g^0 (or particle size) below which the $CO+O_2$ flame cannot persist and the gas phase is necessarily frozen. When the flame exists, it stands at a well defined distance from the particle and in particular it can be adjacent to it; this depends on the particle size and on its surface temperature. Both cases have been analyzed in the present study.

Supported by the U. S. Department of Energy, MHD Division, under Contract No. ET-78-C-01-3084.

INTRODUCTION

The theory of the quasi-steady burning of a carbon particle immersed in an oxidizing atmosphere consists of two basic models (Spalding, 1955). One, first proposed by Nusselt (1924), assumes that the only oxidation occurs at the surface of the particle producing CO and/or CO₂ (the latter is formed at low temperature only). Fig. 1a is a schematic representation of this model when the only product is carbon monoxide. The second model (Fig. 1b) proposed by Burke and Schumann (1934) assumes that carbon is consumed due to the reaction with CO₂ while the CO thus formed reacts with oxygen at a flame sheet to form CO₂ (see also Avedesian and Davidson, 1973).

Research to determine the validity of the models has been carried out by many investigators and summarized by Caram and Amundson (1977). Most of the modelling work starts with a given model and checks the validity of the assumptions. By contrast, their study is based on the conservation laws of mass and energy with surface heterogeneous reactions lumping all the intraparticle effects. In the parameter plane of the surface temperature versus the ambient temperature they were able to determine the regions where solutions of the conservation equations can be found. The present study assumes that the surface temperature T_s is given and in taking this approach the work is more closely related to the current paper by Libby and Blake (1979). Our goal is to determine the burning rate M (the rate of particle mass loss) and its dependence on the heterogeneous Damköhler numbers (D_s , \bar{D}_s) and on the homogeneous Damköhler number (D_g). Note that a relation between M and the Damköhler numbers is indirectly a relation

between M and the particle radius a because D_s and \bar{D}_s are linearly proportional to a and D_g to a^2 .

Libby and Blake (1979) examined both frozen and equilibrium gas phase and determined the burning rate M in each case. For the equilibrium limit they found that M depends solely on the indirect oxidation $C + CO_2$ because the homogeneous reaction was assumed to be infinitely fast and in the absence of oxygen the direct oxidation $C + O_2$ is not active. The maximum value for the burning rate say M_2 , is obtained when the heterogeneous reaction is diffusion controlled. All the values below M_2 are attainable depending on the particle size and the surface temperature. In our treatment of the problem we consider a thin but finite flame for the homogeneous reaction $CO + O_2$ and in particular discuss its structure. When the gas phase Damköhler number $D_g \rightarrow \infty$ we recover the equilibrium limit but as D_g is lowered a departure from equilibrium occurs and the burning rate depends on all three reactions mentioned above (see also Fig. 1). Although it has been recognized that they all play a certain role in the process, the interplay between homogeneous and heterogeneous reactions have not been fully explored. Only limited cases have been discussed (Fendell, 1969).

Another new feature uncovered in the present study is the existence of a minimum D_g^0 below which the oxidation of carbon monoxide is not possible and the gas phase is necessarily frozen. Thus, the burning rate has a minimum value M_{ex} (see Fig. 6) which corresponds to extinction. The other situation corresponding to a weak gas-phase reaction and which for small Damköhler numbers reduces to the frozen limit, will be discussed in a following paper. This case is expected to determine the ignition conditions and as a consequence

the whole response of M versus the Damköhler numbers may be constructed.

In formulating the problem a specification of the different chemical reactions taking place during the process is required. It has been assumed that the primary reactions playing a dominant role are those shown in Fig. 1 and that the heterogeneous reactions are first order, as did Caram and Amundson (1977), Libby and Blake (1979) and others. In general, the temperature at the particle surface T_s is an unknown which must be defined in the course of finding the solution. But for analytic convenience T_s was taken as a given value and therefore the controversy of whether the reaction rates conform a well defined Arrhenius law was avoided. The more precise boundary condition for the temperature given by an energy balance at the particle surface, will be addressed in a later study.

The formulation of the problem is given in the next section after which the method of analysis is discussed. Basically activation energy asymptotics has been employed (Williams 1971, Ludford 1977) in order to confine the gas phase reaction to a thin diffusive-reactive zone which can be analyzed and matched with the convective-diffusive outer flows. The flame structure is similar to the one-dimensional flames discussed by Liñán (1974) and Matalon et al (1979). Note also the work by Buckmaster (1975) and Law (1975) on the analogous problem of droplet combustion of liquid fuels.

FORMULATION

Consider a spherical carbon particle (Fig. 1) immersed in an ambient atmosphere of oxidant-inert mixture. The oxidant in general diffuses towards the particle and two oxidation regions exist; one at the surface where carbon monoxide is formed by the direct ($C + O_2$) and indirect ($C + CO_2$) oxidation of carbon and the other, in the gas phase where CO oxidized to CO_2 . Although the particle size continuously varies as carbon is consumed, the quasi-steady state approximation neglects this effect. Its justification lies in the large ratio of carbon to gas density which implies a slow rate of change in the particle size. Thus, for any particle diameter all physicochemical processes are assumed steady. We also assume that spherical symmetry exists so that the overall continuity equation can be integrated to give

$$r^2 \rho v = M \quad (= \text{constant}) \quad (1)$$

where ρ is the mixture density and r , v are the radial coordinate and velocity respectively. The term "burning rate" is usually given to M and we shall adopt it. Since the mass flux is given by $\rho v = M/r^2$, the momentum equation plays no role other than determining the small pressure variations and will not be considered.

The chemical species assumed present in the gas phase are CO, O_2 , CO_2 and inert (usually N_2) and the subscripts 1-4 will be used respectively. If the homogeneous reaction is



then the species mass balance equations and the overall energy equa-

tion written in a dimensionless form, are:

$$\left\{ \begin{array}{l} -\frac{1}{1-\alpha} L(Y_1) = -\frac{1}{\alpha} L(Y_2) = L(Y_3) = L(T) = \Omega \\ L(Y_4) = 0 \end{array} \right. \quad (2)$$

where the convective-diffusive operator L is given by

$$L \equiv \frac{M-2r}{r^2} \frac{d}{dr} - \frac{d^2}{dr^2}$$

Y_i is the mass fraction of species i , T the mixture temperature and α , which depends on the stoichiometric coefficients of reaction (I) and on the molecular weights of the various species, is given by

$$\alpha = m_{O_2} / 2m_{CO_2} (= .36).$$

In making the variables dimensionless we chose a , Q/c_p and $\lambda a/c_p$ as the characteristic values for length, temperature and mass flux respectively, where a is the instantaneous particle radius, λ the coefficient of heat conduction, c_p the common specific heat and Q the heat of reaction (I) per unit mass of CO_2 . The reaction is assumed to be second order and its rate described by an Arrhenius law as experimental observations indicate; see for example Hottel et al (1965) and Howard et al (1973). Thus, we write

$$\Omega = D_g \rho^2 Y_1 Y_2^{1/2} \exp(-\theta/T) \quad (3)$$

where D_g is the gas-phase Damköhler number given by

$$D_g = \left(\frac{m_{CO_2}}{m_{CO} m_{O_2}^{1/2} m_{H_2O}^{1/2}} \cdot \frac{k C_p^3}{\lambda Q^2 R^2} \right) Y_{H_2O}^{1/2} a^2 p_o^2 \quad (4)$$

Here, k is the pre-exponential factor, p_o the uniform pressure and Y_{H_2O} is the mass fraction of water vapor which presence serves as a catalyst to the CO oxidation. The amount of water vapor is

small enough so that Y_{H_2O} can be considered as a parameter; elsewhere it is included in Y_4 . The other parameters affecting D_g are the particle radius a and the ambient pressure p_0 assumed constant. In (3) the density was made dimensionless by $C_p p_0 / Q \bar{R}$ and the equation of state becomes $\rho T = 1$. It should be mentioned that in writing equs. (2) it has been assumed that all species have equal and constant specific heats, that the diffusion coefficients are all equal and that the Lewis number is one.

Far away from the particle all properties are known and constant

$$Y_i = Y_{i\infty} \text{ for } i = 1, 4, \quad T = T_\infty \text{ as } r \rightarrow \infty. \quad (5)$$

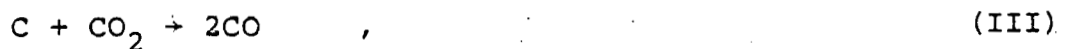
At the particle surface we assume that the temperature is given

$$T = T_s \quad \text{at } r = 1, \quad (6a)$$

and avoid writing an energy balance which leads to additional nonlinearities in the boundary conditions. Mass conservation at the surface requires that the net mass flux equals the rate of consumption/production per unit area by the heterogeneous chemical reactions. We consider both, the direct oxidation of carbon



and its reduction by carbon-dioxide



and assume (Field et al, 1967; Dutta et al, 1975) that they are first order reactions. Then, the conditions at $r = 1$ are

$$\left\{ \begin{array}{l} MY_1 - dY_1/dr = (1-\alpha) D_s Y_2/\alpha + 2(1-\alpha)\bar{D}_s Y_3 \\ MY_2 - dY_2/dr = -D_s Y_2 \\ MY_3 - dY_3/dr = -\bar{D}_s Y_3 \\ MY_4 - dY_4/dr = 0 \end{array} \right. , \quad (6b)$$

where D_s and \bar{D}_s are the surface Damköhler numbers for reactions (II) and (III) respectively, given by

$$D_s = (C_p^2 / \lambda Q \bar{R}) a p_o T_s^{-1} k_2(T_s) \quad , \quad (7)$$

$$\bar{D}_s = (C_p^2 / \lambda Q \bar{R}) a p_o T_s^{-1} k_3(T_s) \quad .$$

In writing these relations we have used the equation of state $pT = 1$ and left the temperature dependence of the reaction rates arbitrary, a point which will be discussed later.

The governing equations sum to five second order equations (2) with ten boundary conditions (5,6). The additional equation

$$Y_1 + Y_2 + Y_3 + Y_4 = 1 \quad (8)$$

resulting from the fact that carbon is a nonvolatile matter serves to determine M . In particular its dependence on the Damköhler numbers is a principal output of the solution which indirectly relates the burning rate to either one of the parameters p , a , T_s .

The problem we are facing can be further reduced if we realize that for a proper combination of the mass fractions, the source terms can be eliminated from both, the differential equation and the boundary conditions at $r = 1$. The resulting linear problem can be solved yielding

$$\alpha(Y_1 - Y_{1\infty} e^{-M/r}) + (1-\alpha)(Y_2 - Y_{2\infty} e^{-M/r}) + 2\alpha(1-\alpha)(Y_3 - Y_{3\infty} e^{-M/r}) = 0 \quad . \quad (9)$$

The solution for the inert mass fraction is also known

$$Y_4 = Y_{4\infty} e^{-M/r} \quad , \quad (10)$$

so that together with (8,9) we obtain

$$\alpha(1 - e^{-M/r}) + (1-2\alpha)(Y_2 - Y_{2\infty} e^{-M/r}) + \alpha(1-2\alpha)(Y_3 - Y_{3\infty} e^{-M/r}) = 0 \quad , \quad (11)$$

which is a relation between Y_2 and Y_3 only. Consequently, one mass-fraction equation remains to be solved; the others result from (9), (10) and (11). Being a nonlinear two point boundary value problem, it is expected that multiple solutions exist as pointed out by Caram and Amundson (1977). Only one solution will be addressed in what follows and the conditions under which it is valid will be discussed.

THE REACTION RATES

It has been mentioned above that the homogeneous reaction (I) may be considered as second order. Thus, relying on the correlation provided by Howard et al (1973), we find that the activation energy is about 30 kcal/mol so that $\exp(-E/RT)$ is at most $5 \cdot 10^{-4}$ for temperatures below 2000K and becomes significant at only higher temperatures. This suggests that the chemical activity may be confined to a thin zone, outside of which the reaction rate is negligibly small. Formally, one can obtain this behavior by assuming that the dimensionless activation energy θ is large (Ludford, 1977, Williams 1971). As to the Damköhler number, we use representative values for the various properties in (4) and take $k = 1.3 \cdot 10^{14}$ $\text{cm}^3/\text{mol} \cdot \text{s}$ to obtain $D_g = 4.2 Y_{\text{H}_2\text{O}}^{1/2} a^2 p_o^2$ where a is measured in microns and p_o in atmospheres. The small amount of water vapor present in the gas phase is of the order $Y_{\text{H}_2\text{O}} \sim 10^{-3}$ so that for a particle size in the range 10-100 μm and for pressures 1-10 atm, we find $1 \leq D_g \leq 10^6$. Since D_g attains relatively large values we may write

$$D_g = \exp(\theta/T_c) \quad (12)$$

and in doing so, define a characteristic temperature T_c which is indirectly related to the parameters a and p_o . Now the chemical reaction rate contains the factor $\exp(\theta/T_c - \theta/T)$ which clearly has different order of magnitude for large θ depending on the relative sizes of T and T_c .

The equilibrium gas phase limit, discussed by Libby and Blake (1979) is obtained when $D_g \exp(-\theta/T) \rightarrow \infty$. Then, a finite Ω requires $Y_1 Y_2^{1/2} \equiv 0$ which is possible only when both CO and O_2 are totally consumed at the flame; i.e. $Y_1 \equiv 0$ for $r > r_*$ (with $Y_{1\infty} = 0$) and

$Y_2 \equiv 0$ for $r < r_*$ where r_* is the location of the flame. The temperature reached at r_* is the so-called adiabatic flame temperature T_a and therefore the equilibrium limit requires $T_c < T_a$.

When the characteristic temperature is close to T_a to within $1/\theta$, say $T_c = T_a - (T_a^2/\theta)t_c$, we can write the reaction rate

$$\Omega = \tilde{D}_g \rho^2 Y_1 Y_2^{1/2} \exp(\theta/T_a - \theta/T) \quad (13)$$

in terms of the reduced Damköhler number $\tilde{D}_g = e^{t_c}$. When $\tilde{D}_g \rightarrow \infty$ we recover the equilibrium limit (see appendix) so that \tilde{D}_g^{-1} measures the departure from equilibrium which is our concern in the present paper.

In analyzing the combustion field, the reaction rate Ω can be neglected everywhere but in a thin region at the neighborhood of r_* , namely the flame. Again $Y_1 \equiv 0$ for $r > r_*$ and $Y_2 \equiv 0$ for $r < r_*$ but only to leading order; thus allowing a small $O(1/\theta)$ leakage of reactants through the flame. When the flame is contiguous to the particle surface ($r_* = 1$), the oxygen is not totally consumed at the flame and a slightly different treatment is required as will be discussed later.

We turn our attention now to the heterogeneous reactions (II) and (III). It has been assumed that they are both first order although this is of considerable doubt in general (Maahs 1971, Gray et al 1973). It should be pointed out that other reaction orders can be used in the following analysis without altering the qualitative results significantly. The temperature dependence of the reaction rates has been left arbitrary at this point as in (7). In doing so we have avoided the controversy of whether an Arrhenius form or a power law best represent the experimental data (Field 1969,

Gray et al 1973). For specific calculations we have used the relations provided by Caram and Amundson (1977). Finally, it should be mentioned that for a specified T_s all the Damköhler numbers are related; in particular $D_g/D_s^2 \sim D_g/\bar{D}_s^2$.

FLAME AT THE INTERIOR OF THE GAS PHASE

When the flame surrounding the particle stands at a distance $r_* > 1$, the mass-fraction profiles are obtained from (8-11) together with $Y_1 Y_2^{1/2} \equiv 0$. It will be convenient to introduce the values

$$M_1 \equiv \ln (1 + \nu Y_{2\infty}^{1/2}) \quad , \quad M_2 \equiv \ln [1 + \nu (Y_{2\infty} + \alpha Y_{3\infty})]$$

where $\nu = (1-2\alpha)/\alpha$. Then

$$Y_1 = \begin{cases} \frac{2(1-\alpha)}{1-2\alpha} [1 - e^{M_1 - M/r}] & \text{for } r < r_* \\ 0 & \text{for } r > r_* \end{cases} \quad (14a)$$

$$Y_2 = \begin{cases} 0 & \text{for } r < r_* \\ \frac{2\alpha}{1-2\alpha} [e^{M_1 - M/r} - 1] & \text{for } r > r_* \end{cases} \quad (14b)$$

$$Y_3 = \begin{cases} \frac{1}{1-2\alpha} [e^{M_2 - M/r} - 1] & \text{for } r < r_* \\ \frac{1}{1-2\alpha} \{1 - [1 - (1-2\alpha) Y_{3\infty}] e^{-M/r}\} & \text{for } r > r_* \end{cases} \quad (14c)$$

where the flame location $r_* = M/M_1$ follows from the continuity of Y_3 which also gives $Y_3^* = (e^{M_2 - M_1} - 1)/(1-2\alpha)$. In order to determine the burning rate M , we use the boundary condition (6b) for Y_3 (all the others are automatically satisfied) and obtain the nonlinear algebraic equation

$$M - \bar{D}_s (e^{M_2 - M} - 1) = 0 \quad (15)$$

which has to be solved numerically for any given \bar{D}_s . Note that in the absence of oxygen near the particle, the only heterogeneous

reaction which takes place is (III) and to leading order, the burning rate solely depends on \bar{D}_s . So far the solution is identical to the equilibrium limit (Libby and Blake, 1979) however, it will be shown that a proper discussion of the flame structure leads to new features describing the departure from equilibrium.

It should be noted that since $r_* > 1$ the lower bound of M is M_1 . On the other hand the mass fractions should be all positive and their sum one leading to the upper bound M_2 . From (15) it follows that M is an increasing function of \bar{D}_s which tends asymptotically to M_2 (see Fig. 4). For $\bar{D}_s \gg 1$ the so called diffusion controlled limit is obtained, M achieves its maximum value M_2 and the flame stands off the particle at a distance $r_* = M_2/M_1$. Spalding (1955) and Avedesian and Davidson (1973) have postulated that the flame position equals twice the particle radius, but this result is obtained when the ambient atmosphere which contains no CO_2 ($Y_{3\infty} = 0$) is lean in oxygen ($Y_{2\infty} \ll 1$) as can easily be verified. As \bar{D}_s is lowered, M decreases and the flame moves towards the particle reaching it for $M = M_1$. Both \bar{D}_s and M can be further decreased with the flame sitting at the particle surface ($r_* = 1$) but their relation which is no longer obtained from (15), will be derived later. Therefore, the kinetic controlled limit $\bar{D}_s \ll 1$ cannot be discussed at this point since it leads to small values of M which in general do not satisfy $M > M_1$.

The mass fraction profiles (14) were obtained under the assumption of a complete gas phase burning, namely $Y_1^* = Y_2^* = 0$. The existence of such a solution depends on whether the jump in the gradients at r_* are permissible by the conservation equations (2) which require a detailed analysis of the thin flame. Since the

reaction rate Ω is temperature dependent, we start by writing the solution

$$T = \begin{cases} T_s + (T_a - T_s) \left(\frac{e^{-M/r} - e^{-M}}{-M_1 - e^{-M}} \right) & \text{for } r < r_* \\ T_\infty + (T_a - T_\infty) \left(\frac{e^{-M/r} - 1}{-M/r_* - 1} \right) & \text{for } r > r_* \end{cases} \quad (16)$$

which satisfies the two boundary conditions, is continuous at r_* and has the value T_a there. The determination of the adiabatic flame temperature T_a requires the additional information (derived later).

$$\begin{aligned} [dT/dr] &= [dY_3/dr] = - [dY_2/dr]/\alpha = - \\ &= - [dY_3/dr]/(1-\alpha) \end{aligned} \quad (17)$$

which relates the jump conditions of the different variables. In (17) the square brackets denote the jump across r_* ; e.g. $[dT/dr] = (dT/dr)_{r_*^+} - (dT/dr)_{r_*^-}$. Now

$$T_a = T_s + (T_\infty + Y_2 \alpha / \alpha - T_s) \left(\frac{e^{-M_1} - e^{-M}}{1 - e^{-M}} \right), \quad (18)$$

achieves its maximum value when $M = M_2$ whereas at $M = M_1$, since the flame is contiguous to the particle, we have $T_a = T_s$ as it should. We also find that when the particle surface temperature T_s is below T_a , the additional restriction

$$T_s \leq T_\infty + Y_2 \alpha / \alpha \quad (19)$$

should be imposed; otherwise this inequality is reversed. The former case is the physically most interesting one that we shall consider here.

Flame Structure

In analyzing the flame structure, we perturb all variables about their values at the flame

$$T = T_a + \varepsilon(\phi + \beta\xi) + \dots, \quad Y_1 = \varepsilon y_1 + \dots,$$

$$Y_2 = \varepsilon y_2 + \dots, \quad Y_3 = Y_3^* + \varepsilon y_3 + \dots,$$

and with the proper choice of the flame thickness

$$r = r_* + (2\varepsilon/\Delta)\xi,$$

we obtain in the governing equations (2) a balance between diffusion and chemical reaction

$$\frac{d^2\phi}{d\xi^2} = \frac{d^2Y_3}{d\xi^2} = -\frac{1}{\alpha} \frac{d^2Y_2}{d\xi^2} = -\frac{1}{1-\alpha} \frac{d^2Y_1}{d\xi^2} = -$$

$$= -\frac{\Lambda}{\alpha^{1/2}(1-\alpha)} Y_1 Y_2^{1/2} e^{\phi + \beta\xi} \quad (20)$$

The parameter

$$\beta = \frac{(dT/dr)_{r_*^+} + (dT/dr)_{r_*^-}}{(dT/dr)_{r_*^+} - (dT/dr)_{r_*^-}} = 1 - (1-2\alpha) \frac{Y_2^{\omega/\alpha} - (T_s - T_\infty)}{M_1(1-e^{-M_1})} \quad (21)$$

represents the fraction of the excess of heat conducted to one side of the flame from the total heat generated at the flame.

Therefore if the particle is not very hot ($T_s < T_a$) and not too cold ($T_s > T_\infty$), heat cannot be transferred from the ambient to the flame and $|\beta| < 1$. This inequality is readily obtained from (21).

When $\beta = 0$, heat is conducted equally to both sides of the flame; $\beta > 0$ corresponds to the case of more heat transferred towards the oxidant supply and $\beta < 0$ to the case of more heat transferred towards the particle. The parameter Δ is the negative sign of the common jump value (17) which can be evaluated as

$$\Delta = - [dT/dr] = 2M_1^2 / (1-2\alpha)M > 0$$

In order to retain the chemical term and in particular its temperature dependence in (20) we chose $\epsilon = T_a^2/\theta \ll 1$; then

$$\Lambda = 4\alpha^{1/2} (1-\alpha) \tilde{D}_g \Delta^{-2} T_a^3 \theta^{-5/2} \quad (22)$$

The four equations in (20) have the same righthand side so that the combination of any two of them can be integrated immediately leading to the jump condition (17) mentioned above. A second integration yields

$$y_1 = (1-\alpha)(-\phi-\xi) \quad , \quad y_2 = \alpha(\xi-\phi) \quad , \quad y_3 = (e^{M_2-M} - 1)\xi + \phi \quad , \quad (23)$$

and the structure problem reduces to

$$d^2\phi/d\xi^2 = \Lambda(\phi+\xi)(-\phi-\xi)^{1/2} e^{\phi+\beta\xi} \quad (24a)$$

Matching on both sides of the flame with (16) provides the boundary conditions

$$d\phi/d\xi = \pm 1 \quad \text{as } \xi \rightarrow \mp \infty \quad (24b)$$

The nonlinear two-point boundary value problem (24) was solved numerically using a shooting technique. For given values of β and Λ , we assigned a value for ϕ at large negative ξ and together with $d\phi/d\xi = 1$, the equation was integrated out to large positive ξ to check whether the slope tends to -1 as required. A solution was obtained by subsequent guessing and refining until both conditions (24b) were satisfied. The results (shown in Figs. 2) indicate that the problem possess two distinguished solutions for $\Lambda > \Lambda_0 > 0$ and none for $\Lambda < \Lambda_0$. The two solutions tend to a unique limit as $\Lambda \rightarrow \Lambda_0$ and the critical value Λ_0 depends on β as in Fig. 3. Note that the temperature perturbation ϕ does not peak in general at r_* but is shifted away; for $\beta \approx -1$ the maximum is on the particle side and it moves towards the oxidant side as β increases to 1.

The results are explained in terms of the Damköhler number \tilde{D}_g as follows. When $\tilde{D}_g \rightarrow \infty$ the structure of the exponentially thin flame (see appendix) has a unique solution. All the perturbations inside and outside the flame are negligibly small so that (14) is the solution to all orders and M is the burning rate. When \tilde{D}_g is lowered, oxygen and carbon monoxide will leak through the flame in small but finite amounts given by

$$\epsilon \lim_{\xi \rightarrow -\infty} |\xi - \phi|, \quad \epsilon(1-\alpha) \lim_{\xi \rightarrow \infty} |\phi + \xi|$$

respectively. Then the burning rate will decrease below the equilibrium value M and a correction ϵm which depends explicitly on the solution of (24) has to be added. The flame temperature

$$T_f = T_a - \epsilon |\phi + \beta \xi|_{\max}$$

will be lower than the adiabatic flame temperature T_a , as it should. Because of the double structure of (24) all these variables will be represented by C-shape curves; e.g. in Figs. 2, the O_2 leakage has been plotted versus Λ . Following the lower branch as we depart from the equilibrium limit ($\Lambda \rightarrow \infty$), the leak of oxygen increases until the critical Λ_0 is obtained. The flame structure does not exist for $\Lambda < \Lambda_0$ and therefore the outer flow (14) is not acceptable. The upper branch describes another possible solution which tends to a partial burning flame as $\Lambda \rightarrow \infty$ and is believed to be unstable (Williams, 1971). Thus, the critical Damköhler number \tilde{D}_g^0 (corresponding to Λ_0) is the minimum value below which the oxidation of carbon monoxide will not take place in the gas phase.

The extinction phenomenon described above can be well understood if the correction to the burning rate M obtained from (15) is calcu-

lated. For this purpose the first order corrections $\tilde{\epsilon}Y_i$ should be added to the mass fractions (14). They should satisfy the equations

$$L(\tilde{Y}_i) = -(m/r^2) dY_i/dr, \quad i = 1, 4 \quad (25)$$

with appropriate conditions at $r = 1$ derived from (6b) and when $r \rightarrow \infty$ they all vanish. In particular, the expressions (9) and (10) provide certain relations between the \tilde{Y}_i 's so that only one among them remains to be solved. We will avoid writing the complete solution but concentrate on the determination of m . The solution \tilde{Y}_2 of (25) for $r < r_*$ can be readily obtained after which the boundary condition

$$M\tilde{Y}_s - d\tilde{Y}_2/dr = -D_s\tilde{Y}_2, \quad \text{at } r = 1$$

and the matching requirement

$$\tilde{Y}_2 = \alpha \lim_{\xi \rightarrow -\infty} |\xi - \phi|, \quad \text{at } r = r_* \quad (26)$$

should be imposed. The amount of oxygen reaching the particle is found to be

$$\epsilon\tilde{Y}_{2s} = \epsilon\alpha \lim_{\xi \rightarrow -\infty} |\xi - \phi| \left\{ (1 + D_s/M) (e^{M-M_1} - 1) + 1 \right\}^{-1} \quad (27)$$

Now, solutions for \tilde{Y}_1 and \tilde{Y}_3 can immediately be written; in particular when the condition

$$M\tilde{Y}_3 - d\tilde{Y}_3/dr = -\bar{D}_s\tilde{Y}_3 - mY_3, \quad \text{at } r = 1$$

is satisfied, we obtain

$$m = -v\tilde{Y}_{2s} (\bar{D}_s - D_s) / (1 + \bar{D}_s e^{M_2 - M}). \quad (28)$$

While the leading term M was found to depend only on the indirect carbon oxidation (III) its first order correction m depends on the two heterogeneous reactions as well as on the homogeneous

reaction. Near equilibrium $\tilde{D}_g \rightarrow \infty$ and the correction to the burning rate is negligibly small because $\tilde{Y}_{2s} \rightarrow 0$. As \tilde{D}_g is lowered the correction m is expected to be negative so that the burning rate $M + \epsilon m$ is below its equilibrium value. According to (28) this leads to $\bar{D}_s/D_s \geq 1$ which indirectly is a restriction on T_s (see equ. 7). Since (26) is double valued as shown in Figs. 2, the burning rate is also such so that by excluding the unstable branch we find that the lowest value \tilde{D}_g attainable is the extinction Damköhler number \tilde{D}_g° .

It has been emphasized earlier that the double structure of the solution depends on whether $|\beta| < 1$. When this condition is not satisfied, the heat conducted from the ambient towards the flame allows for the steady burning to persist and the extinction phenomenon is not met. This may occur when the particle surface temperature T_s exceeds the flame temperature or if the surrounding atmosphere is extremely hot, namely $T_\infty > T_a$.

FLAME CONTIGUOUS TO THE PARTICLE

It has been indicated earlier that as the value of M approaches M_1 , the flame reaches the particle and $r_* = 1$. For $r > 1$, the mass fraction profiles are given by (14) and the temperature by (16). In particular the values at the surface

$$Y_{1s} = 0, \quad Y_{2s} = 2(e^{M_1 - M} - 1)/v,$$

$$Y_{3s} = \{1 - [1 - (1 - 2\alpha)Y_{3\infty}]e^{-M}\} / (1 - 2\alpha)$$

indicate that there is a substantial amount of oxygen for the direct carbon oxidation (II) to be as significant as the indirect reaction (III). And indeed in calculating the leading order term of the burning rate by combining the relation (11) with the boundary conditions at $r = 1$, we obtain the nonlinear algebraic equation

$$M - \bar{D}_s (e^{M_2 - M} - 1) + 2(\bar{D}_s - D_s) (e^{M_1 - M} - 1) = 0 \quad (29)$$

which should be solved numerically for any given D_s and \bar{D}_s . The results indicate that M increases from $M = 0$ when $D_s, \bar{D}_s \rightarrow 0$ up to the value M_1 (see Fig. 4); at this point (29) reduces to (15).

Also when $M = 0$ the surface mass fractions coincide with the ambient values $Y_{2\infty}$ and $Y_{3\infty}$ as they should.

Next, we consider the flame zone which is now adjacent to the particle surface and perturb all variables about their values at $r = 1$:

$$Y_1 = \epsilon Y_{1s} + \dots, \quad Y_2 = Y_{2s} + \epsilon Y_{2s} + \dots,$$

$$Y_3 = Y_{3s} + \epsilon Y_{3s} + \dots, \quad T = T_s + \epsilon [\phi - t_s + Y_{1s} / (1 - \alpha)] + \dots;$$

where $\epsilon = T_s^2/\theta$. With the new scaling $r = 1 + (\epsilon/\Delta)\xi$, the governing equations for y_1 and ϕ reduce to

$$\frac{1}{1-\alpha} \frac{d^2 y_1}{d\xi^2} = - \frac{d^2 \phi}{d\xi^2} = \frac{\Lambda}{1-\alpha} y_1 e^\phi \quad (30)$$

after which y_2 and y_3 can be evaluated from

$$y_2 + \alpha y_3 = e^{M_2 - M} (M\xi/\Delta - m)/v \quad (31)$$

$$y_1 + (1-\alpha)y_2/\alpha + 2(1-\alpha)y_3 = (1-\alpha)e^{-M} (y_{2\infty}/\alpha + 2y_{3\infty}) (M\xi/\Delta - m)$$

The parameter Λ introduced in (30) is given by

$$\Lambda = (1-\alpha) \tilde{D}_g T_s^2 \Delta^{-2} Y_{2s}^{1/2} \theta^{-2} e^{-t_s + Y_{1s}/(1-\alpha)}$$

where $-\epsilon t_s$ is the given variation from the surface temperature T_s . ϵy_{1s} the mass fraction of CO at the surface, as yet unspecified and $\Delta = M(T_s - T_\infty)/(e^M - 1)$. The correction ϵm which has been added to M in (31) will be obtained after the solution to (30) is found and the boundary conditions (6b) satisfied.

It is apparent from (30) that the combination of $(1-\alpha)y_1$ and ϕ is a linear function of ξ . Therefore, matching at large ξ leads to

$$y_1 = -(1-\alpha)(\phi + \xi) \quad (33)$$

and the structure problem becomes

$$d^2 \phi / d\xi^2 = \Lambda (\phi + \xi) e^\phi \quad (34a)$$

The boundary conditions associated with (34a) are

$$d\phi/d\xi = (D_s Y_{2s} + 2\alpha \bar{D}_s Y_{3s}) / \Delta - 1 \quad \text{at } \xi = 0, \quad (34b)$$

$$d\phi/d\xi = -1 \quad \text{as } \xi \rightarrow \infty ;$$

the former has been derived from (6a) and (33) while the latter

latter is a matching requirement. We are facing again a non-linear two point boundary value problem which has been solved numerically using a shooting technique. With \tilde{D}_g given, the surface Damköhler numbers D_s and \bar{D}_s are determined. Then with an assigned value for $\phi(0)$, we calculate y_{1s} from (33) and Λ according to its definition. Equ. (34a) can be integrated from $\xi = 0$ with the given slope in order to check whether the condition at ∞ is met. The solution is obtained by subsequent guessing $\phi(0)$ until both conditions (34b) are satisfied.

The numerical results indicate that two distinguished solutions exist for $\tilde{D}_g > \tilde{D}_g^0$ and none for $\tilde{D}_g < \tilde{D}_g^0$ so that the double structure of the flame zone is continued even when it is adjacent to the particle surface. In order to calculate the correction to M we use the boundary conditions (6b) together with (31) and obtain once more the relation (28) for m but with \tilde{Y}_{2s} replaced by y_{2s} . The latter is given by

$$y_{2s} = \alpha\phi(0)\{2e^{M_1}(\bar{D}_s - D_s)/(1 + \bar{D}_s e^{M_2 - M}) - 1\}^{-1}$$

Near equilibrium $\tilde{D}_g \rightarrow \infty$, the correction m is negligibly small and the burning rate is M . For lower values of \tilde{D}_g , the correction m increases and since it is expected to be negative, the resulting burning rate $M + \epsilon m$ is below its equilibrium value. \tilde{D}_g can be reduced down to \tilde{D}_g^0 only and this critical value marks the extinction Damköhler number.

THE BURNING RATE

The primary aim of the analysis has been to determine the burning rate and its dependence on the Damköhler numbers. It is therefore appropriate at this point to describe a simple algorithm which in practice must be carried out numerically. For given ambient conditions and a prescribed particle size all the parameters involved in the problem are determined. If in addition the particle surface temperature is given, all the Damköhler numbers are known and proportional. The leading order of the burning rate M is first calculated from (15) and if $M > M_1$ this is the correct value; otherwise equ. (29) should be used instead. Then all the parameters involved in the structure problem whether (24) or (34) are determined and in particular the critical Λ_0 is obtained and subsequently \tilde{D}_g° . Since the gas phase Damköhler number \tilde{D} was fixed by the particle size, it remains to check whether $\tilde{D}_g \geq \tilde{D}_g^\circ$ or not. In the former case the correction m obtained from the numerical solution is double valued and in the latter the structure does not possess a solution. Thus the burning rate $M + \epsilon m$ forms a C-curve when plotted versus \tilde{D}_g ; the turning point being the extinction Damköhler number \tilde{D}_g° .

Before constructing the general response of M versus the Damköhler numbers we shall start by considering several limiting cases:

Equilibrium Gas Phase: $\tilde{D}_g \rightarrow \infty$. It has been shown in the appendix that an exponentially thin diffusion flame always exists in the gas phase separating a region with no carbon monoxide from another with no oxygen. For large \bar{D}_s , the flame sheet stands at a distance $r_* = M_2/M_1$ and the burning rate is M_2 . As \bar{D}_s is lowered, by reducing either the particle size or its

surface temperature, the flame moves towards the particle and the burning rate M decreases as shown in Fig. 4. The first order correction m is exponentially small and therefore negligible. When the flame reaches the particle the burning rate is M_1 ; it can be further decreased when \bar{D}_s is lowered but with the flame remaining adjacent to the particle.

Diffusion controlled heterogeneous reaction: $\bar{D}_s \rightarrow \infty$. This limit corresponds to a high surface temperature T_s and according to (15) the leading term of M is M_2 . Its first order correction can then be evaluated leading to the burning rate.

$$M_2 \rightarrow \epsilon(1-2\alpha) \lim_{\xi \rightarrow -\infty} |\xi - \phi| [(1 + D_s/M_2) (e^{M_2 - M_1} - 1) + 1]^{-1}. \quad (33)$$

Note the dependence on both the direct oxidation of carbon (II) and the homogeneous reaction (I). For large D_g , the correction term is negligibly small and (33) reduces to M_2 . When D_g is lowered, the gas phase departs from equilibrium and the burning rate decreases until the critical Damköhler number D_g° is reached (see Fig. 5). For a further decrease in D_g the flame sitting at $r_* = M_2/M_1$ can no longer exist; thus the minimum D_g° marks the extinction Damköhler number. The second solution shown in Fig. 5 is presumably unstable (Williams, 1971).

Kinetically controlled heterogeneous reactions $D_s, \bar{D}_s \rightarrow 0$.

When the surface temperature T_s of the particle is low, D_s and $\bar{D}_s \rightarrow 0$ and the burning occurs at a slow rate. The homogeneous reaction is effectively frozen and the burning rate reduces to

$$\frac{1-2\alpha}{\alpha} \{ \alpha \bar{D}_s Y_{3\infty} + D_s Y_{2\infty} \} .$$

Finite reaction rates. With all the Damköhler numbers proportional, we choose to represent their dependence on the burning rate by plotting M versus $D_g = \bar{D}_g \exp(\theta/T_a)$. Starting with large D_g the CO oxidation takes place at a distance $r_* = M_2/M_1$ while the burning rate is M_2 . As D_g is lowered, the flame moves towards the particle and when reaching it remains adjacent to its surface. The burning rate decreases below the value M obtained at equilibrium; its corrected value $M + \epsilon m$ is double valued for all $D_g > D_g^\circ$ and does not exist below the critical D_g° (see Fig. 6). As before, the lower branch is believed to be unstable so that the turning point (D_g°, M_{ex}) corresponds to extinction. These values are obtained by solving simultaneously (22) and (15) if $M > M_1$, or (32) and (29) otherwise, with $\Lambda = \Lambda_0$.

CONCLUSION

A careful treatment of the different zones of the combustion field surrounding a carbon particle was given for the case that both heterogeneous and homogeneous reactions are present. While in previous analyses it was found that the burning rate may attain any value below M_2 , the present work indicates that this is so only when $D_g \rightarrow \infty$ and equilibrium prevails in the gas phase (Fig. 4). In departing from equilibrium we uncover a minimum Damköhler number D_g° (and therefore a minimum particle size) below which the gas phase is frozen. Only for $D_g > D_g^\circ$ the CO oxidation is possible (Figs. 5,6) and it takes place at a well defined distance from the particle. The flame which is thin but finite allows a small leakage of oxygen on one side and carbon monoxide on the other. As a consequence some O_2 may reach the particle surface. In the equilibrium limit no such leakage is possible and the direct carbon oxidation (II) is not active; then the burning rate depends solely on the indirect reaction (III). Here all the three reactions play an essential role in determining the burning rate.

Although the particle surface temperature T_s has been assumed given in the present study, its value cannot be chosen arbitrarily. Some restrictions were discussed throughout the analysis and they are in general agreement with the region of feasible solutions on the T_s, T_∞ plane, given by Caram and Amundson (1977). As mentioned above only one possible solution of the governing equations (2) has been discussed in the present work; thus in order to complete the picture of the response of M versus the Damköhler number the case of a weak $CO+O_2$ reaction

should be considered. This will be the subject of a following paper which will describe the burning from the frozen limit up to ignition.

APPENDIX

The characteristic temperature T_c as defined by (12) is indirectly related to the parameters appearing in D_g in such a way that an increase in ap_0 leads to a smaller T_c . The solution discussed in the present paper allows T_c to be at most equal to the adiabatic flame temperature T_a ; otherwise the exponential in (3) is small everywhere and the gas phase is essentially frozen.

When $T_c < T_a$, the reaction rate becomes

$$(A) \quad \Omega = \rho^2 Y_1 Y_2^{1/2} \exp(\theta/T_c - \theta/T)$$

and since in the limit $\theta \rightarrow \infty$ the exponent is very large near T_a , we must have $Y_1 Y_2^{1/2} \equiv 0$ to all order in $1/\theta$. The analysis of the flame zone standing away from the surface implies that its thickness is $\epsilon \sim \exp[2(\theta/T_a - \theta/T_c)/5]$, i.e. exponentially small; then the governing equation reduces to (24a) but without the factor $\exp(\phi + \beta\xi)$ in its righthand side. For the flame contiguous to the particle $\epsilon \sim \exp[(\theta/T_s - \theta/T_c)/2]$ and the governing equation reduces to (34a) without the factor $\exp \phi$ in its righthand side. The same conclusions are obtained directly from (24) and (34) if the asymptotic limit $\Lambda \rightarrow \infty$ is considered. The former case has been solved numerically; the latter possess a solution of the form $\phi = B \cdot \exp(-\xi) - \xi$ where the constant B is determined from the condition at $\xi = 0$. Both cases yield a unique solution for the structure problem and since the outer flow (14) is valid to all orders in $1/\theta$, the burning rate is M as defined from equs. (15) or (29). These results are identical to those given by Libby and Blake (1979) describing equilibrium conditions in the gas phase although the structure of the exponentially thin flame has not been discussed in

their work.

When T_c is close to T_a to within $1/\theta$, the exponential in (A) becomes $O(1)$ in the flame zone and therefore must be added to Ω as in (24a) and (34a). The flame thickness is only algebraically small, namely $\epsilon \sim 1/\theta$. Now T_c in (A) may be replaced by T_a and the small derivations $\epsilon t_c = T_a - T_c$ define the reduced Damköhler number $\tilde{D}_g = e^{t_c}$ as in (13). When $t_c \rightarrow \infty$ we recover the equilibrium limit so that \tilde{D}_g^{-1} measures the departure from equilibrium which is our concern in the present study.

References

- Avedesian, M. M. and Davidson, J. F. (1973), Combustion of Carbon Particles in a Fluidized Bed, Trans. Instn. Chem. Engrs., 51, 121-131.
- Buckmaster, J. D. (1975), Combustion of a Fuel Drop Immersed in a Hot Atmosphere, Int. J. Engng. Sci., 13, 915-921.
- Burke, S. P. and Schumann, T. E. W. (1931), Proc. Third Int. Bituminous Coal, 2, 485.
- Caram, H. S. and Amundson, N. R. (1977), Diffusion and Reaction in a Stagnant Boundary Layer About a Carbon Particle, Ind. Eng. Chem. Fundam., 16, 171-181.
- Dutta, S., Wen, C. Y. and Belt, J. (1975), Prepr. Div. Fel. Chem. Am. Chem. Soc., 20, 103.
- Fendell, F. E. (1969), The Burning of Spheres Gasified by Chemical Attack, Combust. Sci. Technol., 1, 13-24.
- Field, M. A., Gill, D. W., Morgan, B. B. and Hawksley, P. G. W. (1967), Coal Utilization Research Assoc. (BCURA), Leatherhead.
- Field, M. A. (1969), Rate of Combustion of Size-Graded Fractions of Char from a Low-rank Coal Between 1200°K and 2000°K, Combust. Flame, 13, 237-252.
- Gray, D., Cogoli, J. C. and Essenhigh, R. H. (1973), Problems in Pulverized Coal and Char Combustion, Adv. Chem. Sci. 131, 72-91.
- Hottel, H. C., Williams, G. C., Nerheim, N. M. and Schneider, G. R., (1965), Tenth Symp. (Int.) on Combustion, 111.
- Howard, J. B., Williams, G. C. and Fine, D. H. (1973), Kinetics of Carbon Monoxide Oxidation in Potflame Gases, Fourteenth Symp. (Int.) on Combustion, 975-986.
- Law, C. K. (1975), Asymptotic Theory for Ignition and Extinction in Droplet Burning, Combust. Flame, 24, 89-98.
- Libby, P. A. and Blake, T. R. (1979), Theoretical Study of Burning Carbon Particles, Combust. Flame, 36, 139-169.
- Linán, A. (1974), The Asymptotic Structure of Counterflow Diffusion Flames for Large Activation Energies, Acta Astronautica, 1, 1007-1039.
- Ludford, G. S. S. (1977), Combustion: Basic Equations and Peculiar Asymptotics, J. Mécanique, 16, 531-551.

Maahr, H. G. (1971), Oxidation of Carbon at High Temperatures: Reaction-Rate Control or Transport Control, NASA TN D-6310.

Matalon, M., Ludford, G. S. S. and Buckmaster, J. D. (1979), Diffusion Flames in a Chamber, Acta Astronautica, 6, 943-959.

Nusselt, W. Z. (1924), Ver. Deut. Ing., 68, 124.

Spalding, D. B. (1955), Some Fundamentals of Combustion, Gas Turbine Series, Vol. 2, Butterworths, London.

Williams, F. A. (1971), Theory of Combustion in Laminar Flows, Ann. Review Fluid Mech., 3, 171-188.

List of Figures

- Fig. 1 Schematic representation of the two classical models describing the burning of a pure carbon in an oxidizing atmosphere.
- Fig. 2 The flame structure (numerical solutions of equ. 24).
- Fig. 3 The critical value Λ_0 as a function of β .
- Fig. 4 The burning rate versus the surface Damköhler number \bar{D}_s for equilibrium gas phase. Calculated for $Y_{2\infty}=0.3$, $Y_{3\infty}=0.1967$ and $T_s=1800K$.
- Fig. 5 The burning rate versus the gas phase Damköhler number, for diffusion controlled heterogeneous reaction ($\bar{D}_s \rightarrow \infty$). Calculated for $Y_{2\infty}=0.3$, $Y_{3\infty}=0.1967$ and $T_s=3150K$. The corresponding $\beta=0.9$ and the flame is located at $r_*=2.3$.
- Fig. 6 The burning rate versus the gas phase Damköhler number for finite reaction rates. Calculated for $Y_{2\infty}=0.3$, $Y_{3\infty}=0.1967$ and $T_s=1650K$. The flame moves from $r_*=2.3$ when $D_g \rightarrow \infty$ down to $r_*=2.1$ at $D_g = D_g^0 \sim 5000$ where extinction occurs.

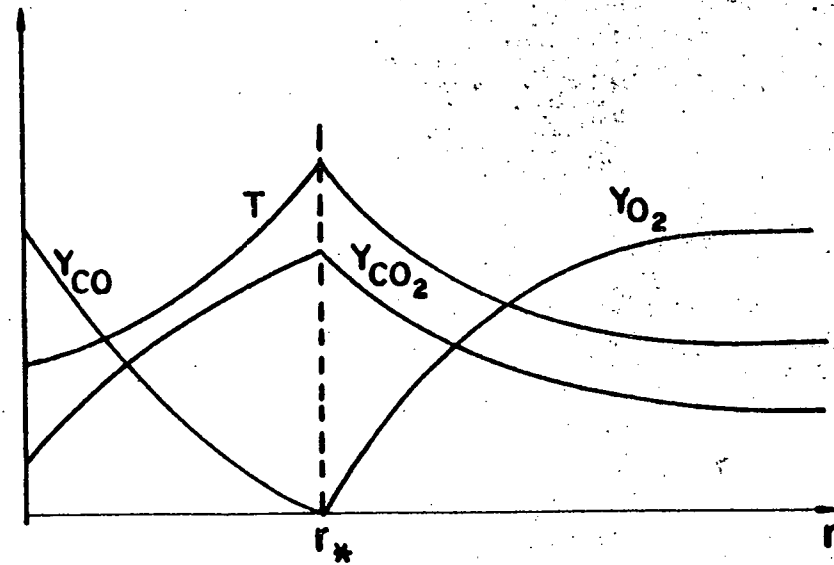
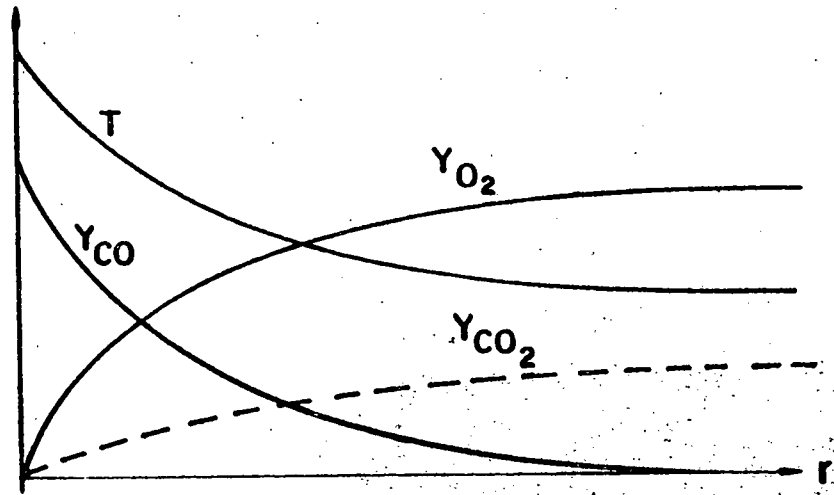
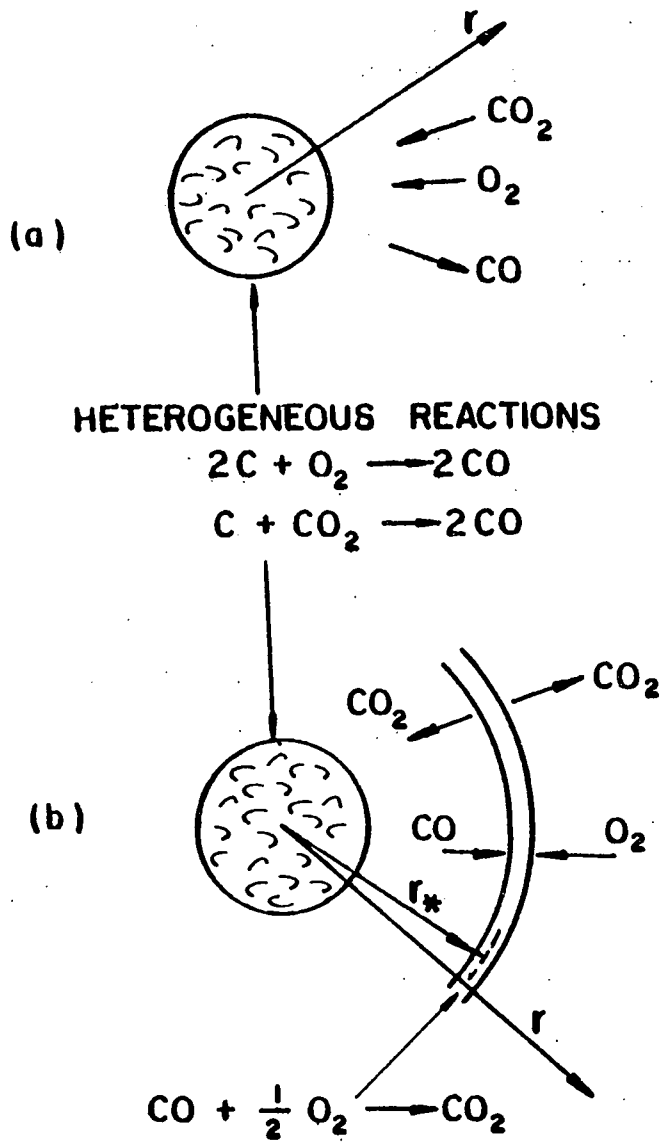


Figure 1

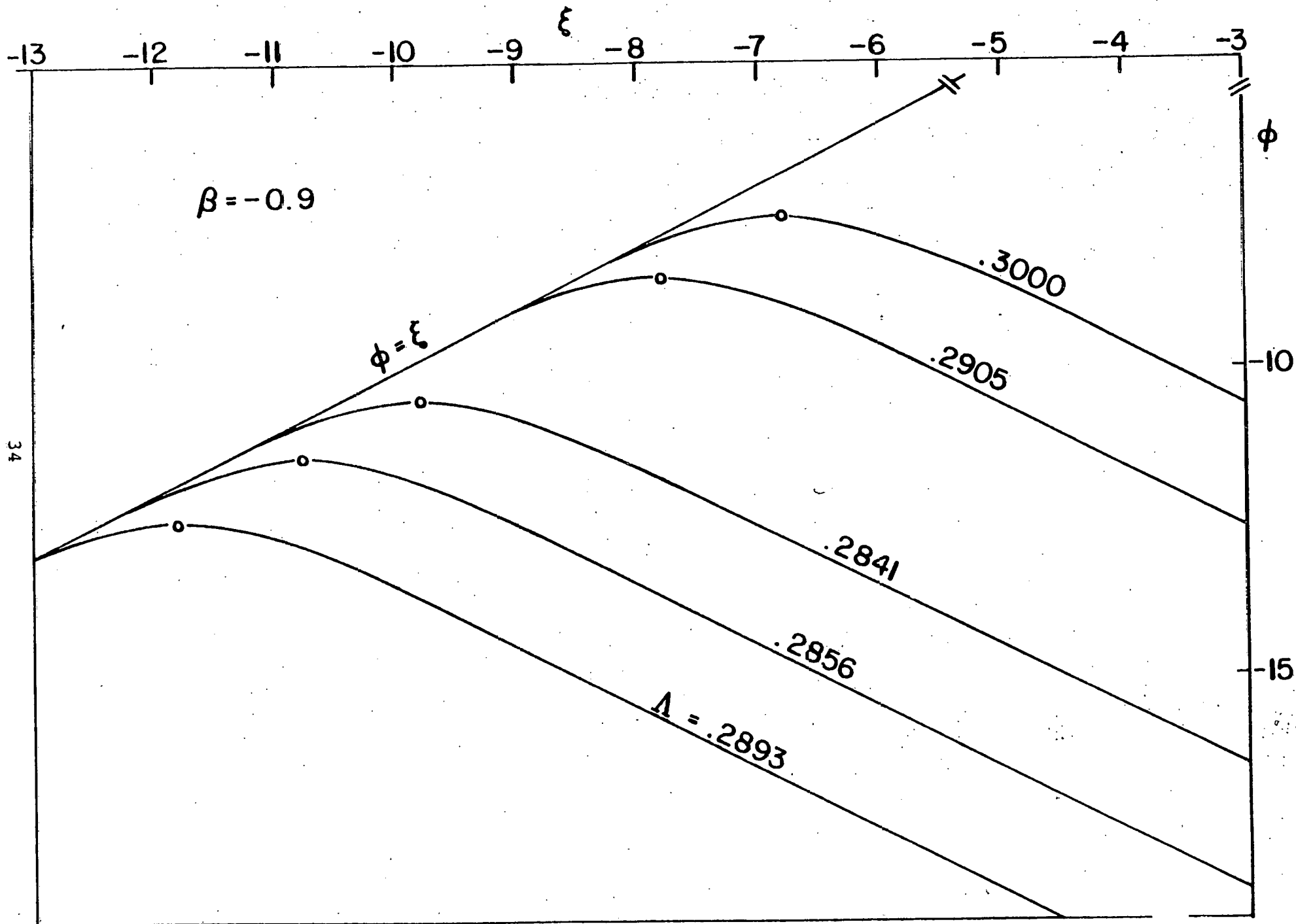


Figure 2a

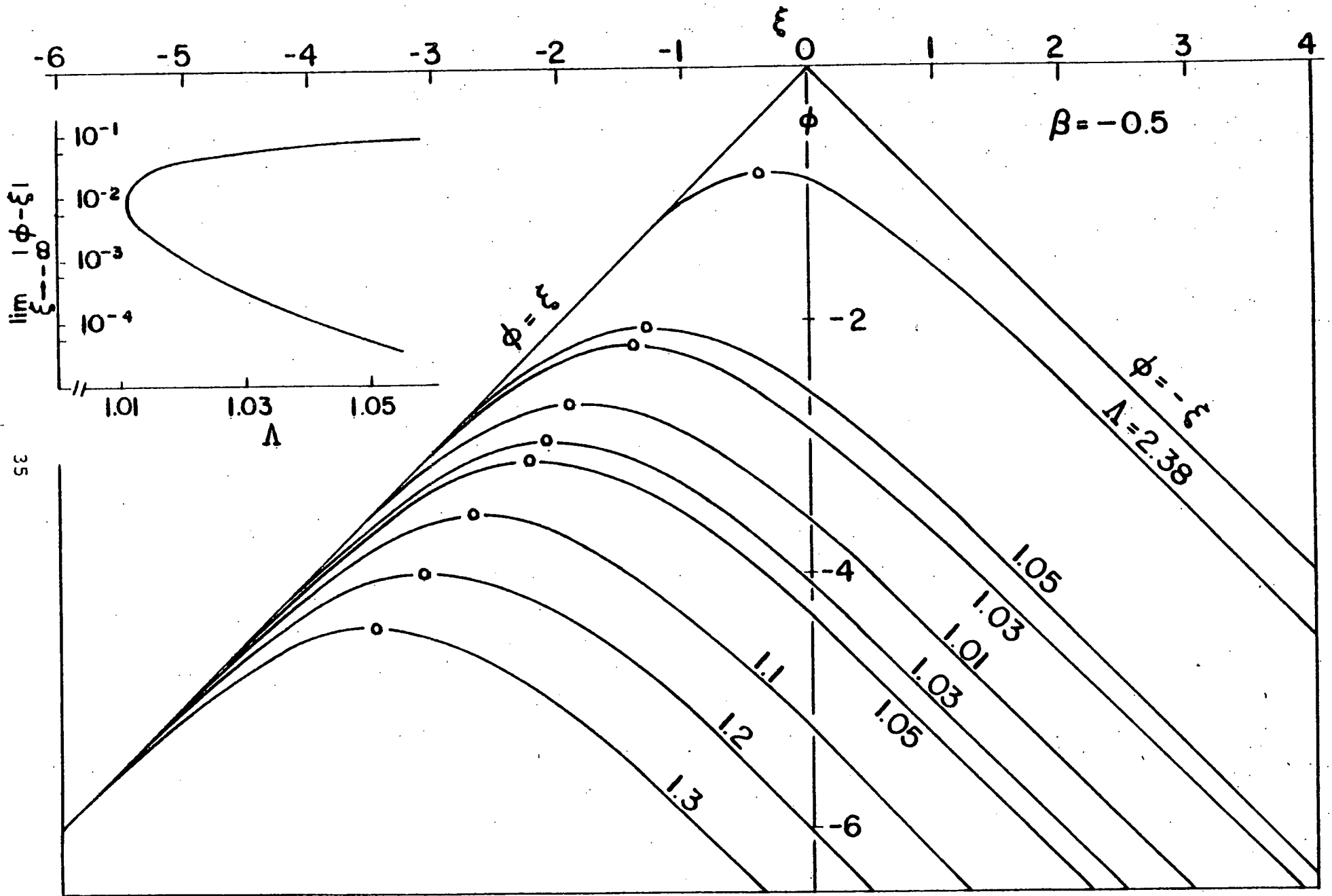


Figure 2b

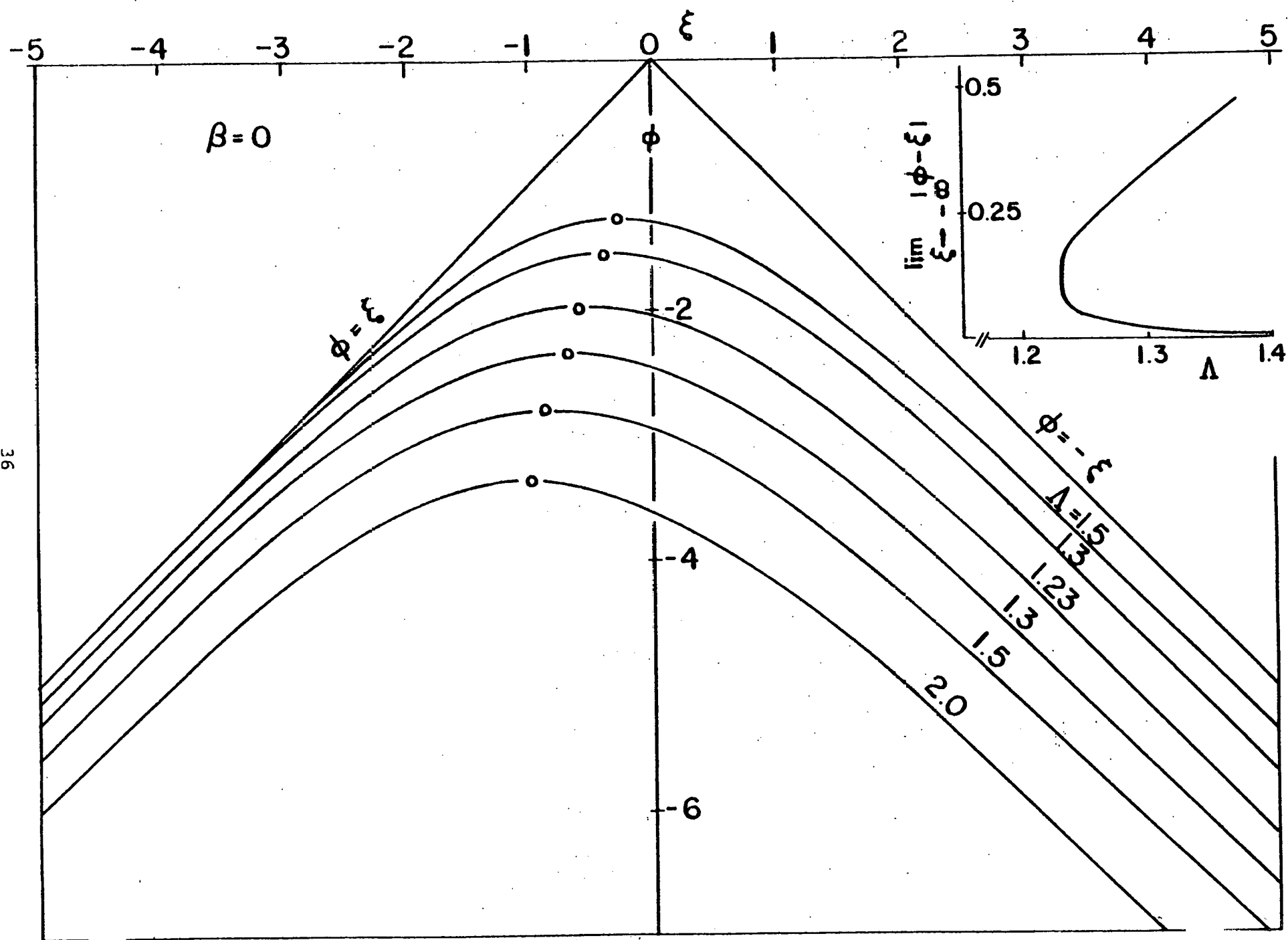


Figure 2c

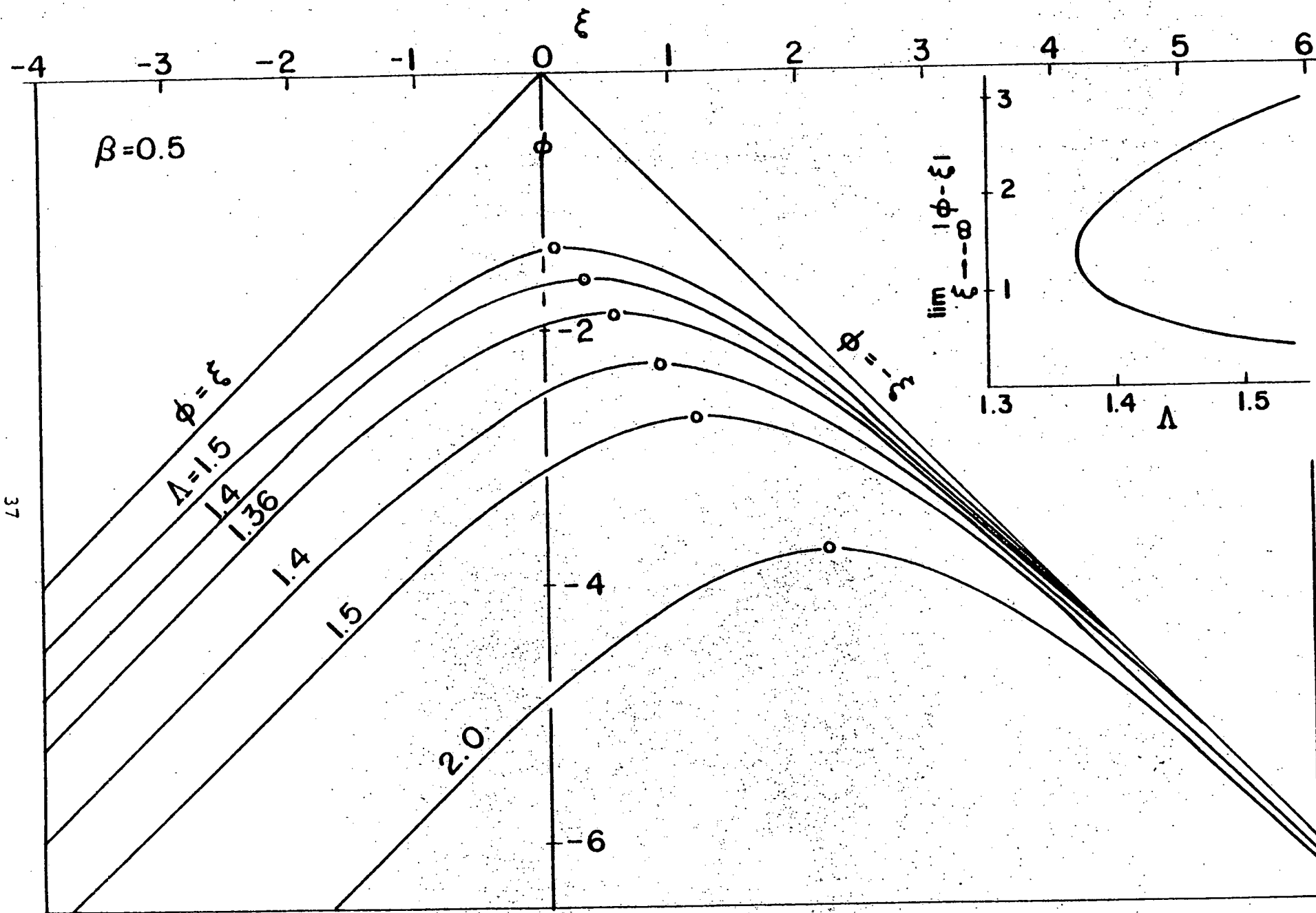


Figure 2d

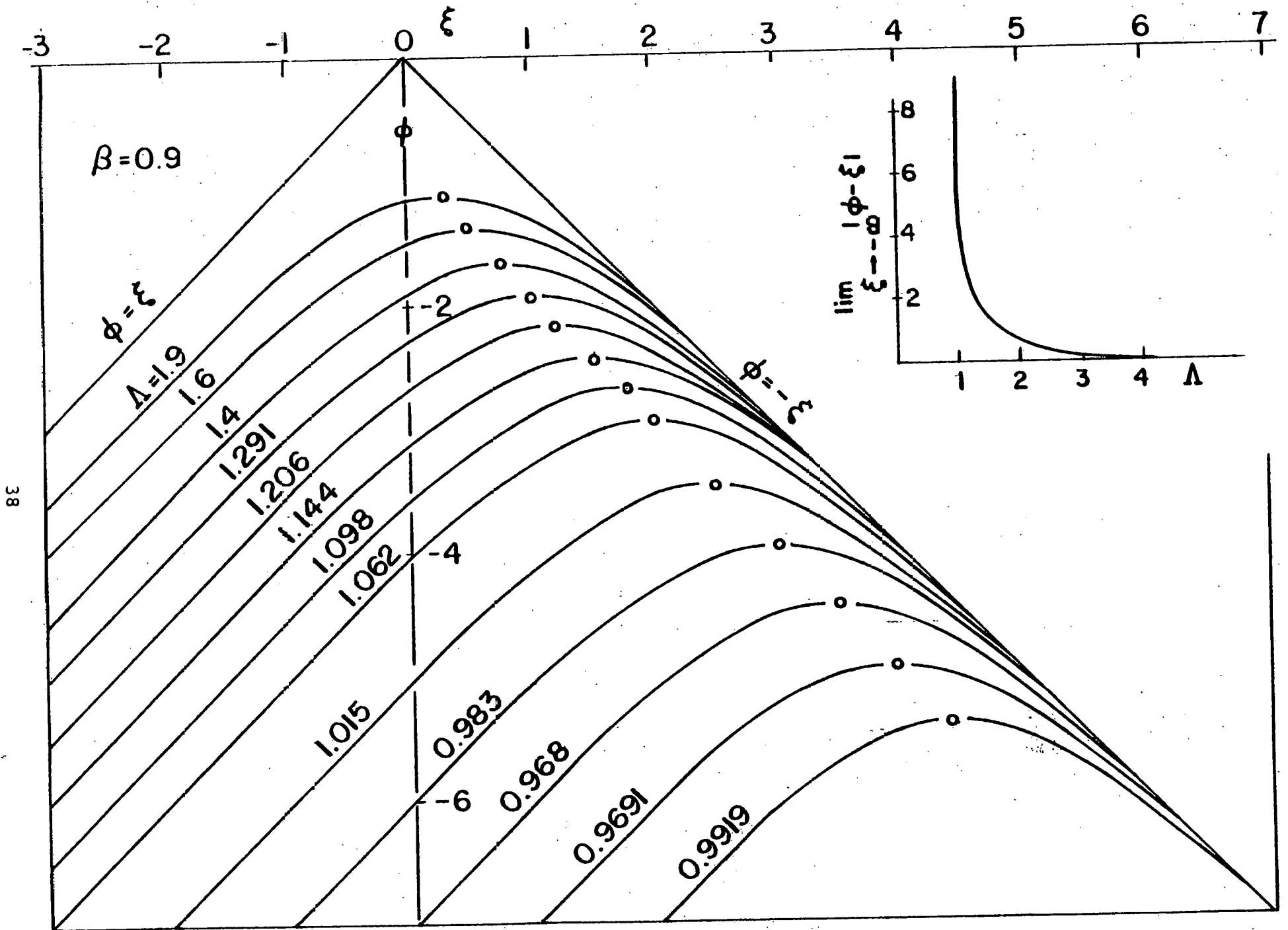


Figure 2e

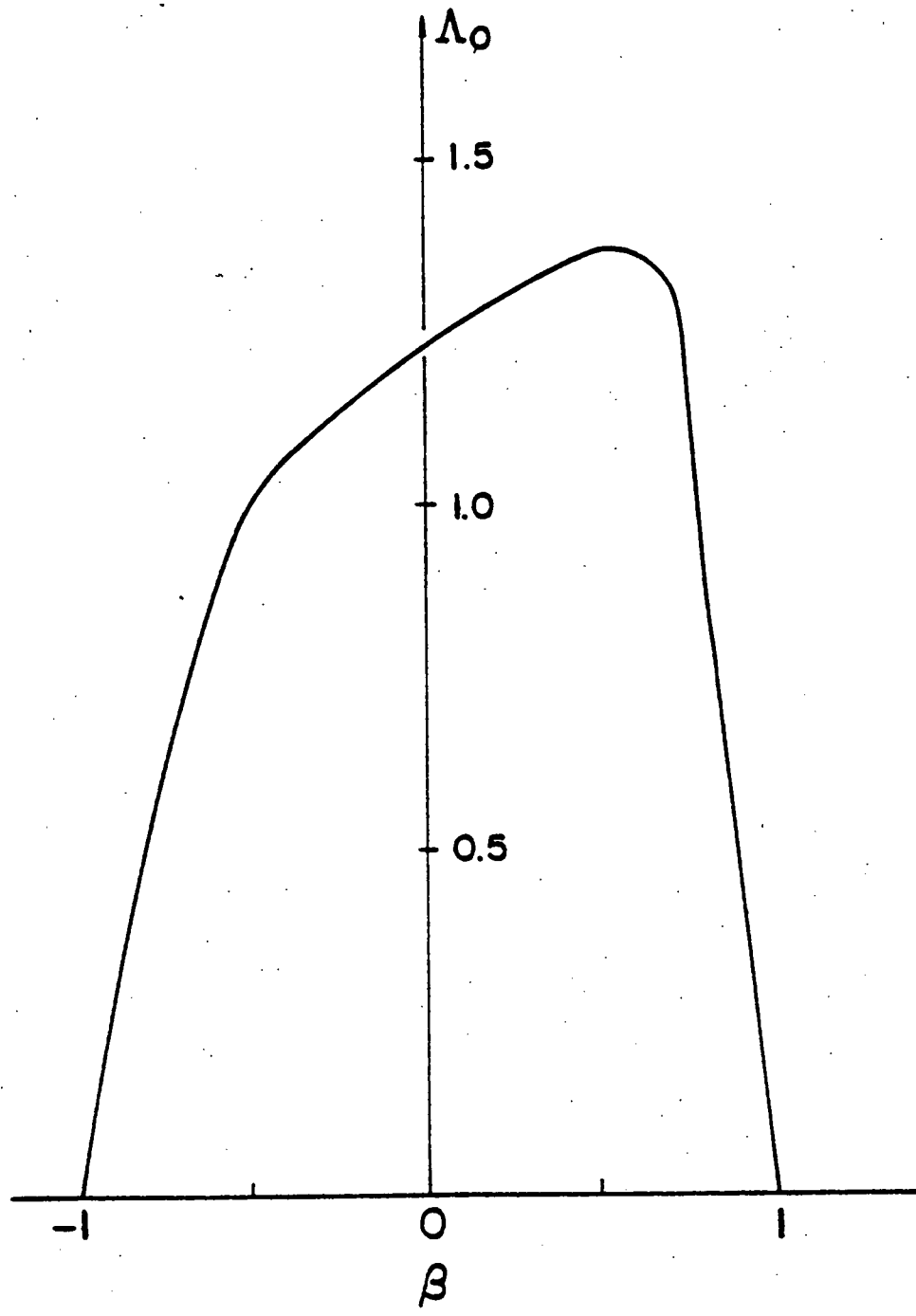


Figure 3

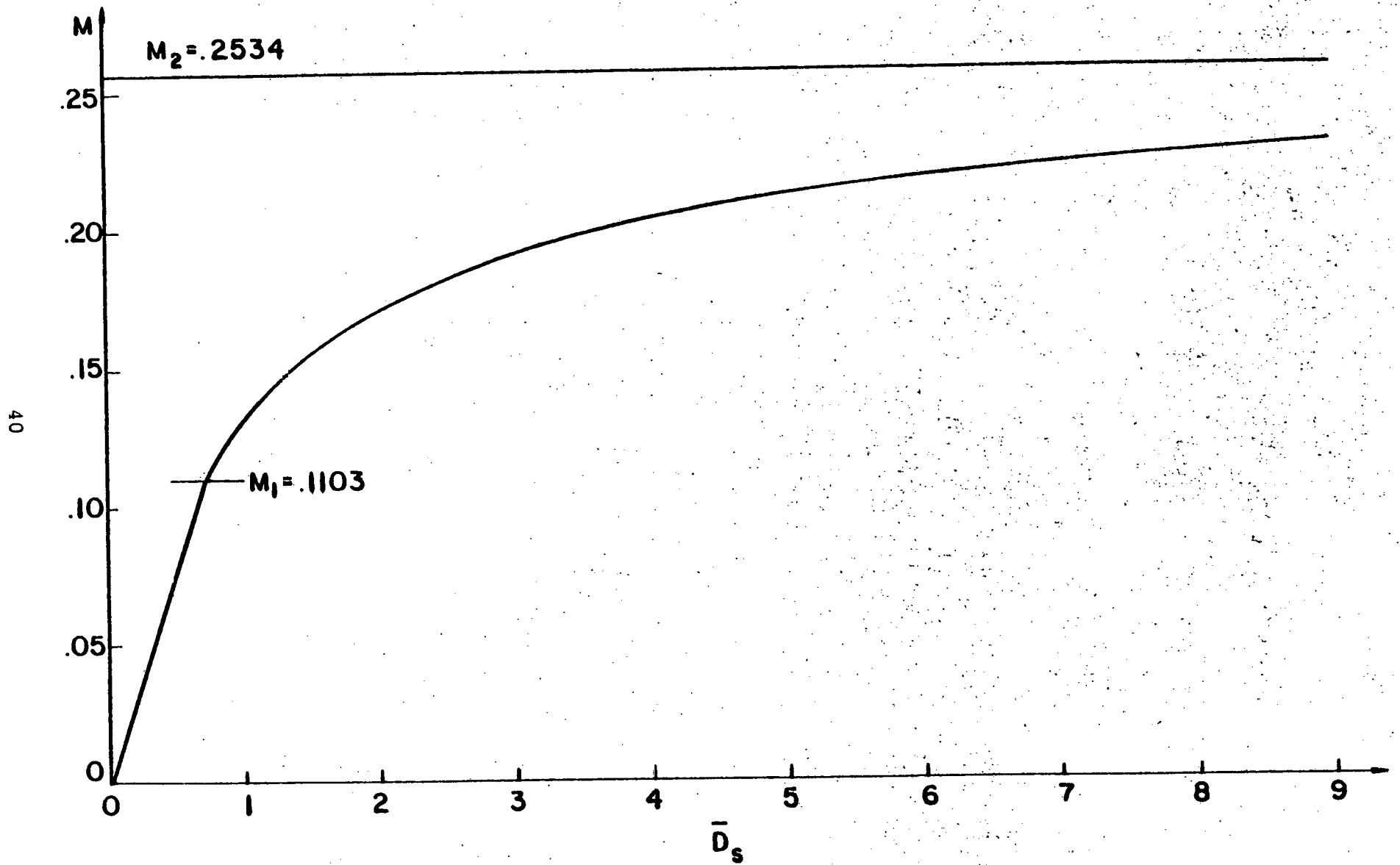


Figure 4

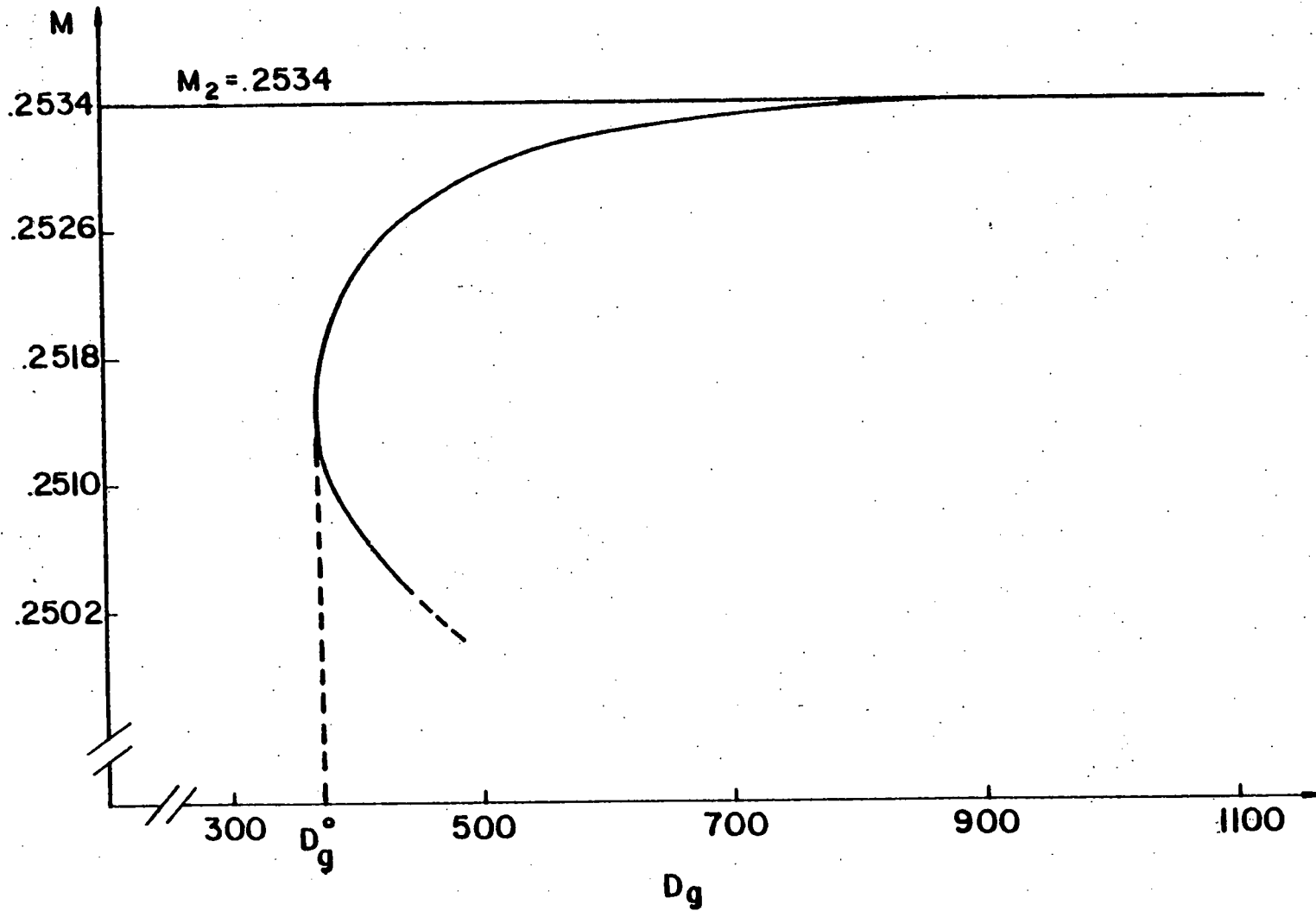


Figure 5

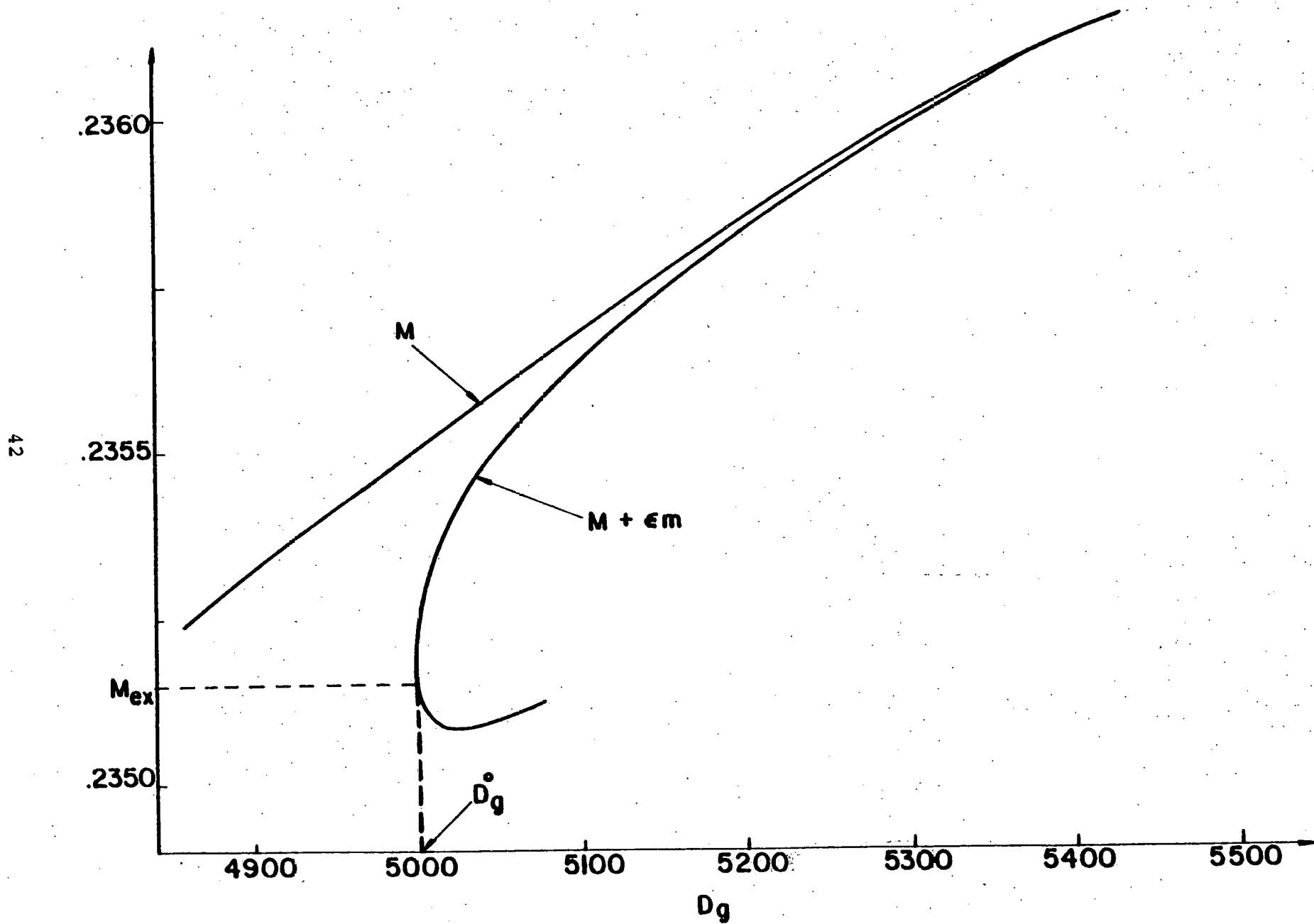


Figure 6

Polytechnic Institute of New York

AERODYNAMICS LABORATORIES

DEPARTMENT OF MECHANICAL
and
AEROSPACE ENGINEERING

WEAK BURNING AND GAS-PHASE IGNITION
ABOUT A CARBON PARTICLE IN AN
OXIDIZING ATMOSPHERE

by Moshe Matalon

JULY 1980

Supported by the U. S. Department of
Energy, MHD Division, under Contract
No. ET-78-C-01-3084

POLY Report No. 80-21

WEAK BURNING AND GAS-PHASE IGNITION

ABOUT A CARBON PARTICLE IN AN

OXIDIZING ATMOSPHERE.

Moshe Matalon
Polytechnic Institute of New York
Aerodynamics Laboratories
Farmingdale, N. Y. 11735

ABSTRACT

The departure from frozen flow behavior about a carbon particle in an oxidizing atmosphere, has been discussed in order to obtain the burning rate M over a wide range of the Damköhler number D_g (representing either the particle size or the ambient pressure). The frozen limit ($D_g \rightarrow 0$) leads to values of M ranging up to M_2 , the maximum burning rate corresponding to diffusion controlled heterogeneous reactions. By contrast, for finite values of D_g we find that the burning rate is limited by $M_{ig} < M_2$. The maximum Damköhler number D_g^0 given by an explicit formula, corresponds to gas phase ignition.

Supported by the U. S. Department of Energy, MHD Division, under Contract No. ET-78-C-01-3084.

INTRODUCTION

In a recent paper (Matalon, 1980), the problem of a carbon particle immersed in an oxidizing atmosphere has been considered. The departure from equilibrium flow corresponding to large gas phase Damköhler number $D_g \rightarrow \infty$, has been studied in order to describe the behavior of the flow field for a wider range of D_g . In the present study, we will address the situation corresponding to a frozen flow $D_g \rightarrow 0$ and its extension to a weak oxidation of carbon monoxide, by increasing D_g .

In the absence of gas phase reactions, the burning rate M (rate of particle mass loss) depends solely on the surface Damköhler numbers D_s and \bar{D}_s corresponding to the direct ($C+O_2$) and indirect ($C+CO_2$) carbon oxidations, respectively. The response of M versus \bar{D}_s (Fig. 1) for various values of \bar{D}_s/D_s , (a function of the surface temperature T_s alone) is a monotonic increasing function which tends asymptotically to a finite value M_2 . All the values up to M_2 are attainable depending on the particle size and its surface temperature. This frozen behavior has been previously worked out by Libby and Blake (1979) and indeed our results coincide in this limit, although their analysis has been carried out in terms of element mass fractions rather than individual species. The new aspect of the present study is the description of the flow field while departing from the limit $D_g \rightarrow 0$. For finite values of the Damköhler number D_g , a weak oxidation of carbon monoxide takes place and the burning rate depends on D_g as well. Furthermore, depending on whether \bar{D}_s/D_s is greater or less than one, the burning rate is larger or smaller than the frozen value, respectively (see Fig. 3). The chemical

activity which is confined to a thin zone near the particle surface, becomes more intense as D_g increases until the maximum value D_g° is reached. Beyond the critical Damköhler number D_g° , only strong gas-phase burning is possible as described by Matalon (1980). Therefore D_g° marks the conditions where the gas-phase is ignited and the $\text{CO}+\text{O}_2$ diffusion flame is formed. It should be mentioned that the particle itself has been ignited while reaching the temperature T_s and the surface reactions remain operative as long as D_s and \bar{D}_s are not negligibly small. Transient effects during ignition and extinction of the particle have been analyzed and reported recently by Libby (1980).

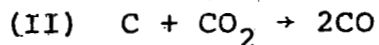
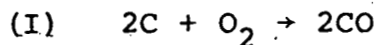
A comparison between the frozen and equilibrium limits (Matalon 1980, Libby and Blake 1979) indicate that both tend to the same burning rate M_2 in the limit of diffusion controlled heterogeneous reactions ($D_s, \bar{D}_s \rightarrow \infty$). Furthermore, both cases lead to the same burning rate for all values of \bar{D}_s , when the latter equals D_s . However, when $\bar{D}_s/D_s < 1$ we find that M for frozen flow exceeds that for equilibrium whereas for $\bar{D}_s/D_s > 1$ the reverse is true. Since the kinetics of carbon oxidation are not very well understood and a variety of data exist for their reaction rates, the ratio \bar{D}_s/D_s would be better considered as a parameter. Libby and Blake (1979) have based their numerical calculations on the correlations provided by Field (1969) and Dobner (1976) for which $\bar{D}_s/D_s < 1$ for all values of T_s . Therefore, their conclusion that M for frozen flow exceeds that for equilibrium is consistent with ours. If the data given by Caram and Amundson (1977) are assumed for example, we find that $\bar{D}_s/D_s < 1$ only for surface temperatures T_s below 1642K. For T_s higher than 1642K, the ratio $\bar{D}_s/D_s > 1$ and M for equilibrium

exceeds that for frozen flow.

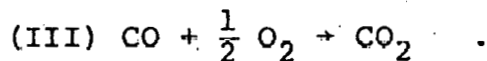
By plotting the response of M versus D_g , we find that starting from $D_g = 0$, the curve branches away from the frozen behavior; it lies above the limiting curve when $\bar{D}_s/D_s > 1$ and below it when $\bar{D}_s/D_s < 1$. On the other hand, we have found (Matalon, 1980) that starting from $D_g = \infty$ the response branches away from the equilibrium behavior in such a way that it lies below the limiting curve when $\bar{D}_s/D_s > 1$ and above it when $\bar{D}_s/D_s < 1$. In any case, the response curve branches away from the frozen limit heading towards its equilibrium counterpart. The middle branch connecting the two ends of the curve corresponds to partial burning of CO and O_2 and will be reported elsewhere (Matalon, 1980a). Similar response curves have been constructed in related problems (e.g. Ludford et al, 1976).

FORMULATION

We consider a spherical carbon particle immersed in an ambient atmosphere of oxidant-inert mixture. At the surface of the particle, carbon oxidizes according to



and the carbon monoxide thus produced may react with O_2 to form carbon dioxide, via



Therefore, the chemical species assumed present in the gas phase are CO, O_2 , CO_2 and inert (usually N_2) and the subscripts 1-4 will be used respectively. Following Matalon (1980) (which should be consulted for more details of the derivation and the assumptions), the governing equations written in a dimensionless form are given by

$$\left\{ \begin{array}{l} -\frac{1}{1-\alpha} L(Y_1) = -\frac{1}{\alpha} L(Y_2) = L(Y_3) = L(T) = \Omega \\ L(Y_4) = 0 \\ L \equiv \frac{M-2r}{r^2} \frac{d}{dr} - \frac{d^2}{dr^2} \end{array} \right. \quad (1)$$

where L is the convective-diffusive operator, r the radial coordinate, Y_i the mass fraction of species i , T the temperature and M the burning rate. The coefficient $\alpha = m_{O_2}/2m_{CO_2}$ is a mass stoichiometric of the system (I)-(III) where m_i is the molecular weight of species i . Finally, if the reaction III is assumed second order (Howard et al, 1973) and its rate satisfied a well defined Arrhenius expression, then

$$\Omega = D_g \rho^2 Y_1 Y_2^{1/2} \exp(-\theta/T) \quad (2)$$

In (2), D_g represents the gas-phase Damköhler number, θ the activation energy and ρ the density of the mixture given by the equation of state $\rho T = 1$.

The boundary conditions associated with (1) are

$$T = T_\infty, \quad Y_i = Y_{i_\infty} \quad \text{for } i = 1, 4 \quad \text{as } r \rightarrow \infty \quad (3)$$

$$\left\{ \begin{array}{l} MY_1 - dY_1/dr = (1-\alpha)D_s Y_2/\alpha + 2(1-\alpha)\bar{D}_s Y_3 \\ MY_2 - dY_2/dr = -D_s Y_2 \\ MY_3 - dY_3/dr = -\bar{D}_s Y_3 \\ MY_4 - dY_4/dr = 0 \end{array} \right. \quad (4)$$

$$T = T_s \quad \text{at } r = 1$$

The conditions at $r = 1$ state that the net mass flux equals the rate of consumption/production per unit area by the heterogeneous reactions and that the particle is isothermal at its surface. The conditions at $r = \infty$ specify the given ambient conditions. The

parameters D_s and \bar{D}_s introduced in (4) are the surface Damköhler numbers corresponding to (I) and (II) respectively. All the Damköhler numbers have been defined in the referred paper (Matalon, 1980): D_g is proportional to $(ap_0)^2$ where a is the particle radius and p_0 the ambient uniform pressure and D_s, \bar{D}_s are each proportional to ap_0 and depend on T_s through the specific reaction rate of the chemical reaction they represent. The ratio \bar{D}_s/D_s is a function of the surface temperature T_s alone.

Our main goal is to determine the burning rate M which can be evaluated if in addition to (1), the overall mass conservation $\sum_{i=1}^4 Y_i = 1$ is used. Instead of solving all the five equations (1) it has been shown (Matalon, 1980) that only one species equation, say Y_3 , has to be solved; the others result from

$$\begin{aligned} \alpha(1 - e^{-M/r}) + (1 - 2\alpha)(Y_2 - Y_{2\infty} e^{-M/r}) + \alpha(1 - \alpha)(Y_3 - Y_{3\infty} e^{-M/r}) &= 0 \\ \alpha(Y_1 - Y_{1\infty} e^{-M/r}) + (1 - \alpha)(Y_2 - Y_{2\infty} e^{-M/r}) + 2\alpha(1 - \alpha)(Y_3 - Y_{3\infty} e^{-M/r}) &= 0 \end{aligned} \quad (5)$$

It should be emphasized that the relations (5) hold everywhere in the flow field and do not involve any approximation while derived from the governing equations.

Following Matalon (1980), we start by writing the gas phase Damköhler number D_g in the form

$$D_g = \exp(\theta/T_c) \quad (6)$$

and in doing so define a characteristic temperature T_c which becomes indirectly related to a and p_0 . Considering the activation energy θ to be large, the nature of the reaction term Ω appearing in (1), is well understood as follows. For relatively large T_c (or small particles, for example) the factor $\exp(\theta/T_c - \theta/T)$ in (2) is exponentially small everywhere and the gas phase is effectively

frozen. While reducing T_c (i.e. for larger particles), this factor increases in magnitude and becomes $O(1)$ in a region where T_c reaches the highest temperature; for a hot particle in a colder ambient this temperature is of course T_s . The gas phase is therefore frozen everywhere but in a thin zone near the particle where Ω is no longer negligible. Replacing T_c in (6) by T_s and letting $\tilde{D}_g = \exp[\theta(T_s - T_c)/T_s^2]$ represents the small deviations between the two temperatures, we obtain

$$\Omega = \tilde{D}_g \rho^2 Y_1 Y_2^{1/2} \exp(\theta/T_s - \theta/T) \quad (7)$$

When $\tilde{D}_g \rightarrow 0$, we recover the frozen limit but for finite values of \tilde{D}_g the departure from the frozen flow behavior is described and this is our concern in the present paper.

FROZEN FLOW ($\tilde{D}_g = 0$)

In the absence of the reaction term Ω , equations (1) can be easily solved, yielding

$$Y_i = Y_{i_\infty} + (Y_{i_s} - Y_{i_\infty}) (1 - e^{-M/r}) / (1 - e^{-M}) \quad , \quad i = 1, 4 \quad (8)$$

where Y_{i_s} stands for the unknown value of the mass fraction of species i at the surface $r = 1$ and Y_{i_∞} the given ambient value, as in (3). A similar expression to (8) can be written for the temperature T . By satisfying the boundary conditions (4), using the expressions (8), we first obtain

$$Y_{4_s} = Y_{4_\infty} e^{-M} \quad ; \quad Y_{3_s} = Y_{3_\infty} [1 + (1 + \bar{D}_s/M) (e^M - 1)]^{-1}$$

after which Y_{1_s} and Y_{2_s} are readily obtained from (5). Furthermore, a transcendental equation for M

$$M - \bar{D}_s (e^{M/2} - 1) + (\bar{D}_s - D_s) \left\{ \frac{v Y_{3_\infty}}{1 + (1 + D_s/M) (e^M - 1)} \right\} = 0 \quad (9)$$

is derived which has to be solved numerically for any given set of Damköhler numbers D_s and \bar{D}_s . In (9) we have introduced $M_2 = \ln[1+(1-2\alpha)(Y_{2\infty}/\alpha+Y_{3\infty})]$ and $\nu = (1-2\alpha)/\alpha$ for convenience.

The burning rate M obtained from (9) has been plotted in Fig. 1 as a function of \bar{D}_s for different values of the ratio \bar{D}_s/D_s , which is fixed once T_s is specified. When $\bar{D}_s = 0$, the surface temperature is low enough for the heterogeneous reactions to take place and $M = 0$. Then, M increases with \bar{D}_s and tends asymptotically to M_2 when the reactions (I,II) are diffusion controlled. The same results have been previously obtained by Libby and Blake (1979) who chose to plot the burning rate (K in their notation) as a function of T_s .

It is appropriate at this point to compare the response curve $M(\bar{D}_s)$ to that obtained for equilibrium gas-phase behavior (Matalon, 1980). Both indicate that the burning ceases when $\bar{D}_s \rightarrow 0$ and that M tends to M_2 for the diffusion controlled limit. Furthermore, when $\bar{D}_s = D_s$ eq. (9) reduces to $M - \bar{D}_s (e^{M_2 - M} - 1) = 0$; i.e. M attains the same value whether equilibrium or frozen flow exist. Thus, the curve corresponding to $\bar{D}_s/D_s = 1$ in Fig. 1 corresponds to equilibrium as well and it is apparent that for $\bar{D}_s/D_s < 1$ the burning rate for frozen flow exceeds that for equilibrium while for $\bar{D}_s/D_s > 1$ the reverse is true.

DEPARTURE FROM FROZEN FLOW.

For finite values of \bar{D}_g , the reaction term Ω can be neglected everywhere but in a thin region near the particle. Therefore, the mass fractions distribution still follow (8) but Y_{i_s} are not determined directly from the boundary conditions (4) as before. Instead, the gradients near $r = 1$ have to be corrected in order to

take into consideration a weak reaction rate; formally this is obtained by perturbing Ω about $T = T_s$. We start by writing the temperature profile

$$T = T_\infty + (T_s - T_\infty) (1 - e^{-M/r}) / (1 - e^{-M}) \quad (10)$$

Then, according to (7), we perturb the temperature about its surface value, namely $T = T_s + \epsilon t + \dots$ and similarly we write for the mass fractions $Y_i = Y_{i_s} + \epsilon y_i + \dots$, $i = 1, 4$. Stretching the coordinate

$$r = 1 + \epsilon [M(T_s - T_\infty) / (e^M - 1)] \xi$$

where $\epsilon = T_s^2 / \theta \ll 1$, the governing equations (1) become

$$-\frac{1}{1-\alpha} \frac{d^2 y_1}{d\xi^2} = -\frac{1}{\alpha} \frac{d^2 y_2}{d\xi^2} = \frac{d^2 y_3}{d\xi^2} = \frac{d^2 t}{d\xi^2} = \frac{1}{2} \Lambda e^t \quad (11)$$

The parameter Λ is related to the Damköhler number and is given by

$$\Lambda = [2Y_{1_s} Y_{2_s}^{1/2} (e^M - 1)^{2/M^2} (T_s - T_\infty)^2 \theta] \tilde{D}_g \quad (12)$$

The boundary conditions associated with (11) for y_i are the original conservation laws (4) applied at $\xi = 0$ after replacing dy_i/dr by $dy_i/d\xi$, and the matching requirement as $\xi \rightarrow \infty$. As to the temperature, its value at the surface has been written as $T_s + \epsilon t_s$ ($-\infty < t_s < \infty$) so that $t = t_s$ at $\xi = 0$ and matching with (10) implies $dt/d\xi = -1$ as $\xi \rightarrow \infty$.

We start by writing the solution for the temperature, namely

$$t = \ln \{ \Lambda^{-1} \operatorname{sech}^2 [(\xi + \xi_0)/2] \} \quad (13)$$

where $\xi_0 = 2 \operatorname{sech}^{-1} (\Lambda e^{t_s})^{1/2}$, and note that it exists for $\Lambda \leq e^{-t_s}$ only. When the equality holds $\xi_0 = 0$ and the solution (13) is single valued. However when $\Lambda < e^{-t_s}$, the two values $\xi_0 = \pm |\xi_0|$

lead to two distinct solutions for t as shown in Fig. 2 for representative values of t_s . Thus, for a given t_s , the critical Damköhler number

$$\tilde{D}_g^\circ = 0.5M^2 (T_s - T_\infty)^2 (e^M - 1)^{-2} Y_{1s}^{-1} Y_{2s}^{-1/2} \theta e^{-t_s} \quad (14)$$

is the maximum value of \tilde{D}_g above which (13) does not possess a solution matchable with the outer flows (10) and (8).

Once the solution for t is written, the remaining of eqs. (11) are linear and therefore can be readily integrated. In particular, the slopes $dy_i/d\xi$ at $\xi = 0$ can be evaluated and together with (4) the surface mass fractions Y_{is} are determined. In addition, the following transcendental equation is derived

$$M - \bar{D}_s (e^{M_2 - M} - 1) + v(\bar{D}_s - D_s) \left\{ \frac{Y_{2\infty}^{-\alpha} (T_s - T_\infty) [1 + (1 - \Lambda e^{t_s})^{1/2}]}{1 + (1 + D_s/M)(e^M - 1)} \right\} = 0 \quad (15)$$

which has to be solved numerically for M given D_s , \bar{D}_s and \tilde{D}_g . The determination of y_{is} requires a higher order approximation than (11), namely $O(\epsilon^2)$, that we shall not discuss here.

For any value of $\tilde{D}_g < \tilde{D}_g^\circ$ (i.e. $\Lambda \ll e^{-t_s}$), eq. (15) yields two distinct solutions for M which tend to a unique value M_{ig} when \tilde{D}_g° is reached. When $\tilde{D}_g \rightarrow 0$, one of the solutions tend to the frozen limit and eq. (15) reduces to (9) as it should; the other solution tends to a different limit which has been recognized (Matalon, 1980a) as a partial burning flame and will not be discussed here. In Fig. 3 the burning rate has been plotted versus \tilde{D}_g indicating the double structure of the solution for $\tilde{D}_g > 0$. The calculations were made for representative values of the concentrations $Y_{1\infty} = 0.05$, $Y_{2\infty} = 0.3$, $Y_{3\infty} = 0.2$, for the ambient temperature $T_\infty = 300\text{K}$ and surface temp-

erature $T_s = 1655\text{K}$ with a correction of the order $\epsilon T_s = 300\text{K}$. For the Damköhler numbers we chose $\bar{D}_s^2/\tilde{D}_g = 70$ and the two different values for $\bar{D}_s/D_s = 2, 0.5$. For $\bar{D}_s/D_s > 1$ (Fig. 3a), the burning rate exceeds its frozen value and the reverse is true for $\bar{D}_s/D_s < 1$ (Fig. 3b). Starting from $\tilde{D}_g = 0$, the gas phase surrounding the particle is frozen and M is given by (9). By slightly increasing \tilde{D}_g , a weak oxidation of carbon monoxide occurs at the vicinity of the particle and the burning rate differs from that obtained in the frozen limit; it achieves a higher or lower value depending on whether $\bar{D}_s/D_s > 1$ or not. This behavior persists until the maximum \tilde{D}_g° is reached; since beyond this value a weak CO oxidation is not possible and according to Matalon (1980) a strong burning occurs with a diffusion flame standing off the particle, \tilde{D}_g° is recognized as the ignition Damköhler number. An explicit formula for $D_g^\circ = \tilde{D}_g^\circ e^{\theta/T_s}$ is given by (14) and the corresponding M_{ig} follows (15). It should be emphasized that in this content ignition is referred to the $\text{CO} + \text{O}_2$ reaction whereas the particle itself has been already ignited once its temperature has reached T_s .

Multiple solutions at near ignition and extinction have been previously obtained while analysing the structure of a one dimensional diffusion flame (Liñan 1974; Matalon et al, 1979). It has been generally believed that one of the possible solutions is unstable (Williams, 1971) and some evidence are found in Peters (1978) and Matalon and Ludford (1980). The unstable branch, which in the present content corresponds to the solution tending towards a partial burning flame, cannot be realized physically and on that basis we have concluded that \tilde{D}_g° marks ignition of the gas-phase reaction.

CONCLUSION.

The departure from frozen flow behavior ($D_g \rightarrow 0$) has been studied in order to obtain the burning rate over a wide range of Damköhler numbers D_g . The frozen limit leads to M ranging up to M_2 where M_2 is the burning rate for diffusion controlled heterogeneous reactions ($D_s, \bar{D}_s \rightarrow \infty$). For finite values of D_g , a weak carbon monoxide oxidation occurs at the vicinity of the particle and the burning rate, which now depends on D_g as well, is corrected accordingly. The value of M is higher or lower than its frozen value depending on whether $\bar{D}_s/D_s < 1$ or not. In any case, the burning rate is limited from above by $M_{ig} < M_2$ and the maximum Damköhler number is D_g^0 . The analysis provides an explicit formula for D_g^0 which was recognized as the gas-phase ignition Damköhler number.

The present analysis leads to the construction of only one part of the response curve of M versus D_g (Fig. 3). Completion of the curve has been reported by Matalon (1980a) and is based on the two studies: the departure from frozen flow behavior (discussed above) and the departure from equilibrium (Matalon, 1980). Starting from $D_g = 0$, the gas phase is first totally frozen; however by increasing D_g , a weak CO oxidation takes place near the particle and the response curve branches away heading towards the equilibrium limit. On the other hand, starting from $D_g = \infty$ complete burning of CO and O_2 occurs at a diffusion flame which, for lower D_g allows some leakages of reactants. As a consequence the burning rate branches away from the limiting curve heading towards the frozen limit. These two cases which consist of the end parts of the response curve are connected by a middle branch corresponding to partial burning of CO and O_2 .

Acknowledgement.

The author gratefully acknowledges Professor M. H. Bloom's hospitality at the Aerodynamics Laboratories PINY, during which this study was undertaken.

References.

1. Buckmaster, J.D. (1975), Combustion of a Liquid Fuel Drop, Letters in Appl. Engr. Sci., 3, pp. 365-372.
2. Caram, H.S. and Amundson, N.R. (1977), Diffusion and Reaction in a Stagnant Boundary Layer about a Carbon Particle, Ind. Eng. Chem. Fundam, 16, pp. 171-181.
3. Dobner, S. (1976), Modelling of Entrained Bed Gasification: The Issues, Elect. Power Res. Inst. Memo.
4. Field, M.A. (1979), Rate of Combustion of Size-Graded Fractions of Char from a Low-Rank Coal between 1200°K and 2000°K. Combustion Flame, 13, pp. 237-252.
5. Libby, A.P. and Blake, T.R. (1979), Theoretical Study of Burning Carbon Particles, Combust. Flame, 36, (2); 139-170.
6. Libby, A.P. (1980), Ignition, Combustion and Extinction of Carbon Particles, Combust. Flame, to appear.
7. Liñán, A. (1974), The Asymptotic Structure of Counterflow Diffusion Flames for Large Activation Energies, Acta Astronautica, 1, pp. 1007-1039.
8. Ludford, G.S.S., Yanitell, D.W. and Buckmaster, J.D. (1976), The Decomposition of a Cold Monopropellant in an Inert Atmosphere, Combust. Sci. Tech., 14, pp. 133-146.
9. Matalon, M., Ludford, G.S.S. and Buckmaster, J.D. (1979), Diffusion Flames in a Chamber, Acta Astronautica, 6, pp. 943-959.
10. Matalon, M. and Ludford, G.S.S. (1980), On the Near-Ignition Stability of Diffusion Flames, Int. J. Engr. Sciences, to appear.
11. Matalon, M. (1980), Complete Burning and Gas-Phase Extinction about a Carbon Particle in an Oxidizing Atmosphere, submitted for publication.
12. Matalon, M. (1980a), A Quasi-Steady State Theory of the Burning of a Carbon Particle Immersed in an Oxidizing Atmosphere, PINY report.
13. Peters, N. (1978), Liñán's Premixed Flame Stability, Combust. Flame, 33, pp. 315-318.
14. Williams, F.A. (1971), Theory of Combustion in Laminar Flows, Annual Review Fluid Mech., 3, pp. 171-188.

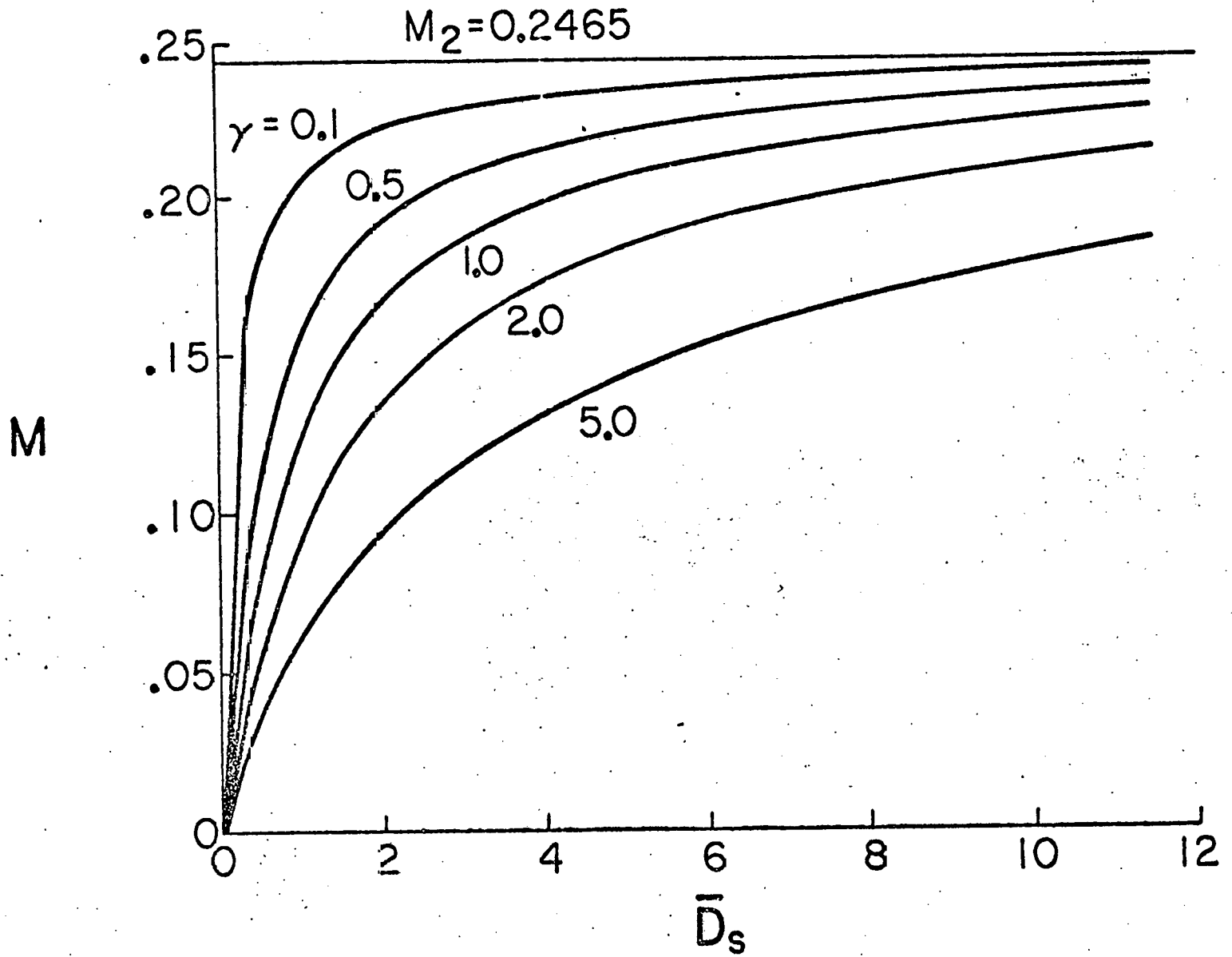
List of Figures.

Fig. 1 The variations of the burning rate with the surface Damköhler numbers for a frozen flow situation. (M plotted versus \bar{D}_s for various $\gamma = \bar{D}_s/D_s$).

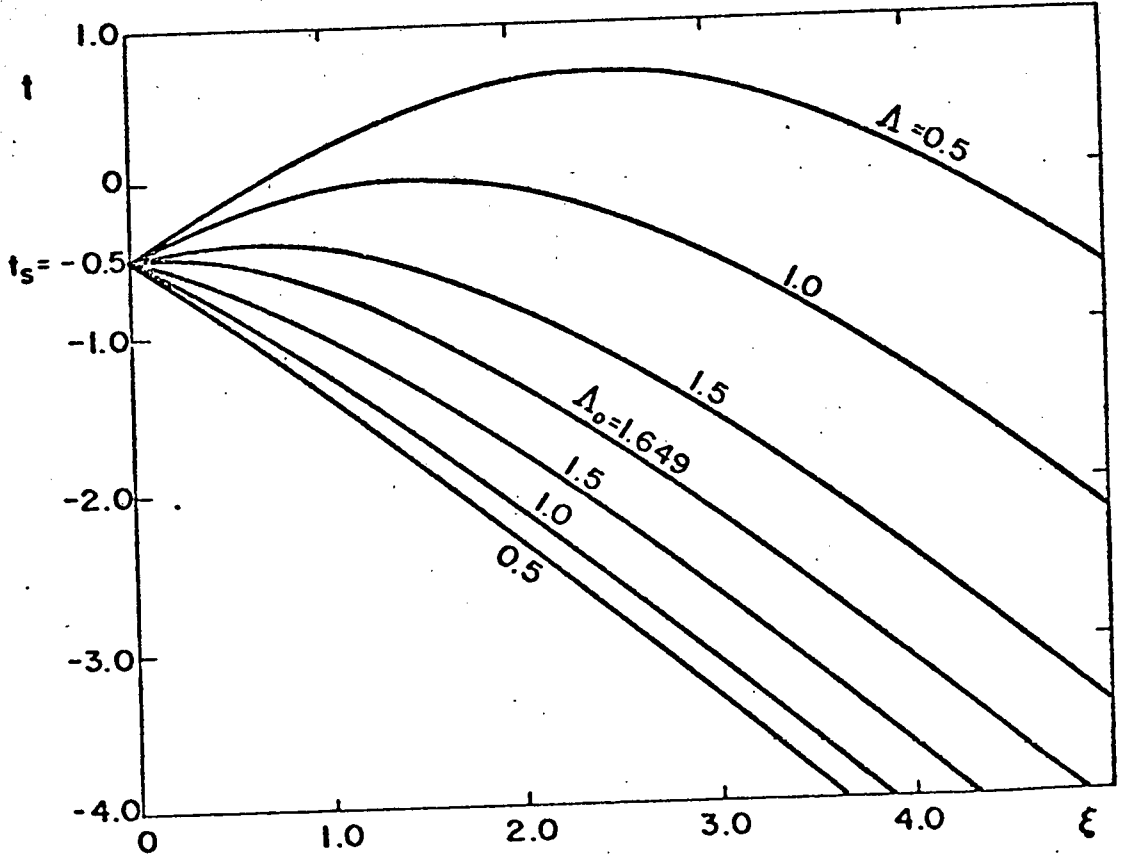
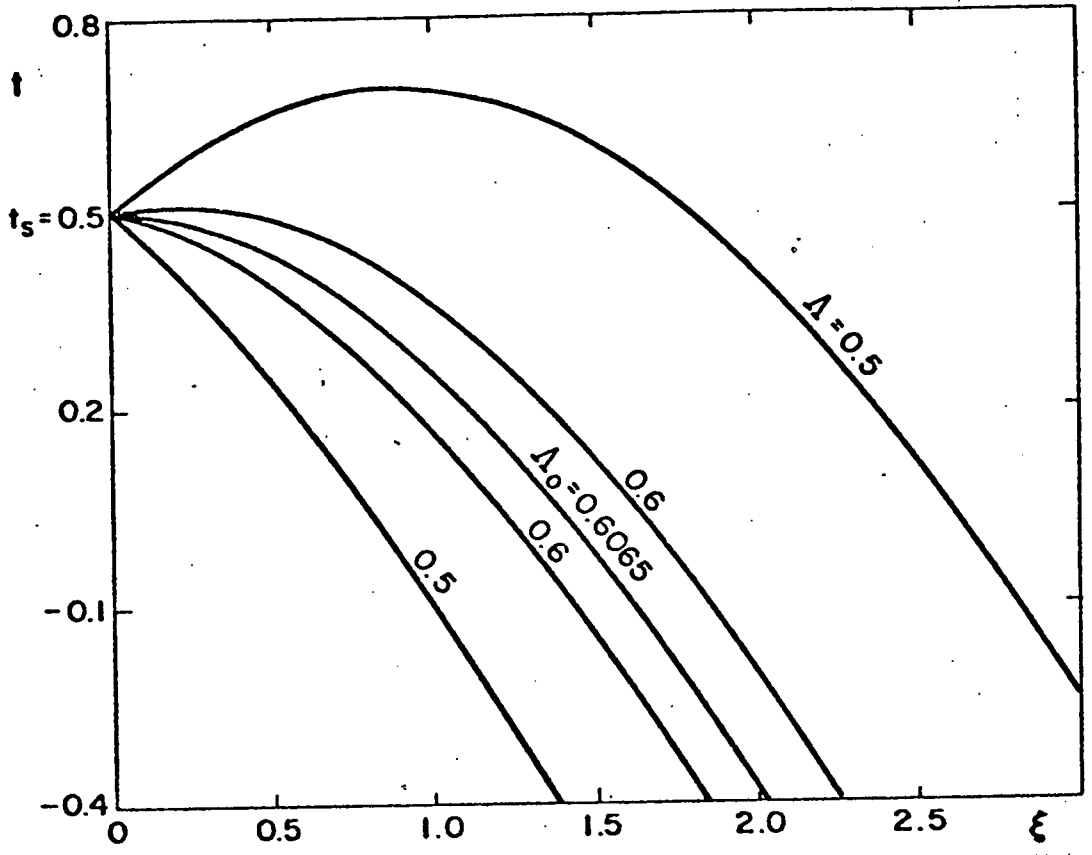
Fig. 2 The temperature profile in the reaction zone for various values of Λ indicating the double structure of the solution. Calculated for (a) $t_s = 0.5$, (b) $t_s = -0.5$.

Fig. 3 The burning rate versus the gas phase Damköhler number (finite values of \tilde{D}_g); (a) $\bar{D}_s/D_s = 2 > 1$, (b) $\bar{D}_s/D_s = 0.5 < 1$.

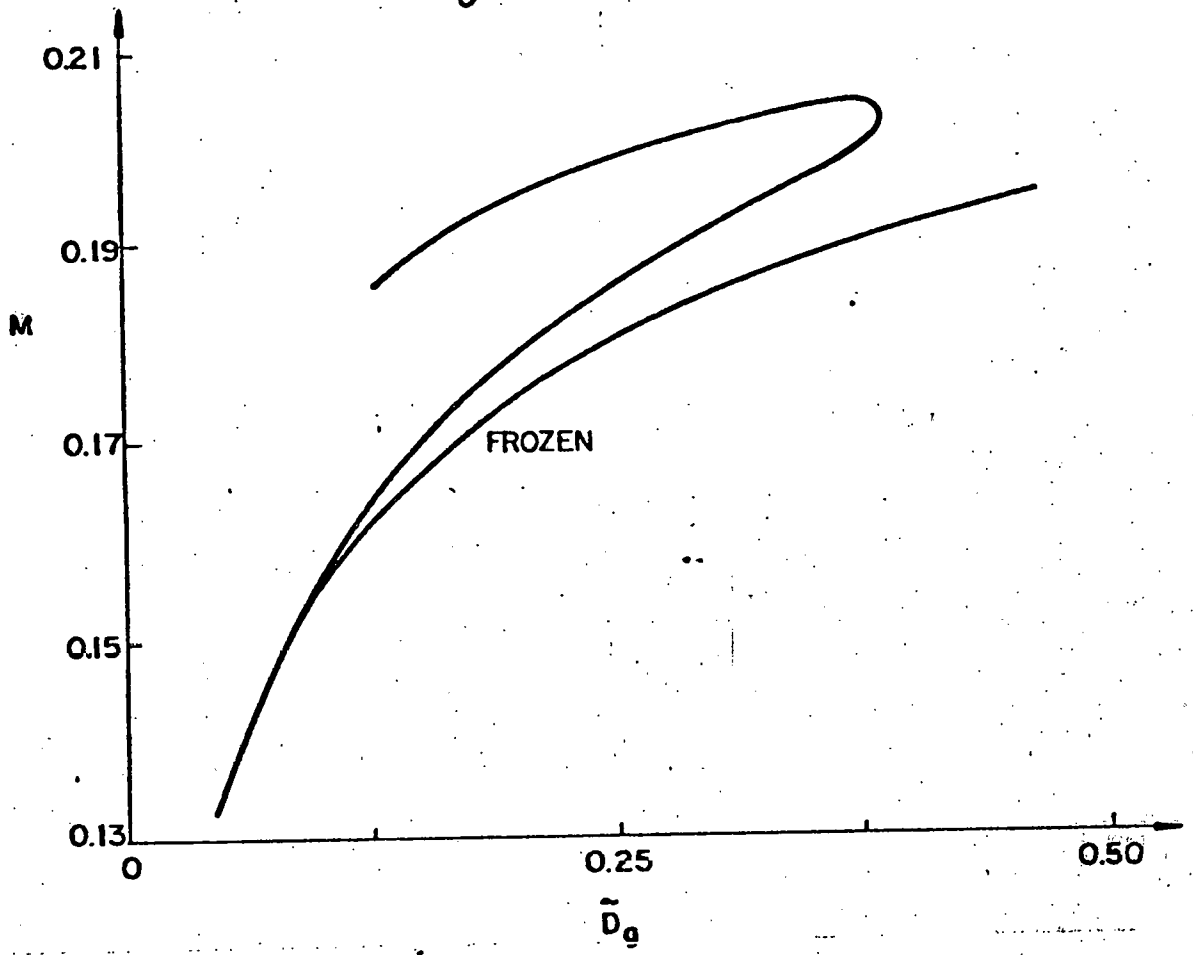
Fig. 1.



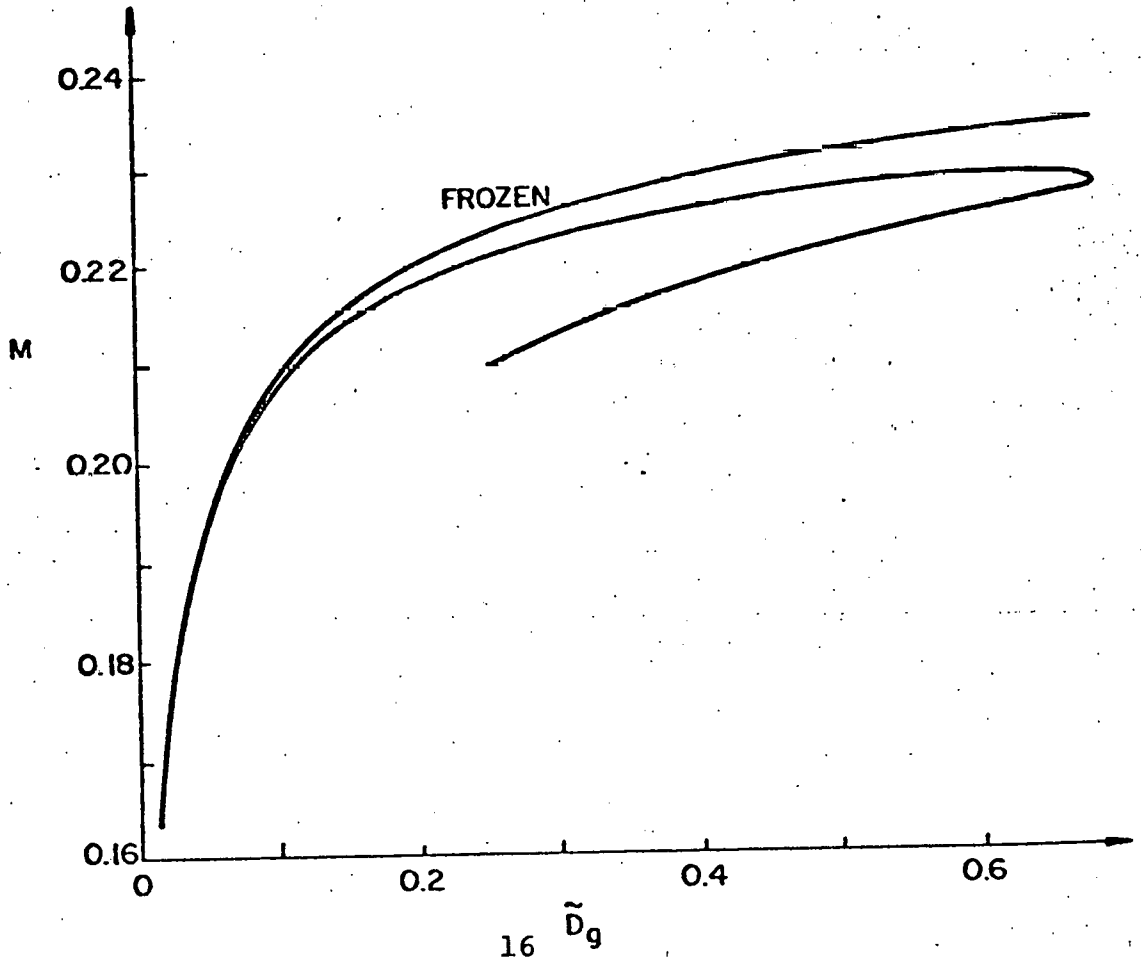
Handwritten signature



(a)



(b)



APPENDIX J

Polytechnic Institute of New York

Aerodynamics Laboratories

Department of Mechanical and
Aerospace Engineering

+

COMBUSTION OF A SOLID PARTICLE

by Moshe Matalon

of Engineering Sciences and Applied Mathematics
The Technological Institute
Northwestern University
Evanston, Illinois 60201

Supported partly by the U. S. Department of Energy, MHD Division
under Contract No. ET-78-C-01-3084

COMBUSTION OF A SOLID PARTICLE

Moshe Matalon

Engineering Sciences and Applied Mathematics

The Technological Institute

Northwestern University

Evanston, Illinois 60201

Abstract

We consider the quasi-steady burning of a carbon particle which undergoes gasification at its surface by chemical reactions, followed by a homogeneous reaction in the gas phase. The burning rate M is found as a function of the gas phase Damköhler number D_g for the whole range $0 < D_g < \infty$. The monotonic $M(D_g)$ curve, obtained for relatively very hot or very cold particles, describes the gradual transition from frozen flow to equilibrium. For moderate particle temperatures the transition is abrupt and the $M(D_g)$ curve is either S-shaped or Z-shaped. In the former the burning is enhanced at ignition while in the latter it is slowed down; this depends on the relative importance of the two competitive surface reactions. At extinction, the reverse is true: burning is slowed down in the case of an S curve and is enhanced in the case of a Z curve.

Supported partly by the U. S. Department of Energy, MHD Division under Contract No. ET-78-C-01-3084.

INTRODUCTION

The current theory of combustion of solid particles is based on the quasi-steady approximation. Accordingly, one assumes a slow rate of change in the particle size and considers a steady burning for a given particle diameter. For definiteness, we consider here the problem of a carbon particle in a quiescent oxidant atmosphere as representing heterogeneous combustion between solid and gas followed by homogeneous burning in the gas-phase.

Two basic models have been proposed [1]: Nusselt [2] assumes that the only oxidation of carbon ($C+O_2$) occurs at the surface of the particle and Burke and Schumann [3] assumes that carbon is consumed by CO_2 at the surface while the CO thus formed reacts with O_2 at a flame sheet to form CO_2 . They have been called the single and double film models respectively. Indeed, they correspond to the limits in which the homogeneous reaction is either frozen ($D_g \rightarrow 0$) or is very fast and equilibrium prevails in the gas phase ($D_g \rightarrow \infty$); here D_g is the Damköhler number. Recently, Matalon [4,5] studied the departure from these limiting cases in order to determine the behavior of the system over a wider range of D_g . Other works on the subject have been cited in the referred papers. The present study gives a complete picture of the process spanning the whole range of parameter values. Starting with the conservation equations of mass and energy governing the combustion process, we look for solutions over the whole range $0 \leq D_g \leq \infty$ (D_g represents either the particle size or the ambient pressure). Furthermore, the whole parameter plane T_s (surface temperature) - T_∞ (ambient temperature) will be considered and the response of the burning rate M versus D_g will be determined in each case. There

are two different types of response curves (see Fig. 4): the monotonic curve characterized by a unique solution for each D_g (regions II, III) and S or Z curves characterized by multiple solutions for a certain range of D_g (regions I). The monotonic curve describes the gradual transition from a frozen gas phase through partial burning to equilibrium. The S or Z curves, indicate that the transition from weak to strong burning or vice versa, is abrupt (assuming that the middle branch is unstable) so that the system exhibits ignition and extinction phenomena. The various states followed along the curves have been delineated as well as the mode of the combustion along each branch.

Since there are two competitive reactions taking place at the surface of the particle, the ratio of their rates γ , which is a function of T_s alone, plays a significant role. It determines whether the burning rate for equilibrium flow exceeds that for frozen behavior and as a consequence whether the response curve is S or Z shaped. In the former case the burning rate is enhanced at ignition whereas in the latter it is slowed down (the reverse is true at extinction). It should be emphasized that in the present context ignition/extinction refer only to the homogeneous reaction $\text{CO} + \text{O}_2$; the heterogeneous reactions at the particle surface are continuously active as long as T_s is high enough to make their rate significant.

FORMULATION

We consider a particle which undergoes gasification by surface chemical reactions followed by an exothermic homogeneous reaction in the surrounding gas phase. For a spherical particle and under suitable conditions, the governing equations in the gas phase in a dimensionless form are

$$(1) \quad L(Y_i) = \beta_i \Omega \quad , \quad i=1,N$$

$$(2) \quad L(T) = \Omega$$

$$(3) \quad \sum_{i=1}^N Y_i = 1$$

where Y_i is the mass fraction of species i and T is the temperature. Equation (1) is a mass balance for species i (N species are in the mixture), (2) an energy balance and (3) an overall mass conservation. The spherically symmetric operator

$$L \equiv \frac{M-2r}{r^2} \frac{d}{dr} - \frac{d^2}{dr^2}$$

is convective-diffusive where M is the burning rate and r the radial coordinate ($1 \leq r < \infty$). The coefficients β_i depend in general on the stoichiometric numbers of the specific chemical reactions involved in the process and Ω is the rate of the homogeneous reaction. The boundary conditions associated with (1-3) are the given ambient conditions, namely as $r \rightarrow \infty$

$$(4) \quad T = T_\infty \quad , \quad Y_i = Y_{i_\infty} \quad \text{for } i=1,N$$

and mass and energy balances at $r=1$, which depend of course, on the specific surface chemical reactions.

For definiteness, we treat the case of a carbon sphere in an oxidizing atmosphere which outlines the way other solid fuels could be analyzed.

The surface reactions associated with carbon are the direct oxidation $2C + O_2 \rightarrow 2CO$ and the indirect reaction $C + CO_2 \rightarrow 2CO$. The carbon

monoxide thus formed may react in the gas phase surrounding the particle according to $\text{CO} + \frac{1}{2}\text{O}_2 \rightarrow \text{CO}_2$. Therefore, in the present $N=4$ and the subscripts $i=1, 4$ stand for CO , O_2 , CO_2 and inert respectively. Then the stoichiometric coefficients [4] are: $\beta_1 = -(1-\alpha)$, $\beta_2 = -\alpha$, $\beta_3 = 1$ and $\beta_4 = 0$ where α is half the molecular weights ratio of O_2 to CO_2 ($\alpha = .3636$). The reaction rate Ω becomes

$$(5) \quad \Omega = D_g \rho^2 Y_1 Y_2^{\frac{1}{2}} \exp(-\theta/T)$$

where D_g is the gas phase Damköhler number, ρ is the mixture density given by $\rho = 1/T$ and θ is the activation energy. For more details on the various assumptions made in this formalism as well as on the dimensionless analysis, reference [4] should be consulted.

The boundary conditions for the Y_i 's at $r=1$ state that the net mass flux equals the rate of consumption/production per unit area by the surface reactions. Thus

$$(6) \quad \begin{aligned} M Y_1 - Y_1' &= [(1-\alpha)/\alpha] [D_s Y_2 + 2\alpha \bar{D}_s Y_3] \\ M Y_2 - Y_2' &= -D_s Y_2 \\ M Y_3 - Y_3' &= -\bar{D}_s Y_3 \\ M Y_4 - Y_4' &= 0 \end{aligned}$$

where prime (') denotes differentiation with respect to r , and D_s, \bar{D}_s are the surface Damköhler numbers corresponding to the direct and indirect reactions respectively. We assume that the surface temperature of the particle is given, namely

$$(7) \quad T = T_s \quad \text{at} \quad r=1,$$

rather than writing an energy balance similar to (6). This simplification, made mainly for analytic convenience, can be justified for large

(1)
activation energies of the surface reactions which indeed is a realistic assumption in the present case.

There are several parameters involved in the problem: the Damköhler numbers D_g , D_s and \bar{D}_s and the burning rate M . Whereas D_g is proportional to $(ap_0)^2$ where a is the radius of the particle and p_0 the uniform ambient pressure, D_s and \bar{D}_s are proportional to ap_0 but depend on T_s as well. Thus, for a specific set of chemical reactions and for a given T_s , all the Damköhler numbers are related. In particular, the ratio $\gamma = \bar{D}_s/D_s$, is a function of T_s alone. By varying D_g from 0 to ∞ , the product ap_0 will continuously increase and we may say that D_g controls either the particle size or the ambient pressure. On the other hand, variations in γ , which measures the relative importance of the surface reactions, are determined explicitly by the surface temperature T_s . Our main goal is to determine the burning rate M and its dependence on D_g and γ .

For the general problem of a solid fuel, the right hand sides of the boundary conditions (6) will be modified to include the relevant surface reactions whereas Ω will be determined by the rate of the homogeneous reaction. As a consequence there may be several Damköhler numbers, but only two independent parameters: one associated with ap_0 and the other with T_s . We see that qualitatively the specific case considered contains the essence of the general problem although they may differ in details.

(1) The surface Damköhler number has the form $D_s = k_s \exp(-\theta_s/T)$ where k_s is the pre-exponential factor and θ_s the surface activation energy. Writing $k_s = \exp(\theta_s/T_s)$ we see that, in the limit $\theta_s \rightarrow \infty$, D_s is $O(1)$ when $T = T_s + O(\theta_s^{-1})$. Similarly, \bar{D}_s can be treated.

This would not be true for example, if only one surface reaction was considered.

THE PROBLEM

The governing equation (1,2) sum to five second order equations for the five unknowns Y_i and T . Associated with them are ten boundary conditions (4,6,7). The additional equation (3) serves to determine M . Solutions for the Y_i 's ($i=1,3$) and T involve nonlinear two point boundary value problems coupled among themselves through Ω . However, not all the equations have to be considered because the system can be simplified as follows.

We start by writing the solution for the inert species

$$(7) \quad Y_4 = Y_{4\infty} \exp(-M/r) .$$

Then, we observe that the source terms can be eliminated from both the equations and the boundary conditions at $r=1$, if a proper combination of the mass fractions is chosen. The resulting linear problem, yields

$$(8) \quad \alpha[Y_1 - Y_{1\infty} \exp(-M/r)] + (1-\alpha)[Y_2 - Y_{2\infty} \exp(-M/r)] + \\ 2\alpha(1-\alpha)[Y_3 - Y_{3\infty} \exp(-M/r)] = 0$$

Using (3) and (7) we obtain a second relation

$$(9) \quad Y_2 + \alpha Y_3 = \nu^{-1} \exp(M_\infty - M/r)$$

where $\nu = (1-2\alpha)/\alpha$ and $M_\infty = \ln[1 + \nu(Y_{2\infty} + \alpha Y_{3\infty})]$ have been introduced for convenience. (The notation M_∞ is based on the results indicating that this value corresponds to the burning rate M when all Damköhler numbers tend to infinity). Now only one mass fraction equation remains to be solved; the others result from (8) and (9).

If the boundary conditions (6) are now introduced in (9), the relation

$$(10) \quad D_s Y_{2s} + \alpha \bar{D}_s Y_{3s} = \nu^{-1} M$$

can be derived, where the subscript s in Y_2 and Y_3 denotes the surface values (at $r=1$), as yet unspecified. It is interesting to note that for the special case $\gamma=1$, (9) and (10) yields the transcendental equation

$$(11) \quad M - \bar{D}_s [\exp(M_\infty - M) - 1] = 0$$

for M . This relation, which has been derived directly from the governing equations, does not involve any approximation; the complete solution however, which will be discussed next for general γ , will be based on an asymptotic limit. We will delay the discussion on (11) to a later stage.

To summarize, we address the problem

$$(12) \quad \begin{aligned} -\alpha^{-1} L(Y_2) &= L(T) = \Omega \\ M Y_2 - Y_2' &= -D_s Y_2, \quad T = T_s \quad \text{at } r=1 \\ Y_2 &= Y_{2_\infty}, \quad T = T_\infty \quad \text{as } r \rightarrow \infty, \end{aligned}$$

after which Y_3 is determined from (9), Y_1 from (8) and M from (10). Considering the limit $\theta \rightarrow \infty$, a realistic approach for many combustion problems [6], we write

$$(13) \quad D_g = \tilde{D}_g \exp(\theta/T_c)$$

and in doing so, define a characteristic temperature $T_c = \tilde{D}_g$, which is at most algebraically large in θ , represents the small $O(\theta^{-1})$ variations⁽²⁾ from T_c and will be determined in the analysis.

(2) This can be easily seen if (13) is rewritten in the form $D_g = \exp[\theta/(T_c + \theta^{-1} T_c^2 \ln \tilde{D}_g)]$.

WEAK BURNING

The limit $D_g \rightarrow 0$ corresponding to a frozen gas phase has been previously analysed [5]. Since Ω is negligibly small for all $r \geq 1$, the problem (12) reduces to a linear one, and

$$(14) \quad \phi_i = \phi_{i_\infty} + (\phi_{i_s} - \phi_{i_\infty}) [1 - \exp(-M/r)] / [1 - \exp(-M)]$$

where ϕ stands for either T or Y_i , $i=1,3$. The values Y_{i_s} can be evaluated by applying the boundary conditions; then we obtain the transcendental equation

$$(15) \quad M - \bar{D}_s [\exp(M_\infty - M) - 1] + v(\bar{D}_s - D_s) \left\{ \frac{Y_{2_\infty}}{1 + (1 + D_s/M)(\exp M - 1)} \right\} = 0$$

for M . Note that when $\gamma=1$, (15) reduces to (11). The dependence of M on \bar{D}_s is shown in Fig. 1 for various values of γ . For small \bar{D}_s , i.e. low surface temperature T_s , the surface reactions are very weak and $M \rightarrow 0$. The burning rate M increases with \bar{D}_s and tends asymptotically to M_∞ .

According to (13) and in the limit $\theta \rightarrow \infty$ the frozen limit is obtained even for small D_g (not necessarily = 0) provided $T_c > T$; the reason being that the factor $\exp(\theta/T_c - \theta/T)$ is then exponentially small everywhere in the flow field. However, when $T_c \approx \max\{T_s, T_\infty\}$, or more precisely when T_c is close to the larger between T_s or T_∞ to within $O(\theta^{-1})$, there exists a boundary layer either adjacent to the particle or at infinity, where Ω cannot be neglected; i.e. a weak reaction develops.

For the case $T_s > T_\infty$, the solution (14) is valid for $r > 1$ and breaks down as the particle surface is reached. Stretching the coordinate near the surface, $r = 1 + \epsilon \Delta \cdot \xi$ where $\Delta = M(T_s - T_\infty) / (\exp M - 1)$ and $\epsilon = T_s^2 \theta^{-1}$, then writing

$$T = T_s + \epsilon t + \dots, \quad Y_i = Y_{i_s} + \epsilon \eta_i + \dots \quad i=1,4,$$

we obtain diffusive-reactive balances in the boundary layer. In particular, the equation for the temperature is

$$(16) \quad \begin{cases} \frac{d^2 t}{d\xi^2} + \frac{1}{2} \Lambda \exp(t) = 0 \\ t(0) = 0, \quad dt/d\xi = -1 \quad \text{as } \xi \rightarrow \infty \end{cases}$$

where $\Lambda = 2Y_{1_s} Y_{2_s} \frac{1}{2} \Delta^{-2} \theta^{-1} D_g \exp(-\theta/T_s)$. Similar equations can be written for the η_i 's. As shown in [5] the structure of the reaction zone which can be solved analytically, leads to the equation

$$(17) \quad M - \bar{D}_s [\exp(M_\infty - M) - 1] + \nu(\bar{D}_s - D_s) \left\{ \frac{\nu Y_{2_\infty} - \alpha(T_s - T_\infty)(1 + \sqrt{1 - \Lambda})}{1 + (1 + D_s/M)(\exp M - 1)} \right\} = 0$$

for the burning rate M . We see that two solutions exist for $\Lambda < 1$ and none for $\Lambda > 1$. In the limit $\Lambda \rightarrow 0$, one of the solutions reduces to that for a frozen flow (i.e. to equation (15)) while the other tends to a different limit the premixed flame, discussed later. As $\Lambda \rightarrow 1$, the two distinct solutions coincide and $\Lambda = 1$ gives the maximum value of the Damköhler number, namely $D_g^I \sim \exp(\theta/T_s)$, for which a weak gas phase burning is possible. It is appropriate to mention at this point that Y_{1_s} and Y_{2_s} appearing in Λ are defined when writing the complete solution in the boundary layer. Note again that for $\gamma = 1$, (17) reduces to (11) as it should. Furthermore, the two values for M are both higher or both lower than the corresponding value for frozen flow, depending on whether $\gamma > 1$ or $\gamma < 1$ respectively (see Fig. 2).

For the case $T_\infty > T_s$ the boundary layer is at $r = \infty$ so that, in the outer region $r < \infty$, the solution (14) is valid only to leading order. In particular, when applying the boundary conditions at $r = 1$,

we obtain (15) for M . The correction to the burning rate comes from the first order term of the outer solution after matching with the structure of the reaction zone. Stretching the coordinate by $r = \epsilon^{-1} \tilde{\Delta} \cdot R$ where $\tilde{\Delta} = M(T_\infty - T_s) / (1 - \exp(-M))$ and $\epsilon = T_\infty^2 \theta^{-1}$, then writing

$$T = T_\infty + \epsilon t + \dots, \quad Y_i = Y_{i_\infty} + \epsilon \eta_i + \dots, \quad i=1,4$$

we obtain for the temperature

$$(18) \quad \begin{cases} \frac{d^2 t}{dR^2} + \frac{2}{R} \frac{dt}{dR} + \Lambda \exp(t) = 0 \\ \lim_{R \rightarrow \infty} t(R) = 0, \quad R^2 \frac{dt}{dR} = 1 \text{ at } R = 0 \end{cases}$$

where $\Lambda = \left[T_\infty^4 Y_{1_\infty} Y_{2_\infty}^{\frac{1}{2}} \tilde{\Delta}^2 / \theta^3 \right] D_g \exp(-\theta/T_\infty)$. The condition as $R \rightarrow \infty$ reflects the original boundary conditions (4) whereas matching with (14) leads to the condition at $R = 0$. Similar equations to (18) can be written for the η_i 's; in particular they lead to

$$(19) \quad \eta_2 / \alpha + t = - [1 + (Y_{2_\infty} - Y_{2_s}) / \alpha (T_\infty - T_s)] R^{-1}$$

and other relations for η_1 and η_3 .

Now, let us include the first order $O(\epsilon)$ terms of the outer solution; writing $Y_i + \epsilon \tilde{Y}_i + \dots$, $T + \epsilon \tilde{T} + \dots$, $M + \epsilon m + \dots$, then substituting into (12), we obtain

$$(20) \quad \begin{cases} L(\tilde{Y}_2) = m r^{-2} (dY_2/dr) \\ (M + D_s) \tilde{Y}_2 - \tilde{Y}_2' = -m Y_2 \text{ at } r = 1 \\ \tilde{Y}_2 = -\alpha c \quad \text{as } r \rightarrow \infty \end{cases}$$

where the constant c is determined from matching. The solution of the linear problem (20) can be readily written and the value \tilde{Y}_{2_s} obtained in terms of c . Then, the correction to the burning rate is given implicitly by

$$(21) \quad m[1 + \bar{D}_s \exp(M_\infty - M)] + v(\bar{D}_s - D_s) \tilde{Y}_{2s} = 0.$$

We see that all is needed for the determination of m is the constant c which, in the absence of an analytical solution to (18), has to be found numerically. Using the transformation $\zeta = 1/R$, the equation takes the form $\zeta^4 t'' + \Lambda e^t = 0$ with the conditions $t(0) = 0$ and $t = -\zeta + c$ as $\zeta \rightarrow \infty$. We start by prescribing a value to c and then integrate from large ζ down to see whether $t(0) = 0$. The correct value of c is determined when both boundary conditions are satisfied. The results indicate that two distinct values for c exist when $\Lambda < \Lambda_0$ and none when $\Lambda > \Lambda_0$; the solution is unique for $\Lambda = \Lambda_0$ and this critical value is determined numerically. In the limit $\Lambda \rightarrow 0$, one of the solutions is $t = -1/R$ with $c = 0$; this corresponds of course, to the frozen limit. The other solution tends to the partial burning flame discussed later. We find again that $M(D_g)$ is double valued for $D_g < D_g^I$ and the maximum Damköhler number D_g^I depends among others on the numerical constant Λ_0 ; in particular $D_g^I \sim \exp(\vartheta/T_\infty)$.

COMPLETE BURNING

The limit $D_g \rightarrow \infty$, corresponds to an equilibrium state in which both reactants CO and O_2 are completely consumed at a flame sheet standing at a well defined distance from the particle. In [4] it has been shown that for $\bar{D}_s > \bar{D}_s^0$ where $\bar{D}_s^0 = M_s / [\exp(M_\infty - M_s) - 1]$ and $M_s \equiv \ln(1 + \nu Y_2 / 2)$ the flame is standing away from the particle at a distance $r_* = M/M_s$ and the burning rate is given by the same equation as (11). The flame temperature is then

$$(22) \quad T_e = T_s + (Y_2 / \alpha + T_\infty - T_s) (\exp(M - M_s) - 1) / (\exp M - 1)$$

where M is the solution of (11). When $\bar{D}_s \rightarrow \bar{D}_s^0$, the flame reaches the particle ($r_* \rightarrow 1$), the burning rate $M \rightarrow M_s$ and $T_e \rightarrow T_s$. For lower values than \bar{D}_s^0 , the flame is sitting at the surface, its temperature remains T_s and M is given by

$$(23) \quad M - \bar{D}_s (\exp(M_\infty - M) - 1) + 2(\bar{D}_s - D_s) (\exp(M_s - M) - 1) = 0.$$

Note the continuous transition in M as \bar{D}_s approaches \bar{D}_s^0 . The $M(\bar{D}_s)$ curve is identical to the one shown in Fig. 1 for $\gamma = 1$. For $\gamma \neq 1$, M depends on γ only for $\bar{D}_s < \bar{D}_s^0$ (see Fig. 5 in [4]) whereas for larger values of \bar{D}_s it follows the same curve as for $\gamma = 1$ and tends asymptotically to M_∞ .

It is easy to verify that in the limit $\theta \rightarrow \infty$ the equilibrium behavior is obtained for large D_g provided $T_c < T_e$; the reason being that the factor $\exp(\theta/T_c - \theta/T_e)$ is then exponentially large and as a consequence Ω is finite only if $Y_1 Y_2 \equiv 0$ (i.e. both reactants do not coexist in the outer regions). Whether the flame is adjacent to the particle surface or is in the interior of the gas phase, its thickness is exponentially small in θ and therefore, the product $Y_1 Y_2 \equiv 0$ to all

orders in θ^{-1} . However, when $T_c = T_e + O(\theta^{-1})$, the flame thickness is $O(\theta^{-1})$ and the last conclusion is no longer true; in particular when $r_* \neq 1$, $Y_2 \equiv 0$ for $r < r_*$ only to leading order. The first order term \tilde{Y}_2 where $\epsilon = T_e^2 \theta^{-1}$, should satisfy the following problem:

$$(24) \quad L(\tilde{Y}_2) = 0, \quad (M + D_s) \tilde{Y}_2 - \tilde{Y}_2' = 0 \quad \text{at } r=1, \quad \tilde{Y}_2 = \text{const. at } r=r_*-,$$

where the constant at r_*- is determined numerically from the details of the flame structure [4]. In particular, the solution for \tilde{Y}_2 leads to the corrected burning rate

$$(25) \quad M = \epsilon \{ \nu(\bar{D}_s - D_s) \tilde{Y}_{2s} [1 + \bar{D}_s \exp(M_\infty - M)]^{-1} \}.$$

When $r_* = 1$, equation (25) is still valid; $\epsilon = T_s^2 \theta^{-1}$ and \tilde{Y}_{2s} is obtained directly from the flame structure problem. In both cases, the evaluation of \tilde{Y}_{2s} indicates that for $D_g > D_g^E$ the solution is double valued and does not exist otherwise. An explicit equation was given in [4] for $D_g^E \sim \exp(\theta/T_e)$. Thus, the $M(D_g)$ curve has a turning point at D_g^E as in Figure 3. When $D_g \rightarrow \infty$, one of the solutions reduces to the equilibrium limit while the other tends to a partial burning, a case which will be discussed next. The dependence on γ is also indicated in Figure 3; the burning rate branches above its equilibrium value when $\gamma > 1$ and below it when $\gamma < 1$. The analysis in [4] was restricted to flame temperatures T_e being the maximum in the flow field. Thus, for a hot particle in a relatively cold ambient, i.e. $T_s > T_\infty$, the requirement $T_s - T_\infty < Y_2/\alpha$ was imposed whereas for a cold particle in a relatively hot ambient, i.e. $T_s < T_\infty$, the requirement is $T_\infty - T_s \leq f(T_s)$. Here, $f(T_s) = 2(\nu\alpha)^{-1} [1 - \exp(M_s - X)]$ and $X(T_s)$ satisfies $X = \bar{D}_s [\exp(M_\infty - X) - 1]$ (the dependence of X on T_s results from \bar{D}_s). The solution is therefore restricted to region I of the parameter plane $T_s - T_\infty$ (see Figure 4).

Complete burning will also occur when the particle is extremely hot or cold (regions II & III in Fig. 4), but with a flame temperature $T_* \neq T_e$ being an intermediate value in the field. The flame structure in this case is slightly different and the results will be discussed later.

PARTIAL BURNING

Under certain conditions, the flame surrounding the particle consumes only a fraction of the reactant CO and O₂. In this case, the flame temperature T_{*} is not necessarily T_e. According to (13), if T_{*} is the maximum in the field then, in the limit $\theta \rightarrow \infty$, T_{*} = T_c and Ω is exponentially small on both sides of the flame. We see in this case that T_{*} is determined explicitly by the Damköhler number D_g. If the location of the flame is denoted by r_{*} to be specified, then the temperature and mass fraction profiles are given by

$$(26) \quad \phi = \begin{cases} \phi_s + (\phi_* - \phi_s) (\exp(M-M/r) - 1) / (\exp(M-M/r_*) - 1), & \text{for } r < r_* \\ \phi_m + (\phi_* - \phi_m) (\exp(-M/r) - 1) / (\exp(-M/r_*) - 1), & \text{for } r > r_* \end{cases}$$

where ϕ stands for either Y_i, i=1,3 or T.

The structure of the flame at r_{*} is analysed by first stretching the coordinates according to $r = r_* + (2/H)\epsilon\xi$, where $\epsilon = T_*^2 \theta^{-1}$ and $H = - \{ (dT/dr)_{r_*^+} - (dT/dr)_{r_*^-} \}$; thus |H| is the magnitude of the jump in the temperature gradients across the flame. Then, perturbing all variables about their values at the flame, namely

$$T = T_* + \epsilon(t + \beta\xi) + \dots, \quad Y_i = Y_i^* + \epsilon\eta_i + \dots, \quad i=1,3,$$

where $\beta = [(dT/dr)_{r_*^+} + (dT/dr)_{r_*^-}] / H$, the resulting equation is a balance between diffusion and chemical reaction. The reaction term differs significantly whether Y₂^{*} = 0 or not; in the former case it will take the form $- \Lambda \eta_2^{1/2} \exp(t + \beta\xi)$ whereas in the latter $\eta_2(\xi)$ will be replaced by the constant Y₂^{*} ≠ 0. When, both Y₁^{*} = Y₂^{*} = 0 the complete burning structure is recovered.

We consider first the case for which $Y_2^* = 0$. This condition implies that $Y_2 = 0$ for $r < r_*$ and provides a formula for r_* given by

$$(27) \quad r_* = M / \ln \left\{ (T_\infty + Y_{2\infty} / \alpha - T_s) / [T_* - T_s + (T_\infty + Y_{2\infty} / \alpha - T_*) \exp(-M)] \right\}.$$

Now Y_1^* and Y_3^* can be readily obtained from (8), (9) and (27). Indeed $Y_{2s} = 0$ and from (9), $Y_{3s} = \exp(M_\infty - M) / (1 - 2\alpha)$, which gives once more the equation (11) for M . In writing the governing equation of the structure problem, we note that both t and $-\eta_2 / \alpha$ satisfy identical equations and, in particular, $t + \eta_2 / \alpha = \xi$ is obtained after matching with the outer solutions. Then

$$(28) \quad \begin{cases} \frac{d^2 t}{d\eta^2} = -\Lambda(\xi - t)^{1/2} \exp(t + \beta\xi) \\ \frac{dt}{d\xi} \rightarrow \pm 1 \quad \text{as } \xi \rightarrow \mp \infty \end{cases}$$

where $\Lambda = (4\alpha^{1/2} Y_1^* T_* / H^2 \theta^{3/2} a) \tilde{D}_g$. An analytical solution to (28) is not available so that a numerical integration is necessary. Using a shooting technique we start with $t = \xi + \text{const.}$ at large negative ξ and integrate out to large positive ξ to see whether $dt/d\xi = -1$ as required. The constant, determined when both boundary conditions are satisfied, equals

$$\alpha^{-1} \lim_{\xi \rightarrow -\infty} \eta_2(\xi); \text{ a value needed for matching as will be discussed next.}$$

In order to find the $O(\epsilon)$ correction to M , we consider the first order terms of the outer solution. In particular, the O_2 mass fraction for $r < r_*$ takes the form \tilde{Y}_2 . The function \tilde{Y}_2 should satisfy the same equation as (24) except that now the constant at r_* is $\lim_{\xi \rightarrow -\infty} \eta_2(\xi)$ obtained numerically from (28). After evaluating \tilde{Y}_2 the corrected burning rate follows from (25). Before discussing the numerical results, we note that after multiplying (28) by $dt/d\xi + \beta$ and integrating from $\xi = -\infty$

to $\xi = +\infty$ while making use of the boundary conditions, we obtain the restriction: $\theta > 0$. This requirement is equivalent to $T_* > T_\infty + Y_{2\infty}/2\alpha$. Another requirement comes from the assumption $Y_1^* \neq 0$ which translates to $T_* < T_e$. Thus, the solution is restricted to T_* satisfying $T_\infty + Y_{2\infty}/2\alpha < T_* < T_e$, or equivalently for a corresponding range of D_g . For such values equation (28) has been integrated as indicated above and a unique solution was found for each D_g ; then the curve $M(D_g)$ has a unique branch in this range.

The next case under consideration is when both Y_1^* and Y_2^* are $O(1)$. As indicated previously, $\tau_2^{1/2}$ in the reaction term is now replaced by the constant $(Y_2^*)^{1/2}$ and as a consequence $\tilde{\Lambda} = (Y_2^* \theta / \alpha T_*^2)^{1/2} \Lambda$ replaces Λ ; then a first integration of the governing equation leads to $\beta = 0$ (3). This condition states that $(dT/dr)_{r_*+}$ and $(dT/dr)_{r_*-}$ have the same magnitude but opposite signs. When applied, this condition provides a formula for r_* , namely

$$(29) \quad r_* = M / \ln \{ (2T_* - T_s - T_\infty) / [(T_* - T_s) + (T_* - T_\infty) \exp(-M)] \},$$

after which Y_i^* , $i=1,3$ can be easily evaluated. The boundary conditions at $r=1$ determine the Y_{i_s} 's and M is obtained from

$$(30) \quad M - \bar{D}_s [\exp(M_\infty - M) - 1] + v(\bar{D}_s - D_s) \left\{ \frac{Y_{2\infty} - 2\alpha(T_* - T_\infty)}{1 + (1 + D_s/M)(\exp M - 1)} \right\} = 0.$$

Although one can proceed in calculating the first order correction to M with no conceptual difficulties, there is no immediate need for such an improvement presently because, unlike previous cases, the leading order of M given by (30) establishes the dependence of M on D_s , \bar{D}_s as well

(3) An analytical solution for the structure problem can be written in this case (e.g. see [7]) but such details will not be discussed in the present.

as on D_g (through T_*). Note that the only condition we have required in deriving (30) is that both reactants do not vanish at the flame which can also be written as $T_* < T_\infty + Y_{2\infty} / 2\alpha$. Therefore, the $M(D_g)$ curve thus obtained is restricted to a certain range of D_g corresponding to $\max\{T_s, T_\infty\} < T_* < T_\infty + Y_{2\infty} / 2\alpha$.

Partial burning will also occur when the particle is extremely hot or cold (regions II & III in Fig. 4), but the flame temperature in this case is at an intermediate value between T_s and T_∞ . The resulting response will be discussed later.

RESPONSE CURVES

In constructing the response of M versus D_g , we consider first region Ia in the parameter plane $T_s - T_\infty$ (see Fig. 4). Starting with small values of D_g , the gas phase is completely frozen and M increases with D_g according to (15). Indeed, the burning rate is controlled only by the surface reactions. By slightly increasing D_g , a weak reaction $\text{CO} + \text{O}_2$ develops in a boundary layer adjacent to the particle surface (because $T_s > T_\infty$). Now M is given by one of the solutions of (17) corresponding to the minus sign in front of the square root. The burning rate exceeds its frozen value or is below it, depending on whether γ is greater or less than one, respectively. This behavior persists until the values D_g^I is reached (or Λ in (17) becomes 1). The response then follows the second solution of (17) while D_g decreases below D_g^I . Therefore, D_g^I marks a turning point of the response curve. This second branch tends eventually to a partial burning flame obtained when $\Lambda \rightarrow 0$ in (17) or, on the other hand, when $T_* = T_s$ in (30). The flame in this limit is adjacent to the particle as suggested by (29). The Damköhler number D_g can be further decreased as T_* increases from T_s to T_e . The flame, which first consumes only a small portion of the reactants CO and O_2 , moves away from the particle according to (29), uses more of the reactants and its temperature T_* increases, simultaneously. The burning rate is now given by (30). When the intermediate value $T_* = T_\infty + Y_{2\infty}/2\alpha$ is reached all the oxygen is consumed at the flame ($Y_2^* = 0$) and (30) for M reduces to (11)⁽⁴⁾.

(4) Although the correction to the burning rate has to be added to M obtained from (11) as described earlier, the leading term in this case is only slightly perturbed and therefore determines the main behavior of the curve. This is not so when complete burning occurs.

Although all the oxygen is depleted at the flame, only a fraction of CO is burnt and $Y_1^* \neq 0$. This behavior persists while decreasing D_g until $T_* \approx T_e$; in this limit a complete burning of reactants take place. Now, the flame is at $r_* = M/M_s$ and the corrected burning rate given by (25) is double valued for all $D_g < D_g^E$. Thus, we first follow one of the branches down to D_g^E which marks a turning point in the response curve. Then increasing D_g again, the other solution of (25) takes over; now the Damköhler number can be increased indefinitely and the burning rate tends asymptotically to M_∞ . Along the branches resulting from complete burning, the flame temperature remains at most within $O(\theta^{-1})$ from T_e and the flames moves $O(\theta^{-1})$ distances from $r_* = M/M_s$. Note that for $\gamma > 1$, M approaches the equilibrium limit from below whereas for $\gamma < 1$ it approaches this limit from above.

In region Ib, the construction of the response curve follows the same outlines indicated previously. However, the physical states followed along the curve are slightly different. Since here $T_\infty > T_s$, the reaction $\text{CO} + \text{O}_2$ starts being active at large distances from the particle until D_g^I is reached, then by decreasing D_g , the weak burning tends to partial burning and a flame thus formed moves towards the particle. The flame temperature T_* increases from T_∞ up to T_e along this branch and when complete burning is achieved the flame is located at $r_* = M/M_s$. Reaching the point D_g^E , the Damköhler number can be only increased again and now indefinitely, so that in the limit $D_g \rightarrow \infty$, the burning rate tends to M_∞ .

The response curves in region I are characterized by having multiple solutions for $D_g^E < D_g < D_g^I$, because

$$D_g^E \sim \exp(\theta/T_e), \quad D_g^I \sim \begin{cases} \exp(\theta/T_s), & \text{for } T_s > T_\infty \\ \exp(\theta/T_\infty), & \text{for } T_\infty > T_s \end{cases}$$

and therefore D_g^I always exceeds D_g^E in this region. It is generally believed that the middle branch is unstable and therefore the corresponding states cannot be realized physically. Some evidence are found in [8] and [9] for example. Indeed the concepts of ignition and extinction depend on these facts. For, if D_g is slowly increased the weak burning solution is followed up to D_g^I where the response jumps to the complete burning solution and it follows that as D_g is increased further. Thus, D_g^I marks the gas-phase ignition. Similarly, D_g^E is the extinction value since the response jumps from a complete burning to a nearly frozen flow.

The parameter γ , representing the relative importance of the two competitive surface reactions, is a function of T_s alone. Thus, assuming $\gamma > 1$ for large T_s (suggested by various experimental data reported in the literature), the parameter plane $T_s - T_\infty$ is divided as in Fig. 4. When $\gamma < 1$ (see Fig. 1), M for frozen flow is lower than M for equilibrium and the response curve is S-shaped. As γ approaches one from below, the middle branch of the S curve coalesce to a single monotonic curve which represents both the frozen and equilibrium limits. Although the three distinct solutions in the range $D_g^E < D_g < D_g^I$ have the same value for M , they still differ in details. They have a different flame temperature, consume different portion of reactants and the flame is located at different positions. As γ increases slightly above one, M takes again different values for each of the three solutions but now the upper and lower branches change their roles. The response curve is now z-shaped. Thus depending on whether γ is less or greater than one, the jump at ignition occurs from a lower to a higher M and vice versa, respectively. The reverse is true at extinction.

When $\gamma = 1$, the burning rate varies continuously along the curve but a jump in the flame temperature, from T_s (or T_∞) to T_e occurs at ignition while the flame suddenly appears at $r_* = M/M_s$. The reverse situation occurs at extinction.

Finally, we will discuss the extreme cases of a very hot (region II in Fig. 4) particle. When $T_s > T_\infty + Y_{2\infty}/\alpha$, the weak burning solution is no longer double valued because one of the solutions of (17) (namely that with the + sign) gives rise to $Y_{2s} < 0$ and is not physically acceptable. Furthermore, its structure differs slightly at an intermediate value of $\Lambda < 1$ as Y_{2s} vanishes and remains so as Λ increases towards 1. The only change in (17) is the replacement of the last $O(1)$ term on the right hand side by an $O(T_s^2 \theta^{-1})$ term. Here D_g can be increased beyond D_g^I and the resulting partial burning flame with complete oxygen depletion ($Y_2^* = 0$), moves away from the particle and its temperature T_* is lowered (5) below T_s . While increasing D_g further, a point is reached where $Y_1^* = 0$, i.e. now the CO is also completely depleted at the flame. Both the partial and the complete burning flames obtained in this case differ slightly from those discussed previously. No leakage of O_2 is allowed through the flame and $Y_2 \equiv 0$ for $r < r_*$ to all orders. As a consequence the burning rate M is given by (11) to all orders in θ^{-1} . Furthermore, the structure of the complete burning flame is unique (6) leading to a single branch of the response

(5) Although T_* is no longer the maximum temperature in the field, Ω is still negligibly small on both sides of the flame because where $T > T_*$ either Y_1 or Y_2 vanish identically to all orders, whereas for $T < T_*$ the previous argument holds.

(6) In [4] the structure was discussed only for $|\beta| < 1$ and the solution was double valued. For $|\beta| > 1$, a unique solution exists for all Λ .

curve. The $M(D_g)$ curve obtained now is a monotonic curve which tends asymptotically to M_∞ .

In region III, the response is again monotonic but now, the partial burning flame originating at infinity is of a different type. CO is totally consumed at the flame ($Y_1^* = 0$) but oxygen is not. As D_g increases and the flame approaches the particle, the flame temperature T_* is lowered below T_∞ until a point is reached where Y_2^* also vanishes. The complete burning thus obtained does not allow any CO leakage, but O_2 can leak through and as a consequence M is given by (11) to leading order. The $O(\theta^{-1})$ correction is unique, leading to a single branch of the response curve. The $M(D_g)$ curve is again a monotonic curve.

In summary, two distinct response curves are found. The monotonic curve obtained in regions II and III, show the gradual transition from a frozen gas phase through partial burning to equilibrium, as D_g increases (by increasing the particle size for example). The reason for such a smooth behavior is due to the excess of heat provided either by the particle or by the ambient. For moderate values of T_s and T_∞ the process is described by the S or Z responses (region I), which exhibit the phenomenon of ignition and extinction. A flame is suddenly ignited as D_g increases slightly above D_g^I and is extinguished as D_g decreases slightly below D_g^E . The transition from frozen gas phase to equilibrium is abrupt in this case.

References

- 1) Spalding, D. B. (1955), Some Fundamentals of Combustion, Gas Turbine Series, Vol. 2, Butterworths, London.
- 2) Nusselt, W. Z. (1924), Ver. Deut. Ing., 68, 124.
- 3) Burke, S. P. and Schumann, T. E. W. (1931), Proc. Third Int. Bituminous Coal, 2, 485.
- 4) Matalon, M. (1980), Complete Burning and Extinction of a Carbon Particle in an Oxidizing Atmosphere, Combust. Sci. and Technol., to appear.
- 5) Matalon, M. (1980), Weak burning and gas-phase ignition about a carbon particle in an oxidizing atmosphere, Combust. Sci. and Technol. to appear.
- 6) Ludford, G. S. S. (1977), Combustion: Basic Equations and Peculiar Asymptotics, J. Mecanique, 16, 531-551.
- 7) Ludford, G. S. S., Yanitell, D. W. and Buckmaster, J. D. (1976), The Decomposition of a Cold Monopropellant in an Inert Atmosphere, Combust. Sci. and Technol., 14, 133-146.
- 8) Peters, N. (1978), Linán's premixed flame stability, Combust. Flame, 33, 315.
- 9) Matalon, M. and Ludford, G. S. S. (1980), On the Near Ignition Stability of Diffusion Flames, Int. J. Engr. Sciences, 18, 10.

Captions

Fig. 1

The solution of equation (11) for various values of γ ; calculated for representative values of the ambient conditions:

$$Y_{1\infty} = .05 , \quad Y_{2\infty} = .3 , \quad Y_{3\infty} = .2$$

Fig. 2

The weak burning solution: (a) for $\gamma > 1$, (b) for $\gamma < 1$; calculated for $T_s > T_\infty$ and for representative values of the other parameter.

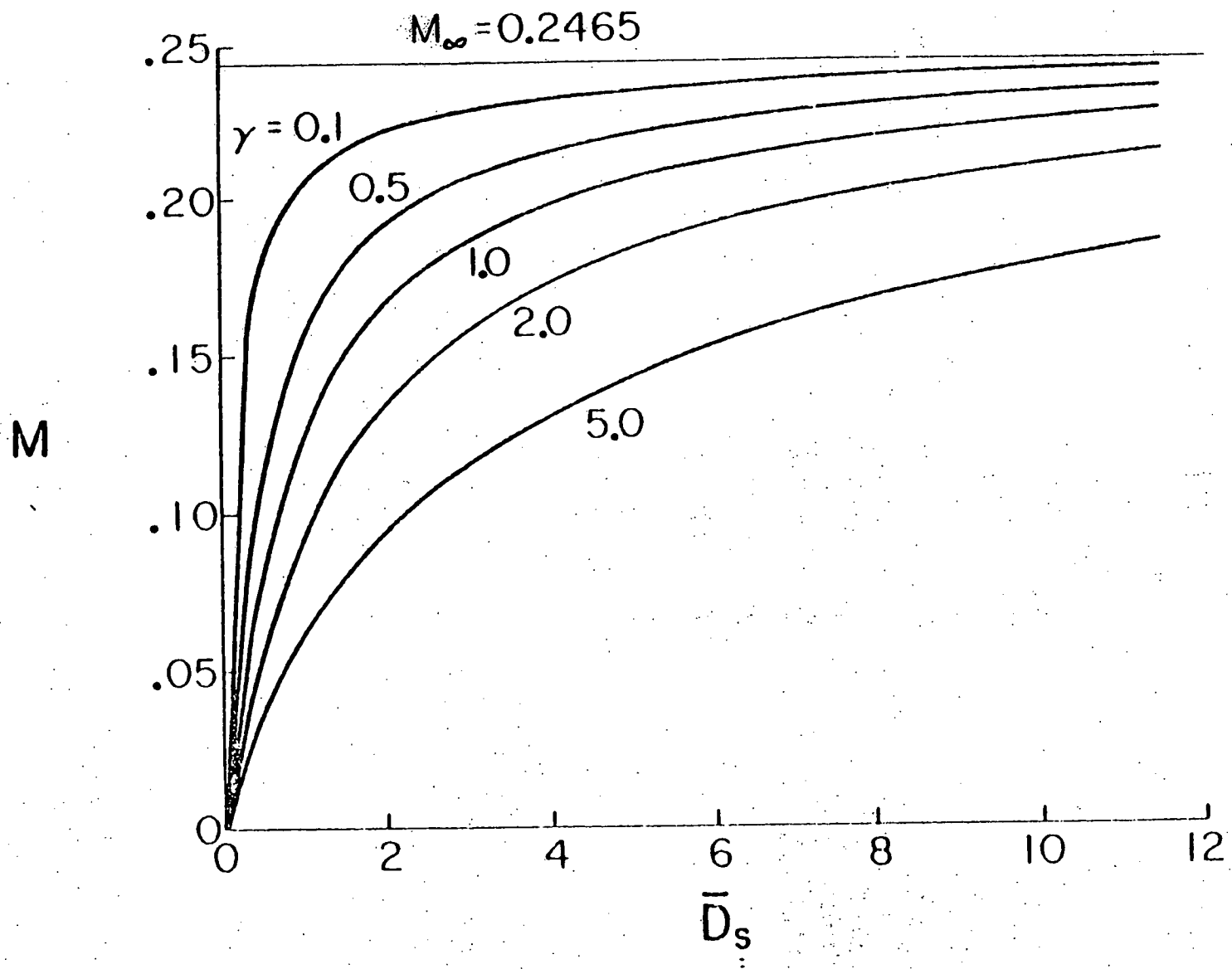
$$\text{Here } \tilde{D}_g = D_g \exp(-\theta/T_s).$$

Fig. 3

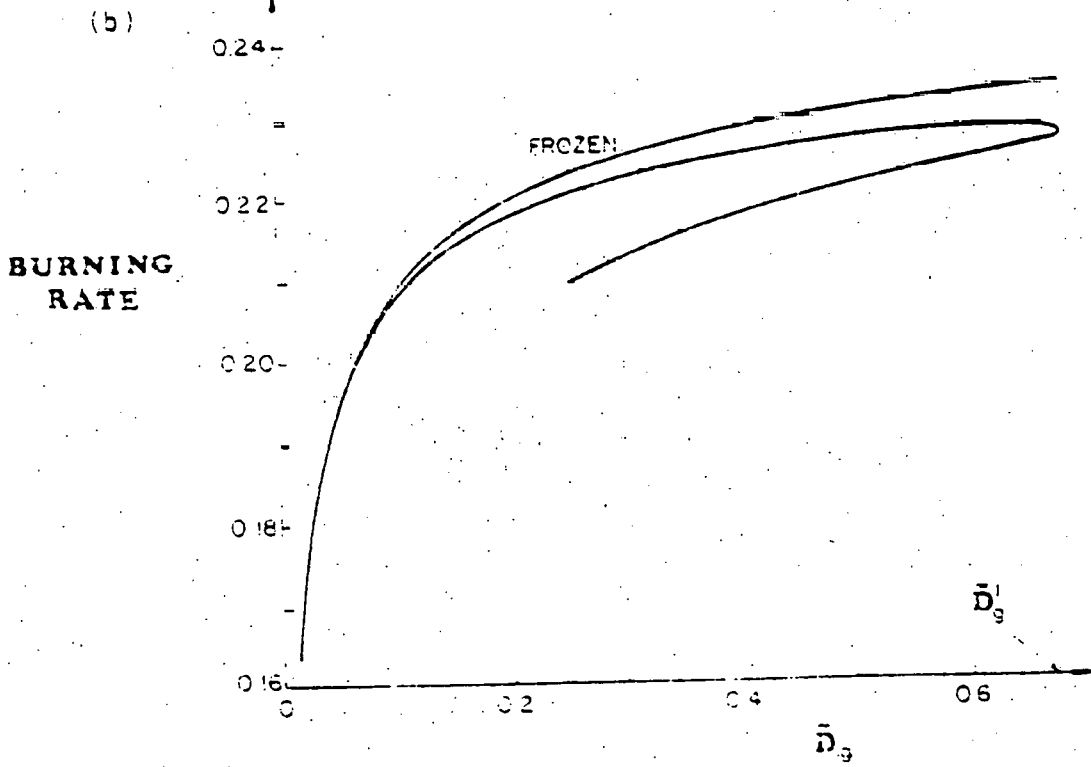
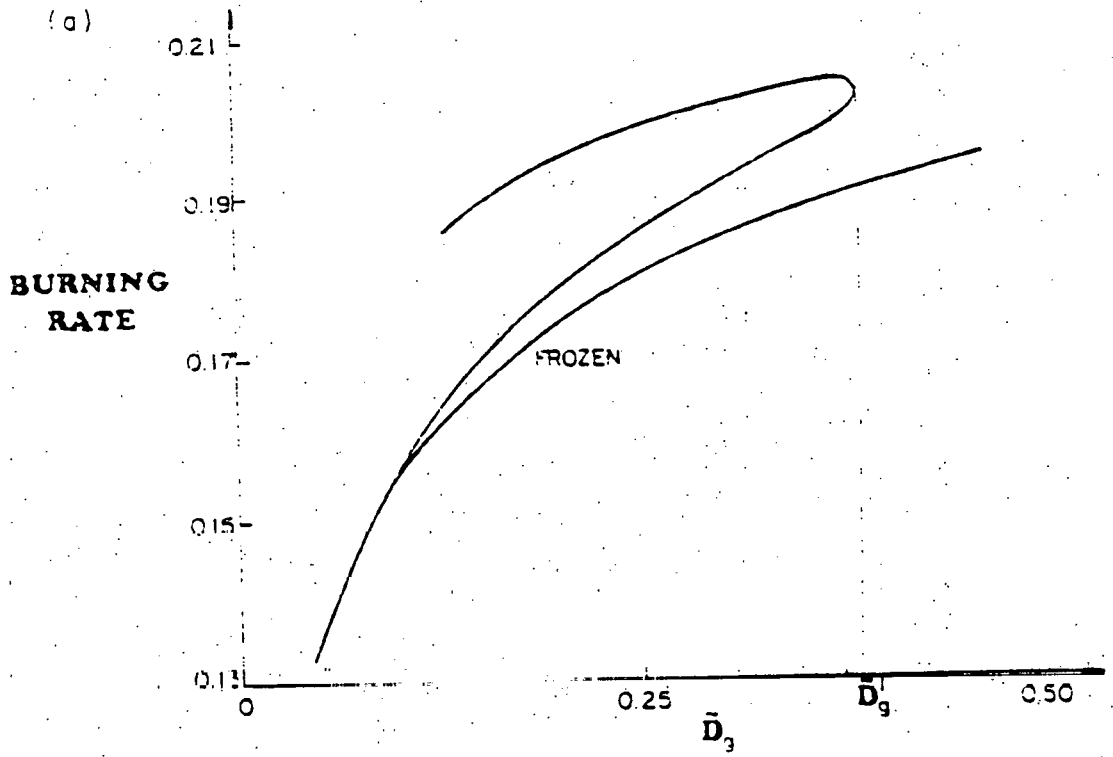
The complete burning solution: (a) for $\gamma > 1$, (b) for $\gamma < 1$; calculated for some representative values.

Fig. 4

The response curves in the different regions of the parameter plane $T_s - T_\infty$. The broken lines with the F,E notation represent the frozen and equilibrium limits, respectively. D_g^I and D_g^E are the ignition and extinction Damköhler numbers respectively.



$\gamma = 1$
(



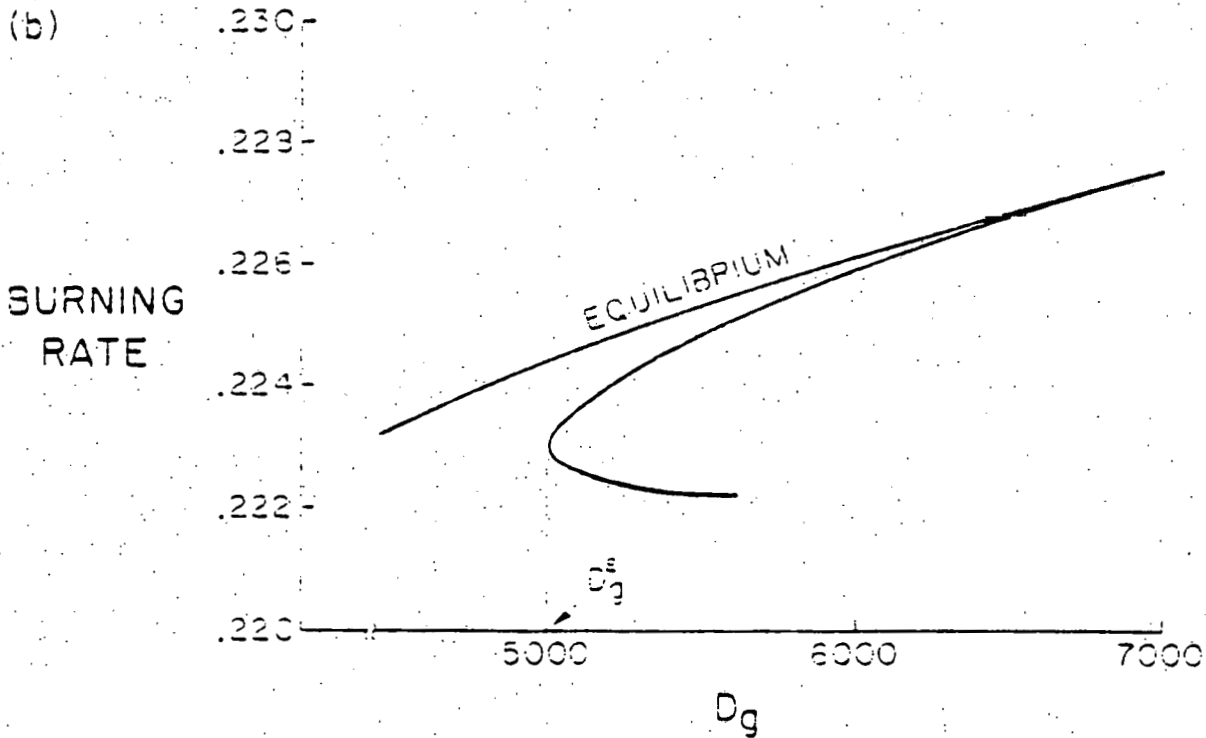
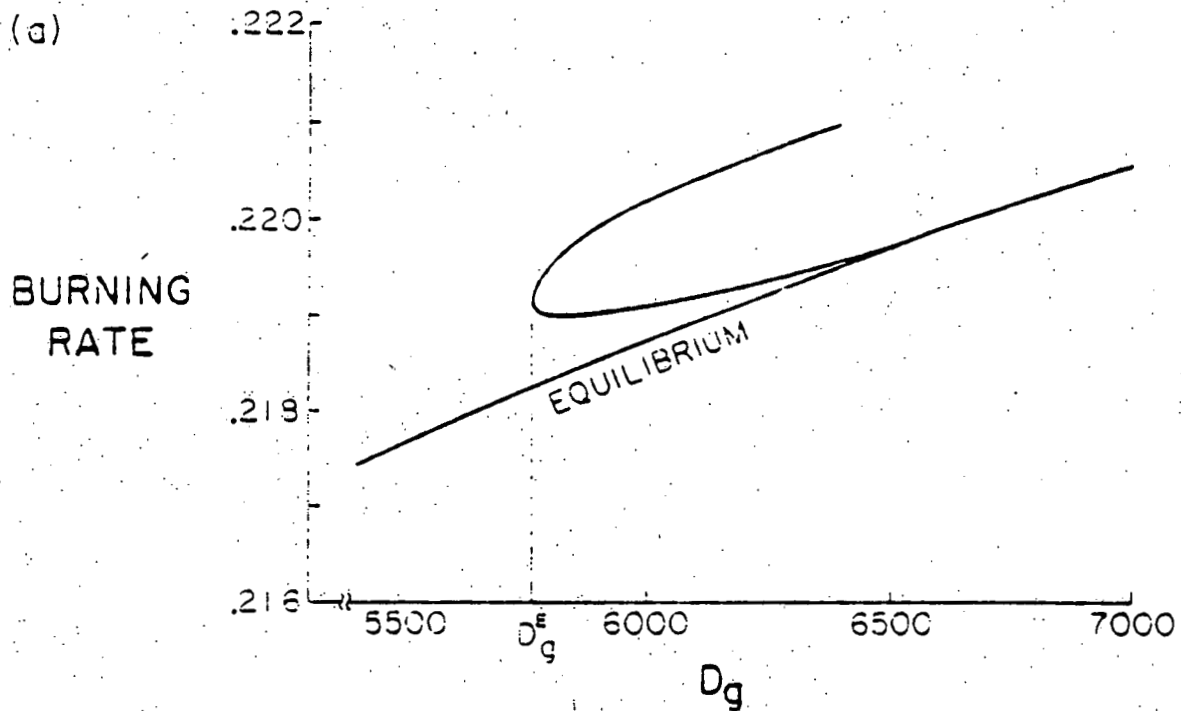


Fig 3

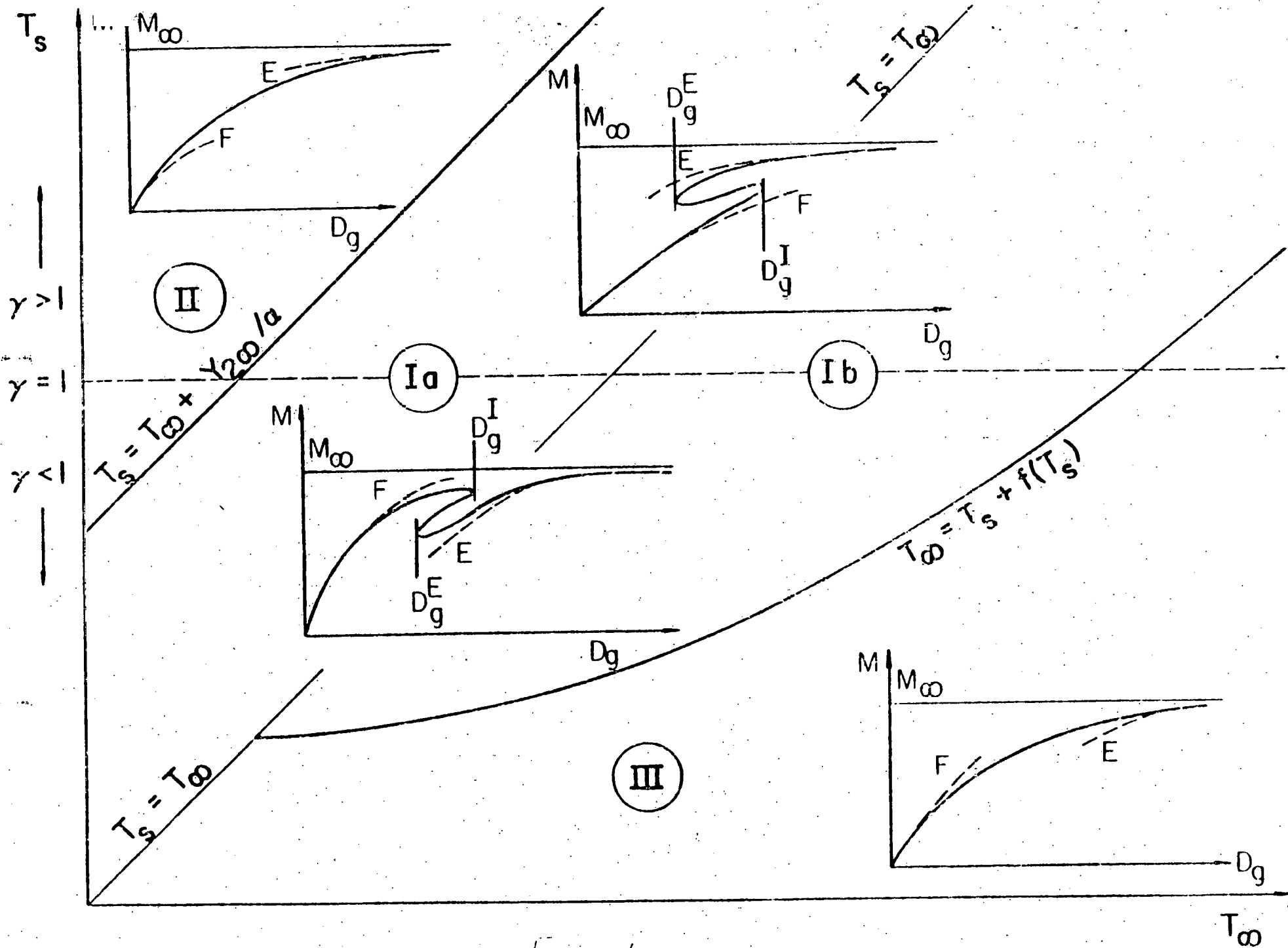


Fig. 4